Final Report:
The Role of Microstructure on the Fatigue
Durability of Aluminum Aircraft Alloys

Paul E. Magnusen
Robert J. Bucci
Andrew J. Hinkle
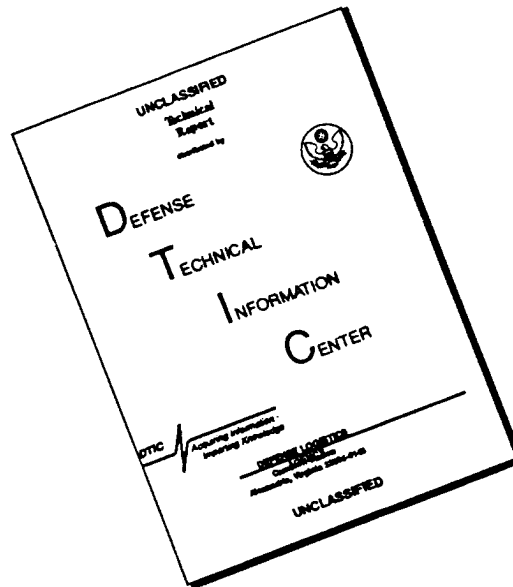John R. Brockenbrough
Harold J. Konish
Shelly M. Miyasato*
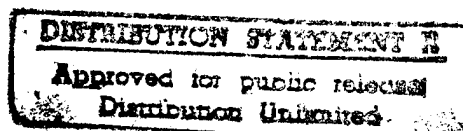
Alcoa Technical Center
*Formerly Alcoa Technical Center

November 1995

19960529 102

DISCLAIMER NOTICE

THIS DOCUMENT IS BEST QUALITY AVAILABLE. THE COPY FURNISHED TO DTIC CONTAINED A SIGNIFICANT NUMBER OF PAGES WHICH DO NOT REPRODUCE LEGIBLY.

SECURITY CLASSIFICATION OF THIS PAGE

REPORT DOCUMENTATION PAGE

1a. REPORT SECURITY CLASSIFICATION Unclassified	1b. RESTRICTIVE MARKINGS
2a. SECURITY CLASSIFICATION AUTHORITY	3. DISTRIBUTION/AVAILABILITY OF REPORT Approved for public release; distribution unlimited
2b. DECLASSIFICATION/DOWNGRADING SCHEDULE	
4. PERFORMING ORGANIZATION REPORT NUMBER(S)	5. MONITORING ORGANIZATION REPORT NUMBER(S)

6a. NAME OF PERFORMING ORGANIZATION Aluminum Company of America	6b. OFFICE SYMBOL (If applicable)	7a. NAME OF MONITORING ORGANIZATION Office of Naval Research

6c. ADDRESS (City, State and ZIP Code) Alcoa Technical Center 100 Technical Drive, Alcoa Center, PA 15069-0001	7b. ADDRESS (City, State and ZIP Code) 800 N. Quincy Street Arlington, VA 22217-5660

8a. NAME OF FUNDING/SPONSORING ORGANIZATION Office of Naval Research	8b. OFFICE SYMBOL (If applicable) Code-332	9. PROCUREMENT INSTRUMENT IDENTIFICATION NUMBER N00014-91-C-0128

8c. ADDRESS (City, State and ZIP Code)
800 N. Quincy Street
Arlington, VA 22217-5660

10. SOURCE OF FUNDING NUMBERS

PROGRAM ELEMENT NO.	PROJECT NO.	TASK NO.	WORK UNIT ACCESSION NO.
61153N			

11. TITLE (Include Security Classification)
The Role of Microstructure on the Fatigue Durability of Aluminum Aircraft Alloys

12. PERSONAL AUTHOR(S)
P. E. Magnusen, R. J. Bucci, A. J. Hinkle, J. R. Brockenbrough, H. J. Konish and S. M. Miyasato

13a. TYPE OF REPORT Final	13b. TIME COVERED FROM 91/09/16 TO 95/12/15	14. DATE OF REPORT (Year, Month, Day) 96/04/15	15. PAGE COUNT 178

16. SUPPLEMENTARY NOTATION

17. COSATI CODES			18. SUBJECT E TERMS (Continue on reverse if necessary and identify by block number
FIELD	GROUP	SUB-GROUP	Aluminum, Fatigue, Microstructure effects, Alloy 7050, Durability, Thick plate, Crack initiation and growth, Fatigue life prediction, Fracture mechanics
11	07		
11	06	01	

19. ABSTRACT (Continue on reverse if necessary and identify by block number)

Although the role of microstructure on the initiation and growth of fatigue cracks, and thus the fatigue performance of a structural metal, has long been recognized, quantitative models of the linkage(s) between microstructural characteristics and structural fatigue performance have not been widely available. The absence of such models, coupled with the compositional basis of material specifications, has limited the ability to exploit improvements in material performance which have been generated by microstructural consequences of manufacturing process improvements. The potential performance benefits of quality-improved materials have thus remained inaccessible to airframers, who lack the means of specifying such materials or characterizing their merits without committing massive testing resources. Opportunities for reducing airframe weight and/or cost have thus been lost.

A program of experimental and analytical tasks has been conducted to develop a path for defining the linkage(s) between microstructural characteristics and fatigue performance in an aluminum alloy typically used for airframe structural applications. Within the framework of this overall objective, life-limiting microstructural features have been classified and ranked by severity, and models to quantitatively describe the evolution and growth of macrostructural cracks from those features have been developed. The use of these models to probabilistically describe the structural implications of different levels of microstructural quality has been demonstrated, thereby allowing the effects of material pedigree to be predictively linked with the structural integrity of end components.

The focus of this work was on several process variants of aluminum alloy 7050-T7451 thick plate. This was dictated by customer interest, the widespread use of thick plate for flight-critical airframe structural components, and the particular characteristics associated with the manufacturing, service, and maintenance of thick section components. Despite this very specific basis, the results of this contracted activity are expected to be generally applicable to other structural metals as well. The conceptual framework developed within this program is also broadly applicable to evaluating structural implications of extrinsic damage forms introduced during manufacturing or service (e.g., corrosion pits, scratches, tool marks) in addition to intrinsic microstructural features.

Implications of the program results are broad and far-reaching. The modeling framework has potential applications in the airframe design process, and is a potentially significant enabler for the material and product form selection processes. It also provides an avenue for predictively assessing the implications of manufacturing and maintenance operations on airframe structural integrity, and thus, on service life. A number of validation and demonstration tasks must be conducted, however, before the full potential of the basic technology can be realized.

20. DISTRIBUTION/AVAILABILITY OF ABSTRACT ☐ UNCLASSIFIED/UNLIMITED [X] SAME AS RPT ☐ DTIC USERS	21. ABSTRACT SECURITY CLASSIFICATION Unclassified
22a NAME OF RESPONSIBLE INDIVIDUAL Dr. L. E. Sloter	22b. TELEPHONE (Include Area Code) (703) 696-1453	22c. OFFICE SYMBOL Code-332

DD FORM 1473, 84 MAR   83 APR edition may be used until exhausted   SECURITY CLASSIFICATION OF THIS PAGE
                            All other editions are obsolete   UNCLASSIFIED

Abstract

Although the role of microstructure on the initiation and growth of fatigue cracks, and thus the fatigue performance of a structural metal, has long been recognized, quantitative models of the linkage(s) between microstructural characteristics and structural fatigue performance have not been widely available. The absence of such models, coupled with the compositional basis of material specifications, has limited the ability to exploit improvements in material performance which have been generated by microstructural consequences of manufacturing process improvements. The potential performance benefits of quality-improved materials have thus remained inaccessible to airframers, who lack the means of specifying such materials or characterizing their merits without committing massive testing resources. Opportunities for reducing airframe weight and/or cost have thus been lost.

A program of experimental and analytical tasks has been conducted to develop a path for defining the linkage(s) between microstructural characteristics and fatigue performance in an aluminum alloy typically used for airframe structural applications. Within the framework of this overall objective, life-limiting microstructural features have been classified and ranked by severity, and models to quantitatively describe the evolution and growth of macrostructural cracks from those features have been developed. The use of these models to probabilistically describe the structural implications of different levels of microstructural quality has been demonstrated, thereby allowing the effects of material pedigree to be predictively linked with the structural integrity of end components.

The focus of this work was on several process variants of aluminum alloy 7050-T7451 thick plate. This was dictated by customer interest, the widespread use of thick plate for flight-critical airframe structural components, and the particular characteristics associated with the manufacturing, service, and maintenance of thick section components. Despite this very specific basis, the results of this contracted activity are expected to be generally applicable to other structural metals as well. The conceptual framework developed within this program is also broadly applicable to evaluating structural implications of extrinsic damage forms introduced during manufacturing or service (e.g., corrosion pits, scratches, tool marks) in addition to intrinsic microstructural features.

Implications of the program results are broad and far-reaching. The modeling framework has potential applications in the airframe design process, and is a potentially significant enabler for the material and product form selection processes. It also provides an avenue for predictively assessing the implications of manufacturing and maintenance operations on airframe structural

integrity, and thus, on service life. A number of validation and demonstration tasks must be conducted, however, before the full potential of the basic technology can be realized.

Contents

List of Figures

List of Tables

Acknowledgments

9(PEM)PDM

1. Introduction

Cracks in metallic structural components caused by cyclic fatigue loads are a major threat to airframe structural integrity and a significant contributor to retirements of airframes from service [1-9]. All metallic airframe structures will ultimately develop cracks as a result of cyclic service loads, either in isolation or in potentially synergistic combination with other damage mechanisms such as corrosion. In the absence of remedial actions, these cracks will grow as a result of continued cyclic service loads, with consequent degradation of airframe structural integrity and subsequent deleterious effects on aircraft serviceability and operating economics [1, 6, 10, 11]. Design and operation of safe, reliable, and cost-effective metallic airframes thus requires data and analytical methods for predicting the origination and growth of cracks, as well as their implications with regard to airframe structural integrity. These technical tools provide the basis for defining safe operating limits, efficient maintenance practices, and meaningful estimates of system reliability [5, 9, 12-19].

Aircraft fleet operators and regulatory agencies have developed a variety of protocols for assuring that adequate levels of airframe structural integrity are maintained during service. The U.S. Navy, for example, has historically adopted the approach of requiring component repair or replacement when a detectable macroscopic crack is discovered [15]. The U.S. Air Force has adopted a more rigorous approach to schedule inspections based on design for slow crack growth in rogue defective parts. The Air Force approach affirms fail-safety by assuring that partial failure will be found through a sequence of scheduled inspections designed to promptly detect cracks and remove from service, cracked components that would fail catastrophically prior to the next scheduled inspection [5, 12, 13]. The Federal Aviation Administration has largely adopted the Air Force approach in its requirements for commercial aircraft fleets, but also requires demonstration that catastrophic failure (loss of aircraft) is not probable after obvious partial structural failure, such as that imposed by the classical severed stiffener, two-bay crack criteria [6, 8, 16-18].

While these protocols aim to assure adequate margins of safety for airframe structures, they are directed toward detection and characterization of macroscopic cracks, i.e., those which are large in relation to the microstructural scale of the material. Although it is cracks of this scale which are the most immediate threats to airframe structural integrity, initiation and growth of cracks at the microstructural scale, and the growth of these cracks to a macrostructural scale is not explicitly addressed by the traditional structural integrity assessment protocols. The microcrack initiation and early-stage crack growth processes, which occupy the largest portion of a component's serviceable fatigue life (Figure 1.1), are instead commonly integrated into

experience based design rules and procedures for setting cyclic operating stress allowables. These procedures, which integrate all aspects of representative structural element tests, full component tests, and fleet experience, have had a long history of satisfactory service. They are highly empirical in nature, however, and the large degree of scatter inherent to fatigue test data often requires generous factors of safety in the design process. The inherent variability of fatigue data also dictates significant levels of testing effort to characterize sensitivities to material, specimen configuration and loading conditions on structural element test response and its linkage to actual component performance.

Alternative approaches for describing and predicting the processes of microcrack initiation and growth are needed to improve efficiencies of airframe design and airworthiness assurance processes, and to facilitate the introduction, acceptance, and exploitation of new and improved metallic materials. This need is increasing, as the rising cost of replacing aging aircraft with newer ones becomes increasingly untenable in times of reduced military budgets and lower civilian transport revenues.. Operators of both civil and military fleets are now faced with the necessity of extending the service lives of their aircraft far beyond those envisioned during design. The consequent need to contend with ever-increasing levels of airframe fatigue damage will require greater levels of increasingly sophisticated attention to airframe fatigue damage and its structural integrity implications.

Existing understanding of the fatigue damage process can be applied to produce the needed alternatives to traditional fatigue design approaches. It has long been accepted within the technical community that development of fatigue damage in a metallic structural element begins at the microstructural level. In most cases the process involves the interaction of remote cyclic stresses, coupled with the stress concentrating effect of notched structural details (e.g., a fastener hole or web-rib fillet) that locally constrains capacity of the material to absorb the energy of loading and a crack is formed. Postmortem evaluations of mild and/or blunt notched element failures reveal that lower bound fatigue strength is often linked to accelerated microcrack formation and growth originating from either intrinsic inhomogeneities (e.g., micropores, particles) or extrinsic inhomogeneities associated with specimen manufacture (e.g., tool marks) and/or simulated in-service damage (e.g., corrosion pits, joint fretting). With continued applications of cyclic loads, the emerging lead macrocrack grows to a terminal size at which rapid fracture ensues. Rates of microcrack growth and coalescence can be accelerated by other microstructural inhomogeneities, which may locally increase the stress field at the tip of the advancing microcrack and/or create secondary microcracks which subsequently link with the lead crack.

9(PEM)PDM   2

The initiation of microcracks and their growth to macrostructural size comprise a large portion of the total fatigue life of a structural component. Results from a number of investigations suggest that fatigue microcracks frequently originate at microfeatures on the scale of 0.0005 inch to 0.020 inch at a relatively early stage of the fatigue process, and that propagation of these cracks to macrostructural size often occupies a large percentage (50% to 90%) of the fatigue life, regardless of applied cyclic stress levels [10, 19-49]. Once the crack reaches a macrostructural size (at which point it becomes a detectable flaw), its rate of fatigue growth is usually fast enough to require prompt remedial action to assure continued component functionality. The microcrack initiation and growth processes are thus the keys to structural fatigue performance of metallic airframe components. The distribution and size of microfeatures, in turn, are the keys to microcrack initiation and growth.

Although the role of microstructure on structural fatigue performance has been widely recognized for some time, a quantitative link between microstructural quality of a material and fatigue performance of a structural component has not evolved. Because existing materials specifications reflect only static mechanical properties, chemical composition and product form, the absence of a predictive model for the fatigue implications of microstructural quality has inhibited attempts to exploit improvements in material performance which have been generated by microstructural consequences of processing improvements. While this shortcoming affects all types of metallic aerospace structural materials, it is particularly significant in the case of thicker product forms such as forgings, thick plate, and thick extrusions.

Several factors contribute to the particular importance of the microstructure/fatigue link in thick product forms. Microstructural uniformity is much more difficult to achieve in thick product forms than in their thinner counterparts, due to practical limitations in foundry, heat-treating, and mechanical-working practices. Thick product forms thus inherently exhibit higher densities of larger microstructural features with the potential of initiating macrocracks than do thinner product forms. The cost of thick product forms is relatively high, and their use may entail significant machining effort. They are thus significant investments, which sometimes require substantial production lead times. These types of products are commonly used for internal airframe structure, moreover, which increases the difficulty and cost of inspection and repair or replacement procedures. Thick internal components are also relatively immune from macrostructural service damage such as nicks and dings, which elevates the importance of microstructural features as the initiator of life-limiting damage.

The need to more accurately and predictively model the effects of microstructural characteristics on structural fatigue performance led the Office of Naval Research (ONR) to initiate a program

toward that end in 1991. In addition to related programs investigating steels, nickel based alloys, polymers and electronic materials, a program was initiated to examine and model microstructural influences in thick aluminum based structural airframe components. This program consisted of two parallel elements, one conducted at UCLA under the direction of Professor M. A. Przystupa of the Department of Materials Science and Engineering, and one conducted at the Alcoa Technical Center. The latter element of the ONR program is described in this report.

1.1 Objectives

The overall objective of the work reported herein was to establish a technical path for quantitatively and predictively defining the effects of microstructural characteristics on the fatigue performance of thick-section metallic airframe structural components. This objective was intended to support a number of fundamental technical needs. Development of the technical path would improve the predictability of durability and damage tolerance characteristics for thick-section airframe structural components beyond the level achievable with existing technology. It would also establish a technical basis for defining guidance to extend the service lives of such components beyond the conservative bounds dictated by the uncertainties of current technology. The envisioned technical path would also provide insights into ways to improve the fatigue performance of thick-section product forms of metallic aerospace products by process control of microstructural characteristics.

A number of subsidiary objectives were defined within the context of the overall program objective. These subsidiary objectives, all of which support the main program objective, are the goals for the main phases of the program. The first such goal is to develop data for quantitatively linking measurable characteristics of material microstructure with long-term fatigue performance. The second phase goal was to develop models to predict fatigue performance based on the microstructural characteristics, and apply the data and models to generate quantitative results which would demonstrate the potential fatigue performance improvements to be realized from the use of material and process controls which reduce the number and size of life-limiting microfeatures. The third subsidiary objective of the program was to define a path for integrating the modeling of microstructure and its fatigue performance implications into existing airframe design and risk assessment methodologies.

1.2 Technical Approach

The technical approach for the program was divided into three main, and generally consecutive, phases, each corresponding to one of the three subsidiary program objectives. The first phase, that of generating data and quantitatively linking microstructural characteristics with macrostructural fatigue performance, was conducted in two parallel and interlinked tasks. The first task consisted of a series of fatigue tests, carried out on samples of thick plate of a single alloy and temper but of differing processing pedigrees. Results of these tests provided the required fatigue characterization of the material as a function of processing pedigree. Subsequent microstructural characterization and examination of the failed specimens provided data concerning the microstructural characteristics of the different material pedigrees and the specific microstructural feature(s) at which specimen failure had originated. These data and characterizations provide the quantitative link between material microstructure and fatigue performance.

The second task of the program was focused on modeling, the basis of which has foundation in the crack growth based durability evaluation framework introduced by the Air Force [14, 34, 37, 50-53]. The modeling approach utilizes conventional fracture mechanics technology and the assumption that lifetime is predictable as crack growth from material life-limiting microfeatures, that in turn can be modeled as pre-existing cracks. The effects of crack-initiating microstructural feature type are incorporated into the life analysis through their effects on the crack driving force, and the statistical aspects of microfeature distribution within each material pedigree are accounted for by incorporating a probabilistic sampling method. The model crack growth calculations are made deterministically to verify and tune the model for each material pedigree. Probabilistic predictions are then made using knowledge of microfeature distribution. Finally, the model is used for parametric studies of effects of material/microstructural parameters on test performance.

The third task was to define a path for technology transfer which enables the capture of value from the program. Three opportunities for technology transfer have been envisioned. Material design is one of the three technology transfer paths where material optimization can be achieved faster and more economically. The modeling technology can also be transferred to structural design and evaluation enabling employment of improved materials to reduce weight, increase service life, and/or improve durability. Finally, the program can be applied for life extension studies to evaluate structural implications of a variety of discrete damage forms incurred during service.

2. Alloy 7050 Plate Characterization

2.1 Background

The scope of this program has focused on the use of alloy 7050 thick plate because of its relevance to Naval aircraft. Alloy 7050 was developed to meet the Navy's demand for high strength combined with optimum balance of ductility, damage tolerance, and corrosion resisting properties in thick product gauges (typically > 4 in.) [54-56]. Over the past two decades, alloy 7050 plate has attained widespread use as the aluminum product of choice for many military and civil airframe component applications denoted as fracture critical. Of these, the most demanding 7050 usages typically entail large, machined web-rib components such as bulkheads, spars, and assorted structural fittings that form the airframe support structure.

The interest in thick plate product is based on several practical considerations. In general, thick plate fatigue strength ranks lower than that of thin plate of the same alloy. In thick plate gauges ($\geq$ 4 in.), uniform metal quality is difficult to achieve because deformation during rolling is often insufficient to effectively heal microporosity and/or break up remnants of the original cast structure. These features can shorten life of cyclically loaded components by accelerating the initiation of fatigue cracks. The effect is demonstrated by the result of Figure 2.1, which shows that the mechanical work associated with rolling to a thinner gauge plate results in longer cyclic life [32]. In this instance, high resolution fractography confirmed microporosity as the failure initiating microfeature, and the size of microporosity was observed to decrease with plate thickness reduction.

Other issues impacted this program's decision to focus on thick plate product. Integrally ribbed parts machined from thick plate often constitute an appreciable percentage of airplane structural weight. Thus, higher performing materials that enable operating stress increases in such parts offer the promise of substantial saving in airframe structural weight. Though thick internal structure does not experience the same level of traffic damage as outside skins, crack prevention and control within the former is even more critical since the internal frame carries a higher percentage of the applied loadings. Thick internal structure is generally more difficult to inspect because of its limited visual access, and necessary repair and/or replacement of such parts can involve appreciable downtime and expense. In addition, monolithic web-rib parts possess neither the redundancy nor crack stopping features of mechanically-fastened skin/stiffener arrangements. As such, implementation of strategies to resist nucleation and growth of cracks from intrinsic material microfeatures represents a key planning element to meeting the safety and economic demands of thick internal airframe structure. All of the above factors indicate that

there is significant weight, safety and economic benefits to be gained by improving upon the predictive and performance aspects of thick aluminum product fatigue behavior.

2.1.1 7050 Thick Plate Historical Perspective. Continuous improvements to alloy 7050 plate production practices have been ongoing since product inception [54, 55]. Alloy 7050 continuous improvement activities during the late 1970's to early 1980's focused on static strength properties and mill recovery rates, the latter having the aim to reduce the number of thick plate ultrasonic quality rejections. By the early 1980's, modest increases over original 7050 strength properties had been achieved and incorporated into MIL-HDBK 5 [32]. Over this same time frame, Alcoa's 7050 production practices had also evolved to a stage where the commercially produced plate routinely met industry specification requirements for ultrasonic soundness [32]. Despite these improvements, airframers still had concern over the quality of thick 7050 plate because some finish machined parts were experiencing problems with dye penetrant rejections [57]. Consequently, throughout the 1980's Alcoa and other producers stepped-up activity to further improve quality of 7050 thick plate [32].

As further continuous improvements evolved during the mid 1980's, little additional increase in 7050 static strength properties was noted, except for a modest elevation in short transverse ductility. The same process refinements, however, produced dramatic reductions in dye penetrant indications and increases in smooth axial fatigue lifetimes [32]. Fractography of the failed smooth fatigue specimens revealed a correlation between cyclic performance and size of the failure-initiating microfeature (in this case microporosity) where longer lifetimes were achieved with a reduction in feature size [32-34, 37, 38, 43]. These observations led to the subsequent adaptation of smooth fatigue testing as a quality assurance tool for control of production material quality [32, 58].

One of the first attempts to evaluate the potential service implications of fatigue improved 7050 plate utilized a probabilistic fracture mechanics based durability assessment model developed under the auspices of the U.S. Air Force [10, 14, 50-53]. The analytical procedure entailed developing probabilistic projections of component cracks arriving at some predetermined size after a specified period of simulated service loads. The size distribution of smooth specimen failure initiating microfeatures and the material da/dN relationship comprised the material inputs used in the calculation. The model then calculated crack size exceedance probabilities as a function of the loading conditions representative of a fighter aircraft lower wing. The analysis showed that the level of 7050 plate quality improvement which had been achieved had substantial structural benefit potential as measured by reduced incidences of cracking in process-improved material [34].

The above analytical computation relied on a measure of the size population of life-limiting microfeatures as a starting point for the probabilistic crack growth analysis. In this case, the size distribution of the failure-initiating microfeatures was obtained by direct measurement from the fatigue specimen fractures. This approach is both time-consuming and costly. To simplify, fracture mechanics computational analysis was used to convert cyclic lifetime data into an equivalent initial flaw size (EIFS) population [37]. The EIFS represents an idealized (elliptical) shaped flaw of given size, which if grown forward according to the conventional fracture mechanics crack growth law, produces a lifetime equal to that measured by experiment. In principle the EIFS distribution can be envisioned as a material characteristic indicative of the "initial fatigue quality" of the material.

The calculation of the EIFS distribution is done by back-extrapolating the smooth specimen lifetime data to zero cycles. To verify applicability of the EIFS concept, fatigue damage from microstructural features was calculated according to classical linear elastic fracture mechanics [37]. The calculation utilized a stress intensity factor solution from Newman and Raju [59, 60] to approximate an equivalent initial surface flaw in a round bar specimen. An aspect ratio (a/c) of 0.8 was chosen since it approximates the equilibrium shape partial-thickness crack for a uniformly loaded round tensile bar [32, 60]. The fatigue crack growth rate relationship used was obtained from archival data developed from commercial 7050 plate product. Figure 2.2 shows the predicted relationship of EIFS and specimen life alongside experimental results portraying the size of actual failure-initiating microfeatures and their corresponding test lives. The experimental data were smoothed using a running average of ten successive data points to more clearly define the trend. The predicted lifetimes are in good agreement with the experimental data. Also shown in the figure are experimental data from specimens containing small machined flaws. Again the data show good agreement with the lifetime calculations. These results are significant for a couple of reasons. First, the data show a consistent relationship between microfeature size and fatigue lifetime regardless of whether they are naturally occurring microstructural features or machined flaws. Secondly, the calculations verify the applicability of fracture mechanics to describe fatigue crack growth from features on the scale of the life-limiting microstructural features. Further details on the analytical modeling process is deferred to a later section of the report.

Through the mid-1980's the 7050 fatigue quality improvement had been mostly substantiated by smooth coupon testing and the Air Force analytical methodology. However, the question still remained whether the material improvement would translate to an increase in structural performance where geometric stress concentrations and possibly machining defects could

override the microstructural influence. An experimental investigation was conducted which examined the open hole fatigue performance of low and high microporosity material using specimens containing open holes subjected to constant amplitude loading [33]. The test results clearly showed longer lifetimes for the low porosity material. Postmortem failure analysis showed that the fatigue failures initiated from micropores, and not from machining flaws, even though no special care was taken in the preparation of the holes. Later open-hole specimen testing on 7050 alloy plate which contained even lower levels of microporosity showed failures initiating from micropores in the more porous material, whereas machining burrs at the hole edge acted as initiation sites in the higher pedigree material [38]. This demonstrated that improved material quality should lead to improved structural performance in the presence of engineering detail, but attention to manufacturing quality is essential to capture full benefit of improved materials. Procedures have since been developed to establish improved fatigue strength allowables resulting from the increase in lifetime due to metal quality improvement [61].

The material quality improvements which have been shown to increase coupon fatigue lifetimes were attractive enough to undertake the next stage of verification involving test conditions more representative of actual service. To do this, a cooperative test program was initiated between the Air Force Wright Laboratories and Alcoa aimed at investigating the effect of material quality on fatigue performance as measured by various types of structural element tests, each containing representative aspects of geometric detail, flight loadings and airplane assembly practices [43, 62]. The fatigue testing was performed on two 7050 alloy thick plate variants possessing different levels of microporosity. The 7050 variant of lesser pedigree (greater number of micropores) was purposely made to be representative of the pre-1984 commercial product capability, while the variant of higher pedigree was representative post-1985 product capability (later referred to in this report as the "old" and "now" materials, respectively). The Alcoa/USAF program evaluated specimens containing open holes, specimens with filled fastener holes, multi-holed panels and assembled double lap joint specimens. All specimens were prepared using standard airplane machining/manufacturing practices. Under all test conditions examined, the material with lower microporosity levels outperformed the material with higher microporosity levels. Moreover, the performance improvement demonstrated by the higher pedigree material was more than incremental [43]. The findings from this program helped lend credence to the claim that structural upgrading should be highly attainable through improvement and control of intrinsic metal quality.

The previous work had clearly demonstrated advantage of metal quality improvement on fatigue performance and its potential benefit in structural airframe applications. Despite the apparent advantages to airframe longevity and performance, the industry has not amply utilized the available knowledge and tools to develop and capture the full advantage of improved quality materials and manufacturing processes. As stated previously, the objectives of this program are to: (1) link microstructure with fatigue damage evolution and crack growth, (2) quantify fatigue durability improvements attainable through optimizations of microstructure, and (3) develop and refine tools for prediction of the above.

The considerable historical fatigue test data and analysis that have been generated for alloy 7050 provide an excellent opportunity to pursue these objectives. Material with varying intrinsic inhomogeneity populations are made available to this program to quantify their effect on fatigue performance and to provide benchmark data to establish predictive protocols which incorporate microstructure.

2.2 Materials

Alloy 7050 plate was selected as the material for evaluation in this program. This was due in part to the relevant Navy interests discussed previously. In addition, different processing routes were used to controllably modify the 7050 plate microstructure. Four microstructural variants of 7050 plate in the T7451 temper condition were produced for this program. All four variants were manufactured on a plant scale to provide a range of microstructural feature types and distributions known to affect fatigue life [32, 37, 38, 44, 63-65]. The principal types of microstructural features of concern to this program are micropores, constituent particles and grain structure, as described below:

- Microporosity forms during ingot casting and is concentrated at the center of the ingot since that is the last region to solidify during casting. Microporosity present in the original cast starting stock heals during rolling, however, in thicker ($\geq$ 4 in.) plate gauges there is seldom enough deformation to effectively heal all of the microporosity, particularly so at the midthickness location. Fractographic examinations of cyclically loaded specimens removed from the midplane (T/2) location of thick plate will often reveal microporosity at the failure origin. Failure-initiating micropores of sizes ranging between 0.001 and 0.020 in. diameter is typical of aerospace thick plate commercially produced within the last two decades. Increasing the rolling deformation to produce thinner plate will generally result in better healing and smaller crack initiating micropores. Given enough mechanical work, the

healing process can become so effective that microporosity no longer remains the dominant crack-initiating microfeature.

- Alloy 7050 has two common insoluble <u>constituent particle</u> phases, Al_7Cu_2Fe and Mg_2Si. These intermetallic compounds form during ingot casting. Once they form, they cannot be dissolved by a solid state transformation so they are present in the final product. The particles can be broken up through mechanical work, thus, they often lie in stringers which are elongated in the plate rolling direction. In thick plate the particle size distribution typically ranges from 0.0003 to 0.0100 in. In the absence of microporosity, constituent particles tend to become the dominant life-limiting material microfeature.

- In the absence of large microstructural inhomogeneities, fatigue damage initiation can be controlled by the <u>grain structure</u>. Stage I type slip based fatigue initiation mechanisms can occur and are influenced by the grain structure. Rolling of thick plate flattens the original cast grain structure producing a pancaked grain morphology. Thinner plate gauges possess a more flattened or refined grain structure than thick plate gauges. This refinement may provide more resistance to slip-based fatigue initiation mechanisms because of the reduced free slip distances. Grain structure can be thought of as the "default" intrinsic crack-initiating microfeature that becomes operative in the absence of overriding microfeatures such as micropores or particles.

A description of the four 7050-T7451 plate microstructural variants provided for use in this program follows.

The first microstructural variant is called *old material*. *Old material* is fabricated using plant production practices typical of those used prior to 1984. This variant is characterized by significant levels of microporosity located primarily at the plate centerline. Two production lots of plate which were both 5.7 in. thick were used to supply this material variant for the program. Despite the levels of microporosity which exist in the plate, it still meets the current specification limits on mechanical properties. Thus, if existing certification were to be based on static properties alone (as is commonly done today for most plate procurements), the material would be considered acceptable.

The second microstructural variant is called *now material*. The *now material* variant represented the standard plant production product which was available commercially at the inception of this program. (Author's note: Originally this microstructural variant was referred to in this program as *new quality* plate. Since Alcoa is continuing to develop improvements to its plate products,

this variant is no longer referred to as *new* but is called *now material*.) Two production lots of plate which were both 5.7 in. thick were used to supply this material variant for the program. The plate is characterized by reduced levels of midplane microporosity compared to the *old* plate. The reductions in microporosity have resulted in improvements in the material's fatigue performance. In recognition of this improvement, this material is sold to several customers with a guarantee on fatigue performance and every production lot of material is fatigue tested.

The third microstructural variant used in this program is called *low porosity material*. The *low porosity* variant is fabricated using special practices which further reduce the midplane microporosity compared to the *now* variant. A single lot of 6.0 in. thick plate of *low porosity* plate was made available for the program. This variant is produced on a plant scale, but the manufacturing methods used are more costly than today's standard commercial fabricating practices. As a consequence this material is not available commercially at this time. The *low porosity* plate is characterized by further reduced levels of midplane microporosity compared to the *now* variant.

The final material which was made available for this program is *thin material*. The *thin material* is 1.0 in. thick plate produced according to standard production practices for that product. The large thickness reductions which this material receives during rolling to the thinner gauge result in almost no microporosity present in the material. In addition, the microstructure is more refined due to break-up of the original cast structure and flattening of the original cast grains. Thus, constituent particles which form in the ingot during solidification are broken up and are of a smaller size than in thicker products.

These four materials present a hierarchy of microstructural features that influence the fatigue longevity of aluminum alloy 7050 plate. The principle types of microstructural features of concern to this program are micropores, constituent particles and grain structure. These intrinsic microstructural features act as sites for the initiation of fatigue cracks. The key microstructural features of the four 7050 plate microstructural variants are summarized in Table 2.1a, and the static mechanical properties of the materials are given in Table 2.1b.

2.3 7050 Fatigue Testing

Fatigue testing has been performed on the four 7050-T7451 microstructural variants to quantify the influences of the various microstructural features on fatigue. Both smooth round specimens and flat bar specimens with two open holes were tested. Drawings of both are shown in Figure 2.3. The two specimen types were used for a couple of reasons. The smooth specimen

test is the most sensitive to microstructural influences because the test section is uniformly stressed, and the failure will seek out the dominant (generally the largest) inhomogeneity in the specimen test section. The open hole specimen, on the other hand, has a notch stress concentration at the holes, and the volume of material seeing the highest stress is much smaller. Thus, this test will be more sensitive to the frequency distribution of microstructural inhomogeneities. It is important to understand the influences of stress concentration gradients and microfeature type, size and frequency distributions if this work is to be scaled for design and life assessment of actual aircraft parts.

The smooth fatigue test specimens were machined with the long (or axial load) dimension parallel to the long transverse direction of the plate (LT test direction) and centered about the plate midplane (T/2 plane). This test orientation was chosen to place the most elongated dimension of the life-controlling microfeature normal to the direction of specimen loading. The tests were conducted in laboratory air with a stress ratio of 0.1, with maximum cyclic stresses of 35 ksi for the *old* and *now material*, 40 ksi for the *low porosity material*, and 45 ksi for the *thin material*. The stresses were increased for the *low porosity* and *thin* variants because the lifetimes would have been excessively long at a lower maximum cyclic stress. The specimen test sections were prepared prior to testing by sanding longitudinally with progressively finer sanding paper to remove circumferential machining marks which could act as stress risers.

The open hole test specimens were also oriented in the plate LT direction and taken from T/2 location of the host plate. The tests were conducted in laboratory air with a stress ratio of 0.1. For each of the material variants, several stress levels were tested to generate stress versus lifetime (S/N) curves. The holes were deburred by polishing with diamond compound prior to testing. The polishing was only done on the corners and not in the bore of the hole, and resulted in slight rounding of the corners. This prevented specimen failure initiation from machining defects. Hole deburring was implemented as a standard specimen preparation practice after noting that the failure mode was intermixed between hole quality and intrinsic material features in the higher pedigree materials. It was found for the *old material* that specimen failure initiated at microstructural inhomogeneities even when the holes were not deburred.

The fatigue test results for both the smooth and open hole tests of the four 7050 plate variants are summarized in Tables 2.2-2.9. The tables additionally document the initiation feature type, size and location, as analyzed by SEM fractography. The fractography results and the analysis protocols for locating and identifying the fatigue initiating microfeatures are detailed in the next section. The smooth specimen fatigue data are plotted as cumulative lifetime distributions in Figure 2.4. Despite the differences in cyclic stress for two of the variants, the data still show the

ranking of fatigue performance to be *old material, now material, low porosity material* and *thin material.*

Open-hole specimen fatigue lifetime data for each of the material variants are plotted as stress versus lifetime (S/N) curves in Figures 2.5-2.8. Also shown are bounds around the data which represent the 90% confidence limits. These confidence limits are calculated using a statistical transformation analysis of the data after Box and Cox [66] which has been applied to the analysis of fatigue data [61]. This analysis method allows for the handling of censored data, or data in which the test is stopped prior to failure due to reaching some prescribed number of cycles. Using this transformation analysis, the lower 5% and upper 95% failure probability curves are defined. In addition, the method can be used to obtain a fit to the mean (50%) failure probability curve. Mathematical representations of S/N response in the above fashion permit calculation of fatigue strength corresponding to a prescribed lifetime and failure probability. For example, for each of the material variants a maximum cyclic stress which yields a lifetime of 10^5 cycles or greater can be calculated with either 50% (mean) or 95% certainty.

The results of the open-hole specimen tests gave the same relative ranking of materials, except that the *now material* and the *low porosity material* had the same lifetimes. This occurred despite the observed differences in smooth fatigue lifetimes. The reason for the difference in smooth and open hole specimen performance lie in the mechanisms of fatigue initiation. The details of the mechanisms of fatigue crack initiation and the correlation with key microstructural features is discussed in the next section on fractography.

The fatigue data presented represent a substantial database and are a primary program deliverable to the Navy. These data clearly show that fatigue lifetime capability of plate can be affected by changes in manufacturing practices, which in turn alter the distribution statistics of life-limiting microfeature populations. The differences in smooth and open hole data show that the relative effects of microstructure are dependent upon loading condition and local stress concentration. These results coupled with post test fracture analysis provide a means for understanding the mechanisms by which microstructure affects fatigue durability performance, and provides a basis for the development of models which link microstructure, processing and performance.

2.4 Fractography

Fractography of failed smooth and open hole fatigue specimens for the four variants of 7050 plate has been conducted. The purpose of this work is to identify the controlling microstructural

features which limit the fatigue durability of the material, and provide a quantification of the controlling features for use as input to fatigue lifetime prediction models. The dominant microstructural features for each of the materials and test types is identified and the size distributions of features measured. This work establishes a hierarchy of microstructural features, based on their effectiveness as crack initiators, which control the total fatigue life capability of each material variant. It is also important to establish the fact that the impact of intrinsic material microstructure on fatigue performance is not superseded by the presence of notch stress concentrations.

The development of microstructure based models for probabilistic fatigue life assessment requires that size distributions of crack initiators be quantified for each of the material variants. The crack initiating features typically represent the extreme values or high-end tail of the feature size distribution, since the fatigue damage process generally seeks out the largest flaw within the material volume subjected to the highest cyclic stress. Verification of the modeling capability is done by correlating model predictions with coupon specimen lifetimes, using the measured inhomogeneity size distribution developed from the characterization of fracture surfaces as the starting point for the calculations.

A program objective is to synthesize and demonstrate feasibility of a modeling approach that will enable prediction of material fatigue performance directly from knowledge of the material microstructure. The motivation here is to examine an alternative evaluation practice that permits reduction in the scope and scale of necessary fatigue testing. Meeting this objective requires that methods be developed to scale random plane microstructural characterization to the extreme value size distribution of crack initiators. Thus, the fracture surface characterization of the extreme value inhomogeneity distribution is critical in establishing life prediction capability based on microstructure.

Scanning electron microscopy (SEM) was conducted for all of the smooth and open hole specimen fracture surfaces for all four material variants. This work was performed at both Alcoa Laboratories and at UCLA under Dr. Marek Przystupa's ONR funded program "Development of the Microstructure Based Stochastic Life Prediction Models," [ONR Grant No. N00014-91-J-1299]. Tables 2.2-2.9 summarize the smooth and open hole fatigue lifetime data and the identified crack initiating microstructural features for the four 7050 plate material variants. Also shown are the measurements of the size and location of the crack initiating microfeatures relative to the specimen dimensions. Measurement nomenclature for the crack initiating features is defined in Figure 2.9. A question mark in the tables denotes cases where the size of the crack initiating feature could not be identified.

2.4.1 <u>Smooth Specimen Fractography</u>. The smooth fatigue failures for both the *old* and the *now* variants were seen to initiate from surface or near-surface microporosity. Failure-initiating micropores typical of specimens from the *old and now material* variants are shown in Figure 2.10. The differentiated cyclic lifetimes of the two materials is attributed to the size differential of the crack-initiating micropores, in this case the *old* material variant has the larger micropore and the correspondingly shorter lifetime. Correlation of fatigue specimen lifetimes with size of fatigue initiating micropores, represented by the maximum micropore dimension measured from the SEM photographs, is shown in Figure 2.11. The data show that for increasing size of crack initiating micropores there is a decrease in fatigue lifetime. As can be seen in Figure 2.11, the longer lived *now material* had the smaller fatigue initiating micropores.

Fractography of smooth specimen fatigue failures of *low porosity* material revealed that failures initiated predominantly at microporosity which was smaller than the crack initiating micropores in either the *old* or the *now* materials. In several cases there were constituent particles near the micropores, and in some of specimens only constituent particles were observed at the failure initiation site. Typical smooth fatigue failure origins in the *low porosity material* are shown in Figure 2.12.

The predominant crack initiation mechanism identified for the *thin material* was dislocation slip leading to Stage I cracking. Figure 2.13 shows a typical initiation site in the *thin material*. The appearance is typical of the classic Stage I fatigue crack initiation characterized by repeated slip along crystallographic planes leading to the formation of a crack along the persistent slip bands. One feature of this type of fatigue initiation mechanism is the faceted appearance of the initiation site with the crack propagating initially at an angle to the stress axis along planes of high shear stress. This characteristic is evident in the micrograph shown in Figure 2.13. It is likely for the *thin* variant that there were not any microstructural inhomogeneities of sufficient size and severity to initiate fatigue cracking. In only one specimen did a constituent particle act as the initiation site.

2.4.2 <u>Open Hole Specimen Fractography</u>. Fractography of the failed open hole specimens for the *old material* showed microporosity at the initiation site for the fatigue failures, which typically were located within the bore of the hole. In some of the failures there were multiple fatigue cracks where microporosity was observed at the origin of each of the cracks that were present. The location of the multiple initiation sites varied; they were sometimes observed on opposite sides of the hole, sometimes more than one initiation site was observed on one side of the hole, and occasionally a combination of the two cases was observed. An example of the microporosity observed at the initiation sites in the *old material* is shown in Figure 2.14.

Observation of the open hole fractures from the *now material* showed that failures also originated at microporosity. An initiation site for this material is shown in Figure 2.15, which shows a micropore initiated fatigue crack. It is worth pointing out here that prior to establishing the practice of deburring holes, open hole fatigue tests were performed for both materials without deburring the holes. The *old material* failed at micropores while all of the *now material* failures started at burrs at the hole corners. The lifetimes of the *now* variant specimens were longer than the *old* variant, but shorter than when the holes were deburred. This will be discussed in more detail later in the section on hole quality effects.

The open hole specimen fractography for the *low porosity material* showed that the failures originated predominantly from constituent particles, and in most cases the particles were located at the corner of the hole and the specimen surface. Figure 2.16 shows a fatigue crack initiation site to be a constituent particle located at the hole corner. Detailed SEM observation of the initiation site on opposite specimen halves was performed to determine the mechanism of crack initiation from particles. Figure 2.17 shows the opposite specimen halves at the initiation site revealing that particles are located on each half and that they appear fragmented. This indicates that either a closely spaced particle cluster acted as the initiation site or the particle present fractured leaving portions of the particle in each specimen half.

The transition in fatigue crack initiating features from microporosity in smooth specimen fatigue tests to particles in open hole specimens for the *low porosity material* affects the fatigue performance relative to the *now material*. In the smooth specimen tests the *low porosity* variant showed significantly longer lifetimes than the *now* variant, whereas in the open hole tests the lifetimes of the two materials are similar. The transition to the particle initiated open hole failures in the *low porosity material* is most likely related to the size and distribution of micropores and particles and the volume of material subjected to the high stress. Since there are many more constituent particles than there are micropores within the material, there is a greater probability of having a particle or cluster of particles located at a localized region of high stress. For the open hole specimen geometry, the most detrimental position for crack initiation is the hole corner stress concentration, where k_t is about 20% higher than in the bore of the hole [67]. The corner effect will be shown later in the modeling portion of this report which will also examine the relative driving force for crack growth from micropores and constituent particles.

The distribution of particles within the hole bore of an open hole fatigue specimen can influence the fatigue performance. To observe the nature of the constituent particle distribution in the bore of the hole of an open hole specimen, low magnification (25X) SEM using the backscattered electron detector was performed. In backscattered mode the Fe-bearing constituent particles

appear lighter than the matrix since more electrons are reflected from the higher atomic number elements (Fe vs. Al). Figure 2.18 shows the constituent particles which are present in the bore of the hole for both the *now* and the *low porosity* variants. In both materials there are significant numbers of Fe-bearing constituent particles present, and it is easily seen that there is a high probability of having a particle located in a region of high stress concentration near the corner of the hole which would favor fatigue crack initiation. Figure 2.19 shows the constituent particles in the bore of the hole at higher magnification. It can be seen that the particles exist as clusters of smaller particles. The fatigue crack initiation site shown previously in Figure 2.17, where the particle appeared fragmented, is likely a result of crack initiation from a cluster of finer particles as shown in Figure 2.19.

There is considerably more microporosity in the *now material* compared to the *low porosity material*. Thus, for the *now material* there is a higher probability of having a micropore located in the bore of the hole which could act as a site for fatigue crack initiation. The reduced microporosity distribution in the *low porosity* plate is such that the probability of having a micropore located at the bore of the hole is low, and thus fatigue cracks initiate at constituent particles at the more highly stressed hole corner. The observance of micropore initiated failures in both materials in the smooth specimen tests is due to the greater volume of material sampled in the smooth test compared to the open hole test. Because the volume of material which sees the highest stress in the smooth specimen is so much larger than in the open hole test, there is a much higher probability of finding a micropore favorably located for fatigue crack initiation, even for the *low porosity material*.

Open hole specimen fatigue failures from the *thin material* were also examined under the SEM. Some of the fatigue failures were observed to initiate at constituent particles. Figure 2.20 shows two examples of constituent particles at the origin of the fatigue failures. The size of the constituents is considerably smaller than the constituent particles seen to initiate failure in the *low porosity material*. Additionally, the *thin* variant lifetimes were much longer. It is believed that the increased lifetime is due to a combination of the reduction in particle size and the change in grain shape with larger reductions during rolling. In addition to the particle initiated failures in the *thin material*, dislocation slip leading to Stage I cracking was also observed. Figure 2.21 shows this type of initiation site observed in the open hole specimens from the *thin* variant. This mechanism was also observed for smooth specimen fatigue tests of the *thin material*.

2.5 Effect of Hole Quality

In addition to intrinsic microstructural features which affect airframe fatigue durability, an important consideration for structures is initiation from extrinsic sources such as manufacturing imperfections. If severe enough, the influence of manufacturing imperfections on fatigue damage initiation can override increases in durability due to improvements in metal quality. Thus, it is important to understand the relative effects of manufacturing imperfections on durability in order to capitalize on improvements in metal quality.

Prior to establishing the practice of hole deburring, open hole fatigue tests on the *old* and *now materials* were performed using specimens in the as-machined condition. In this condition the life limiting feature in the *old* variant was microporosity, but for the *now* variant hole edge burrs initiated the fatigue cracks. A micrograph showing an edge burr as the crack initiation site in the *now material* is shown in Figure 2.22. The fatigue lifetime of the *now* variant is affected by crack initiation at hole burrs. Figure 2.23 shows stress versus lifetime plots for open hole fatigue tests for both the as-machined and the deburred specimens compared to the *old material* performance. In the as-machined condition the *now* variant exhibits longer lifetimes than the *old* variant, but the level of improvement is greater when the holes are deburred. These data underscore the importance of attending to manufacturing quality in concert with material quality to gain a structural benefit. Increasing metal quality improves the material performance, but manufacturing imperfections can limit the magnitude of the end-product improvement. Enacting "total quality management" requires imposing good quality manufacturing practices to reduce extrinsic sources of damage, and thereby provide better opportunity to realize the full benefit potential of the material.

The fatigue tests coupled with SEM fractography have identified the life-limiting features which control damage initiation for each of the material variants. As seen here, hole quality can also affect damage initiation and can be included in the hierarchy of life-limiting features. The hierarchy of key microstructural features which control damage initiation in both smooth and open hole tests of the four material variants is presented in Table 2.10. Identification of the critical life-limiting microstructural features in each of the material variants and specimen types represents a key element of understanding required to integrate effects of microstructure and geometric stress concentration into a life assessment model. The next section deals with quantitative microstructural characterization of the critical variables for each of the materials, which will serve as inputs to models to explore prediction of material fatigue performance based on characterizations of microstructure along random metallographic planes.

2.6 Constituent Particle Characterization

The preceding discussion illustrates that micropore and particle populations can, and often do, compete for dominance as the overriding life-limiting feature. While microporosity is generally regarded to be more degrading to fatigue performance than particles, the spatial and frequency distributions of the two feature types are vastly different and affected by material pedigree. In contrast to microporosity which is sparse, and largely confined to the centerline region of thick plate, constituent particles are copious and more evenly distributed throughout the volume of both thick and thin plate materials. Thus highly localized geometric stress concentrations will always have particles associated with them. In contrast the likelihood of encountering a large micropore within a small material volume is considerably more remote, particularly so if the plate is thin and/or the most highly stressed material volume resides near the plate surface.

Because of the observed higher order of importance given to particles in the presence of engineering notches (e.g., the sharp-cornered hole), constituent particle distributions were quantified for the *now, low porosity, and thin* variants of 7050 using automated image analysis. Constituent particle distributions were not quantified for the *old material* variant since microporosity was consistently observed to be the life-limiting microfeature for all test conditions evaluated.

The constituent particles which are typically present in alloy 7050 are Al_7Cu_2Fe and Mg_2Si. These particles form during ingot solidification and cannot be dissolved by a solid state transformation. Thus, once formed, they persist through to the final product. These particles can be broken up by the mechanical working of an ingot into a wrought product. Therefore, the size and spatial distribution of constituent particles are not only a function of ingot composition and solidification conditions, but also a function of the deformation history of the final product. Rolling of the ingot into plate produces stringers of particles running parallel to the rolling direction through the breakup of large particles. The greater amounts of deformation to produce thinner plate can result in a smaller constituent particle size distribution because of this. Particle sizes may be as large as 0.004 in. (100 µm) in length in thicker plate, and these large particles can act as initiation sites for fatigue cracking. The characterization of large particles is emphasized since these control the fatigue initiation in the absence of microporosity.

Automated image analysis provides a way of obtaining a statistically meaningful characterization of constituent particles. The distribution of particle sizes and the extreme value distribution are more important than the mean value alone since fatigue damage initiation is controlled by the larger particles. In addition to size distribution, spatial distribution can also be

an important parameter. Two materials may have the same particle size distribution, but the particles may be more clustered in one material. The degree of clustering is also likely to have an effect on the fatigue initiation behavior of 7050 thick plate. A simple measure of clustering is the distance between particles, which is easily obtainable using automated image analysis systems.

Samples of the *now* and *low porosity* materials were sectioned to examine the longitudinal plane (the plane defined by the L and ST directions) at the one-tenth, quarter and half thickness (T/10, T/4, and T/2) locations. Automated quantitative optical metallography was performed on as-polished cross sections to characterize the size and spatial distributions of constituent particles. Low magnification was used, which maximized the area characterized thus improving the chances of encountering the largest particles. However, the lower magnification degraded the spatial resolution so that closely spaced particles may be measured as one particle, and the small particles below the resolution limit could not be measured. Forty fields, each 0.77 mm^2, were analyzed at 100X magnification for a total area of 31 mm^2 (0.048 in^2). For both materials, between 4200 and 9400 particles were characterized per location in the thickness. Particles smaller than 1.6 µm (0.062 x 10^{-3} in) in projected length could not be resolved and thus were not analyzed.

The particle size was defined to be the maximum projected particle dimension ("DMAX") since this is believed to be the most influential particle dimension relative to material properties. Particle spacing ("FERET X") was measured as the distance between particles parallel to the rolling direction only. While this is not sufficient to uniquely define the spatial distribution of particles in the material, this distance does indicate the relative amount of particle clustering in similar samples. It is also relevant because particles tend to be clustered in stringers which lay along the rolling direction and this distance would characterize this type of clustering. Distances larger than a single view field could not be measured, which truncated the upper particle spacings at the length of the view field. This is not considered significant since fatigue initiation will not be affected by large particle spacings but rather by clustering of particles. For simplicity and to save time, this characterization method was selected over more complex characterization methods.

Quantitative metallography was also performed on a similarly designed SEM-based image analysis system for the *now*, *low porosity*, and *thin materials* at T/2 only. The differentiation of particle types by chemistry on the SEM system was used to separate Fe- and Si-containing constituent particles in order to evaluate whether particle type affects fatigue initiation

mechanisms. For these analyses, 20 fields were analyzed at 250X magnification, for a total area of 1.2 mm^2 (0.002 in^2). Particle dimensions as small as 0.4 µm (0.016 x 10^{-3} in) were detected.

2.7 Quantitative Optical Metallography: *Now vs. Low Porosity Material*

The particle distributions for the *now* and *low porosity* variants are compared because of the effects of the particle population on open hole fatigue. The *low porosity material* had predominantly particles at the initiation sites whereas the *now material* had microporosity, and yet both variants exhibited similar lifetimes. The particle populations are compared to determine if differences exist which may explain the differences in initiation mechanisms and the similarities in open hole lifetimes despite the different mechanisms. For both of the materials, the particle distributions are measured at the T/10, T/4, and T/2 locations. The particle distribution is expected to vary with plate depth for several reasons. Solute variation during casting coupled with differences in cooling rates will result in differences in particle size and volume fraction. Also, the amount of deformation during rolling varies inversely with plate depth, which can affect the particle size, shape and number density. Table 2.11 contains the results of the quantitative optical metallography at various thickness locations in the *now* and *low porosity* variants.

2.7.1 Particle Area Fraction: *Now vs. Low Porosity Material*. In both the *now* and *low porosity* variants, the area fraction of constituent particles larger than 1.6 µm varied only slightly between the T/10, T/4 and T/2 locations, as shown in the bar graphs in Figure 2.24a. The T/10 location had the largest area fraction of particles while the T/2 location had the smallest. Since the area fraction was calculated by averaging the area fraction for each of the 40 fields, another important value is the standard deviation (indicated by arrows in Figure 2.24a), which indicates the field-to-field microstructural variability. The large standard deviations suggest variability in the distribution of particles through the material, even when examining only one location in the thickness; this emphasizes the importance of characterizing sufficient area to overcome the inherent variability in constituent particle population.

The number of particles observed in both materials decreased monotonically with depth in the plate (Figure 2.24b). Since the number of particles decreased by almost 50% from the T/10 to T/2 location while the area fraction varied only slightly, the mean particle size increased with plate depth. This is consistent with the slower cooling rate during solidification, as well as the decreased amount of deformation during rolling with increasing depth in the thick plate.

2.7.2 Particle Size Distribution: *Now vs. Low Porosity Material*. Figure 2.25 shows particle size distributions for the two materials at the different plate locations on a logarithmic scale; this same information is also included in Table 2.12. The T/10 location is seen to have almost twice as many small (< 10 µm) particles as the T/4 and T/2 locations. However, all three locations showed about the same number of large particles. The histograms in Figure 2.25 demonstrate the truncation of the particle size distribution due to the resolution limit at this magnification. Since the particle size distribution is cut off at the resolution limit of the image digitizer, the results cannot be fit to a normal distribution in a valid way. Thus, the mean and standard deviation values reported in Table 2.11 are representative of the particles 1.6 µm or larger, and are not representative of the actual particle population in the material. This calculated mean particle size is therefore an overestimation of the actual value, since the mean value would decrease with the addition of smaller particles to the distribution. These calculated values can be used to compare materials characterized in this study, but comparisons with data reported elsewhere should be made cautiously.

Comparison between the particle distributions for the *now material* (Figure 2.25a) and *low porosity material* (Figure 2.25b) reveals that the size distributions in the two materials are nearly the same at all thickness locations. This indicates that the different processing conditions used to reduce the microporosity in the *low porosity* variant had very little effect on the constituent particle distribution, and the different processing had a smaller effect than depth within the plate on the constituent particle distribution characteristics.

Microstructural based models for fatigue crack initiation require quantification of the particle size distribution. One way to represent the data is a cumulative probability plot of particle sizes where the number of particles below a given size is normalized by the total number of particles measured. Figure 2.26 shows the resulting cumulative probability plots of particle sizes in both the *now* and *low porosity materials* at the three different plate depths. At small particle sizes, the distributions were not affected by either the thickness location or the type of material. The distributions show divergence at the larger particle sizes with the T/2 locations having a higher percentage of larger particles than the T/10 locations.

2.7.3 Particle Spacing: *Now vs. Low Porosity Material*. There was a trend towards decreasing mean particle spacing (feret x distance) in the rolling direction with plate depth (Table 2.12). The particle spacings measured here encompassed two lengths: an interparticle spacing of relatively short lengths for particles within a cluster or stringer, and an interstringer spacing of relatively large lengths. Histograms of particle spacing (Figure 2.27 and Table 2.13) show that the plate location has a strong effect on the longer, interstringer spacings. At the T/10 location, a

larger number of long spacings were observed compared to the T/2 location which corresponds to the greater deformation near the plate surface during hot rolling. There seemed to be less of an effect of plate depth on the small interparticle spacings.

2.7.4 Particle Area: *Now vs. Low Porosity Material*. The constituent particles were irregular in shape, and thus it was of interest to check whether the actual area of the particles followed the same behavior as the longest projected dimension. Because the image analyzer captured the real cross-sectional area of the particles, it was not necessary to make assumptions about the particle shape. Figure 2.28 displays the probability plots for the particle area, which follow the same characteristic curve as the longest projected dimension plots in Figure 2.26. As was found for particle length, the smaller particles showed no effect of either thickness location or the type of material, and the divergence increased with increasing particle size. The distributions for both *now* and *low porosity material* were slightly narrower at the T/10 plate depth than the T/2. Although particle length and area are equally easy to obtain in automated image analysis, length will continue to be used to characterize particles because it can be easily measured by hand from fracture surface pictures, and it was seen to correlate well with fatigue lifetimes.

2.7.5 Quantitative SEM Metallography: *Now vs. Low Porosity Material*. Quantification of the constituent particle distributions using a SEM-based automated image analysis system was used to separate particle types by chemistry. A comparison of the SEM results to the optical microscopy characterization will be provided later. The characterization of constituent particle distributions using SEM was performed for the *now*, *low porosity*, and *thin* variants.

Since the primary insoluble constituents in alloy 7050 are Al_7Cu_2Fe and Mg_2Si, particles were characterized as either Fe-containing or Si-containing. Table 2.14 contains the image analysis data from *now* and *low porosity materials*, at the T/2 location, obtained from SEM images at 250X over a sample area of 1.2 mm^2. A relatively small number of particles (around 300) were analyzed in both materials, with more than half of the particles being Si-containing in both materials.

The histograms in Figure 2.29 show the size distributions for Fe-containing and Si-containing particles. The Si-containing particle distributions are skewed left to the smaller end on the logarithmic plots, while the Fe-containing particles are more normally distributed. The trends for the Si- and Fe-particle sizes are particularly dramatic for the low porosity plate. The Si-containing particle distribution is truncated because of the resolution limit and thus the mean value reported in Table 2.14 is an overestimate of the actual particle distribution mean. In

contrast, the Fe-containing particle distribution does not appear to be significantly truncated since the Fe particles are generally larger in size.

The cumulative probability plots for *now* and *low porosity* variants (Figure 2.30) also show the difference in size between types of particles. The thick solid line represents the total constituent particle population. For both materials the distribution of Fe-containing particles lies to the right, indicating larger sizes, and the Si-containing particles lie to the left, indicating smaller sizes. Although Si particles are more numerous, they are smaller and may not play as significant a role as Fe-containing particles on fatigue crack initiation.

2.7.6 Optical vs. SEM Characterization: *Now vs. Low Porosity Material*. A comparison between the particle measurements made using optical metallography and those performed using SEM is necessary to provide particle distribution characteristics as input into models of fatigue initiation. Differences in magnification and number of fields measured may account for differences in the quantitative results. The SEM analysis was performed at a magnification of 250X compared to 100X for optical, and the number of fields measured was 20 compared to 40 for optical characterization. This reduced the area of material characterized by over 12 times. Since both the magnification and the number of fields changed, the effect of optical versus SEM methods alone could not be deconvoluted. With this caveat, the following are some comments that can be made.

The quantitative metallographic data from both the optical- and SEM-based characterizations are given in Table 2.15. The particle area fraction when measured optically is significantly higher for both *now* and *low porosity materials*, despite the fact that a large number of particles were below the resolution limit when using the lower magnification (over 50% of the particles measured at 250X were below the detection limit at 100X). For example, the area fraction of constituent particles in the *low porosity material* was 0.98% optically and 0.55% using SEM. The resolution limit at the lower magnification may have partially contributed to the higher area fraction, since the matrix area between closely spaced particles may be measured as particle area. Another possible factor is that the limited sampling at 250X was not representative of the total population. Since constituent particles are not uniformly distributed through the material, a large area must be sampled to experimentally characterize the high-end tail of the particle size distribution.

Figure 2.31 compares the particle size distributions measured using the different techniques. For both *now* and *low porosity* variants, the SEM gave a lower median particle size. This also stems at least partially from the fact that particles separated by very small distances may be measured

separately at the higher magnification but measured together as one large particle at the lower magnification. One consequence is that the particle number density be greater for the higher magnification analysis, which is indeed the case: *now material* had 166 particles/mm^2 at 100X and 259 particles/mm^2 at 250X.

Based on this comparison of the particle populations between the *now* and *low porosity materials*, several things can be concluded. There does not appear to be significant differences in the constituent particle populations between the two which would account for the different initiation mechanisms in the open hole fatigue tests. It is most likely related to the microporosity population differences between the two. The quantitative measurement results can vary depending on the measurement technique and magnifications used. When comparing materials, care should be taken to use consistent measurement methods. Finally, Fe-containing constituent particle populations are typically of a larger size than Si-containing particles.

2.8 Quantitative SEM Metallography: *Thin Material*

Quantification of the particles at T/2 in the *thin material* provided an opportunity to study the effect of higher amounts of deformation on particle distributions. These results complement the study of different plate depths presented earlier because the T/10 location in 6-inch thick plate received more deformation than the T/2 location; however, the *thin* variant has absorbed even larger amounts of deformation and as a consequence should have a different particle size distribution. The quantification of the particle distribution in the *thin* material was performed using the SEM-based image analysis system. In the *thin* variant, the area fraction of particles was roughly the same as for both the *now* and *low porosity* materials. This similarity in particle area fraction is reasonable since no control was used to limit particle volume fraction. However, the number of particles was three times as large for the *thin material* as for the thicker materials. This is due to the larger amount of deformation during rolling down to 1-inch thick compared to rolling only to 6-inch thick plate. Figure 2.32 graphically shows the high constituent particle number density in the *thin material*. The increased deformation breaks up the larger particles thus refining the particle size distribution. The mean area of individual particles dropped from 11 µm^2 in *now* variant to 5.3 µm^2 in the *thin material*, and the particle number density increased from 259 particles/mm^2 to 768 particles/mm^2 in the *thin material*.

Figure 2.33 shows the cumulative distribution of Fe- and Si-containing particles in the *thin material*. The Fe-containing particles are larger than the Si-containing particles even after high amounts of deformation. Thus, the Fe-containing particles are either larger than the Si-containing particles in the cast condition and persist that way through processing, or the Si-

containing particles are broken up early in the processing and are smaller at the plate thicknesses examined here.

The mean particle size was also smaller in the *thin material* compared to *now* and *low porosity materials*. In the *thin* variant the particles lay in stringers, and it is possible that these clusters of particles affect fatigue crack initiation more dramatically than individual particles. Unfortunately, no measure of the spatial distribution was obtained during the SEM-based image analyses. Curiously, the aspect ratio of the particles did not change with amount of deformation. The mean aspect ratio (minimum particle diameter divided by maximum particle diameter) of all particles in the *now material* was 0.52, and the mean aspect ratio in the *thin material* was 0.53.

Based on the quantitative analysis of constituent particle distributions in the *thin material*, the following can be concluded. The particle size distribution is significantly reduced compared to the thicker material variants due to the increased amount of deformation during rolling to the thinner gauge. The particle area fractions, however, were similar among the material variants. Also, as with the other material variants, the Fe-containing particle size distribution was larger than the Si-containing particle size distribution.

2.9 Scaling Random Plane Metallography to Extreme Value Distributions

The quantification of the constituent particle sizes in the previous section was used to obtain a size distribution of microstructural features within a material. For a sufficiently large sample size, this distribution represents the population of features within the material. When a coupon specimen or a structural airframe component manufactured from this material is subjected to cyclic loading, a particular surface area or volume of material will be subjected to the highest stress. Thus, within this high stressed area or volume there is a sample of microstructural features which will see the highest stress. The failure process will seek out the worst (largest) feature within this sample to act as the crack-initiator. For replicate coupon tests of a material, the distribution of features which act as crack initiators is the extreme value distribution from the initial population. The extreme value distribution of microstructural crack-initiators can be obtained from a series of replicate coupon fatigue tests through fractography and measurement of the feature sizes. Alternatively, the extreme value distribution can be calculated based on the population of features obtained from quantitative metallography. The following details an approach used to obtain the extreme value distribution of constituent particles by scaling the particle size distribution obtained through quantitative metallographic analysis on random planes.

The scaling of random plane metallography provides a method to obtain the extreme value distribution of life-limiting microstructural features within a material. The extreme value distributions obtained by scaling the random plane metallographic characterizations will be used later as input into the models to assess the feasibility of making predictions of fatigue performance based solely on characterization of the critical material microfeature distribution. This capability could reduce the need for costly, time-consuming tests and provide guidance for producing improved fatigue resistant variations of existing materials.

2.9.1 Scaling *Low Porosity Material* Particle Distributions. It is important to understand the role of constituent particle distribution in the *low porosity material* since there is a transition in initiation mechanisms from micropores in the smooth tests to particles in the open hole tests. The random plane particle size measurement was scaled to obtain the extreme value distribution of particles in the open hole tests. The particle size distribution obtained from the optical metallography was used because there is a larger sample size than from the SEM measured distribution. The data presented in Figure 2.26 for the *low porosity material* at T/2 which is shown as a cumulative probability plot can be fit to a log-normal distribution. The form of the log-normal distribution is :

$$f(x) = \left(\frac{1}{(\zeta \times \sqrt{2\pi})}\right) \exp\left(-\frac{1}{2}\left(\frac{\ln(x) - \lambda}{\zeta}\right)^2\right)$$ (2.1)

Using a graphical fit to the data, the distribution parameters obtained for the *low porosity* variant are, $\zeta = 0.694$, and $\lambda = 2.10$. The comparison between the measured particle size distribution and the fit to the data is shown in Figure 2.34.

The method of scaling the log-normal distribution of features to the extreme value distribution from the open hole tests is based on the area of material in the open hole specimen which is subjected to the highest stress. Because of the stress gradient which exists at the hole, a high stress region exists within which fatigue cracks will initiate at the largest microstructural feature. Since the initiation site is typically located at the surface of the hole, the scaling is done based on a high stress surface area. The high stress surface area, A, can be estimated for a specimen with two open holes by the method developed by Yang et al.[53], giving:

$$A = 8r\theta\left(t + 2\delta + \frac{\delta^2}{r}\right)$$ (2.2)

where r is the hole radius, t is the specimen thickness, 2θ is the angle which defines the arc which sees the highest stress, and δ is the width on the specimen surface subject to the high stress. These parameters are defined in Figure 2.35. The angle θ was taken such that the average stress within the arc was 95% of the maximum stress concentration, which gave $\theta = 19.45°$. The value of δ was chosen which also gave average stress within 95% of the maximum stress concentration. Based on these assumptions, the effective high stress area for an open hole fatigue specimen was estimated to be 15.7 mm^2.

To obtain the extreme value distribution for a series of open hole tests with this high stress area, the number of particles within the high stress region, N^*, must be estimated. The particle density within the material was calculated from the quantitative optical metallography and the value of N^* was 2150.

The extreme value distribution can be obtained according to [68]:

$$F_Y(y) = \exp\left[-\left(\frac{\upsilon}{y}\right)^\kappa\right] \tag{2.3}$$

where the parameters which define the distribution are υ, which is the characteristic value, and κ, which is a shape parameter. The values of υ and κ can be obtained from the parent log-normal particle distribution and the number of particles within the high stress area according to:

$$\upsilon = \exp[\mu_n] \tag{2.4}$$

where
$$\mu_n = \zeta\sqrt{2}\ln(N^*) - \zeta\left[\frac{\ln(\ln(N^*)) + \ln(4\pi)}{2\sqrt{2}\ln(N^*)}\right] + \lambda \tag{2.5}$$

and
$$\kappa = \frac{\sqrt{2}\ln(N^*)}{\zeta} \tag{2.6}$$

From the estimated value of N^* and the log-normal distributional parameters determined previously for the quantitative metallographic data, the parameters for the extreme value distribution were calculated to be $\upsilon = 82.6$ μm, and $\kappa = 5.645$. This extreme value size distribution is plotted in Figure 2.36 along with the data obtained from the fractography of the *low porosity material* open hole fatigue failures. The calculated extreme value size distribution

is larger than the measured size distribution by a factor of about two, but there is overlap of the two distributions. Thus, the calculated extreme value distribution is conservative.

Another method of obtaining the extreme value size distribution would be through a Monte Carlo type simulation. Standard statistical software was used to sample N^* particles from the log-normal distribution which represents the number of particles within the high stress area for one open hole specimen test. The largest particle within the sample will initiate the fatigue crack. The distribution of crack-initiating particles from a number of simulations should approximate the extreme value distribution. This was done for a sample size of 16, and the resulting simulated distribution is compared to the measured fracture-initiating particle size distribution and the calculated extreme value distribution in Figure 2.37. The simulated distribution agrees well with the calculated extreme value distribution and over-predicts the actual particle distribution.

One possible reason that the extreme value size distribution overpredicts the observed distribution is the estimate of the high stress area may be too large. The high stress area here was estimated using the procedure according to Yang et al. [53]. They calculated the radial and surface distances on the specimen which gave average stress concentrations which were 95% of the maximum, and determined the area contained within those points. However, the fractography of failed specimens has shown that the cracks tend to initiate at or near the specimen corner and at radial angles less than what was used in the previous work. Thus, the calculation of the high stress area is most likely an overestimate of the actual area within which fatigue cracks will initiate at particles. In order to obtain a more reasonable estimate of the high stress area for the open hole tests of *low porosity material*, an equivalent high stress area was back-calculated which would yield an extreme value distribution which agrees with the distribution of measured fracture-initiating particles. The characteristic value of the extreme value distribution, υ, was taken to be the average value of the measured particle distribution. The value of N^* was then calculated from equations 2.4 and 2.5 which gave $N^* = 145$. Based on the particle density obtained from the quantitative metallography, the back calculated high stress area came out to be $A = 1.05$ mm^2. This is considerably smaller than the value of 15.7 mm^2 obtained by the method due to Yang et al. [53]. From equation 2.6, the other extreme value distribution parameter, κ, was calculated to be 4.546. A comparison of the extreme value distribution based on a high stress area of 1.05 mm^2 and the measured fracture-initiating particle distribution is shown in Figure 2.38. Based on the smaller area, the calculated distribution matches the upper tail of the curve very well and tends to be conservative in predicting the lower portion of the distribution.

9(PEM)PDM   30

2.9.2 Scaling _Thin Material_ Particle Distributions. Constituent particles are the dominant microstructural feature controlling fatigue damage initiation in the _thin material_. The constituent particle population was measured using the SEM which provided differentiation of particle type based on composition. As was done for the _low porosity material_, the random plane particle size measurement was scaled to obtain the extreme value distribution of particles in the open hole fatigue tests. Since the fatigue crack initiation in the _thin_ variant was controlled by the Fe-bearing constituent particles, the scaling was performed using the Fe-containing particle distribution as well as with the total particle distribution. The cumulative particle size distributions are shown in Figure 2.33. The Fe-containing particle distribution is shifted to larger particle sizes than the total particle distribution. Using the mean and standard deviation values for both the Fe and total particle distributions, they were fit to a log-normal distribution according to equation 2.1. The distribution parameters obtained for the Fe particle distribution was $\zeta = 0.648$ and $\lambda = 2.10$, and for the total particle distribution $\zeta = 0.557$ and $\lambda = 1.603$.

The next step was to calculate the number of particles from each distribution within the high stress region of an open hole test, N^*. The high stress area was taken to be the same value calculated by Yang et al. [53] of $A = 15.7$ mm^2. The particle densities for the total population and the Fe-bearing particle population were obtained from the quantitative metallography. The number of particles in the high stress region were calculated to be $N^* = 12058$ for the total particle population, and $N^* = 2606$ for the Fe particles.

The extreme value distribution parameters were calculated according to equations 2.4 to 2.6 to obtain the extreme value distributions (equation 2.3). For the total particle population the parameters of the extreme value distribution were calculated to be $\upsilon = 33.92$ μm, and $\kappa = 6.69$. For the Fe constituent particle extreme value distribution $\upsilon = 32.78$ μm, and $\kappa = 7.12$. The extreme value distributions along with the measured particle size distribution measured from fractography of the failed open hole specimens are plotted in Figure 2.39. There is very little difference between the two extreme value distributions, but they are both larger than the particle size distribution measured from fractography. Again it is possible that the estimate of the high stress area from Yang et al. [53] is too high resulting in a conservative estimate of the extreme value distributions. The fractography did show, however, that the initiation sites in the open hole tests of _thin material_ were not predominantly located at the hole corners as in the _low porosity material_ tests. Despite this, the estimate of the high stress area still may be too high since the angle θ was large, and no cracks were seen to initiate along the specimen surface implying that $\delta = 0$.

As was done for the *low porosity material*, an equivalent high stress area was back-calculated for the *thin material* which yields an extreme value distribution that agrees with the measured crack-initiating particle size distribution. This was done for the Fe particle distribution only. The characteristic value of the extreme value distribution, υ, was taken to be the particle size median value from fractography. The value of N^* calculated from equations 2.4 and 2.5 was 140. Using the particle density from the quantitative metallography, the equivalent area was calculated to be 0.843 mm^2. This value is close to the equivalent area calculated for the *low porosity material* of 1.05 mm^2. The extreme value distribution based on a high stress area of 0.843 mm^2 was calculated and is compared to the crack-initiating particle size distribution in Figure 2.40. The calculated distribution agrees well with the measured distribution at the larger particle sizes and somewhat overpredicts the particle sizes at the low end of the curve. Thus, the extreme value size calculation is very good at the larger sizes which would yield the shortest fatigue lifetimes, and it is conservative in estimating the lower portion of the curve.

2.10 Summary of Alloy 7050 Characterization

The characterization of alloy 7050 plate variants has yielded several significant results, and the data and mechanistic understanding developed here provide the necessary inputs for the modeling work presented in the next chapter. Among the results of the characterization work, the following aspects are noteworthy.

- The existence of a linkage among processing, microstructure, and fatigue performance for the microstructural variants of 7050 plate has been confirmed.

    - The ability to alter microstructure of a single alloy and product form by process control has been demonstrated.

    - Material variants which have more reduced populations of microstructural inhomogeneities exhibit superior fatigue performance.

- Microstructural features which dominate fatigue performance of different material variants have been identified, classified and statistically characterized.

- A hierarchy of fatigue crack initiators has been identified for the different material variants and specimen types.

    - Geometric effects of fatigue life do not mask those of the microstructure.

    - Machining effects can limit fatigue improvements due to microstructure control.

3. Develop and Validate Fracture Mechanics Based Model(s)

This stage of the report addresses the integration of microstructure effects into conventional fracture mechanics based life prediction methodology.

3.1 Background

Classically, the fatigue failure process of metallic materials has been thought of in three stages: crack nucleation, slow crack growth and rapid fracture. As crack measurement techniques have improved in recent years, researchers have discovered that a major fraction (50% to 90%) of material fatigue life is often spent in crack propagation from material microfeatures (0.0005 to 0.010 in. typical size) to macrocracks on the order of 0.1 in. length and greater [10, 19-49]. Many of the same works have also revealed that crack growth from material microfeatures, such as micropores, particles or slip bands, can and often does occur early within a material's total fatigue life capability. These observations suggest the viability of applying fracture mechanics to life assessment based on the assumption that cyclic life is entirely composed of crack growth.

Fracture mechanics and damage tolerant practices are being used extensively within the aircraft materials and design communities [12, 15, 16]. Under this methodology, crack growth lifetimes for a structure are calculable by integrating the material crack growth rate properties along with stress intensity factor range (ΔK) solutions [7, 69]. Appreciable fracture mechanics data obtained for a variety of engineering applications has validated the principle of similitude, which furnishes the basis for crack growth life prediction. Similitude implies that for a given material, stress ratio and test environment, cracked elements which experience equivalent cyclic stress intensity factors (ΔK) will exhibit the same rate of crack growth (da/dN) regardless of the combination of stress, crack size and part geometry to produce the ΔK. Most practical applications of fracture mechanics to date have been for macrocracks whose size scale are 0.05 in. and greater. This is understandable since the widest utility of fracture mechanics involves defining inspection intervals and product fail/safe criteria in the presence of cracks which are observable during inspection. Recent extensions of ΔK-rate analyses to the small crack regime (present investigation included) have shown encouraging promise in the ability to link long-term performance with early stage crack evolution from microfeatures [32-35, 37, 38, 40-43, 45-49]. This involves mechanical flaw representations of natural microfeature populations. The extension of fracture mechanics based life assessment methods to model the early stage (small crack) propagation from material microstructural features offers some distinct analytical advantages:

- A unified life prediction alternative to cumulative initiation plus propagation life summation would be provided; that is, total life prediction entails one calculation procedure rather than two.

- The approach offers a simpler alternative to extensive S-N type fatigue test programs involving large numbers of structural element tests.

- Damage evolution and total life analysis can be integrated into damage tolerance design and problem solving processes.

- Fatigue scatter effects can be linked to the distribution statistics of crack-originating microfeatures. It is shown in later discussion (Section 3.2.3) that the same microfeatures have little or no effect on material fatigue crack growth rate (da/dN-ΔK) relationships.

- The impact of material and end-product manufacturing processes on performance can be evaluated from knowledge of the microstructure.

Despite the potential benefit of extending the fracture mechanics life assessment to small cracks, the methods have not been exploited within the airframe design and support communities. This is because the models to extend fracture mechanics to the microstructural scale are not well developed, and relatively little microstructure data exists to corroborate mechanical flaw representations with natural (small) flaw populations. In addition, fracture mechanics extension to small, natural flaws takes on the added complexity of the so-called "small crack effect." Designers currently perceive that the generation and analysis of small crack data is more difficult than conventional S-N testing. The analysis in turn requires integrating crack-tip shielding phenomena (i.e., crack closure effects) into the crack drive analysis so that the similitude principle can be applied interchangeably to ΔK-rate data from both large and small crack specimens [40, 70, 71]. Because of the complexities attached to generation and interpretation of small crack data, engineering organizations have been reluctant to invest resources to convert to a wholly fracture mechanics based life assessment approach.

If it could be shown that satisfactory total life projections are achievable without the need for very demanding fracture mechanics analysis (for example, without entailing the tracking of small cracks, or complex stress intensity factor calibration, or crack closure measurement, or FCG threshold determinations), then broader utilization of propagation-based lifting tools would be facilitated. In addition, if existing fatigue crack growth data generation practices and current industry handbook data [72] could be utilized, then implementation of a fracture mechanics based life assessment approach would be accelerated.

Within the airframe industry the call for enhanced life assessment tools is increasing. As the service lifetimes of existing planes are extended beyond their planned lifetime, and newer planes are designed for increasing lifetimes, the demands to ensure airworthiness will require more stringent crack prevention and control strategies. Also, requirements instituted in the aftermath of the Aloha airline accident [6, 16, 73] now stipulate that the occurrence of multiple crack initiations must be considered in the design and maintenance planning for transport aircraft to ensure that damage tolerance capabilities are maintained [11]. It is expected that fracture mechanics based lifeing tools will become an important outgrowth of increasing regulatory pressure to prevent and control cracks.

3.1.1 Modeling Framework. The modeling focus of this investigation was to establish predictive capability to evaluate effects of material microstructure on fatigue durability as defined by cracking that originates from natural material inhomogeneities (e.g., micropores, particles or slip-bands) and grows to a size of adverse structural consequence. More specifically, modeling activity under the present investigation centered on the following objectives:

- To define and validate a fracture mechanics based approach for predicting fatigue damage evolution for cracks originating from microstructural inhomogeneities.

- To assess sensitivities of stress, material properties and microstructure on smooth and notched specimen fatigue performances of the subject 7050 plate alloy variants.

- To demonstrate viability of probabilistic component life assessments derived from random plane microstructural characterizations of material microfeature distributions.

The modeling approach taken assumes that fatigue life is composed entirely of crack growth from critical (life-limiting) microfeatures which are modeled as pre-existing cracks. The aspects of the microfeature type, size, shape and location distributions are modeled into the crack drive solution for the specific product and specimen configuration of interest. The crack propagation rate is dependent upon the crack drive for the specimen/crack configuration and the material crack growth rate (da/dN-ΔK) behavior. Crack growth prediction with accrued cycles entails the standard ΔK-rate integration process of linear elastic fracture mechanics, until the specimen residual strength capacity is exceeded as prescribed by the material strength and toughness properties.

The prediction entails growth of small, naturally forming cracks at a size scale below typical fracture mechanics application. In this study, ΔK-rate data obtained from long crack specimens are employed. To compensate for the growth of small cracks below the long crack threshold, a

simple linear extrapolation to low growth rates is used. This method offers advantage over short crack data generation. Long crack specimen da/dN-ΔK data generation is performed routinely within the industry. Often in practice, small crack data are unavailable because of the resource investment and complexities involved in its generation. Thus, while the small crack effect is an important aspect of understanding, the present 7050 material investigation placed emphasis on analytical protocols enabling utilization of well-established long crack ΔK-rate data generation practices. The rationale for this choice is that fit to existing industry infrastructure will be an essential element to broad industry acceptance.

The incorporation of microstructural effects into fatigue life analysis requires that the type, size and spatial distributions of crack-initiating microfeatures be defined. For the present 7050 alloy variants this was done using a combination of metallography and post-fatigue test fractography (see Chapter 2). Once identified, the features are modeled as pre-existing cracks whose size is equivalent to the size of their natural feature counterparts. This equivalent initial flaw size (EIFS) distribution can be viewed as a material characteristic, Figure 3.1, and serves as a starting point for fracture mechanics life analysis [10, 14, 32, 34, 37].

The EIFS distributions can be determined by any one of three methods; obtained from direct measurement of failure-initiating microfeatures, back-calculated from fatigue lifetime distributions, and by applying a scaling factor to microstructural feature measurements taken from random metallographic planes. Whatever the method used, however, the goal is to ascertain the EIFS distribution descriptive of the life-limiting microfeatures (i.e., the flaw size population extreme values, or weakest links).

The effect of crack-initiating microfeature type on fatigue cracking behavior is incorporated through the crack drive solution. Classical solutions for a semi-elliptical crack do not account for effects of microfeature type (i.e., micropore, cracked particle or de-bonded particle). For this purpose, the Trantina-Barishpolsky effective stress intensity factor [74] is used to integrate crack-initiating microfeature type into the crack drive solution.

Changes in structural geometry will affect life depending on the size and location distributions of the crack-initiating microfeatures. To account for the effect of microfeature size and location distribution, the fracture mechanics model can be linked to general purpose probability software enabling calculation of fatigue curves based on the microfeature distributional statistics.

The conceptual framework which links microstructure and life-cycle performance through basic coupon tests and modeling is illustrated in Figures 3.2 and 3.3 [75]. The analysis path employed

to back-calculate EIFS distribution from lifetime data of smooth fatigue quality screening tests is presented in Figure 3.2, and good agreement of the model with experimental observation is shown [37]. The utility of EIFS distribution as a starting point for integrating product initial quality into life analysis which transcends from coupon to component, to aircraft, to entire fleet is conceptually shown in Figure 3.3.

Microfeature populations from different life-limiting feature distributions, may then be used to assess the effect of material manufacturing processes, composition and other process variables on structural component performance. The hypothetical calculation of Figure 3.4 was undertaken to illustrate how three representative input material "qualities" or "pedigrees" (linked to identifiable micropore populations) might affect the potential for multi-site fatigue damage in the lower wing of a military fighter. The three EIFS populations A, B, and C represent the evolution of microporosity reduction in the old, now, and low porosity 7050 product variants, respectively. For each EIFS distribution, an expected number of cracks exceeding a given size per 1000 fastener holes was calculated for one and two simulated airplane lifetimes according to performance models described in References [10, 14, 34, 37]. It can be seen that distribution C (the low porosity variant) has the lowest probability of multi-site damage.

In review, the assumptions and steps of the modeling process are summarized as follows:

- Fatigue testing is used to determine:
  - The fatigue lifetime distribution for a series of coupon tests.
  - The type, size and spatial distributions of critical (life-limiting) microfeatures from the coupon tests.
  - The da/dN-ΔK fatigue crack growth rate relationship.

- The critical microfeatures are modeled as pre-existing cracks, denoted as equivalent initial flaws, whose size corresponds to the size of their natural feature counterparts.

- Aspects of the critical microfeature type, size, shape and location distributions are modeled into the crack drive solution for the specific product form and specimen configuration of interest.

- Upon cyclic load application, cracks are presumed to initiate immediately from critical microfeature locations.

- Crack propagation occurs at a rate dictated by the specimen crack drive and the material crack growth rate (da/dN-ΔK) relationship. (Correction of long crack data may be necessary to address the small crack effect, e.g., Figure 3.2.)

- Specimen failure is defined from a residual strength model and material strength-toughness properties.

- A general purpose probability software program is used to compute lifetime and/or crack size exceedance probabilities from characterizations of the critical microfeature population, material properties and loading inputs.

For any new set of materials and or loading conditions it would be recommended that the modeling assumptions be validated with experiments. If needed, the model contains tuning parameters to achieve a more favorable fit to the experimental data. Additional discussion of the models and their utilization is deferred to later sections of the report. As a final note, though the main focus of the current investigation is on developing analytical capability to study impact of intrinsic microstructural inhomogeneities (e.g., micropore and particle distributions) on fatigue longevity, other extrinsic discontinuity populations (e.g., corrosion pits, scratches, tool marks) and their effects can be analyzed under the same conceptual modeling framework.

3.2 Model Elements

The model development requires several critical elements that are the building blocks for a fracture mechanics based approach to life prediction. The model elements are described in the following sections.

3.2.1 Equivalent Flaw Representation. The fatigue testing and the associated fracture analysis for the 7050 material variants has identified a hierarchy of microstructural features which affect the fatigue durability (Chapter 2). The failure process seeks out the weakest links within the test material, and they act as sites for the development of fatigue cracking leading to specimen failure. The classical mechanism for fatigue crack formation is associated with crystallographic slip [76]. This mechanism, however, can be circumvented by initiation at intrinsic material discontinuities such as micropores and particles, and is controlled by their size, frequency, and spatial distribution relative to the specimen configuration and loading details. The distribution of features which initiate the fatigue cracks is an extreme value distribution or high-end tail of the total population of like features within the material.

The development of life prediction modeling based on microstructural sources of fatigue damage initiation require representation of the crack-initiation feature distributions capable of being input into the analysis format. Furthermore, if the predictions are to be made based on quantitative microstructural analyses of the material, without performing measurement on failed coupon test failures, then it is necessary to consider the statistics of the microfeature population.

The correlation of smooth specimen lifetimes with crack-initiating feature size showed that the longest feature dimension correlated well with the specimen lifetime (see Figure 2.11). Thus, for the extreme value distributions from the smooth specimen tests, the longest dimension of the crack-initiating features was used to represent the "characteristic" size dimension of an equivalent flaw for the modeling. The depth of the equivalent flaw is taken as the maximum feature dimension. For analysis purposes, the shape of the flaw is assumed to be a semi-elliptical surface crack with an aspect ratio, a/c, of 0.8, where "a" is the half surface length of the flaw and "c" is the depth of the flaw. This aspect ratio represents the "equilibrium" shape where the crack driving force during cyclic loading is the same where the flaw intersects the specimen surface and at the maximum depth within the specimen interior [60]. The rationale for this assumption is that cracks emanating from an irregularly shaped microstructural feature at the surface of a cylindrical specimen will very quickly grow to the equilibrium shape. This equivalent flaw representation of a crack-initiating microstructural feature in a smooth fatigue specimen is shown in Figure 3.5a.

Open hole specimen fatigue failures were observed to initiate at microfeatures located along the surface of the hole bore or at the corner of the hole and the specimen surface. Since the specimens were excised from the original plate in the long-transverse direction, the specimen width is parallel to the plate rolling direction. Thus, the features which initiate the failures tend to be aligned perpendicular to the hole bore. This facilitates representation of the feature sizes as equivalent semi-elliptical flaws with dimensions directly measured from the crack-initiating feature sizes. This equivalent flaw representation of a crack-initiating microstructural feature in an open hole fatigue specimen is shown in Figure 3.5b.

The distribution of crack-initiating microstructural features from a series of coupon specimen tests represents the extreme value distribution of features. This distribution is dependent upon their size and spatial distribution of features within the material, their population density, and the test specimen geometry and loading conditions. It has been shown for a population of constituent particles, the extreme value distribution of features can be approximately calculated based on quantitative metallographic results and specimen geometry effects (see Section 2.9). The test results of the *low porosity material* have shown that there is a competition between

different microfeature populations, where the micropore population controlled the lifetime in smooth specimen tests and the particle population was controlling in the open hole specimen tests. Thus, the life-limiting feature distribution is dependent upon the feature population statistics and the specimen geometry. The interaction of the feature size distributions and population density with specimen geometry and the resulting crack driving forces will be examined in Section 3.3.3.

The equivalent flaw representations of crack-initiating microstructural features presented here allows incorporation of microstructural effects into fracture mechanics based fatigue lifetime prediction models. The equivalent semi-elliptical shaped flaw does not consider the type of microstructural feature present; e.g. micropore or particle. The next section of the report details the crack driving force solutions used for lifetime predictions from the various microstructural features.

3.2.2 <u>Crack Growth Model</u>. The fracture mechanics based approach to fatigue life modeling employed here assumes that the microstructural inhomogeneities behave as pre-existing cracks, and that fatigue life is entirely composed of crack growth from an initial inhomogeneity. The influence of the crack-initiating microfeature type is incorporated into the crack drive solution. This section details the numerical algorithm used to calculate crack growth and the crack drive solutions used to describe the influence of the crack-initiating microfeature type.

The basis of the modeling is a fracture mechanics program on crack coalescence from Grandt et al. [77-79]. The original numerical algorithm calculated the fatigue life of an open hole fatigue specimen containing one or more elliptical cracks which is subject to a remote cyclic loading. The initial layout of the cracked specimen, shown in Figure 3.6, will grow with the application of a remote cyclic stress. Assuming the crack will grow a distance Δc_1 at point 2, then, assuming the increment of crack growth is sufficiently small, the cyclic life for this to occur can be approximated by:

$$\Delta N = \frac{\Delta c_1}{da_2/dN} \qquad (3.1)$$

where ΔN is the number of cycles to grow the crack and da_2/dN is the crack growth rate at point 2. The growth at any other point can then be calculated by:

$$\Delta c_i = \frac{da_i}{dN} * \Delta N = \frac{da_i}{dN} * \frac{\Delta c_1}{da_2/dN} \qquad (3.2)$$

where i is the crack location and da_i/dN is the crack growth rate at point i. If the stress intensity factors are known then the crack growth rates for the various flaw positions may be calculated using an appropriate fatigue crack growth model generalized in equation 3.3.

$$\frac{da_i}{dN} = F(\Delta K_i) \tag{3.3}$$

Grandt's algorithm made the assumption that the initial cracks could be represented as "ideal elliptical" surface or corner cracks. This assumption enables the use of the Newman and Raju [59] stress intensity factor solutions. Crack interaction was included by modifying these stress intensity factors at points 3 and 4. When crack points 3 and 4 touch, it is assumed that they immediately join to form a single crack [78, 79].

To incorporate different microstructural features (in particular micropores and particles) as initiation sites for crack growth, a modification of the Newman and Raju stress intensity factor solution is required. Trantina and Barishpolsky [74] examined the stress intensity factor solution of an ellipsoidal micropore or particle which contains an equatorial crack of length b as shown in Figure 3.7. The micropore height is h, its diameter is $2R$, the crack extends a uniform length b around the feature equator (x-y plane), and a remote stress σ is applied in the z direction perpendicular to the plane of crack growth. An effective stress intensity factor K for this flaw geometry is

$$K_{T-B} = \beta \sigma \sqrt{\pi b} \tag{3.4}$$

where the dimensionless geometric term β is given by

$$\beta = \frac{2}{\pi} + B\left(1.12 k_t - \frac{2}{\pi} - 1\right)\left(\frac{R}{b+R}\right)^{10} + \left(\frac{R}{b+R}\right)^{1.8} \tag{3.5}$$

Here k_t is the elastic stress concentration factor for the ellipsoidal micropore or particle (without the crack), and depends on the aspect ratio $h/2R$. The value of k_t can be obtained from standard fracture mechanics stress concentration handbooks. The constant B is 1.0 for a micropore, 2.0 for a bonded cracked particle, and 0.3 for an unbonded particle. Note in Figure 3.7 that the total length of the crack for modeling purposes is $2R + 2b$, and the ratio $R/(b + R)$ in equation 3.5 represents that portion of the crack ascribed to the initial inhomogeneity. Note that for a void with $B = 1$, and for a crack size $b \gg R$, equation 3.5 reduces to $2/\pi$, the well known result for a penny shaped crack in an infinite body [80]. In this case, the micropore no longer influences the crack tip stress intensity factor. At the other extreme, when $b = 0$, $R/(b + R) = 1$, so that the

stress intensity factor is zero from equations 3.4 and 3.5 (i.e., the inhomogeneity is no longer a crack but behaves as a notch).

The ratio of the Trantina-Barishpolsky stress intensity factor to the stress intensity factor of a penny shaped crack is used to modify the Newman-Raju stress intensity factor to account for the type of crack-initiating feature [42]. Thus, the stress intensity factor is given by:

$$K = \frac{K_{T-B}}{K_{penny}} * K_{N-R}$$
(3.6)

Here K_{T-B} is the Trantina-Barishpolsky stress intensity solution for an infinite plate [74], K_{penny} is the stress intensity solution for a circular penny shaped crack in an infinite body [80], and K_{N-R} is the appropriate Newman and Raju stress intensity factor solution for a surface or corner crack [59]. The equivalent flaw representation of crack-initiating features uses a semi-elliptical shaped crack whose major and minor axes are defined by the size of the natural feature. To account for differences in the major and minor dimensions, crack growth in those directions is analyzed by defining K_{penny} with respect to the major and minor axes. Thus, two crack drive solutions are used for non-circular flaws.

Under the imposition of a far-field cyclic stress range $\Delta\sigma$, the Trantina-Barishpolsky cyclic stress intensity factor is,

$$\Delta K_{T-B} = \beta\Delta\sigma\sqrt{\pi b}$$
(3.7)

It is assumed that for a given far-field cyclic stress, $\Delta\sigma$, a crack of length b forms in the first few cycles. The length b of the pupative crack is assumed to be proportional to the cyclic plastic zone size ahead of the crack as shown in Figure 3.7. An estimate of the cyclic plastic zone size associated with ΔK_{T-B} is, [81]

$$r^* = \frac{1}{\pi}\left(\frac{\Delta K_{T-B}}{2\sigma_y}\right)^2$$
(3.8)

where σ_y is the yield strength of the material. The material's static yield strength was used in this study, but alternately the cyclic yield or flow stress could be used if they are significantly different than the static yield. The parameter, b, is equated to this measure of plastic zone size. Thus, solve equation 3.7 for b and equate it to the plastic zone size of equation 3.8. This amounts to finding the ratio $R/(b + R)$ that satisfies

$$\frac{\beta\Delta\sigma}{2\sigma_y} = 1 \qquad\qquad (3.9)$$

The above methods provide a means for estimating the crack drive and calculating the crack growth from a microstructural feature.

3.2.3 Crack Growth Rate Laws. The fracture mechanics approach to modeling the fatigue durability of the 7050 product variants requires that the fatigue crack growth behavior be represented in a manner amenable to analysis based on the crack driving force. Considerable historical data from Alcoa on the crack growth behavior of 7050-T7451 plate products are used to obtain the relationship between the rate of crack propagation and the crack driving force. Figure 3.8 shows the crack growth rate data versus the cyclic stress intensity (da/dN vs. ΔK) for plate of various thicknesses. The data show that the rate of crack growth is independent of the product thickness. It has been shown previously (Section 2.7) that processing path affects the distribution of microstructural features which initiate fatigue failures. Presumably, the different thickness materials contain different microstructural feature distributions, yet these differences have no effect on the material fatigue crack growth rate relationship. Thus, for the four microstructural variants of 7050 plate used in this program, the da/dN-ΔK crack growth relationship is assumed to be similar. This relationship can be represented by the Paris equation [82]:

$$\frac{da}{dN} = C\Delta K^m \qquad\qquad (3.10)$$

where C and m are constants. For the data in Figure 3.8, $C = 3.9 \times 10^{-10}$, and $m = 4.175$. The Paris equation represents the data well for values of ΔK greater than 4 ksi $\sqrt{\text{in}}$.

The approach used to model the fatigue durability performance of the 7050 materials is based on the application of fracture mechanics to the fatigue crack growth from intrinsic microstructural features. The rationale for this is the well-known small crack effect where microstructurally small cracks can grow at stress intensities below the long crack threshold, and at rates faster than predicted by long crack growth data (for a comprehensive review, see [25]). The growth of small cracks at stress intensities below which long cracks are observed to grow is represented by a simple linear extrapolation of the Paris law to low growth rates. As mentioned previously, the study of the small crack effect for the materials examined here was beyond the scope of this study, and this simplistic approach was taken to demonstrate easy fit to the industry's current analytical infrastructure.

43

3.2.4 Termination Requirements. The model proposed in the previous sections grows an idealized crack independently in two perpendicular directions. The program tracks the major dimensions of an elliptical shaped crack. Two main failure limit states control the termination of the crack growth model; net section strength and fast fracture of the material. To determine net section stress, the area of the elliptical crack is subtracted from the total specimen area and divided into the maximum far field load. If this value exceeds the limit stress (taken here as the material static yield strength) the calculation is terminated. The fast fracture limit state can be controlled in either of two ways; exceedance of a crack growth rate or exceedance of the material fracture toughness. The model software checks whether either of these criteria are met after each incremental cyclic crack growth step.

There are two methods to control intermediate stops of the analysis. The program can be set to stop after a crack has reached a given size. This provides the analysts with the lifetime distribution to reach a given crack size. Additionally, the stop can be set for a given number of cycles providing the distribution of crack sizes for a given life. Both the life distribution to a given crack size and the crack size distribution at a given lifetime can be useful for assessing structural durability and in determining inspection intervals.

3.2.5 Probabilistic Modeling. In the proceeding sections, a damage model for fatigue has been presented. This model calculates the fatigue lifetime of specimens for crack growth from microfeatures in the 0.001 to 0.02 in. size range. The microfeature size and location relative to the specimen geometry can be measured after the test specimen fails by examining the fracture surface via scanning electron microscopy. The development of life-limiting microstructural characteristics was described in detail in the preceding chapter. Using these data, the model can then calculate the known fatigue life of the failed test specimens. This is required for calibration and to check the validity of the model. However, it is desirable to use the model in a predictive manner, relying on inputs of the microfeature distributional statistics and the material properties rather than post-test information. An examination of fracture surfaces quickly reveals that the microfeature size and location values vary from specimen to specimen and that there is no way to apriori determine the exact values. Thus, a probabilistic approach must be used which relies on the microstructural feature distribution statistical information to predict the fatigue life.

The microfeature distributional statistics are incorporated into the model by linking with the general purpose probabilistic software program PROBAN [83]. The above fatigue life prediction model is expressed as a FORTRAN subroutine and linked to PROBAN which enables the inputs to be considered as random variables. The distributional statistics for the microfeature

populations within the material serve as input data and the microfeature size, location and type can be treated in a probabilistic manner.

With these distributions as inputs, a stratified Monte Carlo sampling method, Latin Hypercube sampling, was used to determine the distribution of fatigue life. By altering the input stress an entire probabilistic stress-life curve can be developed. In general the data is contained within the 5%, 50%, and 95% fractiles (a X% life fractile is the life value for which X% of the specimens will have a shorter life) for a material. The probabilistic nature of the model enables prediction of the effects of initial inhomogeneity size, shape, and location distributions on specimen fatigue life distributions for any stress level.

3.3 Discussion of Model Results

The model developed here has been applied in several ways. Verification of the modeling approach is achieved by calculation of known smooth specimen fatigue lifetimes of the four 7050 microstructural variants based on measured crack-initiating microfeature distributions. Next, the open hole stress versus lifetime curves for the four variants are calculated from the extreme value microfeature distributions incorporating the statistical aspects of microfeature size and location distribution. Open hole specimen fatigue lifetimes are also calculated from the random plane microstructural characterizations scaled to obtain the extreme value distributions for the *thin* and *low porosity* variants. The model is then used for parametric studies which assess the impact of microstructural variables on fatigue performance. Finally, model calculations are made to examine the influence of competing microfeature distributions on failure mode, and to define microstructural refinement required to enhance fatigue performance. The results of these model calculations are presented in the following sections.

3.3.1 Model Calculations of Smooth Specimen Fatigue Data. The first application of the model described above is to validate the ability to predict fatigue crack growth from life-limiting microfeatures for the 7050 product variants used in this program. The smooth axial fatigue testing described in Section 2.3 and the fractography of the failed specimens in Section 2.4 identified the critical microstructural features which cause failure in the 7050 materials. For the *old, now* and *low porosity materials*, the type and size of crack-initiating feature were quantified. The many of the failures in the *thin* variant exhibited slip induced fatigue cracking, and were associated with crystallographic slip and not an identifiable microstructural inhomogeneity. The first step in model verification was to deterministically calculate the smooth specimen fatigue lifetimes for crack growth from the measured crack-initiating feature. The initial calculations were performed without incorporating the Trantina-Barishpolsky stress intensity factor solution,

but based solely on the size of the life-limiting microfeature. Recall, the Trantina-Barishpolsky analysis was used to incorporate effects of microfeature type into the crack drive solution (Section 3.2.2). Figure 3.9 plots the predicted fatigue lifetime versus the actual life for the *old*, *now* and *low porosity materials*. As can be seen, the model does a good job in predicting the lifetimes for the *old* and *now* variants, but underpredicts the lifetime of the *low porosity material*.

While microporosity was observed as the dominant failure initiating microfeature in the *old* and *now materials,* the *low porosity material* smooth fatigue failures were observe in some cases to initiate from clusters of micropores and particles. This may account for some of the difference in predicted versus actual lifetimes. To improve the accuracy of the prediction, the Trantina-Barishpolsky analysis was employed to consider the effects of the crack-initiating microfeature on the crack drive. The prediction results incorporating the Trantina-Barishpolsky solution are plotted in Figure 3.10 as predicted lifetime versus the actual lifetime. The data show that the predicted results more closely match the actual data with incorporation of the Trantina-Barishpolsky analysis, however, the agreement is still not as good as for the *old* and *now* variants. Again, this may be due to several of the initiations occurring at a combination of micropores and particles, whereas the Trantina-Barishpolsky stress intensity factor only considers micropores or particles individually.

Predictions of the smooth specimen fatigue lifetimes were also made using as input the statistical information for the crack-initiating extreme value feature distributions for the materials. The depth and width size distributions of crack initiating microfeatures obtained from fractography were fit to either a Weibull or log-normal distribution, and the parameters which describe these distributions for the *old, now* and *low porosity materials* are given in Table 3.1. A Latin Hypercube sampling method was used to obtain crack-initiator sizes from the extreme value distributions and a distribution of smooth fatigue lifetimes for each of these materials was calculated. The calculated fatigue lifetime distributions for the *old, now* and *low porosity* variants are plotted along with the actual lifetime distributions in Figures 3.11-3.13 respectively. Again, there is good agreement between the predicted and actual distributions with the *old* and *now* variants, while the prediction for the *low porosity material* is conservative. Overall the prediction accuracy is impressive, however, additional work may be needed to account for the combination of micropores and particles as initiation sites in the *low porosity* variant.

3.3.2 <u>Model Calculation of Open Hole Specimen Fatigue Data</u>. As was done for the smooth specimen fatigue tests, the fracture surfaces from the open hole specimen fatigue failures were examined and the crack-initiating features were quantified (Sections 2.3 and 2.4). These values

can be input directly into the model to perform deterministic calculations of fatigue life to either calibrate or test the model. Figure 3.14 compares results of two tests, one showing a micropore at the center of the hole bore, and the other showing the failure initiating particle located at the hole corner. The figure also compares the calculated and actual fatigue lifetimes associated with these tests. Knowing the exact size and location of the crack-initiating features, the model accurately calculated the fatigue lives for both cases. However, it is desirable to use the model in a predictive manner where the exact location and size of the crack-initiating features are both unknown and considered as random variables.

From the quantification of the open hole specimen fracture surfaces of the 7050 material variants, the crack-initiating microfeature type and the extreme value distributions for the feature size, shape, location were determined (see Sections 2.3 and 2.4). The statistics of these distributions can then be used to calculate the distribution of fatigue lifetimes for each material variant. The statistical aspects of the crack-initiating feature distributions were incorporated into the modeling through the use of a general purpose probabilistic software program PROBAN [83]. The growth model was linked to the program PROBAN and the microfeature distributions were treated as random variables. The distributional parameters used for the open hole fatigue lifetime calculations for each of the material variants are listed in Table 3.1.

Also required for the model calculations (equation 3.5) is an estimate of the local stress concentration factor, k_t, for the crack-initiating features in each of the material variants. This can be obtained from handbooks for regularly shaped crack-initiating inhomogeneities when their shape is known, but needs to be estimated here for irregular micropores and particles. The values of k_t for each of the material variants was estimated by fitting the model to the open hole S/N data at the stress level which resulted in infinite life (the fatigue limit) and using the value of k_t which gave the best fit. It will be shown later that the local stress concentration factor is a function of the crack-initiating feature type and shape. The k_t values obtained for each material are listed in Table 3.1. The value of the stress concentration for the *old, now, low porosity*, and *thin* materials gets progressively smaller. This trend suggests that a decline in life-limiting feature severity can be linked to refinement of microstructure in material of higher pedigree.

The calculated stress versus life curves for each material variant, along with the open hole fatigue test data are shown in Figures 3.15-3.18. The model was used to calculate the 5%, 50%, and 95% fractiles for each material. In general, the results of the model are in good agreement with the test data. Exceptions are the predicted lifetimes at high stresses in the *thin material* where the model tends to overpredict the lifetimes. This may be due in part to "short crack" effect not being well represented by the input fatigue crack growth rate data at the smaller initial

crack sizes in the *thin material*. Despite this difference, the data for the other variants are very well represented by the model results.

3.3.3 Model Calculations Based on Scaled Random Plane Microstructural Characterizations.

The previous fatigue lifetime predictions for the open hole specimens are based on the extreme value distributions of crack-initiating microfeatures obtained by direct measurement from the fatigue fracture surfaces. It would be desirable to predict fatigue performance based on random plane metallographic characterizations of the microstructure. This capability could facilitate faster material development by reducing the need for costly, time-consuming tests. In addition, it can provide guidance for producing more fatigue resistant variants of existing materials.

It has been shown that random plane microstructural characterizations can be scaled to obtain the extreme value size distribution of features (see Section 2.9). Model predictions are made here using as input the scaled microfeature distributions for the *low porosity* and *thin* plate variants presented previously. Results from the previous chapter showed that when a scaled area of approximately 1.0 mm^2 was used, the extreme value feature size distribution parameters obtained for the two materials are: *low porosity* $v = 0.00182$ and $\kappa = 4.546$ and *thin material* $v = 0.00063$ and $\kappa = 5.062$. The extreme value size distribution shown previously is given by equation (2.3) [68]:

$$F_Y(y) = \exp\left[-\left(\frac{v_n}{y}\right)^{\kappa}\right]$$

Using these distributions as input, the open hole fatigue life S/N curves predicted are shown along with the actual fatigue data in Figures 3.19 and 3.20 for the *low porosity* and *thin* variants respectively. For both materials, the predicted fatigue lifetimes agree well with those determined by testing. This work demonstrates that reasonable estimates of statistical fatigue performance can be made from scaling of random plane characterizations of life-limiting microfeature populations.

3.3.4 Parametric Studies.

The model developed has been shown to reasonably predict the material fatigue behavior based on quantitative measures of critical microstructural features. One potential utility of the model is application to material design. An analytical approach to assess effects of processing and composition on microstructure and material performance can greatly reduce material development costs and shorten the development time. As an illustration of the model utility, a parametric study was performed to assess impact of microstructural

parameters on material performance. Specifically, the effect of particle size and shape, and material yield strength on fatigue performance are evaluated.

The fatigue endurance limit, or the stress which yields infinite life, $\Delta\sigma_\infty$, can be directly estimated from equations 3.9 and 3.5. To obtain the stress at infinite live, it is assumed that $b = 0$, which results in:

$$\Delta\sigma_\infty = \frac{2\sigma_y}{\frac{2}{\pi} + B\left(1.12k_t - \frac{2}{\pi} - 1\right) + 1} \qquad (3.11)$$

Although the number of cycles to failure is sensitive to the initial micropore or particle size, equation 3.10 suggests the infinite life stress is independent of the micropore or particle size. It is proportional to yield strength and shows a strong dependence on local stress concentration factor, k_t, and the type of inhomogeneity through B. For micropores, $B = 1$ and equation 3.10 becomes,

$$\Delta\sigma_{\infty-voids} = \frac{2\sigma_y}{1.12k_t} \qquad (3.12)$$

For cracked particles, $B = 2$ and equation 3.10 becomes,

$$\Delta\sigma_{\infty-particles} = \frac{2\sigma_y}{2.24k_t - 1 - \frac{2}{\pi}} \qquad (3.13)$$

A plot of the sensitivity of the infinite life stress to the local stress concentration factor is shown in Figure 3.21 for both micropores and cracked particles. For micropores, a lower limit on the stress concentration factor is a smooth sphere for which k_t is about 2. At this point, the ratio of infinite life stress to yield stress is about 0.9. For equations 3.12 and 3.13, it is assumed that the yield strength is an upper limit on the infinite life stress for the mechanism of fatigue crack growth from a micropore or particle. This assumption sets limits on the stress concentration factors below which little improvement in infinite life stress is expected. For micropores, improvements are possible up to the point at which the micropore is the shape of a smooth sphere. For non-spheres there is a dramatic drop in the infinite life stress for small increases in the local stress concentration. For a stress concentration of 3, the ratio of infinite life stress to yield strength has dropped to about 0.6. This corresponds to a circular cavity of elliptical cross section with aspect ratio 2.5, as depicted in Figure 3.22. For particles, the value of stress

9(PEM)PDM   49

concentration factor at which the infinite life stress begins to decrease is 1.62. The stress concentration of the particle depends both on particle shape and particle elastic modulus. For a bonded uncracked particle, stress concentrations in the matrix are typically less than 2 [84]. A plot of the stress concentration factor for an isolated rigid elliptical cylindrical particle is shown in Figure 3.23. For far-field uniform tension, the stress concentration factor for tangential tension is less than 2 for aspect ratios ranging up to about 30. A comparison between the stress concentration for uncracked particles in Figure 3.23 and for micropores in Figure 3.22 shows that micropores have a much more severe stress concentration than particles at equivalent aspect ratios. This suggests that particles must first crack before they have a significant effect on the infinite life stress as shown in Figure 3.21. In previous studies on the effects of cracked particles [85, 86], it has been shown that cracked particles behave like high aspect ratio voids. This is expected to severely limit the infinite life stress, as shown in Figure 3.21.

The sensitivity of the fatigue model to changing material and microstructural parameters can be assessed by calculating the cyclic stress versus life (S/N) curves for the varying material conditions. The influence of particle size on fatigue life is shown in Figure 3.24 for particle sizes ranging from 0.001 in. to 0.01 in. at a stress concentration value of 2. The yield strength was taken to be 70 ksi. The effect of increasing particle size is to decrease life throughout the range of stress levels. The infinite life stress, however, is insensitive to particle size. A similar trend holds for increasing micropore size at constant aspect ratio.

The sensitivity of fatigue life to the material yield strength has also been examined by calculating cyclic S/N curves at different levels of material yield strength. The data are shown in Figure 3.25 based on a fixed particle size of 0.005 in. and the yield strength is varied from 60 ksi to 80 ksi. As seen in the figure, fatigue life is almost independent of yield strength at stresses well above the infinite life stress, $\Delta\sigma_\infty$. However, material yield strength has a dramatic effect on the endurance limit, $\Delta\sigma_\infty$, where increases in the yield stress result in increases in the endurance limit.

The local stress concentration resulting from the inhomogeneity aspect ratio has a similar effect on the fatigue life curve as does yield strength. Figure 3.26 shows a comparison of fatigue S/N curves for particles and micropores of differing shape and therefore different k_t values. The yield strength was fixed at 70 ksi and the micropore or particle size was taken to be 0.005 in. The calculations show that increasing the local stress concentration has a large effect on decreasing the infinite life stress. The calculated results suggest that dramatic increases in fatigue performance could be achieved by simultaneously decreasing the micropore or particle size, reducing the micropore or particle aspect ratio while increasing the yield strength.

9(PEM)PDM   50

3.3.5 <u>Competing Microfeature Distributions</u>. The fatigue testing and fractography reported in Chapter 2 of this report revealed a transition in fatigue crack-initiating features in the *low porosity material* from predominantly one of microporosity initiated failures in smooth specimen fatigue tests to one of particle initiated failures in open hole specimen tests. This transition was seen to affect the performance relative to the *now material*, where the *low porosity* variant exhibited longer lifetimes in the smooth specimen tests, but in open hole tests the two materials exhibited similar lifetimes (see Section 2.3). This transition was qualitatively explained by the interactive effects of micropore/particle size and spatial distributions and the volume of highly stressed material associated with each specimen type. Because the particle population density is so much larger than that for micropores, there is a higher probability of encountering a particle at a local region of high stress. For an open hole specimen, the area of highest stress is the corner where the stress concentration is about 20% higher than in the bore of the hole. Thus, because of the differences in population density, there is a high likelihood of a particle being located at the corner (see Section 2.4.2). This section uses the model to compare the extreme value distributions for cracking from corner particles compared to micropores within the hole bore to understand the transition in fatigue crack-initiating features in the *low porosity material*.

The model was applied to calculate the extreme value size distribution of particles which resulted in equivalent open hole specimen fatigue lifetimes as the micropore-initiated failures of the *now material*. The critical particles are assumed to occur at the corner in the open hole specimen and should represent the particle extreme value size distribution from the open hole tests of the *low porosity material*. The procedure used is schematically illustrated in Figure 3.27. For a series of smooth specimen fatigue tests of the *now material*, there is a resultant distribution of specimen lifetimes. From this distribution, the extreme value micropore size distribution can be obtained either by back-calculation from the lifetime population or by direct measurement on the fracture surfaces. It is then assumed that the resultant microporosity distribution also represents the extreme value micropore size distribution for the open hole specimen tests. This may not necessarily be the case because of the differences in the high stress area between the two specimen types, but this assumption should err on the conservative side. From this micropore distribution, the distribution of open hole specimen lifetimes can be calculated. Now, assuming particle initiation sites at the corner, the extreme value particle size distribution can be back-calculated from the previously calculated open hole lifetime distribution. The extreme value micropore size distribution from smooth specimen tests of the *now material* and the back-calculated equivalent life particle size distribution are plotted in Figure 3.28. The presence of these two distributions in open hole fatigue specimens results in equivalent fatigue lifetime

distributions. A decrease in either of these size distributions would drive failure initiation to the other mechanism.

For the *low porosity material* the micropore size distribution is smaller than that of the *now material*. The extreme value micropore distribution for the *low porosity* variant, back-calculated from smooth specimen lifetime data, is plotted in Figure 3.29 along with the back calculated particle distribution from Figure 3.28. The micropore size distribution is smaller than the particle distribution and much smaller than the micropore size distribution from the *now material*. Thus, the extreme value micropore size distribution for the *low porosity* material is not expected to be the life-limiting feature distribution in the open hole tests.

To obtain further improvement in open hole fatigue performance of the *low porosity material*, the model can be used to calculate the extreme value particle size distribution where they are no longer the life-limiting feature distribution. Using the procedure outlined previously, the equivalent life particle distribution was calculated starting with the smooth specimen extreme value micropore size distribution. The equivalent life micropore and particle distributions for the *low porosity material* are plotted in Figure 3.30. The maximum improvement in open hole specimen fatigue performance through reductions in particle population would be obtained by reducing the particle size such that the resulting extreme value distribution is the size shown in Figure 3.30. At this point, the failures would have equal lifetimes from either micropores or particles and further reduction in the particle distribution would have no effect on the lifetime distribution without commensurate decreases in the micropore population.

This application of the model demonstrates the utility of this methodology in material design. For a material with competing microfeature distributions, the model can be used to calculate the level of microstructure refinement necessary to achieve property enhancements. The model was used here to calculate the extreme value size distribution of particles required to drive the failure mode to micropores. From this extreme value distribution, the population distribution of particles within the material needs to be obtained so that material designers can appropriately modify composition and process variables to achieve the desired microstructure. In other words, the extreme value size distribution needs to be converted to the particle size distribution within a material. This can be accomplished using the scaling procedure described in Section 2.9 to back-calculate the parent distribution which results in the desired extreme value distribution.

3.4 Summary of Modeling

The analytical modeling task has successfully provided a method to reasonably estimate the performance capabilities of a material based on the life-limiting microstructural feature populations. Some of the significant aspects of the modeling work are:

- Fracture mechanics principles can be applied to the scale of the microstructural features which govern fatigue life.

- Fatigue life estimates can be obtained based on an understanding of the size distributions of crack-initiating microstructural features. These feature distributions can be measured directly from fracture surface examinations or calculated from random plane metallographic microstructural characterizations.

- The effects of the initial inhomogeneity size, shape, and location distributions on specimen fatigue life distributions can be analytically predicted.

The modeling provides a set of analytical tools to translate understanding of life-limiting features of material microstructure, known to emanate from the compositional and processing history of an aluminum alloy product, into useful life-cycle design guidance for new airplanes entering the fleet, or support guidance for economical operation of high time aircraft already in the fleet. Such models can and have been successfully applied to several practical design and materials evaluation problems [37, 38, 49, 87, 88].

4. Technology Transfer

The previous sections of this report have detailed the development of a technical path for quantitative linking of material microstructure to fatigue performance. In that work, the ability of the modeling approach to predictively bound coupon fatigue specimen (S/N) test response was verified for an aluminum aerospace alloy. The findings are significant in that they solidify the utility of fracture mechanics modeling logic to predict total life as crack growth accrued from life-limiting microfeatures. For the technology to have broader impact, it must confer value to evaluations of material/structure durability.

One task of this program is to more specifically define opportunities and make recommendations for broadening the impact of the developed technology to Navy interests. This section of the report presents three envisioned paths where the application of the technical modeling approach could add value. Each of these paths are beyond the scope of the current work and would require additional development to carry the technology benefit beyond the current level.

4.1 Model Application to Material/Process Development and Selection

The first envisioned opportunity for capturing value from this work lies in the area of material/process development and selection. The continued use of airframes beyond their design lifetime has created a need for material replacement solutions for durability related problems. Material solutions are also being sought for newer airplanes which are being designed to last longer and/or surpass previous durability/reliability targets to reduce maintenance costs. In addition, as airframers are seeking to reduce manufacturing costs through part consolidation, the classical crack arrest advantages of built-up structure must be countered with more demanding durability and damage tolerant assurances in the unitized material forms being contemplated for replacing the former assembly methods. Given today's economic constraints, these material needs are best served by the exploitation of proven technologies enabling efficient selection and use of quality-improved processes, derivative alloys and product form alternatives (e.g., machined hogouts vs. die-forgings). Regardless of technology route, the emerging paradigm implies that guarantee of fewer and smaller microfeatures to act as crack initiation sites will be welcomed.

Traditional approaches to material development which involve iterative trials and extensive characterization can be expensive and time-consuming, and can result in lost opportunities if cost goals and/or timetables for implementation cannot be met. The implementation of an analytical approach to assessing impact of material microstructure on durability performance has

the potential to aid the material design process by enabling faster, more focused and more economical definition of results. Analytically the optimal processing and composition parameters can be defined earlier, and a much wider range of alloy/process options can be addressed. Thus once the infrastructure is in place, routes can be chosen to better tailor material characteristics to the needs of the specific applications.

The technological approach presented in this report has already been proven suitable for evaluating the relative merits of competing product forms such as plate, forgings, extrusions and castings [35, 37, 43, 49, 87, 89]. The traditional methods of specifying material properties do not discern durability enhancing aspects of process induced changes in microfeature populations, the impact of which is beyond the standard array of static mechanical property tests. Thus, the developed analytic framework is appealing for contrast of machined hogouts and competing net-shape product technologies in trade studies targeted to defining optimal balance of performance and manufacturing cost.

Analytical enhancements can result in faster, more economical material development processes which may translate to more rapid, less costly introductions into service. This is achieved through reductions in the number of iteration trials necessary, and a reduction in the scope and scale of verification testing. In short, the methodology applied to material design can result in the development of better material, facilitate the selection of material processing options, and reduce the cost and time associated with implementation of newer materials.

While the results of this investigation clearly demonstrate the potential life-limiting impact of crack-initiating microfeatures, raw material suppliers and part vendors have not historically provided quantitative information on populations of microvoids, particles, metal phases, and other potential life-limiting microfeatures (e.g., corrosion, manufacturing/assembly marks, traffic damage, etc.). Life-limiting feature databases must therefore become more widely available to capture of the full benefit potential of analytic durability methodology. The results of this study provide guidance helpful to the development of standardized protocols for generation of this database and its eventual integration into Navy and industry-wide technology standards.

4.2 Model Application to Structural Design

Traditional design processes have been unable to capture the benefit of material quality improvements which may improve material durability. Classical safe-life fatigue design practices, which entail representative testing and statistical methods to move design curves

outside the realm of experimental scatter, often render change uneconomical because of the large testing burden involved. Moreover, design for slow crack growth in certain items of fracture critical hardware (e.g., aircraft large structural bones, rotorcraft components and mechanical systems) may be difficult to manage because of the small critical crack sizes and inspection economics involved. The industry's drive for more unitized structure in concert with new regulation that non-pristine or aging structure be accounted for in design implies that strategies for crack prevention and control will become increasingly crucial to the assurance of structural airworthiness objectives.

The more modern analytic view of durability assessment entails description of material/structure degradation embodied in prediction of cracks, growth of cracks and residual strength with cracks. Since cyclic failure processes will generally seek out system weak links to start cracks, the analytic framework of the present investigation offers a means to define and quantify the structural consequences of material related weak links. Moreover, while the types and/or root causes of life-limiting feature populations may vary with end-application, the analytic framework and its associated protocols are envisioned to be generic to a wide class of damage features associated with other raw material forms, manufacturing processes and applied service [43, 49, 87, 88, 90-92].

The implementation of analytical methods to assess material effects on durability performance will enable consideration of improved materials with reduced testing burden. Using the developed methods, the performance and cost savings advantages of improved materials can be demonstrated with paper studies at a much earlier stage to reduce engineering risks entailed in exploiting microstructurally tailored materials. Sensitivities to design features can be quantitatively and simultaneously evaluated to gain optimal enhancements for component lightweighting and long term damage tolerance.

Efforts by airframers to reduce manufacturing costs have included the use of monolithic structure to replace assemblies thereby reducing part numbers and assembly costs. The technological application of data and concepts developed permits advances in design and producibility rules for monolithic structure, particularly so for candidate applications where experimental results are lacking and the experience gap is large. These advancements are critical for effective crack prevention and control because of the lack of inherent crack stoppers and the higher repair and replacement costs associated with large monolithic structural components.

In order to take advantage of the modeling approach, some modification of existing structural design and evaluation techniques may be required. The long-term advantages of improved

materials and the associated component benefits may not be apparent under existing design and evaluation procedures, and current procurement practices do not allow differentiation of microstructurally enhanced materials. State-of-the-art damage tolerant design practices and test procedures typically do not embody microstructure/process relationships nor the more advanced elements of fracture mechanics technology, such as crack propagation from life-limiting microfeatures and crack closure. Moreover, current ASTM testing guidelines and long-standing test methods are often not helpful in quantifying the structural implications of product durability. Thus, the value of improved durability may not be clear if the existing component meets the existing design and durability requirements. That is, materials whose microstructure may be altered to improve long-term performance may be recognized as beneficial, but the current requirements do not show these benefits. Accordingly, broadening impact of the modeling technology requires additional work in the following areas: (1) understanding the competition between life-limiting feature populations associated with raw material, component manufacture and service damage, (2) establishment of standardized protocols for defining life-limiting microfeature populations to integrate with equivalent initial flaw lifing concepts, (3) synthesis and standardization of stress intensity factors (linear elastic and elastic plastic) for shaped parts and assembled structure in a common database, (4) user friendly crack propagation models that encompass complexities of representative structural details, loads and environments, (5) incorporation of small crack growth and crack closure concepts into the above crack growth model, (6) coupon-based models for prediction of terminal crack sizes and residual strength in prototypical elements of actual structural scale (e.g., wide-stiffened panels), and (7) structural verification.

In order for the developed technology to be considered for structural design it may be necessary to conduct one or more component scale technology validation programs to confirm the analytical results. This necessary step will be vital to gaining designer's comfort and eventual acceptance of the methodology by the at large technical community.

Finally, information technology can be expected to play a major role in ultimate transition of durability design technology. Future activity should therefore incorporate planning to integrate the results into user-friendly computer packages in order to streamline use of the modeling technology and management of the technology transition tasks involved.

4.3 Model Application for Life Extension

In latter or extended stages of airframe service life it is possible for widespread and/or multi-site fatigue damage state to exist that could imperil the structural integrity of the aircraft. The most

detrimental form of widespread damage is manifested as multiple, service induced fatigue cracks, that in the presence of a larger rogue crack could impair residual strength and damage tolerant derived inspection intervals below safe limits [8, 9, 11, 18]. Incidents such as the Aloha Airlines 737 accident in April of 1988 [73] have demonstrated in the strongest possible way, the need for attention to this type of failure. Incidents of this sort have lead to new airworthiness regulation mandating control, prediction and prevention of failure due to widespread and/or multi-site fatigue damage [73].

Currently, there is no universally accepted predictive methodology to predict onset and implications of widespread fatigue damage. The technical concepts developed in this program are being considered for use in evaluating structural implications of widespread damage states under various life extension scenarios [75, 90-92]. The damage induced through service can be modeled as distributions of damage sites at the microstructural scale. In this manner, the effects of corrosion can be addressed as well as the possibility of widespread fatigue damage and multi-component damage.

During long-term service, aircraft materials often do not perform to their intended level. This can result in chronic problem components which require remedial action to ensure continued safe operation of aircraft. If the remediation consists of component replacement with the same material, then future occurrence of the same chronic damage form can be expected. Oftentimes enhanced materials may offer solutions by upgrading critical structural elements by direct substitution. For microstructurally improved materials the performance improvements may be obtained through process routes with no changes in alloy. Thus, no new material qualification is involved. The analytical methods to assess material performance based on microstructure allow the performance improvement potential to be quantified. The direct substitution route to upgrading critical components could therefore result in an affordable performance improvement potential without the associated risks of new material implementation.

5. Summary

This program has been successful in defining the methodology and demonstrating an approach to model the effect of microstructure on the fatigue performance of aluminum alloy 7050-T7451 plate. There have been numerous instrumental accomplishments in both the material characterization and the model development phases of this work. However, the real value of this program lies in the definition of how the technology may be applied to impact needs within the aerospace industry, and how the technology is ultimately transferred. This section summarizes the significant accomplishments of the material characterization and model development phases of this program, and also emphasizes how the potential value of this work may be captured.

The use of 7050 thick plate for this program created a unique opportunity to study the effects of microstructure on fatigue durability performance in a commercial material of relevance to the Navy. Microstructural variants of commercial alloy 7050-T7451 plate were produced on a plant scale, through processing variations, and these materials were provided to this program for study. The material characterization phase examined the different pedigrees of material and evaluated their fatigue performance, identified key microstructural features affecting fatigue, and characterized the microstructures. This work has resulted in significant advances in understanding microstructural influences on fatigue; key among these were that the pedigree of a single alloy and product form did influence fatigue, the influences were not masked by specimen geometry or manufacturing effects, and that the effects are substantial. For each of the material variants, the key microstructural features which act as crack initiators were identified and their sizes measured. This established a hierarchy of microstructural features, based on their effectiveness as crack initiators, which influence fatigue. Thus, for each material there was a size distribution of microstructural crack-initiators, and this size distribution represents the extreme values or upper tail of the distribution of features within the material. Metallographic characterization of the microstructural feature distributions for each material variant was performed, and methods for scaling these size distributions measured on random planes to obtain the extreme value size distributions of crack-initiators was developed. This provided a means to characterize a material metallographically and then obtain information on the size distribution of potential life-limiting features influencing fatigue. The material characterization phase of this work provides a unique material performance fatigue database for varying material pedigree, established a hierarchy of microstructural crack-initiators, verified the link between processing, microstructure and fatigue performance, and served as a basis for subsequent fatigue lifetime modeling.

The modeling phase of this program focused on establishing the capability to predictively link material fatigue performance with initial material microstructure based on the understanding and data obtained from the material characterization phase. The modeling work consisted of verifying a fracture mechanics crack growth model, incorporation of microstructural effects on the crack driving force, deterministic model verification for each of the material variants, and

incorporation of probabilistic aspects of microstructure to predict lifetimes based on microfeature distribution for each material. There have been several key outcomes of the modeling work. The application of fracture mechanics principles to the microstructural scale has been verified. The extension of fracture mechanics to model early stage cracking can facilitate integration of total life analysis into damage tolerant design and offers a low cost alternative to extensive S/N fatigue test programs. The effects of the initial micro-feature size, shape and location distributions can be analytically predicted. This allows rapid assessment of the effects of microstructure/process changes on material performance Additionally, it is expected that the analytical methods employed here may be generally applied to metallic materials as a class to assess effects of microstructure as well as other discrete damage forms such as corrosion or machining and manufacturing induced imperfections.

The experimental and analytical tasks conducted have defined the linkages between microstructural characteristics and fatigue performance. The value of the developed technology lies in application to areas of relevant interest to the Navy and the airframe community. Three envisioned opportunities for transfer of this technology have been defined in this program. These are material design, structural design and evaluation, and life extension studies. Application of the methodology to material design can result in the development of better material, facilitate the selection of material processing options, and reduce the cost and time associated with implementation of newer materials. The modeling technology can also have application to structural design and evaluation. Analytically the effects of material alternatives on durability performance can be assessed. This will enable exploitation of improved materials to reduce weight, increase service life, and/or improve durability. Finally, the program holds promise for life extension studies. The technical concepts developed in this program can be used to evaluate the structural implications of service induced damage forms such as corrosion, or address the implications of widespread fatigue damage. Also, the structural implications of upgrading critical components by direct substitution with improved materials can be analytically assessed, enabling affordable performance improvement without the risk of implementing a new material.

Follow-on development, implementation and education efforts are essential to realizing the value of the program technology. User acceptance will require that the technical approach be conveyed to a broad audience of potential users. The technical path must be explained with a clear definition of implementation opportunities. Ultimately, the technology transfer paths must be verified to gain acceptance by airframers, operators, procurement organizations, maintenance/repair facilities and the regulatory agencies.

9(PEM)PDM   60

References

1. R. J. Gran, F. D. Orazio, Jr., P. C. Paris, G. R. Irwin, and R. W. Hertzberg, "Investigation and Analysis Development of Early Life Aircraft Structural Failures," AFFDL-TR-70-149, March 1971.

2. B. J. Pendley, S. P. Henslee, and S. D. Manning, "Durability Methods Development, Volume III - Structural Durability Survey: State-of-the-Art Assessment," AFFDL-TR-79-3118, Wright Patterson Air Force Base, OH, September 1979.

3. T. D. Cooper and C. A. Kelto, "Fatigue in Machines and Structures - Aircraft," Fatigue and Microstructure, American Society for Metals, Metals Park, OH, 1979, P. 29.

4. J. L. Rudd, J. N. Yang, S. D. Manning and W. R. Garver, Durability Design Requirements and Analysis for Metallic Airframes," Design of Fatigue and Fracture Resistant Structures, American Society for Testing and Materials, Philadelphia, PA, 1982, p. 133.

5. M. A. Landy and O. L. Smithers, "Durability and Damage Tolerance Control Plans for U.S. Air Force Aircraft," Journal of Aircraft, Vol. 20, No. 89, 1983, p. 689.

6. U. G. Goranson, "Elements of Structural Integrity Assurance," Fatigue of Aircraft Materials, Proceedings of the Specialists' Conference dedicated to the 65th Birthday of J. Schijve, Delft University Press, the Netherlands, 1992, pp. 275-320.

7. "Damage Tolerance Assessment Handbook, Volume I: Introduction Fracture Mechanics, Fatigue Crack Propagation," Final Report DOT-VNTSC-FAA-93-13.I, U.S. Dept. of Transportation, Volpe National Transportation Systems Center, Cambridge, MA, October 1993.

8. U. G. Goranson, "Damage Tolerance Fact and Fiction," 14th Plantema Memorial Lecture, 17th Symposium of the International Committee on Aeronautical Fatigue, Stockholm, Sweden, June 9, 1993.

9. U. G. Goranson and J. F. McGuire, "Airworthiness," Aerospace Engineering, March 1994, pp. 28-34.

10. J. L. Rudd, J. N. Yang, S. .D. Manning, B. G. W. Yee, "Probabilistic Fracture Mechanics Analysis Methods for Structural Durability," Behavior of Short Cracks in Airframe Components, AGARD Conference Proceedings No. 328, NATO Advisory Group on Aerospace Research and Development, April 1983.

11. T. Swift, "Widespread Fatigue Damage Monitoring - Issues and Concerns," 5th International Conference on Structural Airworthiness of New and Aging Aircraft, Hamburg, Germany, June 16-18, 1993.

12. Department of the Air Force, "Aircraft Structural Integrity Program Requirements," Military Standard MIL-STD-1530A, 1975.

13. A. P. Berens, D. S. Morcock, K. E. Brown, J. C. Davis, R. L. Johnson, C. E. Larson and D. J. White, "Handbook of Force Management Methods," AFWAL-TR-81-3079, Flight Dynamics Laboratory, Air Force Wright Wright Aeronautical Laboratories, Air Force Systems Command, Wright-Patterson Air Force Base, OH, April 1981.

14. S. D. Manning and J. N. Yang, "USAF Durability Design Handbook: Guidelines for the Analysis and Design of Durable Aircraft Structures," AFWAL-TR-83-3027, Flight Dynamics Laboratory, Air Force Wright Wright Aeronautical Laboratories, Air Force Systems Command, Wright-Patterson Air Force Base, OH, August 1988.

15. T. R. Brussat, J. C. Ekuall and J. A. Jauregui, "Documentation of the Navy Aircraft Structural Integrity Program (NASIP), Revision B," Report No. NADC-87089-60, U.S. Naval Air Development Center, Warminster, PA, October 1988.

16. "Damage Tolerance Assessment Handbook, Volume II: Airframe Damage Tolerance Evaluation," Final Report DOT-VNTSC-FAA-93-13.II, U.S. Dept. of Transportation, Volpe National Transportation Systems Center, Cambridge, MA, October 1993.

17. "Airworthiness Standards: Transport Category Airplanes" 14 CFR part 25 of the Federal Aviation Regulations (FAR), Department of Transportation, Federal Aviation Administration.

18. T. Swift, "Damage Tolerance Capability," Fatigue of Aircraft Materials, Proceedings of the Specialists conference, Dedicated to the 65th birthday of J. Schijve, Delft University Press, 1992, P351.

19. J. Lankford and F. N. Kusenberger, "Initiation of Fatigue Cracks in 4340 Steel," *Metallurgical Transactions*, Vol. 4, No. 2, 1973, pp. 553-559.

20. C. Y. Kung and M. E. Fine, "Fatigue-Crack Initiation and Microcrack Growth in 2024-T4 Aluminum Alloys," *Metallurgical. Transactions A*, Vol. 10A, 1977, pp. 603-610.

21. N. M. A. Eid and P. F. Thomason, "The Nucleation of Fatigue Cracks in a Low-Alloy Steel Under High-Cycle Fatigue Conditions and Uniaxial Loading," Acta Metallurgica, Vol. 27, 1979, p. 1239.

22. E. A. Starke, Jr. and G. Lutjering, "Cyclic Plastic Deformation and Microstructure," Fatigue and Microstructure, American Society for Metals, Metals Park, OH, 1979, pp. 205-243.

23. R. O. Richie and S. Suresh, "Mechanics and Physics of the Growth of Small Cracks," Behavior of Short Cracks in Airframe Components, AGARD Conference Proceedings No. 328, 1-1, NATO Advisory Group for Aerospace Research and Development, 1983.

24. K. Detert, R. Scheffel and R. Stunkel, "Influence of Grain Size and Dispersion of Small Particles on Crack Initiation and Growth During Fatigue in Age Hardened Al-Mg-Si Alloys," Strength of Metals and Alloys, (ICSMA7), Vol. 2, Pergamon Journal Inc., Elmsford, NY, 1985, pp. 1219-1224.

25. R. O. Richie and J. Lankford, Eds. Small Fatigue Cracks, TMS-AIME, Warrendale, PA, 1986.

26. B. Dubost, J Bouvaist, J. Mace and M. O. Charue, 7075-101-T73, "Tough Plates and forgings with Improved Strength for Airframe Applications," Proceedings Aluminum Technology '86, London, England, 1986.

27. K. J. Miller, "The Behavior of Short Fatigue Cracks and Their Initiation, Part II, A General Summary," Fatigue and Fracture of Engineering Materials and Structures, Vol. 10, No. 2, 1987, p. 93.

28. J. Lankford, "Effect of Oxide Inclusions on Fatigue Failure," International Metals Reviews, September 1987, p. 221.

29. L. C. Labarre, L. M. Angers, R. J. Bucci, M. R. Emptage, D. D. Leon and F. R. Billman, "CW67 P/M Alloy Product Improvements Through Statistical Quality Control," ASM International ISTFA'87: Advanced Materials, Conference Proceedings, 1987, pp. 27-31.

30. J. C. Newman, Jr., and P. R. Edwards, "Short Crack Growth Behavior in an Aluminum Alloy, An AGARD Cooperative Test Programme, AGARD Report 732, 1988.

31. T. Julta, C. E. Nicholson and G. Jolley, "Nucleation of Fatigue Cracks by Inclusions," Fracture Control of Engineering Structures - ECF6, 1988, p. 1609.

32. C. R. Owen, R. J. Bucci and R. J. Kegarise, "An Aluminum Quality Breakthrough for Aircraft Structural Reliability," *Journal of Aircraft*, Vol. 26, No. 2, Feb. 1989, pp. 178-184.

33. A. J. Hinkle, P. E. Magnusen, R. L. Rolf, and R. J. Bucci, "Effect of Microporosity on Notched Specimen Fatigue Life," Structural Safety and Reliability, Vol. 2, Proceedings ICOSSAR'89, Fifth International Conference on Structural Safety and Reliability, American Society of Civil Engineers, New York, NY, 1989, pp. 1467-1474.

34. P. E. Magnusen, R. J. Bucci, A. J. Hinkle, M. E. Artley and R. L. Rolf, "The Influence of Material Quality on Airframe Structural Durability," Advances in Fracture Research, Vol. 2, Proc. Seventh International Conference on Fracture (ICF 7), 1989 March 20-24, pp. 999-1006.

35. M. J. Couper, A. E. Neeson and J. R. Griffiths, "Casting Defects and the Fatigue Behavior of an Aluminum Casting Alloy, *Fracture of Engineering Materials and Structures*, Vol. 13, No. 3, 1990, pp. 213-227.

36. M. Goto, Y. Yanagawa and H. Nisitani, "Statistical Property in the Initiation and Propagation of Microcracks of a Heat-Treated 0.45% C Steel," *JSME International Journal*, Series I, Vol. 33, No. 2, 1990, pp. 235-241.

37. P. E. Magnusen, A. J. Hinkle, W. Kaiser, R. J. Bucci and R. L. Rolf, "Durability Assessment Based on Initial Material Quality," *Journal of Testing and Evaluation*, Vol. 18, No. 6, Nov. 1990, pp. 439-445.

38. P. E. Magnusen, A. J. Hinkle, R. L. Rolf, R. J. Bucci and D. A. Lukasak, "Methodology for the Assessment of Material Quality Effects on Airframe Fatigue Durability," Fatigue 90, Vol. II, Proc. Fourth International Conf. on Fatigue and Fatigue Thresholds, Materials and Components Engineering Publications Ltd., 1990, pp. 2239-2244.

39. A. F. Grandt, A. J. Hinkle, T. D. Scheumann, and R. E. Todd, "Modeling the Influence of Initial Material Inhomogeneities on the Fatigue Life of Notched Components," Proceedings of the 1991 USAF Structural Integrity Program Conference, Eds., T. W. Cooper, J. W. Lincoln, R. M. Bader, WL-TR-92-4045, Wright Patterson AFB, Ohio, July 1992, pp. 433-445.

40. J. C. Newman, Jr., E. P. Phillips, M. H. Swain and R. H. Everett, Jr., "Fatigue Mechanics: An Assessment of a Unified Approach to Life Prediction," Advances in Fatigue Lifetime Predictive Techniques, ASTM STP 1122, American Society for Testing and Materials, 1992, pp. 5-27.

41. A. F. Grandt, T. D. Scheumann, R. E., Todd and A. J. Hinkle, Modelling the Influence of Initial Material Inhomogeneities on the Fatigue Life of Notched Components," *Fatigue and Fracture of Engineering Materials and Structures*, Vol. 16, No. 2, 1993, pp. 199-213.

42. A. J. Hinkle, A. F. Grandt and L. E. Forsythe, "Predicting the Influence of Initial Material Quality on Fatigue Life," ICAF'93, International Committee on Aeronautical Fatigue, Stockholm, Sweden, June 7-11, 1993.

43. P. E. Magnusen, R. J. Bucci, A. J. Hinkle, J. G. Burns, and J. L. Rudd, "Effect of Microporosity on Fatigue Durability of Thick 7050 Aluminum Plate," Proceedings of the 1992 USAF Structural Integrity Program Conference, WL-TR-93-4080, Materials Directorate, Wright Laboratory, Air Force Materiel Command, Wright Patterson AFB, OH, September 1993, pp. 379-410.

44. R. J. Bucci, J. R. Brockenbrough, A. J. Hinkle, P. E. Magnusen, and S. M. Miyasato, "The Role of Microstructure on Fatigue Performance of Metallic Alloys," Office of Naval Research, Structural Reliability Progress Report Meeting, Reston, VA, December 13, 1993.

45. A. F. Grandt, C. E. Zezula and J. H. Elsner, "Initiation, Growth, and Coalescence of Small Fatigue Cracks at Notches," Purdue University Final Report for Aluminum Company of America, Project No. TC919597TC, April 1994.

46. A. F. Grandt, "Materials Degradation and Fatigue in Aerospace Structures," Purdue University Annual Report for Air Force Office of Scientific Research, Grant No. F49620-93-1-0377, July 1994.

47. A. F. Grandt, A. J. Hinkle, C. E. Zezula and J. H. Elsner, "The Influence of Initial Quality on the Durability of 7050-T7451 Aluminum Plate," Proceedings of the 1993 USAF Structural Integrity Program Conference, WL-TR-94-4079, Materials Directorate, Wright Laboratory, Air Force Materiel Command, Wright Patterson AFB, OH, August 1994, pp. 255-267.

48. J. R. Brockenbrough, A. J. Hinkle, P. E. Magnusen and R. J. Bucci, "Microstructurally Based Model of Fatigue Initiation and Growth," FAA/NASA International Symposium on Advanced Structural Integrity Methods for Airframe Durability and Damage Tolerance, NASA Conference Publication 3274, Part 1, September 1994, pp. 71-84.

49. G. W. Kuhlman, R. J. Bucci, R. W. Bush, A. J. Hinkle, H. J. Konish, M. Kulak and R. H. Wygonik, "Aluminum Alloy Forgings - Property/Performance Attributes; Focus: Fatigue and Durability Service Capabilities," Alcoa Forged Products, June 12, 1995.

50. J. N. Yang, S. D. Manning, J. L. Rudd, M. E. Artley and J. W. Lincoln, "Stochastic Approach for Predicting Functional Impairment of Metallic Airframes," Proceedings AIAA 28th Structures, Structural Dynamics and Materials Conference, 1987, pp. 215-223.

51. S. D. Manning and J. N. Yang, "Advanced Durability Analysis - Vol. 1, Analytical Methods, AFWAL-TR-86-3017, Air Force Wright Aeronautical Laboratories, July 1987.

52. S. D. Manning, J. N. Yang, "Reliability Centered Maintenance for Metallic Airframes based on a Stochastic Crack Growth Approach," ASTM Symposium on Advances in Fatigue Lifetime Predictive Techniques, San Francisco, CA, April 24, 1990.

53. J. N. Yang, S. D. Manning, J. L. Rudd and R. M. Bader, "Investigation of Mechanistic-Based Equivalent Initial Flaw Size Approach," ICAF'95, International Committee on Aeronautical Fatigue, Melbourne, Australia, May 3-5, 1995.

54. J. T. Staley, "Investigation to Develop a High Strength Stress Corrosion Resistant Aluminum Aircraft Alloy," Alcoa Laboratories, Naval Air Systems Command Contract N00019-69-C-0292, Final Report, January 1970.

55. J. T. Staley, "Development of High Strength Stress Corrosion Resistant Naval Aircraft Alloy," Alcoa Laboratories, Naval Air Systems Command Contract N00019-70-C-0118, Final Report, November 1970.

56. L. N. Mueller, Alcoa Aluminum Alloy 7050, Green Letter No. 220, October 1985.

57. K. L. Kremer, "Inspection of Wrought and Finish Machined Metal Products," McDonnell Douglas Aerospace East, October 4, 1995, presented ASM Materials Week'95 October 30 - November 2, 1995.

58. "Air Force directives, such as R&M 2000, are causing material manufacturers to strive for better initial material quality," *Aerospace Engineering*, May 1988, pp. 33-37.

59. J. C. Newman and I. S. Raju, "Stress Intensity Factor Equations for Cracks in Three-Dimensional Finite Bodies," NASA Technical Memorandum 83200, Langley Research Center, Hampton, VA, August 1981.

60. I. S. Raju and J. C. Newman, Jr., "Stress-Intensity Factors for Circumferential Surface Cracks in Pipes and Rods Under Tension and Bending," Fracture Mechanics: Seventeenth Volume, ASTM STP 905, American Society for Testing and Materials, Philadelphia, PA, 1986, p. 789.

61. A. J. Hinkle and M. R. Emptage, "Analysis of Fatigue Life Data Using the Box-Cox Transformation," *Fatigue and Fracture of Engineering Materials and Structures*, Vol. 14, No. 5, 1991, pp. 591-600.

62. J. G. Burns, J. L. Rudd, J. A. Harter, P. E. Magnusen, A. J. Hinkle, and R. J. Bucci, "Probabilistic Durability Evaluation of Alcoa 7050 Aluminum," Proceedings of the 1991 USAF Structural Integrity Program Conference, Eds., T. W. Cooper, J. W. Lincoln, R. M. Bader, WL-TR-92-4045, Wright Patterson AFB, Ohio, July 1992, pp. 305-322.

63. A. J. Hinkle, P. E. Magnusen, R. J. Bucci and J. L. Rudd, "Fatigue Durability Improvement in Thick-Section Metallic Airframe Parts," White Paper, Appendix, Advanced Metallic Structures Technology Development Plan, Aerospace Industries Association, 1993 March 31.

64. J. R. Brockenbrough, R. J. Bucci, A. J. Hinkle, J. Liu, P. E. Magnusen and S. M. Miyasato, Progress Report: "Role of Microstructure on Fatigue Durability of Aluminum Aircraft Alloys," Interim Progress Report, Office of Naval Research Contract No. N00014-91-C-0128, 1993 April 15.

65. P. E. Magnusen, R. J. Bucci, A. J. Hinkle, J. R. Brockenbrough, S. M. Miyasato and H. J. Konish, "The Role of Microstructure on Fatigue Performance of Aluminum Aerospace Alloys," Office of Naval Research, Contract N00014-91-C-0128, Interim Report December 29, 1993.

66. G. E. P. Box and D. R. Cox, "An Analysis of Transformations," *Journal of the Royal Statistical Society*, B, 26, 1982, pp. 211-243.

67. D. Broek and H. Vlieger, "Cracks Emanating from Holes in Plate Stress," *International Journal of Fracture Mechanics*, Vol. 8, 1972, pp. 353-356.

68. A. H. S. Ang and W. H. Tang, Probability Concepts in Engineering Planning and Design, New York, NY, 1984.

69. D. Broek, Elementary Engineering Fracture Mechanics, Martinus Nijhoff Publishers, The Netherlands, 1986.

70. R. O. Ritchie, "Crack Tip Shielding in Fatigue," Fifth International Conference on Mechanical Behavior, Beijing, China, 1987.

71. R. O. Ritchie and W. Yu, "Short Crack Effects in Fatigue: A Consequence of Crack Tip Shielding," Small Fatigue Cracks, TMS-AIME, Warrendale, PA, 1986, p. 167.

72. Damage Tolerant Design Handbook, Metals and Ceramics Information Center, Battelle Columbus Laboratories, Columbus, OH, MCIC-HB-01, 1975.

73. W. R. Hendricks, "The Aloha Airlines Accident - A New Era for Aging Aircraft," Structural Integrity of Aging Airplanes, S. N. Atluri, S. G. Sampath, P. Tong, Eds. Spinger-Verlag, Berlin, Heidelberg, 1991.

74. G. G. Trantina, and M. Barishpolsky, "Elastic-Plastic Analysis of Small Defects - Voids and Inclusions," *Engineering Fracture Mechanics*, Vol. 20, No. 1, 1984, pp. 1-10.

75. R. J. Bucci and H. J. Konish, "A Technology Path for Enhancing Airframe Durability," Alcoa presentation to Materials Directorate, Wright Laboratory, Wright Patterson AFB, OH, February 10, 1994.

76. J. Schijve, "The Fatigue Phenomenon in Aluminum Alloys," Nat. Aerospace Inst. Amsterdam, TR-M-2122, 1964.

77. A. F. Grandt, Jr., R. Perez, and D. E. Tritsch, "Cyclic Growth and Coalescence of Multiple Fatigue Cracks," Advances in Fracture Research, 6th International Conference on Fracture, New Delhi, India, December 1984, Vol. 3, pp. 1571-1578.

78. A. F. Grandt, Jr., A. B. Thakker, and D. E. Trisch, "An Experimental and Numerical Investigation of the Growth and Coalescence of Multiple Fatigue Cracks at Notches," Fracture Mechanics: Seventeenth Vol., ASTM STP 905, 1986, pp. 239-252.

79. J. C. McComb, J. E. Pope, and A. F. Grandt, Jr., "Growth and Coalescence of Multiple Fatigue Cracks in Polycarbonate Test Specimens," *Engineering Fracture Mechanics*, Vol. 24, No. 4, 1986, pp. 601-608.

80. H. Tada, P. Paris and G. Irwin, The Stress Analysis of Cracks Handbook, Paris Productions Inc., St. Louis, MO, 1985.

81. S. Suresh, Fatigue of Materials, Cambridge University Press, 1991.

82. P. C. Paris, "Fatigue - An Interdisciplinary Approach," Proceedings 10th Sagamore Conference, Syracuse University Press, Syracuse, NY, 1964, p. 107.

83. Det Norsk Veritas, PROBAN: General Purpose Probabilistic Analysis Program, Veritas Sesam Systems, Hovik, Norway, January 1992.

84. R. E. Peterson, Stress Concentration Factors, John Wiley, 1974.

85. W. H. Hunt, Jr., J. R. Brockenbrough, P. E. Magnusen, "An Al-Si-Mg Composite Model System: Microstructural Effects on Deformation and Damage Evolution," *Scripta Metallurgica et Materialia*, Vol. 25, p. 15, 1991.

86. J. R. Brockenbrough, F. Zok, "On the Role of Particle Cracking in Flow and Fracture of Metal Matrix Composites," Alcoa Report # 57-14-93, 1993.

87. D. A. Lukasak, B. J. Sova and R. L. Lash, "Thick Product 7050-T74511 Extrusions," AeroMat'94, ASM International's Advanced Aerospace Materials/Processes Conference, Anaheim, CA, June 6-9, 1994.

88. A. J. Hinkle, J. R. Brockenbrough, J. T. Burg, and R. J. Bucci, "Microstructurally Based Performance Models Relevant to Performance of Net-Shaped Parts," AeroMat'95, ASM International's 6th Advanced Aerospace Materials and Processes Conference, Anaheim, CA, May 8-11, 1995.

89. D. A. Lukasak and D. A. Koss, "Microstructural Influences on Fatigue Crack Initiation in a Model Particulate-reinforced Aluminum Alloy MMC," Composites, Vol. 24, No. 3, 1993, pp. 262-269.

90. R. J. Bucci, H. J. Konish, M. Kulak and D. W. Hoeppner, "An Engineering Protocol for Evaluating Implications of Metallic Corrosion on Airframe Damage, Life and Risk Assessment," FAA/NASA International Symposium on: Advanced Structural Integrity Methods for Airframe Durability and Damage Tolerance, May 4-6, 1994.

91. A. P. Berens and J. G. Burns, "Risk Analysis in the Presence of Corrosion Damage," AGARD Specialists' Meeting on Widespread Fatigue Damage in Military Aircraft, Rotterdam, the Netherlands, May 1995.

92. R. J. Bucci, H. J. Konish and B. J. Shaw, "A Technical Plan to Address Aircraft Structural Problems Arising from Corrosion/Corrosion Fatigue," USAF Corrosion/Fatigue Planning Meeting, Wright Laboratories, WPAFB, OH, February 8, 1995.

Table 2.1a. Key microstructural features of the materials produced by Alcoa for this study.

Material	Product Thickness (in.)	Key Microstructural Feature
old material	5.7	coarse porosity
now material	5.7	porosity
low porosity material	6.0	small porosity, constituent particles
thin material	1.0	constituent particles, refined grain size

Table 2.1b. Average mechanical property data for the 7050 alloy product variants used in this study.

Material	Longitudinal				Long Transverse			Short Transeverse		
	UTS (ksi)	TYS (ksi)	% el	L-T K_{1C} (ksi√in.)	UTS (ksi)	TYS (ksi)	% el	UTS (ksi)	TYS (ksi)	% el
Old	74.5	66.5	10.1	31.0	74.9	64.7	6.9	70.5	60.7	3.1
Now	74.6	65.9	10.0	29.4	76.0	65.1	8.5	72.4	60.8	4.8
Low Porosity								71.0	60.6	5.9
Thin	76.1	66.7	13.6	42.6	76.4	66.8	12.7	–	–	–

71

Table 2.2. Old material smooth axial fatigue lifetimes and sizes of crack initiators. 5.7 in. thick plate, 0.5 in. diameter smooth round specimen, 35 ksi max. stress, R=0.1, LT orientation, freq.=10 Hz, lab air.

Specimen #	Cycles	Fail*	Initiation Site	Size (in.)			Dist. from Edge (in.)	Comments
				a	c	L max		
590155-A1	77218	F	Pore	0.0123	0.0030	0.0126	0	
590155-A2	77251	F	Pore	0.0088	0.0078	0.0130	0	
590155-A3	55090	F	Pore	0.0068	0.0111	0.0111	0	
590155-A4	73549	F	Pore	0.0028	0.0094	0.0094	0	
590155-A5	67576	F	Pore	0.0118	0.0054	0.0138	0	
590155-B1	78557	F	Pore	0.0130	0.0117	0.0158	0	
590155-B2	75866	F	Pore	0.0051	0.0070	0.0085	0	
590155-B3	72521	F	Pore	0.0070	0.0098	0.0115	0	
590155-B4	66885	F	Pore	0.0143	0.0120	0.0174	0	
590155-B5	70511	F	Pore	0.0114	0.0131	0.0163	0	
590155-C1	90017	F	Pore	0.0042	0.0086	0.0088	0	
590155-C2	71263	F	Pore	0.0180	0.0100	0.0191	0	
590155-C3	79290	F	Pore	0.0045	0.0145	0.0145	0	
590155-C4	62379	F	Pore	0.0154	0.0058	0.0155	0	
590155-C5	105447	F	Pore	0.0067	0.0075	0.0116	0	
590155-D1	230417	F	Pore	0.0018	0.0033	0.0033	0.0002	slightly sub-surface
590155-D2	149486	F	Pore	0.0030	0.0024	0.0036	0	
590155-D3	151046	F	Pore	0.0048	0.0029	0.0051	0	
590155-D4	84529	F	Pore	0.0142	0.0054	0.0149	0	
590155-D5	121650	F	Pore	0.0056	0.0035	0.0057	0	
590156-A1	86811	F	Pore	0.0096	0.0071	0.0110	0	
590156-A2	64419	F	Pore	0.0081	0.0064	0.0099	0	
590156-A3	49449	F	Pore	0.0288	0.0097	0.0298	0	
590156-A4	57456	F	Pore	0.0172	0.0051	0.0177	0	
590156-A5	63122	F	Pore	0.0119	0.0031	0.0126	0	
590156-B1	76094	F	Pore	0.0127	0.0027	0.0127	0	
590156-B2	58896	F	Pore	0.0161	0.0041	0.0162	0	
590156-B3	62270	F	Pore	0.0092	0.0134	0.0145	0	
590156-B4	58014	F	Pore	0.0107	0.0189	0.0192	0	
590156-B5	68266	F	Pore	0.0076	0.0157	0.0157	0	
590156-C1	74019	F	Pore	0.0072	0.0040	0.0078	0	
590156-C2	78366	F	Pore	0.0088	0.0125	0.0149	0	
590156-C3	58943	F	Pore	0.0088	0.0139	0.0143	0	
590156-C4	71508	F	Pore	0.0072	0.0096	0.0113	0	
590156-C5	101013	F	Pore	0.0050	0.0058	0.0071	0	
590156-D1	73524	F	Pore	0.0041	0.0105	0.0107	0	
590156-D2	64512	F	Pore	0.0071	0.0092	0.0114	0	
590156-D3	70044	F	Pore	0.0081	0.0082	0.0084	0	
590156-D4	68768	F	Pore	0.0078	0.0126	0.0131	0	
590156-D5	100708	F	Pore	0.0074	0.0030	0.0075	0	

* F = fail

DNF = specimen did not fail and test was discontinued

Table 2.3. Old material open hole axial fatigue lifetimes and sizes of crack initiators. 5.7 in. thick plate, two open hole specimen, R=0.1, LT orientation, freq.=30 Hz, lab air.

Specimen #	Max. Net Stress (ksi)	Cycles	Fail*	Initiation Site	Size (in.) a	Size (in.) c	Size (in.) L max	Dist. from Corner (in.)	Dist. from Hole (in.)	Comments
B-2-7	30.8	27500	F	Pore + Al7Cu2Fe	0.00120	0.00233	0.00233	0.0451	0.0000	Opposite side of hole
•				Al7Cu2Fe	0.00073	0.00077	0.00077	0.0495	0.0000	
C-2-1	30.8	28323	F	Pore	0.00138	0.00132	0.00188	0.0633	0.0000	
C-2-6	30.8	20590	F	Pore + Al7Cu2Fe	0.00123	0.00183	0.00183	0.0436	0.0000	Opposite side of hole
•				Al7Cu2Fe + Pore	0.00113	0.00175	0.0019	0.0585	0.0000	
A-2-2	30.8	17806	F	Pore	0.00227	0.00549	0.00549	0.0349	0.0000	
•				Pore	0.00226	0.00277	0.00319	0.0555	0.0000	
B-2-1	30.8	19967	F	Pore	0.00085	0.00145	0.00145	0.0511	0.0000	2 sites on opposite side of hole
•				Pore + Al7Cu2Fe	0.00103	0.00256	0.00256	0.0541	0.0000	
•				Pore + Al7Cu2Fe	0.00131	0.00301	0.00301	0.0320	0.0000	
A-2-4	30.8	17888	F	Pore	0.00330	0.00422	0.00423	0.0462	0.0000	
B-2-5	30.8	22011	F	Pore	0.00394	0.00568	0.00647	0.0145	0.0000	
•				Al7Cu2Fe	0.00087	0.00081	0.00108	?	0.0000	
A-2-3	30.8	23754	F	Mg2Si	0.00061	0.00144	0.00144	0.0318	0.0000	
C-2-7	30.8	25557	F	Pore	0.00232	0.00419	0.0045	0.0248	0.0000	
C-2-4	30.8	15949	F	Pore	0.00837	0.01244	0.01322	0.0135	0.0000	
•				Pore + Al7Cu2Fe	0.00142	0.00360	0.00375	0.0234	0.0000	
C-2-2	24.6	35785	F	Pore	0.00468	0.01188	0.01188	?	0.0000	Opposite side of hole
A-2-6	24.6	33910	F	Pore	0.00335	0.00780	0.0084	0.0040	0.0000	Small secondary crack opposite side, unknown origin
B-2-6	24.6	47812	F	Pore	0.00326	0.00786	0.00786	?	0.0000	opposite half
A-2-4	24.6	45406	F	Pore	0.00568	0.00572	0.00728	?	0.0000	
C-2-5	24.6	46641	F	Pore	0.00557	0.00793	0.00907	0.0115	0.0000	
•				Pore	0.00644	0.01760	0.01776	?	0.0000	
A-2-7	24.6	49285	F	Pore	0.00308	0.01008	0.01008	?	0.0000	opposite half
C-2-3	24.6	42889	F	Pore	0.00460	0.00532	0.00628	?	0.0000	opposite half
B-2-6	24.6	45836	F	Pore	0.00154	0.00368	0.00368	?	0.0000	
B-2-7	24.6	49292	F	Pore	0.00484	0.00952	0.00952	?	0.0000	opposite half
B-2-1	18.5	55290	F	Corner burr	0.00533	0.01080	0.01103	?	0.0000	
C-2-7	18.5	119328	F	Pore	0.00376	0.00728	0.00728	–	0.0000	opposite side of hole
B-2-5	18.5	164739	F	Pore	0.00135	0.00095	0.00135	–	0.0000	some Fe constituent present
C-2-3	18.5	109775	F	Pore	–	–	–	0.0514	0.0000	opposite side of hole
•				Pore + Al7Cu2Fe	0.00312	0.00546	0.00607	0.0348	0.0000	
B-2-3	18.5	119278	F	Pore	0.00083	0.00244	0.00244	0.0053	0.0000	some Fe constituent present
•				Pore	0.00206	0.00280	0.00298	0.0525	0.0000	
C-2-1	18.5	180611	F	Pore	0.00260	0.00450	0.00458	0.0292	0.0000	some Fe constituent present
B-2-3	18.5	181971	F	Pore	0.00348	0.00878	0.00859	0.0229	0.0003	opposite side of hole
A-2-1	18.5	171245	F	Pore + Al7Cu2Fe	0.00408	0.00292	0.00431	0.0674	0.1199	large pore on specimen surface
•				Pore + Al7Cu2Fe	0.00428	0.00933	0.00933	0.0317	0.0000	
B-2-4	18.5	969579	F	Pore	0.00651	0.00651	0.00651	0.0460	0.0000	
A-2-2	18.5	172288	F	Pore	0.00107	0.00371	0.00373	0.0373	0.0000	
A-2-1	14.8	222798	F	Pore	0.00114	0.01161	0.01161	0.0000	0.0000	
C-2-4	14.8	323600	F	Pore + Al7Cu2Fe	0.00717	0.00315	0.00443	0.0234	0.0000	pore at hole corner
B-2-2	14.8	2951624	F	Pore	0.00372	0.00264	0.00273	0.0067	0.0000	
A-2-7	14.8	356549	F	Pore	0.00164	0.00418	0.00418	0.0500	0.0000	
A-2-5	14.8	313328	F	Pore + Al7Cu2Fe	0.00408	0.00545	0.00643	0.0478	0.0000	
C-2-2	14.8	309256	F	Pore	0.00397	0.00460	0.0046	0.0000	0.0000	
C-2-6	14.8	738525	F	Pore	0.00176	0.00630	0.00655	0.0375	0.0000	
A-2-6	14.8	384130	F	Corner burr	0.00210	0.00330	0.0043	0.0408	0.0000	
A-2-5	14.8	4990222	F	Pore	0.00334	0.00903	0.00945	0.0331	0.0000	
B-2-2	14.8	214355	F	Pore + Al7Cu2Fe	0.00374	0.00291	0.00306	0.0214	0.0000	
•				Pore	0.00164	–	–	0.0467	0.0000	
•				Pore	0.00304	0.00371	0.00424	0.0323	0.0000	
•				Pore	0.00436	0.00600	0.00608	0.0523	0.0000	opposite side of hole
•				Pore	0.00203	0.00454	0.00454	0.0523	0.0000	opposite side of hole

* F = fail, DNF = specimen did not fail and test was discontinued

Table 2.4. New material smooth axial fatigue lifetimes and sizes of crack initiators. 5.7 in. thick plate, 0.5 in. diameter smooth round specimen, 35 ksi max. stress, R=0.1, LT orientation, freq.=10 Hz, lab air.

Specimen #	Cycles	Fail*	Initiation Site	Size (in.)			Dist. from Edge (in.)	Comments
				a	c	L max		
590157-A1	183864	F	Pore	0.0031	0.0071	0.0075	0.0007	slightly sub-surface
590157-A2	116371	F	Pore	0.0053	0.0034	0.0057	0	
590157-A3	107810	F	Pore	0.0047	0.0026	0.0047	0.0007	slightly sub-surface
590157-A4	128412	F	Pore	0.0046	0.0074	0.0074	0	
590157-A5	162653	F	Pore	0.0023	0.0025	0.0026	0	
590157-B1	167284	F	Pore	0.0022	0.0030	0.0032	0.0011	slightly sub-surface
590157-B2	119033	F	Pore	0.0049	0.0064	0.0065	0.0002	slightly sub-surface
590157-B3	108906	F	Pore	0.0071	0.0022	0.0072	0	
590157-B4	107024	F	Pore	0.0063	0.0038	0.0064	0	
590157-B5	183048	F	Pore	0.0022	0.0051	0.0051	0.0011	slightly sub-surface
590157-C1	130733	F	Pore	0.0051	0.0023	0.0053	0	
590157-C2	140414	F	Pore	0.0052	0.0037	0.0061	0	
590157-C3	135330	F	Pore	0.0037	0.0013	0.0038	0.0009	slightly sub-surface
590157-C4	75288	F	Pore	0.0073	0.0064	0.0082	0	
590157-C5	207258	F	Pore	0.0023	0.0017	0.0025	0.0009	slightly sub-surface
590157-D1	153272	F	Pore	0.0115	0.0050	0.0120	0	
590157-D2	118400	F	Pore	0.0029	0.0045	0.0049	0	
590157-D3	112761	F	Pore	0.0050	0.0066	0.0073	0	
590157-D4	103836	F	Pore	0.0056	0.0100	0.0104	0	
590157-D5	150869	F	Pore	0.0036	0.0020	0.0038	0.0003	slightly sub-surface

* F = fail

DNF = specimen did not fail and test was discontinued

Table 2.5. New material open hole axial fatigue lifetimes and sizes of crack initiators. 5.7 in. thick plate, two open hole specimen, R=0.1, LT orientation, freq.=30 Hz, lab air.

Specimen #	Max. Net Stress (ksi)	Cycles	Fail*	Initiation Site	Size (in.)			Dist. from Corner (in.)	Dist. from Hole (in.)	Comments
					a	c	L max			
590157-A-4-2	20.0	1140859	F	Mg2Si	0.0004	0.0002	0.0004	0.0018	0.00284	
590157-A-5-1	20.0	5439135	F	Pore cluster	0.0017	0.0031	0.0032	0.0074	0.00887	
590157-B-1-1	20.0	9559168	F	Pore	0.0018	0.0050	0.0052	0.0404	0.01035	
590157-A-5-2	20.0	10000000	DNF	—	—	—				
590157-B-1-2	20.0	10000000	DNF	—	—	—				
590157-C-3-2	22.5	84802	F	Pore	0.0040	0.0042	0.0049	0.0411	0	
590157-C-3-1	22.5	266450	F	?	—	—				
590157-C-1-2	22.5	2556780	F		—	—				
590157-B-5-2	22.5	3682500	F	Pore/Stage 1	0.0009	0.0015	0.0015	0.0187	0.00923	
590157-C-1-1	22.5	4103734	F	Mg2Si	0.0005	0.0004	0.0005	0.0000	0.02502	
590157-A-3-1	25.0	55848	F	Pore	0.0027	0.0039	0.0043	0.0610	0	
590157-A-2-2	25.0	141250	F	Pore	0.0025	0.0048	0.0050	0.0575	0	
590157-A-4-1	25.0	180413	F	Pore	0.0033	0.0056	0.0061	0.0210	0	
590157-A-3-2	25.0	195180	F	Pore	0.0013	0.0044	0.0045	0.0000	0.0278	
590157-A-2-1	25.0	198871	F	Pore	0.0011	0.0039	0.0039	0.0035	0	
590157-B-4-1	30.0	32871	F	Pore + Al7Cu2Fe	0.0017	0.0032	0.0032	0.0191	0.00038	on specimen surface
"				Pore + Al2CuMg	0.0009	0.0017	0.0017	0.0220	0	
590157-B-5-1	30.0	39402	F	?	—	—	—	0.0503		
590157-B-4-2	30.0	39978	F	Pore	0.0011	0.0022	0.0023	0.0437		
590157-B-3-1	30.0	46207	F	Al7Cu2Fe	0.0003	0.0002	0.0003	0.0222		
"				Mg2Si?	0.0004	0.0005	0.0005		0.00007	
590157-B-3-2	30.0	49267	F	Pore	0.0018	0.0020	0.0020	0.0051		

* F = fail

DNF = specimen did not fail and test was discontinued

Table 2.6. Low porosity material smooth axial fatigue lifetimes and sizes of crack initiators. 6.0 in. thick plate, 0.5 in. diameter smooth round specimen, 40 ksi max. stress, R=0.1, LT orientation, freq.=10 Hz, lab air.

Specimen #	Cycles	Fail*	Initiation Site	Size (in.)			Dist. from Edge (in.)	Comments
				a	c	L max		
590553-1	461445	F	Si particle	0.00097	0.00093	0.00098	0.00052	
590553-2	201840	F	Fe const. + pore	0.00126	0.02720	0.00276	0.00104	
590553-3	237544	F	Pore	0.00360	0.00152	0.00360	0	
590553-5	513329	F	?	–	–	–	–	
590553-6	997175	F	–	–	–	–	–	specimen not available
590553-7	422354	F	Pore + Fe const.	0.00215	0.00129	0.00215	0	
590553-8	960660	F	–	–	–	–	–	specimen not available
590883-9	380594	F	Pore + Fe const.	0.00371	0.00356	0.00480	0	
590553-10	702581	F	Si particle	0.00112	0.00096	0.00112	0.00040	
590553-11	497462	F	Pore + Fe const.	0.00206	0.00144	0.00208	0.00028	
590553-12	483758	F	Fe constituent	0.00332	0.00281	0.00405	0	
590553-13	1000000	DNF	–	–	–	–	–	
590553-14	1000000	DNF	–	–	–	–	–	
590553-15	167376	F	Pore + Fe const.	0.00296	0.00189	0.00312	0	
590553-16	612652	F	Particle?	0.00164	0.00168	0.00224	0	dislodged particle
590553-17	1000000	DNF	–	–	–	–	–	
590553-18	250480	F	Pore + Fe const.	0.00394	0.00628	0.00696	0	
590553-19	298211	F	Particle?	0.00200	0.00172	0.00205	0	dislodged particle
590553-20	1000000	DNF	–	–	–	–	–	

* F = fail
DNF = specimen did not fail and test was discontinued

Table 2.7. Low porosity material open hole axial fatigue lifetimes and sizes of crack initiators. 6.0 in. thick plate, two open hole specimen, R=0.1, LT orientation, freq.=30 Hz, lab air.

Specimen #	Max. Net Stress (ksi)	Cycles	Fail*	Initiation Site	Size (in.) a	Size (in.) c	Dist. from Corner (in.)	Dist. from Hole (in.)	Comments
590553-LT11	20.0	428453	F	Fe constituent	0.00126	0.00047	0.03833	0.00000	
590553-LT12	20.0	5877762	F	Stage I	0.00766	0.01011	0.00904	0.00309	internal
590553-LT13	20.0	7428034	F	Stage I	–	–	0.03960	0	
590553-LT14	20.0	10000000	DNF	–	–	–	–	–	
590553-LT15	20.0	10000000	DNF	–	–	–	–	–	
590553-LT16	22.5	230350	F	Fe constituent	0.00370	0.00264	0.00048	0	particle cluster
590553-LT17	22.5	782052	F	Fe constituent	0.00091	0.00145	0.05910	0	
590553-LT18	22.5	1188050	F	Mg2Si particle	0.00030	0.00033	0.01634	0	
590553-LT19	22.5	94081	F	Fe constituent	0.00164	0.00197	0.00000	0	
590553-LT1	25.0	58740	F	Fe constituent	0.00110	0.00179	0.00028	0	
590553-LT2	25.0	106857	F	Fe constituent	0.00144	0.00185	0.00073	0	
590553-LT3	25.0	136467	F	Fe constituent	0.00076	0.00223	0	0	
590553-LT4	25.0	111781	F	Fe const + pores	0.00132	0.00504	0.01240	0.00146	internal
590553-LT5	25.0	852700	F	Fe constituent	0.00177	0.00131	0.02150	0.00043	slightly sub-surface
590553-LT6	30.0	43998	F	Fe constituent	0.00505	0.00394	0.02830	0	
590553-LT7	30.0	52939	F	Fe constituent	0.00056	0.00092	0.00144	0	
"	30.0			Fe constituent	0.00121	0.00105	0.05740	0	secondary site, same side
590553-LT8	30.0	51641	F	Fe constituent	0.00038	0.00050	0	0	
590553-LT9	30.0	49750	F	Fe constituent	0.00244	0.00270	0.00066	0	
590553-LT10	30.0	58535	F	Fe constituent	0.00038	0.00056	0.04964	0	

* F = fail

DNF = specimen did not fail and test was discontinued

77

Table 2.8. Thin material smooth axial fatigue lifetimes and sizes of crack initiators. 1.0 in. thick plate, 0.5 in. diameter smooth round specimen, 45 ksi max. stress, R=0.1, LT orientation, freq.=10 Hz, lab air.

Specimen #	Cycles	Fail*	Initiation Site	Size (in.)			Dist. from Edge (in.)	Comments
				a	c	L max		
705739-1	8510912	F	Stage I					
705739-2	1927933	FG	–	–	–	–	–	Failed in grip
705739-3	8699082	FG	–	–	–	–	–	Failed in grip
705739-4	10000000	DNF	–	–	–	–	–	
705739-5	8251978	F	Stage I					
705739-6	8053290	FG	–	–	–	–	–	Failed in grip
705739-7	6803800	F	Stage I					
705739-8	8357960	F	Stage I					
705739-9	3898379	FG	–	–	–	–	–	Failed in grip
705739-10	1707417	F	Mg2Si particle	0.00049	0.00043	0.00049	0.00027	

* F = fail
DNF = specimen did not fail and test was discontinued
FG = failed in grip

78

Table 2.9. Thin material open hole axial fatigue lifetimes and sizes of crack initiators. 1.0 in. thick plate, two open hole specimen, R=0.1, LT orientation, freq.=30 Hz, lab air.

Specimen #	Max. Net Stress (ksi)	Cycles	Fail*	Initiation Site	Size (in.)		Dist. from Corner (in.)	Dist. from Hole (in.)	Comments
					a	c			
705739-19	22.5	9167960	F	Stage I	–	–	0.06030	0	
705739-4	22.5	10000000	DNF	–	–	–	–	–	
705739-2	25.0	703238	F	Fe constituent	0.00064	0.00080	0.02520	0	
705739-16	25.0	3776572	F	Stage I	–	–	0.05840	–	
705739-11	25.0	5167732	F	Stage I	–	–	0.00160	–	
705739-6	25.0	5207655	F	Stage I	–	–	0.00320	–	
705739-21	25.0	5862604	F	Stage I	–	–	0.04780	0.00164	
705739-12	27.5	66611	F	Mg2Si particle	0.00033	0.00018	0.01440	0.00012	
705739-22	27.5	91406	F	Fe & Mg2Si	0.00042	0.00096	0.00000	0	
705739-7	27.5	91822	F	Fe constituent	0.00035	0.00032	0.02350	0	
705739-3	27.5	103182	F	Fe constituent	0.00026	0.00082	0.00060	0.00006	
705739-17	27.5	266336	F	Mg2Si particle	0.00030	0.00018	0	0.00030	
705739-5	30.0	34907	F	Fe constituent	0.00053	0.00105	0.00200	0	
705739-20	30.0	55981	F	Mg2Si particle	0.00054	0.00049	0.02440	0	
"				Fe constituent	0.00030	0.00050	0.07340	0	secondary crack
705739-15	30.0	61560	F	Fe constituent	0.00088	0.00081	0.02410	0	
"				Fe constituent	0.00047	0.00059	0.03050	0	opposite side
"				Fe constituent	0.00039	0.00042	0	0	opposite side
705739-10	30.0	63478	F	Fe constituent	0.00054	0.00026	0.03180	0	
705739-1	30.0	67134	F	Fe constituent	0.00067	0.00074	0.03300	0	
705739-8	32.5	36256	F	Fe constituent	0.00074	0.00070	0.05080	0	primary site
"				Fe constituent	0.00076	0.00034	0.03600	0	opposite side
705739-9	32.5	42226	F	Fe constituent	0.00106	0.00043	0.05780	0	
"				Fe constituent	0.00050	0.00032	0.03690	0	opposite side
"				Fe constituent	0.00038	0.00026	0.10760	0	opposite side
705739-13	32.5	44094	F	Fe constituent	0.00053	0.00094	0.03870	0	
"				Mg2Si particle	0.00023	0.00031	0.00090	0	opposite side
705739-14	32.5	44280	F	Mg2Si particle	0.00047	0.00030	0.01910	0	primary site
"				Mg2Si particle	0.00058	0.00052	0.04760	0	opposite side
"				?	–	–	–	0	opposite side
705739-18	32.5	52918	F	Fe Constituent	0.00047	0.00023	0.02960	0	
"				Fe Constituent	0.00062	0.00064	0.05450	0	opposite side

* F = fail

DNF = specimen did not fail and test was discontinued

79

Table 2.10. Heirarchy of dominant microstructural features for each of the variants of 7050 plate which result in initiation of fatigue cracks in smooth and open hole fatigue tests.

		Dominant Microstructural Feature		
		Smooth Fatigue	Open Hole Fatigue	
Material	Product Thickness (in.)	(round bars)	As-machined holes*	De-burred holes
Old Material	5.7	Coarse Porosity	Coarse Porosity	Coarse Porosity
Now Material	5.7	Porosity	Hole Quality/ Porosity	Porosity
Low Porosity Material	6.0	Fine Porosity	Hole Quality	Constituent Particles
Thin Material	1.0	Constituent Particles Grain Structure	--	Constituent Particles Grain Structure

*Observations consistent with USAF spectrum fatigue test results (Magnusen et. al., ASIP '92 Conf.)

Table 2.11. Results of quantitative optical metallography at 100X for *now* and *low porosity material* at various thickness locations.

feature	Now Material			Low Porosity Material		
	T/10	T/4	T/2	T/10	T/4	T/2
area fraction						
mean, %	1.31	1.17	0.99	1.17	1.21	0.98
std dev, %	0.17	0.16	0.18	0.12	0.21	0.18
no. of particles	9376	6495	5136	7977	6330	4256
particle density, mm^{-2}	303.1	210.0	166.0	257.9	204.6	137.6
longest dimension						
maximum, μm	80.2	95.8	90.4	53.4	86.0	108.3
mean, μm	10.3	12.0	12.0	10.2	11.9	12.7
std dev, μm	$\pm$ 5.5	$\pm$ 7.4	$\pm$ 7.7	$\pm$ 5.3	$\pm$ 7.2	$\pm$9.3
aspect ratio						
mean	0.587	0.565	0.587	0.616	0.587	0.596
std dev	0.167	0.178	0.171	0.164	0.175	0.170
area						
mean, μm^2	42.0	54.2	57.6	44.2	57.5	67.2
std dev, μm^2	34.4	55.9	60.3	36.6	59.8	82.8
perim						
mean, μm	28.8	33.2	33.9	29.1	33.7	36.1
std dev, μm	14.7	20.8	22.2	14.5	20.9	26.7
feret x distance						
mean, μm	198	191	172	195	173	164
std dev, μm	198	204	211	200	208	214

81

Table 2.12. Number of particles, categorized by size, which were measured by quantitative optical metallography at 100X in *now* and *low porosity materials* at various plate locations for a measured specimen area of 31 mm^2.

particle size		Now Material			Low Porosity Material		
μm	log (μm)	T/10	T/4	T/2	T/10	T/4	T/2
4.8978	0.69	1401	775	643	1215	767	645
6.0256	0.78	2047	1135	936	1664	1108	711
7.4131	0.87	1420	867	688	1304	832	518
9.1201	0.96	1607	1066	829	1377	1038	606
11.220	1.05	1125	809	554	865	783	457
13.804	1.14	808	697	562	698	670	405
16.982	1.23	494	467	374	449	470	351
20.893	1.32	259	329	249	242	336	209
25.704	1.41	132	184	156	112	189	170
31.623	1.50	56	92	83	40	79	93
38.905	1.59	19	49	33	8	39	40
47.863	1.68	5	17	19	3	12	34
58.884	1.77	1	5	6	0	4	7
72.444	1.86	2	1	3	0	3	6
89.125	1.95	0	2	1	0	0	4

Table 2.13. Number of particle spacings, categorized by size, which were measured by quantitative optical metallography at 100X in *now* and *low porosity materials* at various plate locations for a measured specimen area of 31 mm^2.

particle spacing		Number of Measured Particle Spacings					
		Now Material			*Low Porosity Material*		
μm	log (μm)	T/10	T/4	T/2	T/10	T/4	T/2
1.26	0.100	110	84	78	82	111	67
1.96	0.293	83	57	80	69	90	63
3.07	0.487	68	76	58	60	75	64
4.79	0.680	48	60	46	49	58	36
7.47	0.873	112	110	87	102	111	81
11.66	1.07	73	75	72	83	94	75
18.20	1.26	100	71	71	108	112	86
28.40	1.45	146	90	62	96	99	64
44.33	1.65	138	91	71	100	94	75
69.18	1.84	196	113	71	171	124	59
108.0	2.03	268	194	95	250	140	100
168.5	2.23	323	205	132	286	168	92
263.0	2.42	376	238	143	281	207	126
410.5	2.61	292	223	123	242	179	101
640.8	2.81	85	69	60	84	84	58

83

Table 2.14. Results of quantitative SEM metallography at 250X for *now* and *low porosity material* at the T/2 location separating Al_7Cu_2Fe and Mg_2Si particle distributions.

	Now Material			Low Porosity Material		
	all	Fe	Si	all	Fe	Si
area fraction						
mean, %	0.304	0.187	0.090	0.551	0.379	0.118
std dev, %	0.153	0.099	0.079	0.449	0.425	0.077
no. of particles	312	138	170	339	137	199
particle density, mm^{-2}	259	111	137	281	111	161
longest dimension						
maximum, μm	31.1	25.0	31.1	44.8	44.8	28.1
mean (normal), μm	5.3	6.9	4.1	5.8	9.0	3.7
std dev (normal), μm	±4.7	±5.0	±4.0	±5.6	±6.4	±3.6
aspect ratio						
mean	0.52	0.51	0.51	0.56	0.52	0.59
std dev	±0.20	±0.20	±0.20	±0.17	±0.17	±0.17
area						
mean, μm^2	11.0	16.8	6.5	18.2	34.3	7.3
std dev, μm^2	±16.5	±19.7	±11.7	±38.0	±52.6	±16.2
perim						
mean, μm	14.6	19.3	11.0	16.4	25.5	10.3
std dev, μm	±13.1	±14.8	±10.2	±17.3	±21.5	±9.7

	Thin Material		
	all	Fe	Si
area fraction			
mean, %	0.427	0.184	0.210
std dev, %	0.111	0.085	0.054
no. of particles	926	206	714
particle density, mm^{-2}	768	166	577
longest dimension			
maximum, μm	24.5	24.5	14.0
mean (normal), μm	3.6	5.8	3.0
std dev (normal), μm	±2.6	±3.5	±1.9
aspect ratio			
mean	0.53	0.45	0.55
std dev	±0.19	±0.17	±0.18
area			
mean, μm^2	5.3	11.1	3.6
std dev, μm^2	±8.4	±14.6	±4.1
perim			
mean, μm	9.6	15.2	8.0
std dev, μm	±7.0	±10.1	±4.6

Table 2.15. Comparison of quantitative metallographic results obtained at 100X (sample area 30.9 mm^2) on optical images and 250X (sample area 1.24 mm^2) on SEM images.

	Now Material		Low Porosity Material	
	100X	250X	100X	250X
area fraction				
mean, %	0.99	0.30	0.98	0.55
std dev, %	0.18	0.15	0.18	0.45
no. of particles	5136	312	4256	339
particle density, mm^{-2}	166.0	258.7	137.6	281.1
longest dimension				
maximum, μm	90.4	31.1	108.3	44.8
mean (normal), μm	12.0	5.3	12.7	5.8
std dev (normal), μm	± 7.7	±4.7	±9.3	±5.6
aspect ratio				
mean	0.59	0.52	0.60	0.56
std dev	±0.17	±0.20	±0.17	±0.17
area				
mean, μm^2	57.6	11.0	67.2	18.2
std dev, μm^2	±60.3	±16.5	±82.8	±38.0
perim				
mean, μm	33.9	14.6	36.1	16.4
std dev, μm	±22.2	±13.1	±26.7	±17.3

85

Table 3.1. Input parametes for the *old*, *now*, and *low porosity* variants used in the model calculations of fatigue performance. The depth and width parameters represent the extreme value distribution parameters for crack-initiating inhomogenieties from smooth specimen fatigue tests.

Variable	Old Material	Now Material	Low Porosity Material
Crack-Initiator Type	Pore	Pore	Particle
Crack Depth Distribution Parameters	Weibull m=8.22E-3 s=4.05E-3 lower bound = 1.35E-3	Wiebull m=4.33E-3 s=1.42E-3 lower bound = 0.0	Lognormal m=2.64E-3 s=2.41E-3 lower bound = 2.0E-4
Crack Width Distribution Parameters	Lognormal m=4.08E-3 s=1.62E-3 lower bound = 5.0E-4	Lognormal m=2.1E-3 s=9.0E-4 lower bound = 5.0E-4	Lognormal m=1.76E-3 s=1.83E-3 lower bound = 2.0E-4
Crack Growth Rate Paris Law	C=3.9E-10 m=4.175	C=3.9E-10 m=4.175	C=3.9E-10 m=4.175
Yield Stress	Lognormal m=66.5 cov=5.0E-2 lower bound = 60.0	Lognormal m=66.5 cov=5.0E-2 lower bound = 60.0	Lognormal m=66.5 cov=5.0E-2 lower bound = 60.0
Local Stress Concentration Factor, k_t	11.0	7.5	4.25
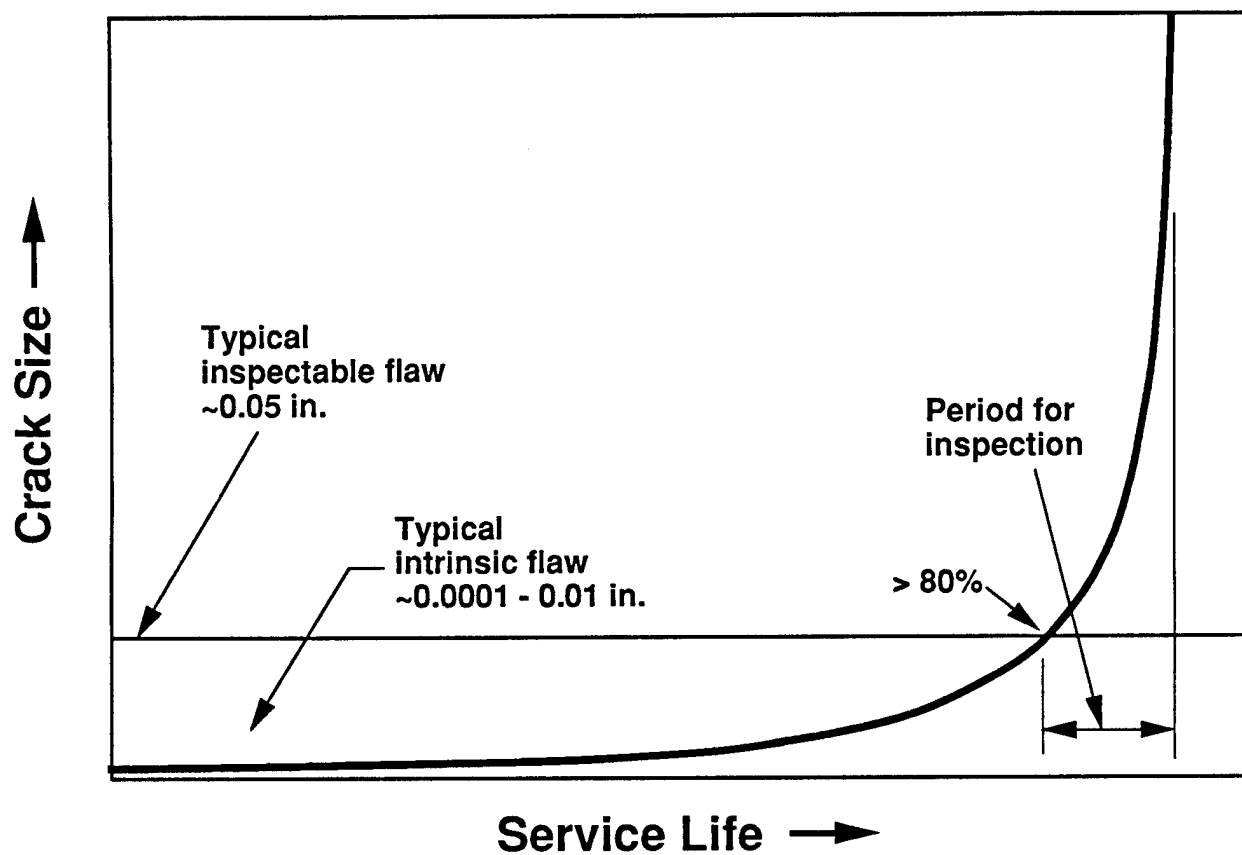
Figure 1.1. Schematic representation of crack evolution with service life showing the majority of life spent when cracks are below detectable limits of inspection.
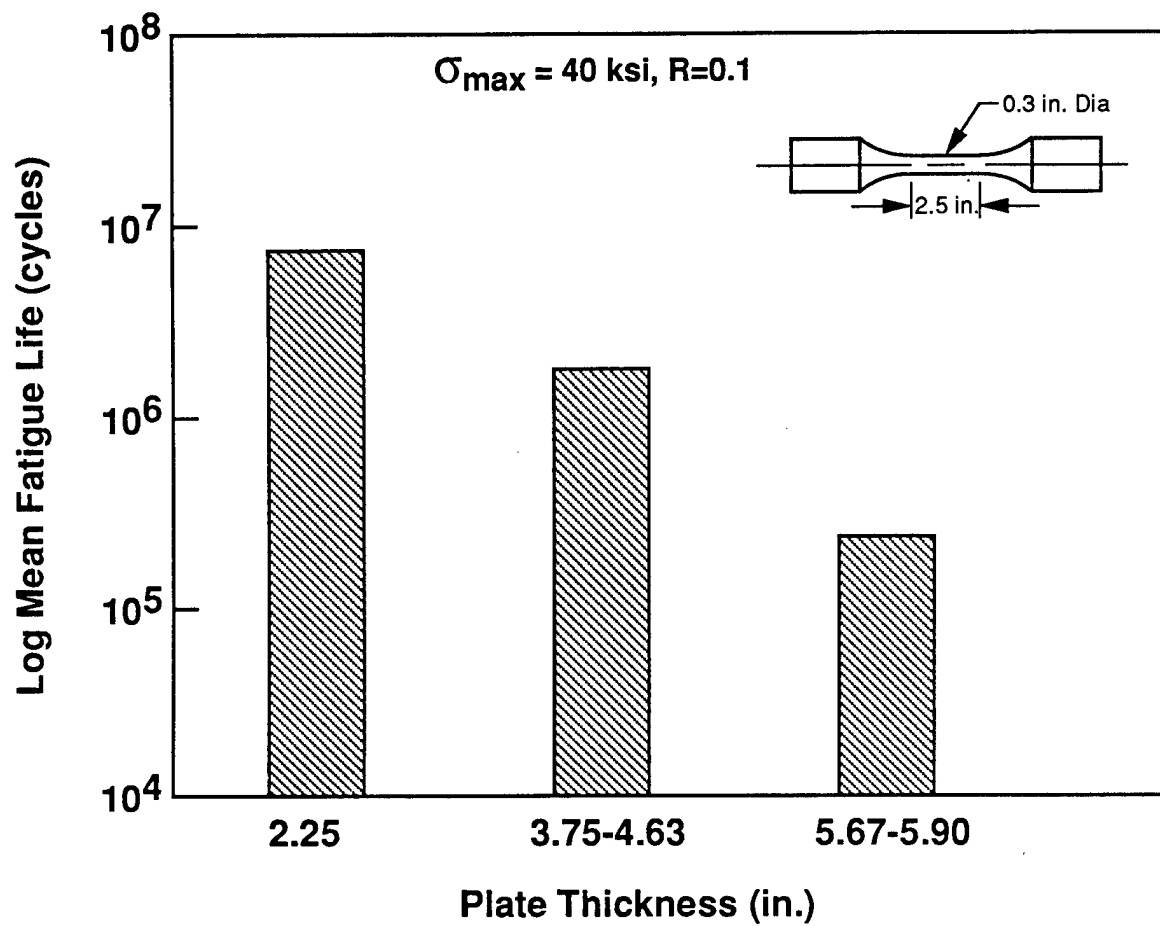
Figure 2.1. Historical data showing the effect of 7050 alloy plate thickness on smooth axial specimen fatigue lifetime.
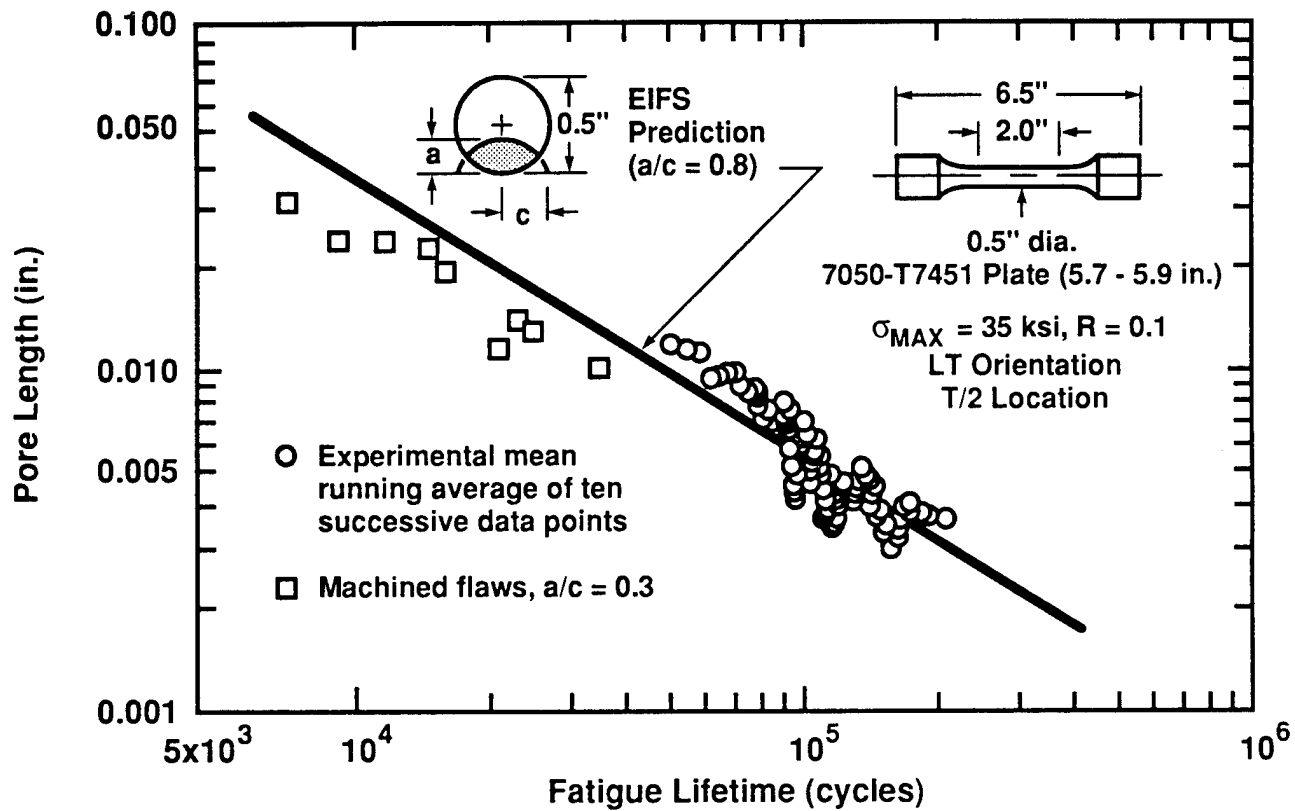
Figure 2.2. Plot of pore size vs. smooth fatigue lifetime showing EIFS prediction, experimental data which were smoothed using a running average of ten successive data points, and lifetime data for specimens with small machined flaws.
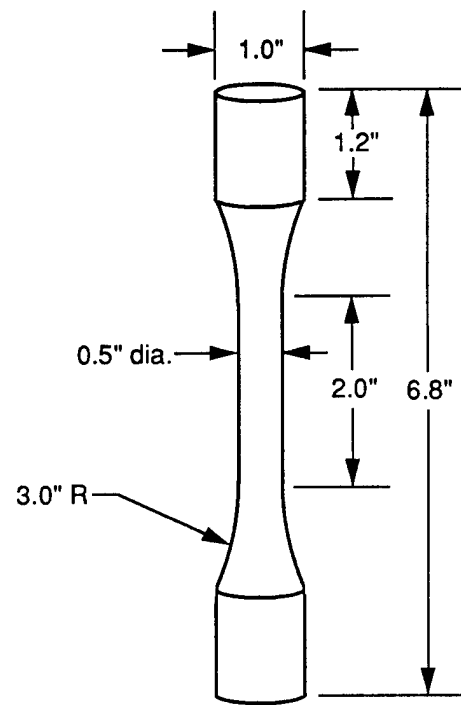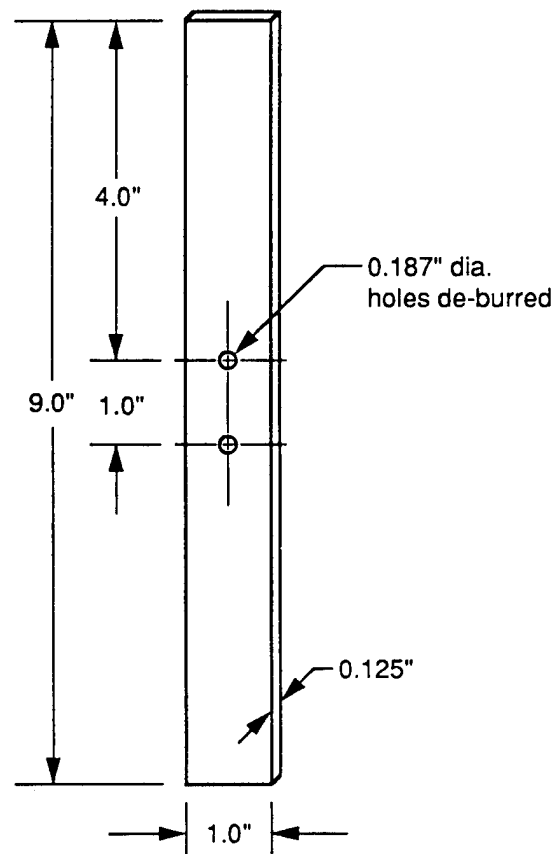
Figure 2.3. Drawings of the fatigue specimens used in this study. (a) Smooth and (b) open hole specimens.
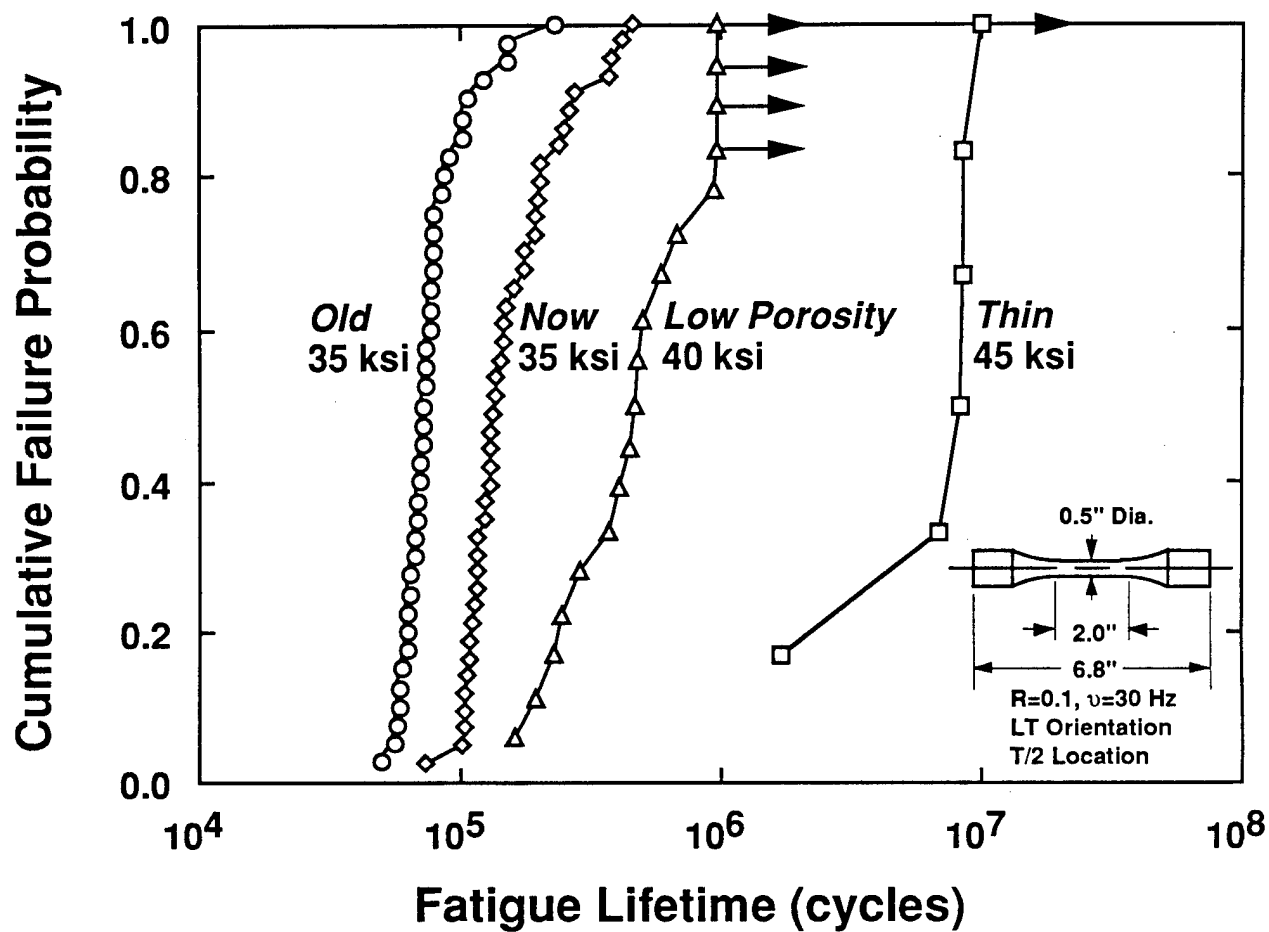
Figure 2.4. Cumulative fatigue lifetime distributions for the four microstructural variants.
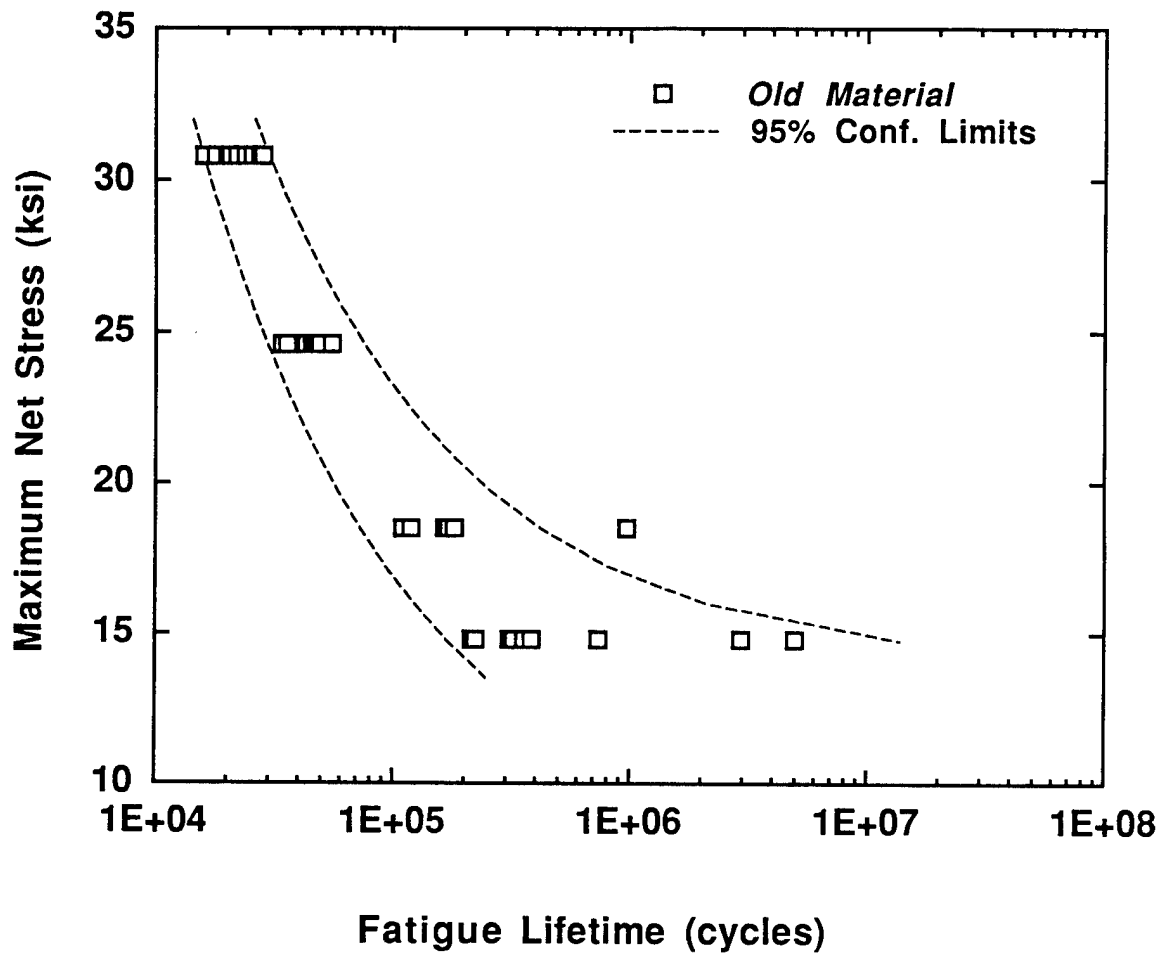
Figure 2.5. Open hole fatigue stress versus lifetime plot for the *old material* variant. Tests conducted at R=0.1, 30 Hz, LT orientation, lab air.
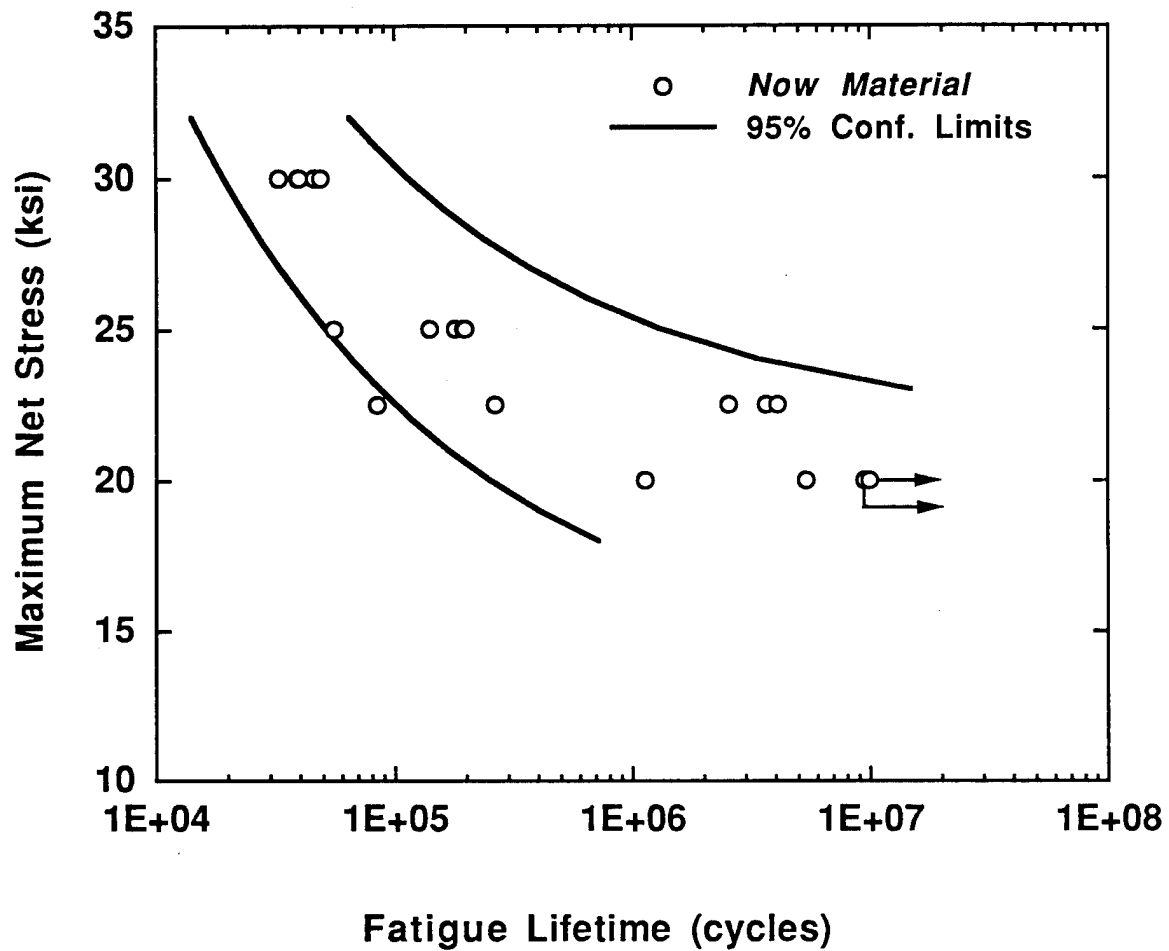
Figure 2.6. Open hole fatigue stress versus lifetime plot for the *now material* variant. Tests conducted at R=0.1, 30 Hz, LT orientation, lab air.
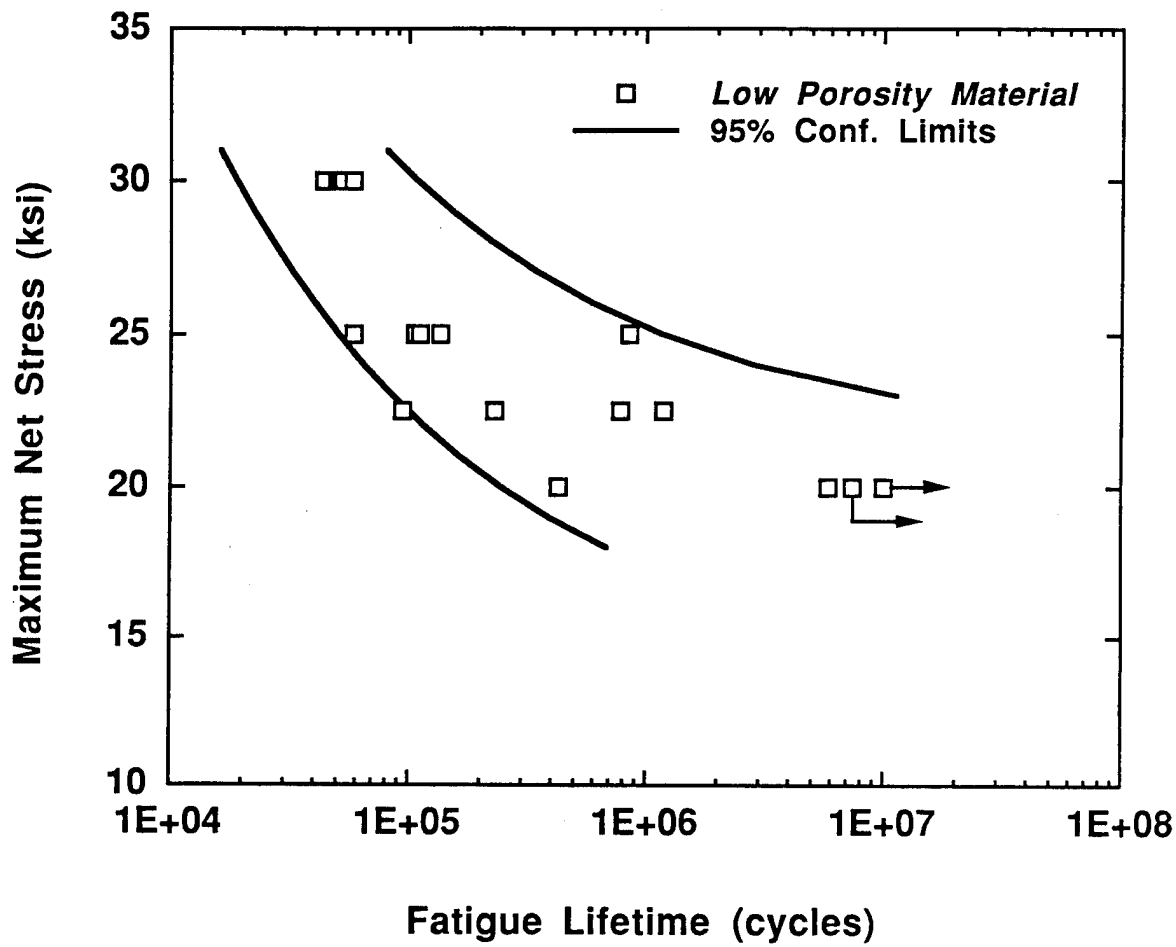
Figure 2.7. Open hole fatigue stress versus lifetime plot for the *low porosity material* variant. Tests conducted at R=0.1, 30 Hz, LT orientation, lab air.
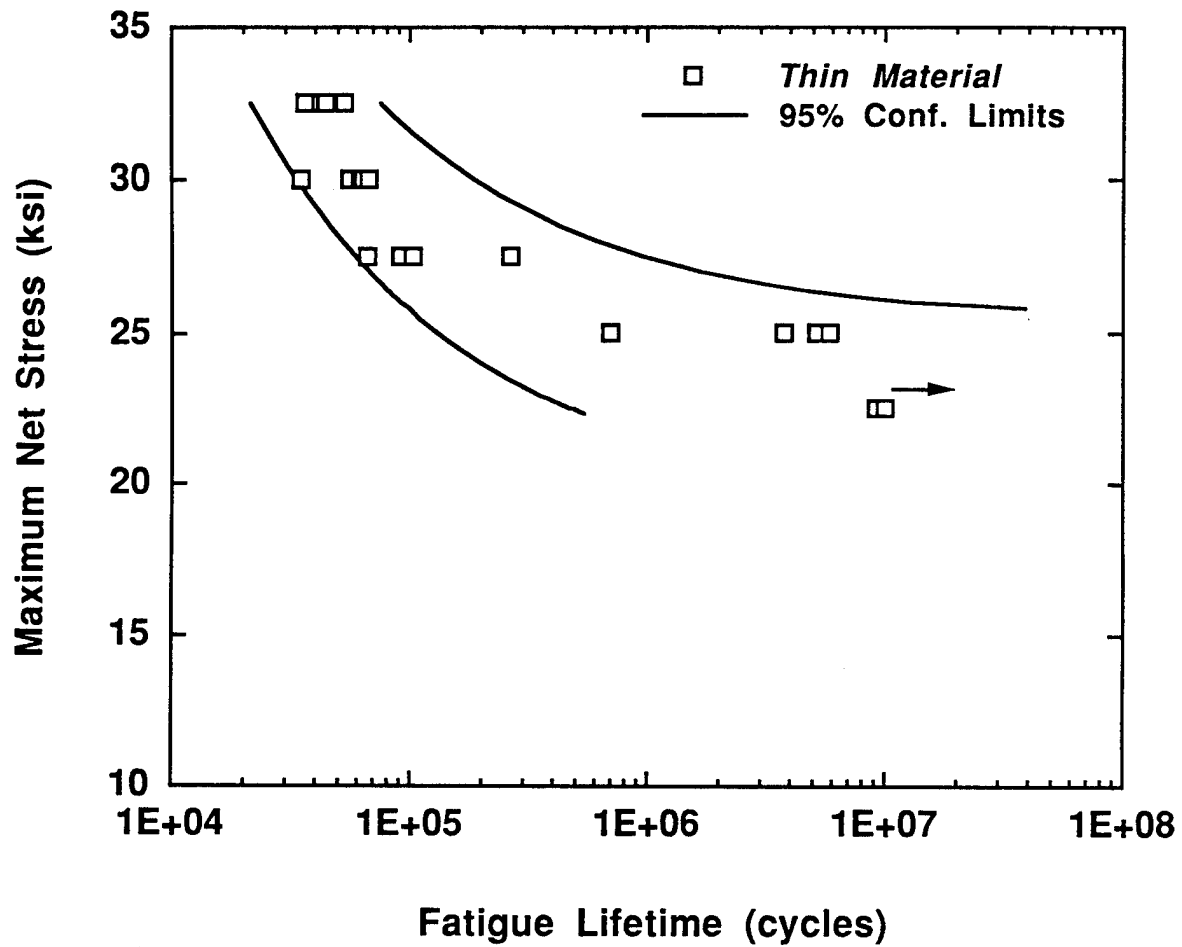
Figure 2.8. Open hole fatigue stress versus lifetime plot for the *thin material* variant. Tests conducted at R=0.1, 30 Hz, LT orientation. lab air.

hole bore | fracture surface

(a)

distance from hole

c

a

crack initiator

distance from edge

(b)

fracture surface

a

crack initiator

c

L_{max}

distance from edge
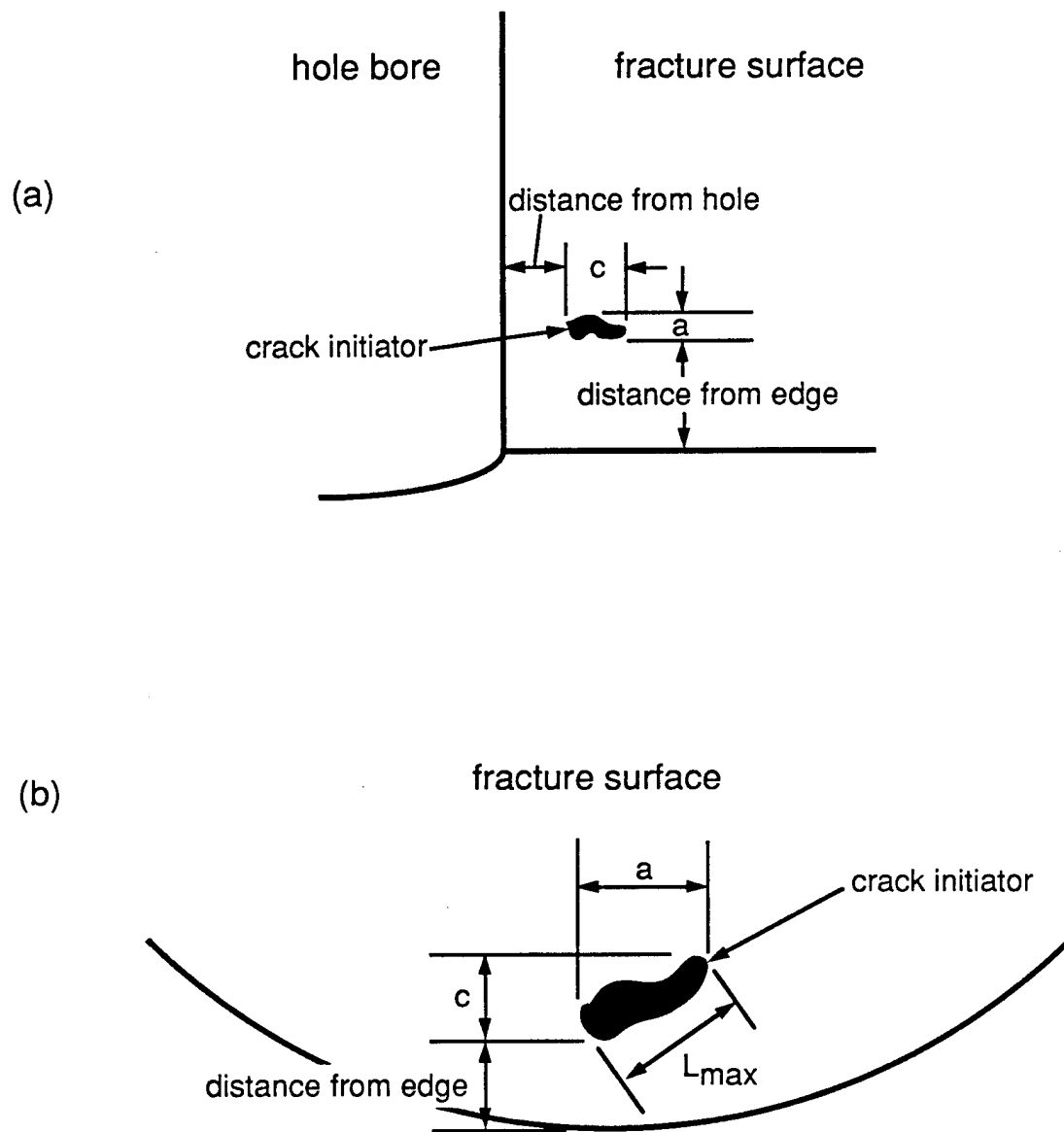
Figure 2.9. Schematic drawings of the methods used to measure the size and location of the microsturctural features which initiate fatigue failures in (a) open hole fatigue specimens and (b) smooth fatigue specimens.

(a)

Micropore

0.001 in.

(b)

Micropore

0.001 in.
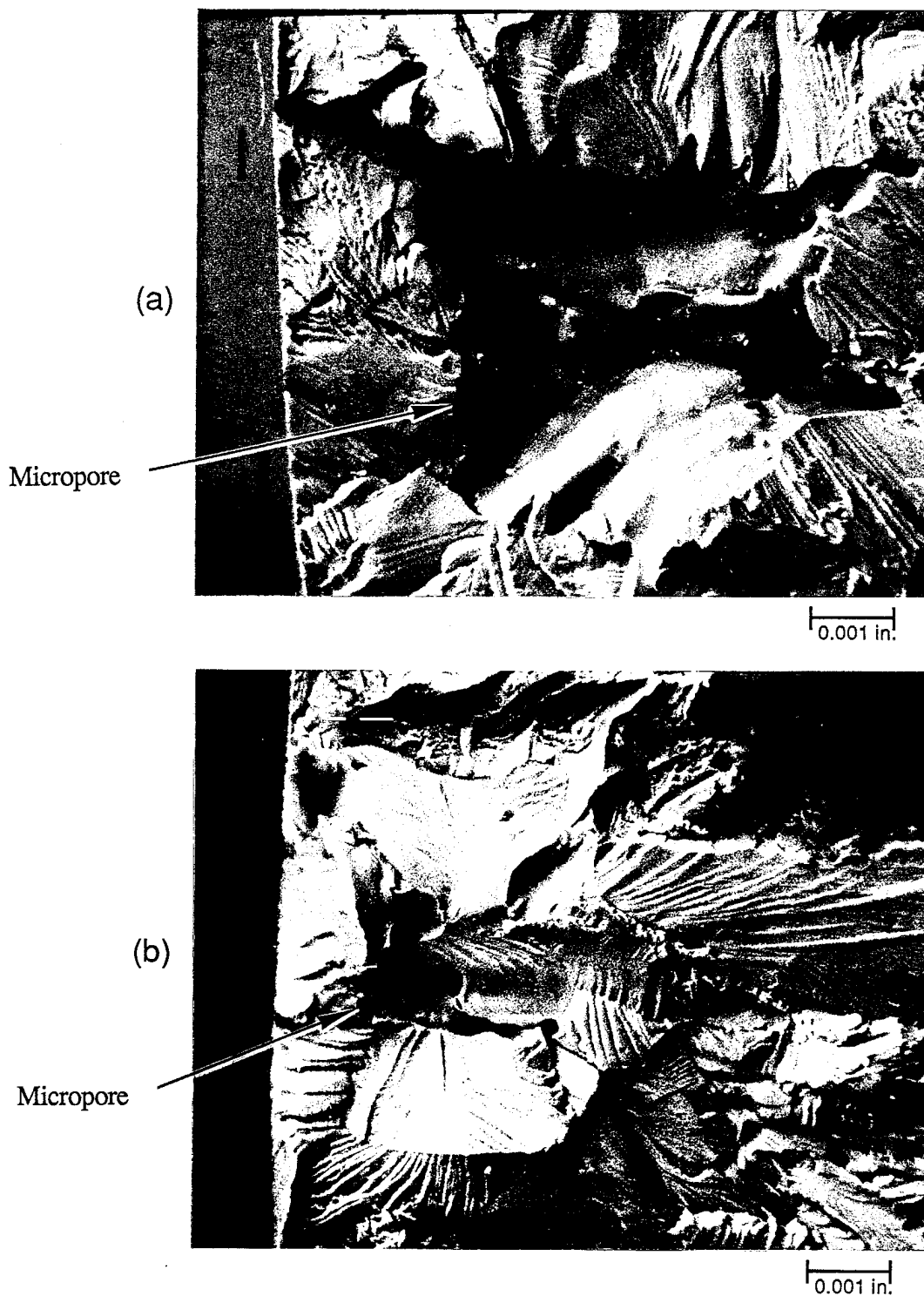
Figure 2.10. Typical smooth fatigue crack initiation from pores in 7050 plate. (a) *Old material*, maximum pore length = 0.0069 in. (b) *Now material*, maximum pore length = 0.0027 in.
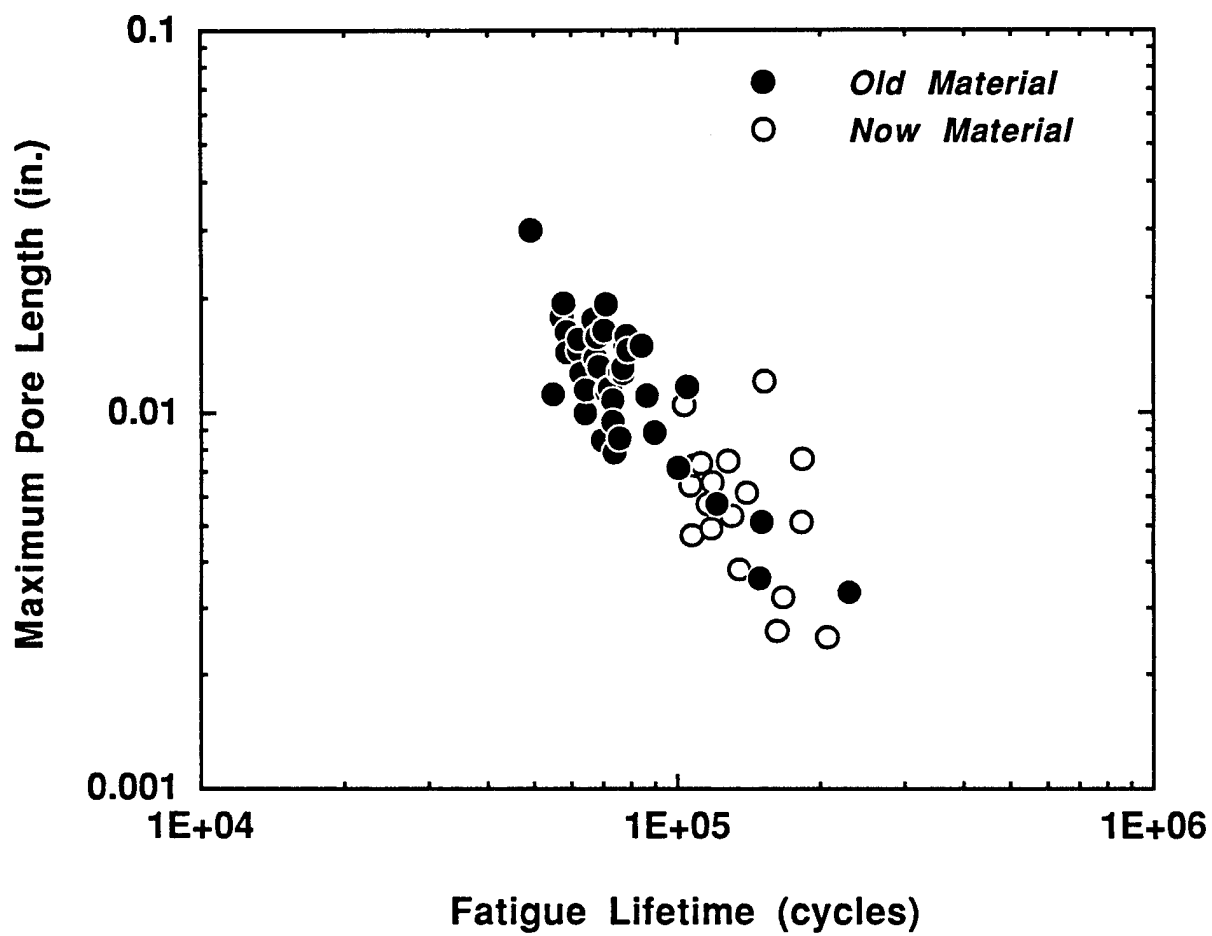
Figure 2.11. Crack initiating pore length versus fatigue lifetime in smooth fatigue specimens of *old* and *now materials* tested at 35 ksi maximum stress, R=0.1, 10 Hz, in lab air.

(a)

Micropore

0.001 in.

(b)

Constituent
Particles

0.001 in.
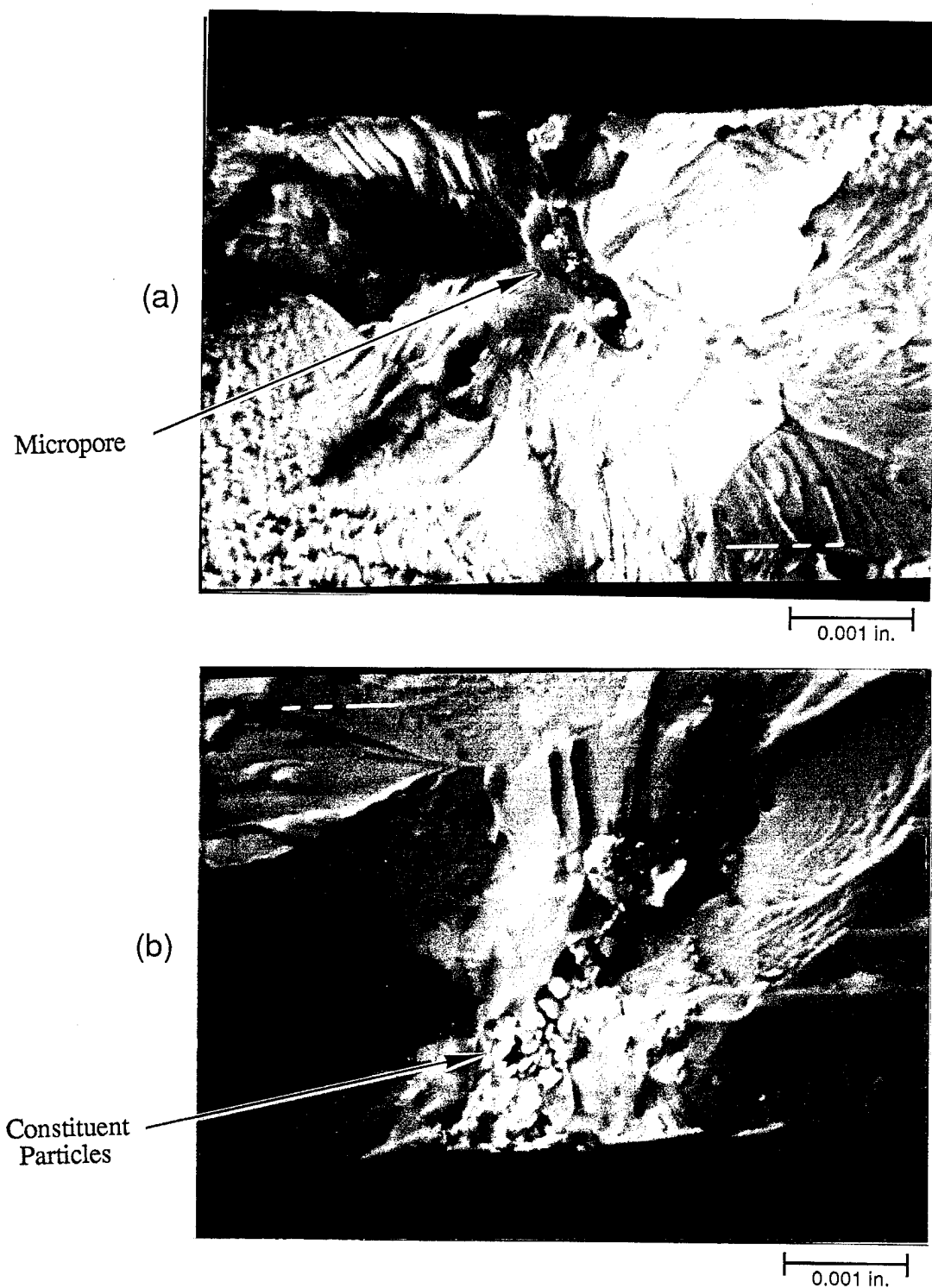
Figure 2.12. Typical smooth fatigue crack initiation sites in *low porosity material* (a) from a micropore and (b) from constituent particles.
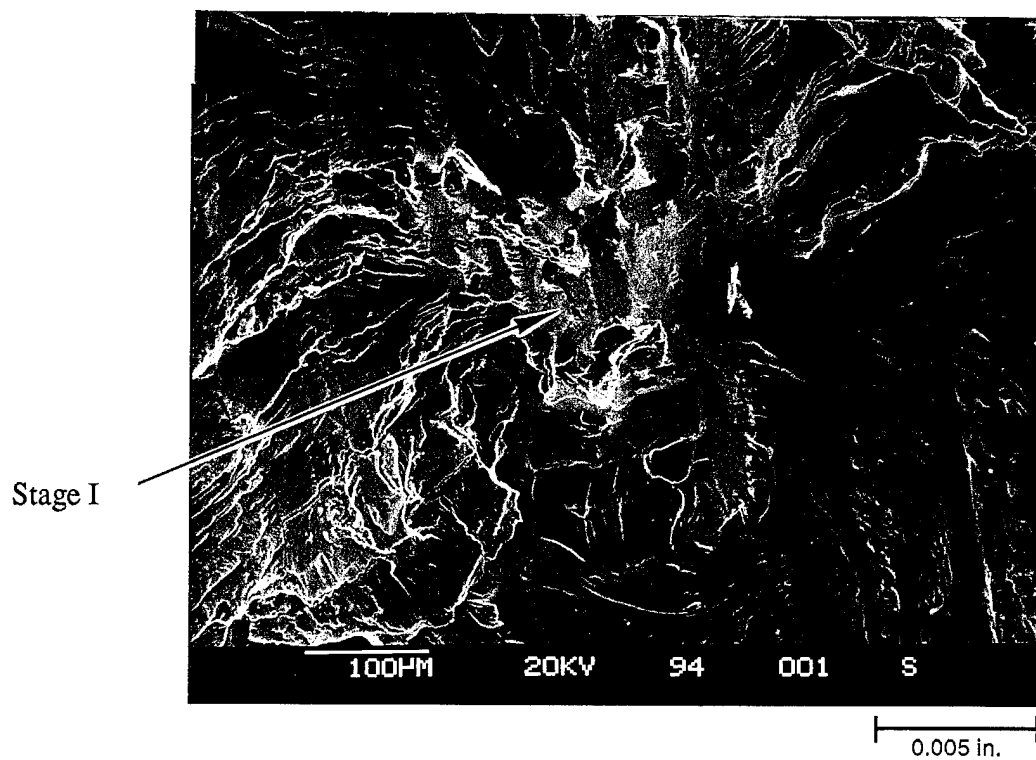
Stage I

Figure 2.13. Typical smooth fatigue crack initiation site showing stage I cracking in the *thin material*.

Micropore

0.001 in.
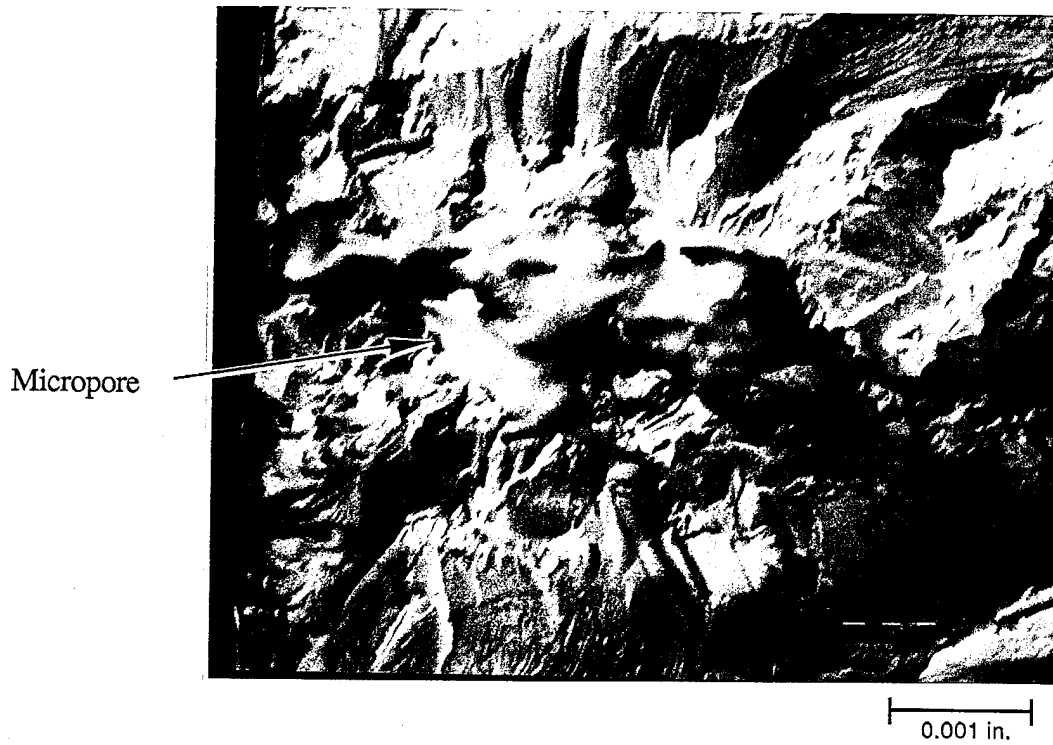
Figure 2.14. Fatigue initiation in open hole specimen from a pore in *old material*, micropore size = 0.011 in.
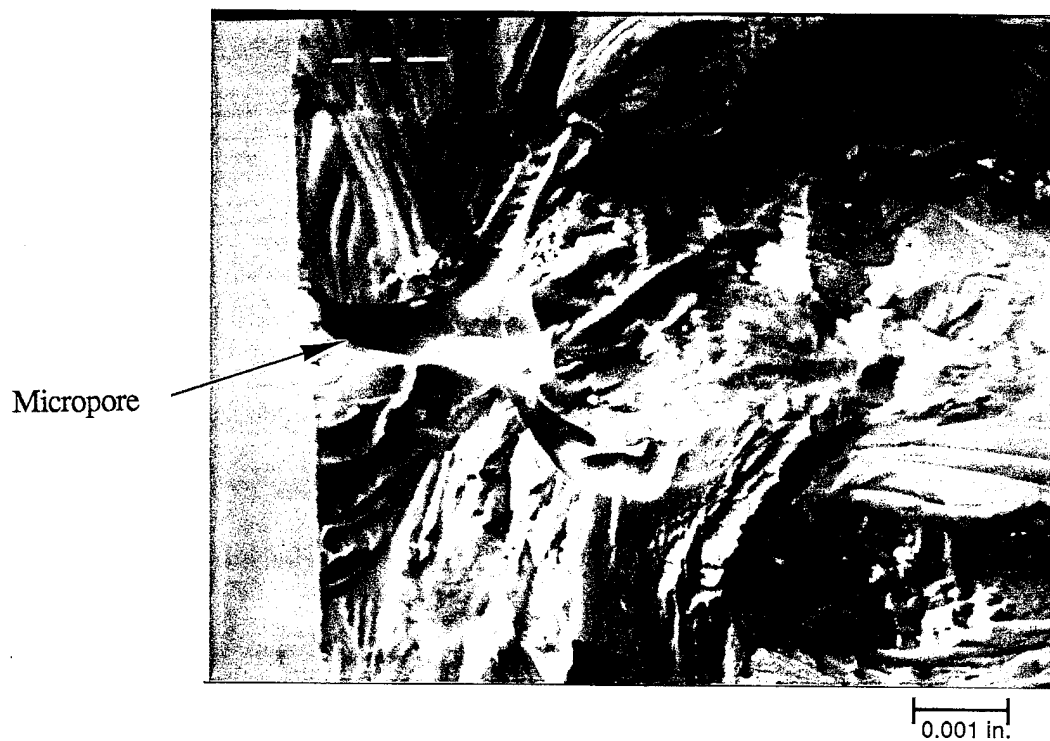
Figure 2.15. Fatigue initiation in open hole specimen from pore in *now material*, micropore size = 0.0044 in.
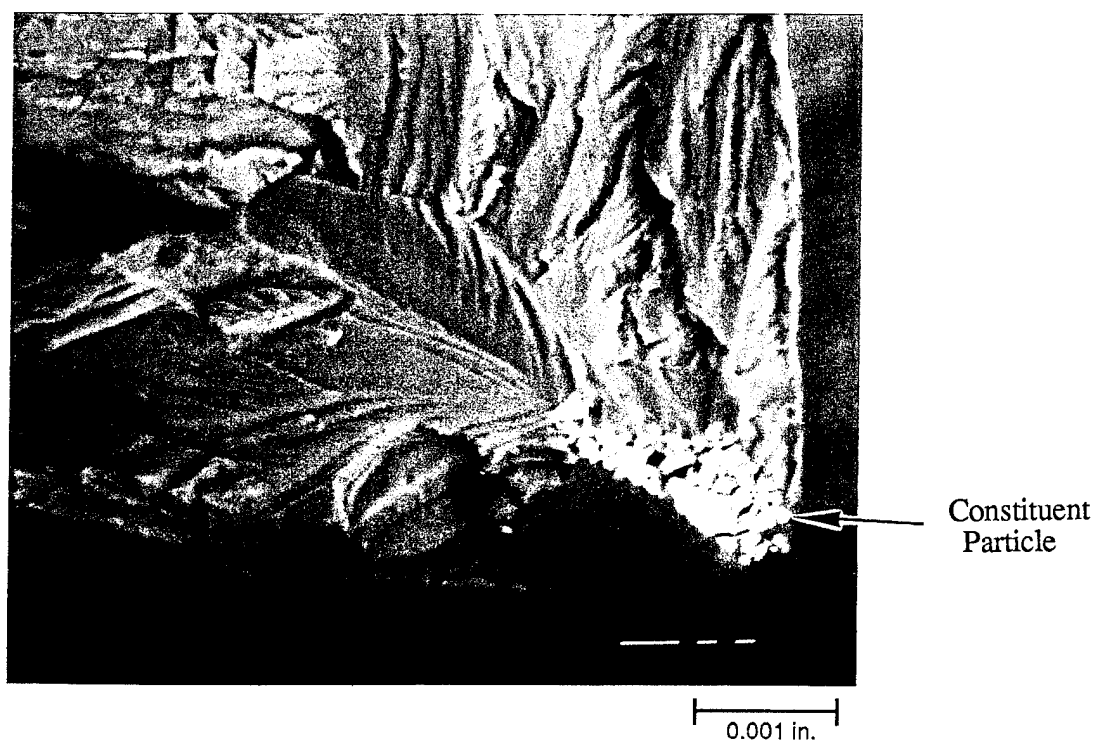
Figure 2.16. Fatigue initiation in open hole specimen from constituent particle located at the hole corner in *low porosity material*, constituent particle size = 0.0019 in.
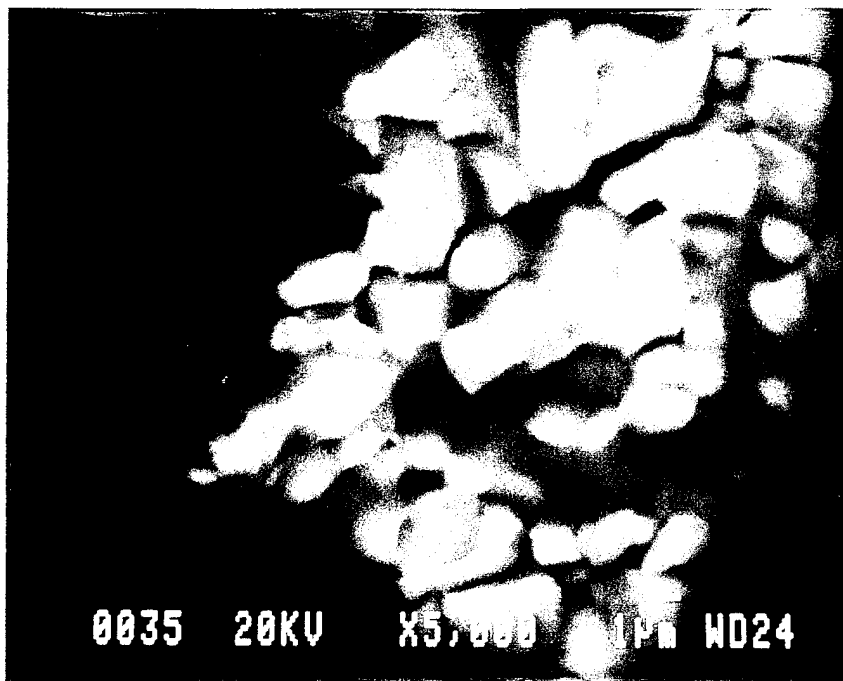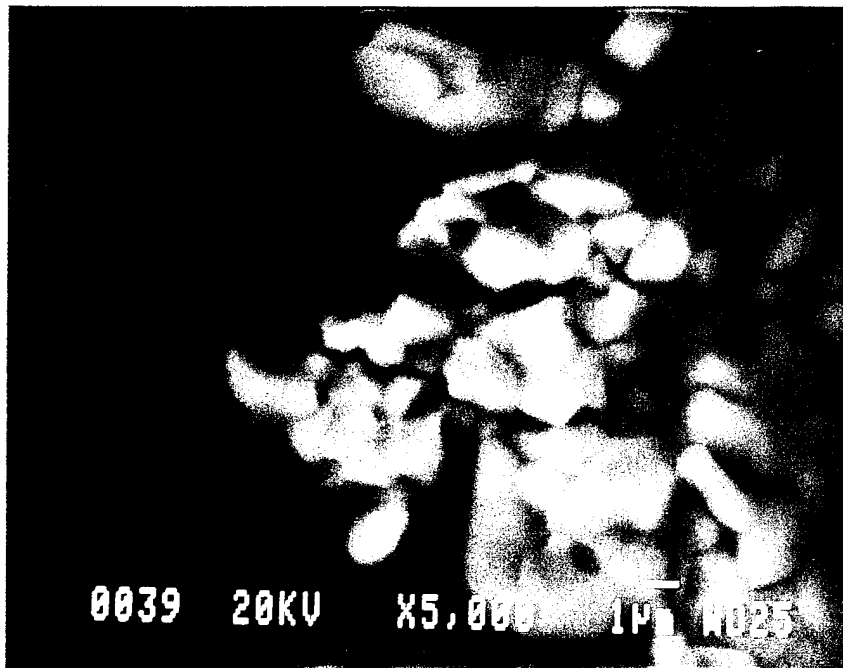
Figure 2.17. Opposite halves of open hole fatigue failure showing constituent particle at fatigue initiation site in *low porosity material*.
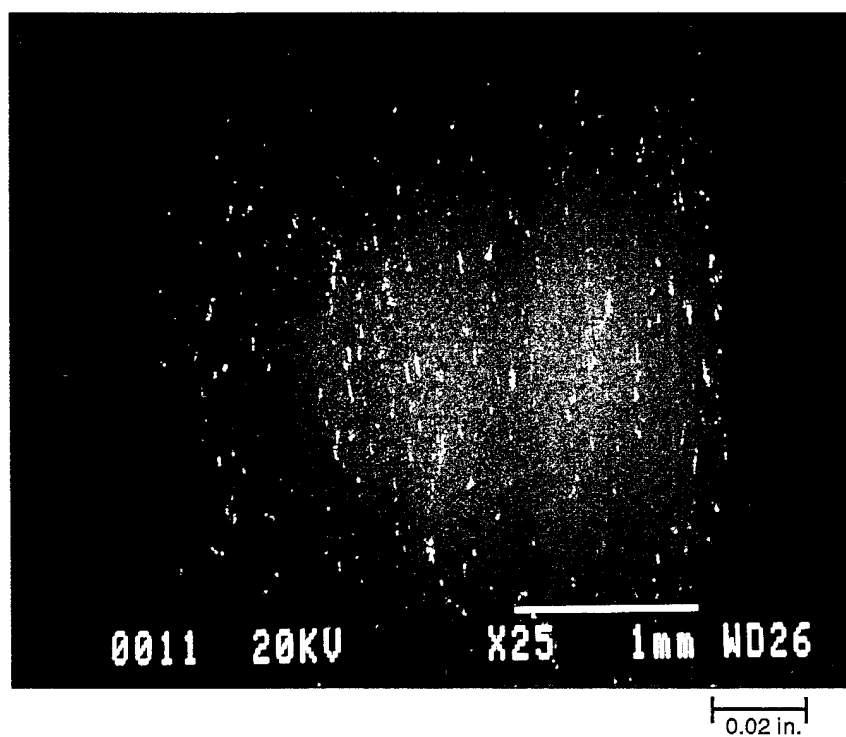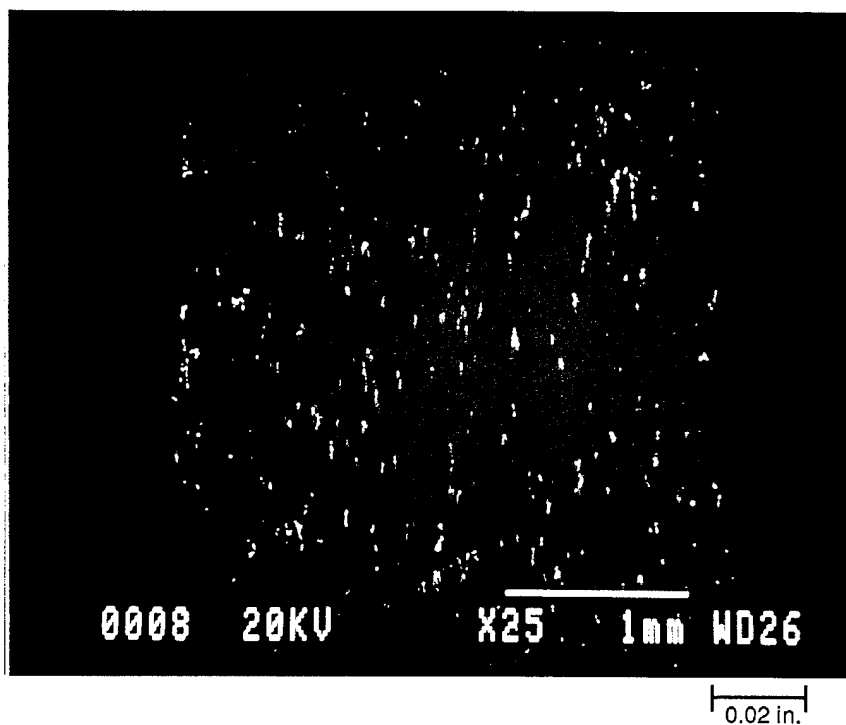
Figure 2.18. Low magnification SEM images showing constituent particles located in the hole bore in open hole specimens in (a) *now material* and (b) *low porosity material*.

0.0005 in.

0.0001 in.
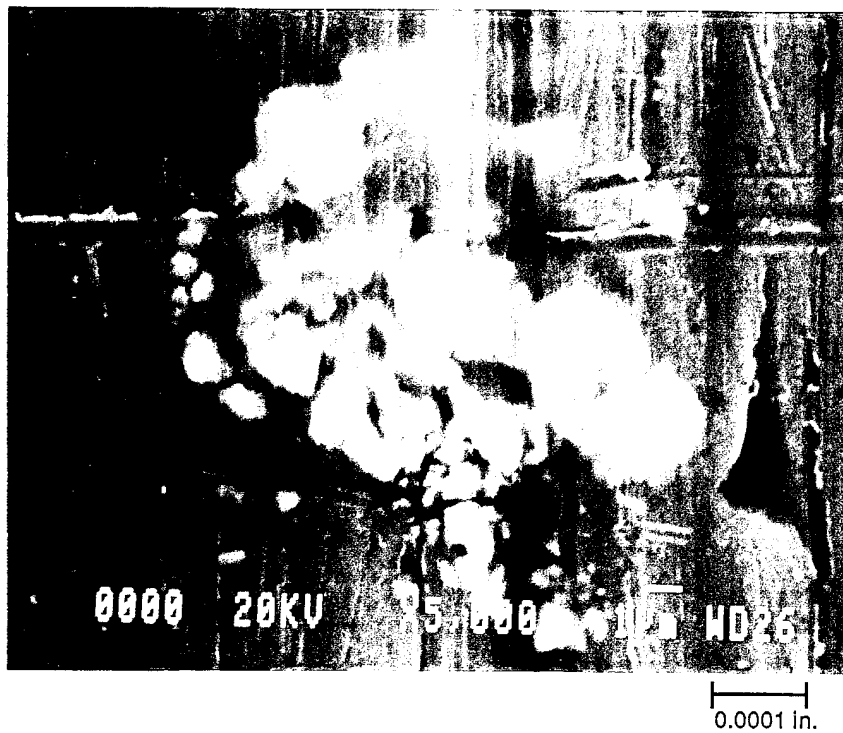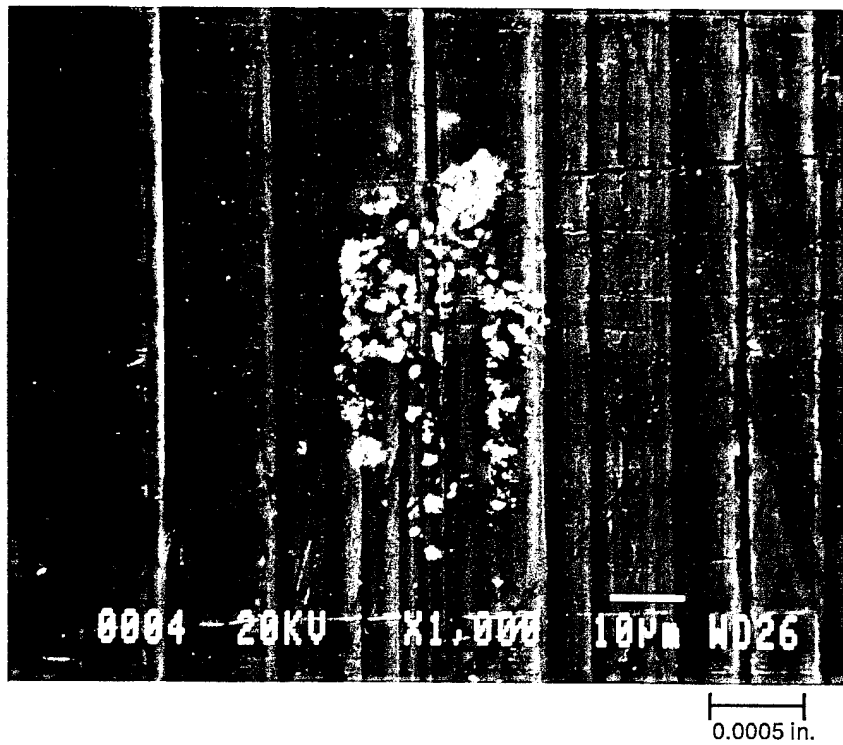
Figure 2.19. Constituent particles located in the hole bore of open hole specimens of *low porosity material.*
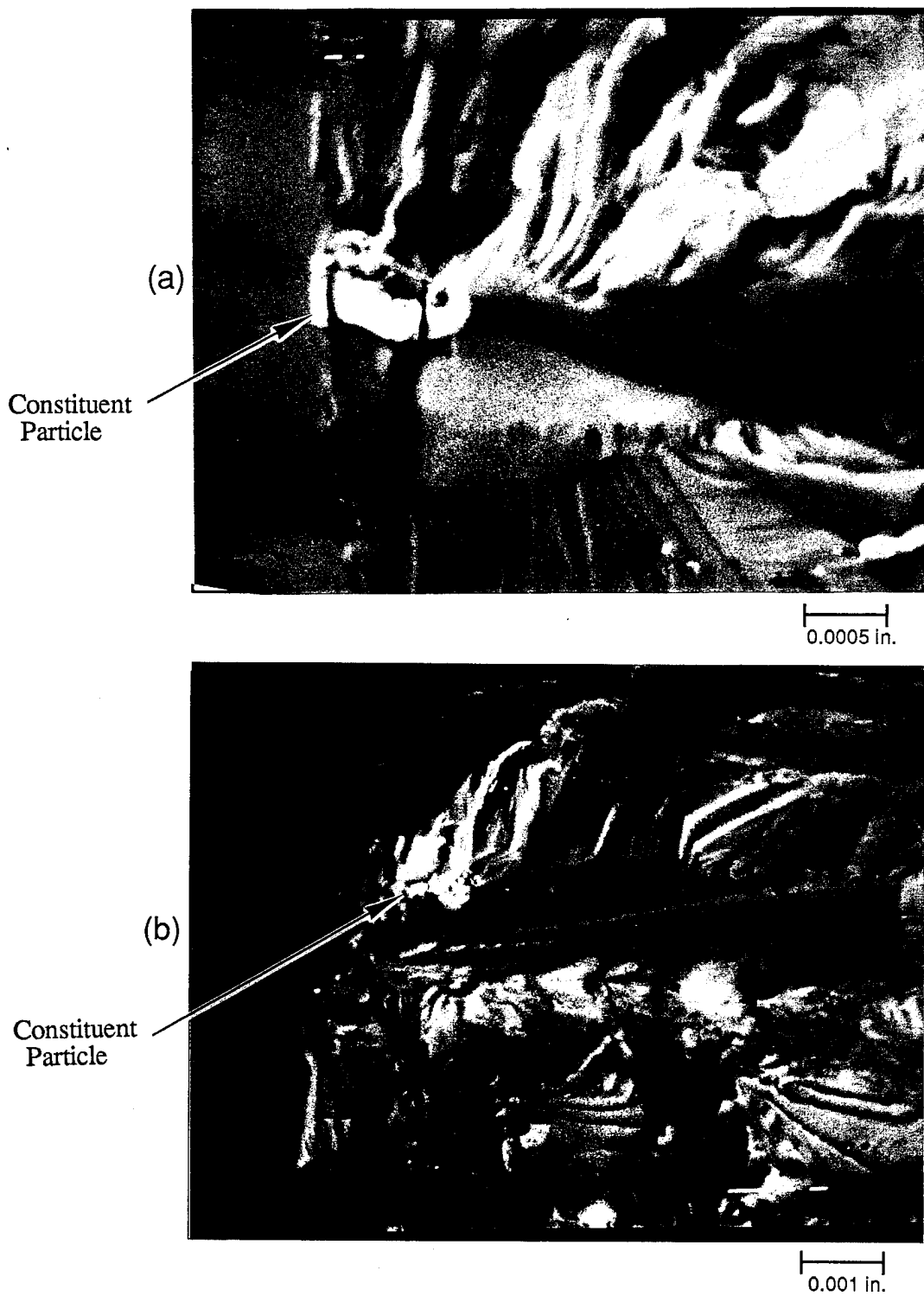
Figure 2.20. Fatigue crack initiation in open hole specimens from constituent particles in the *thin material*. (a) Constituent particle size = 0.00097 in. and (b) constituent particle size = 0.0009 in.

Stage I

0.002 in.
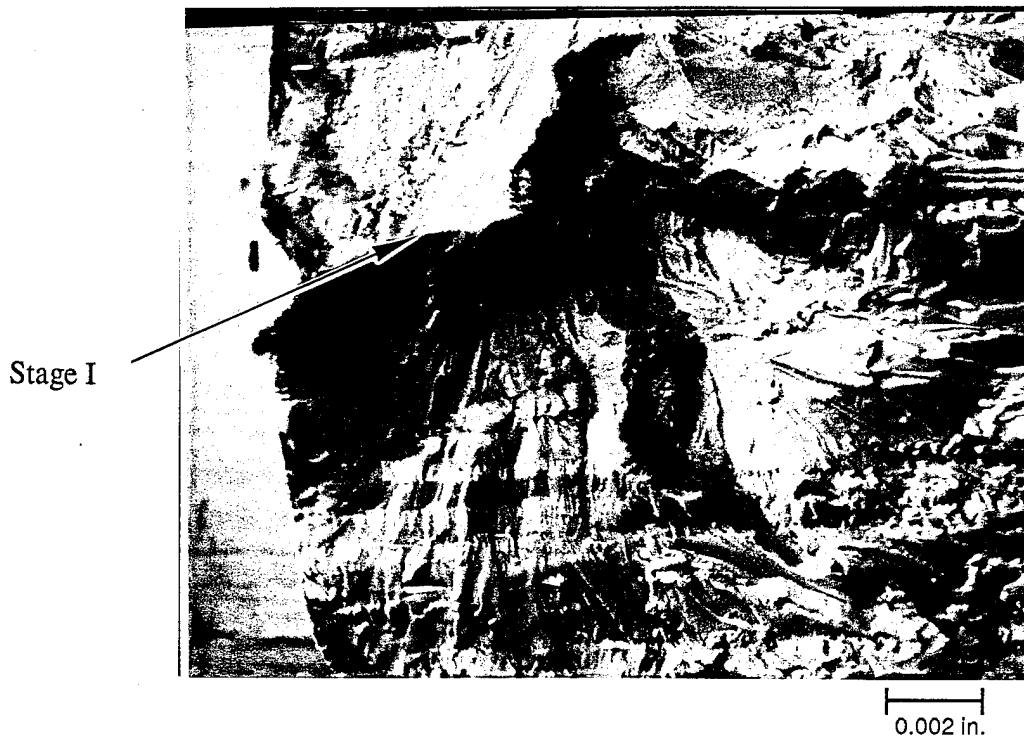
Figure 2.21. Fatigue crack initiation in open hole specimens showing stage I type initiation in the *thin material.*

Burr

0.001 in.
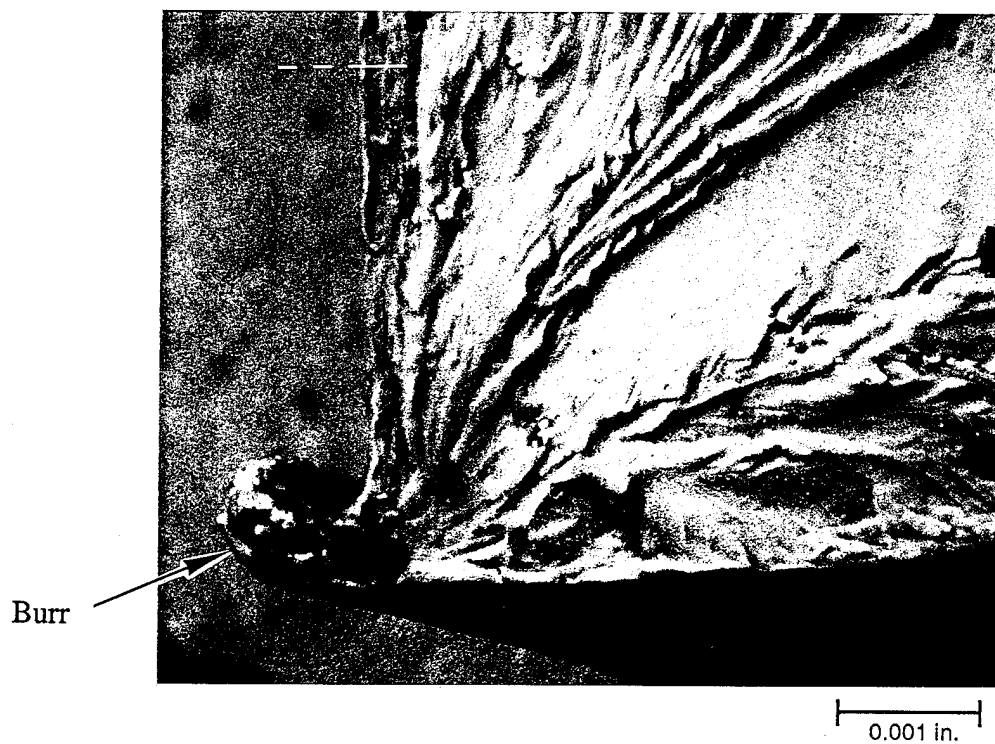
Figure 2.22. Fatigue initiation in open hole specimen from hole edge burr in *now material* for specimen which was not de-burred.
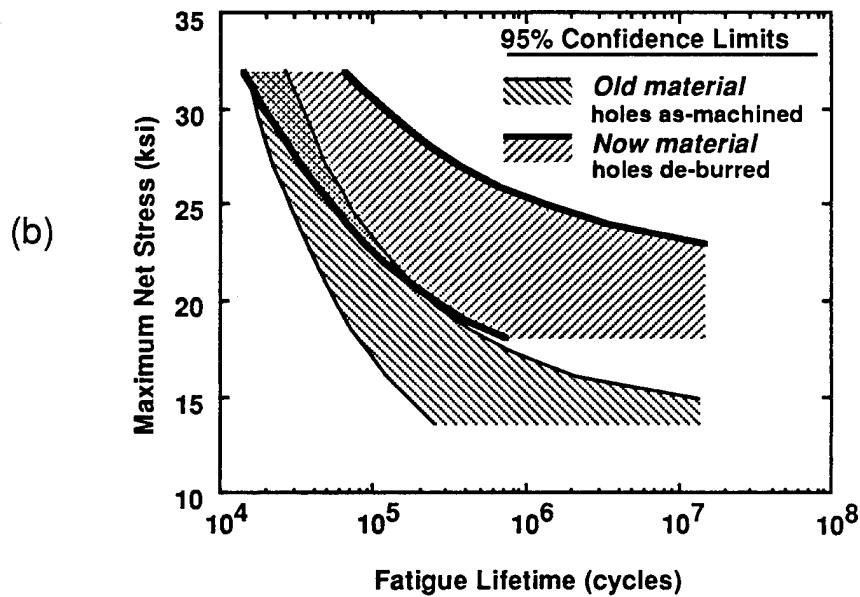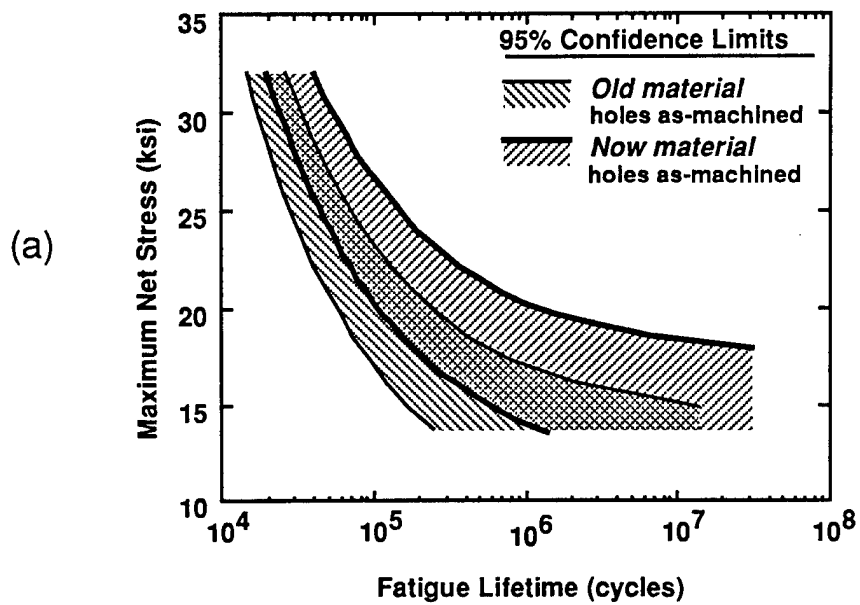
Figure 2.23. Open hole stress versus lifetime plots showing the effect of hole de-burring. (a) *Old material* and *now material* in the as-machined condition and (b) *old material* as-machined and *now material* de-burred.

110
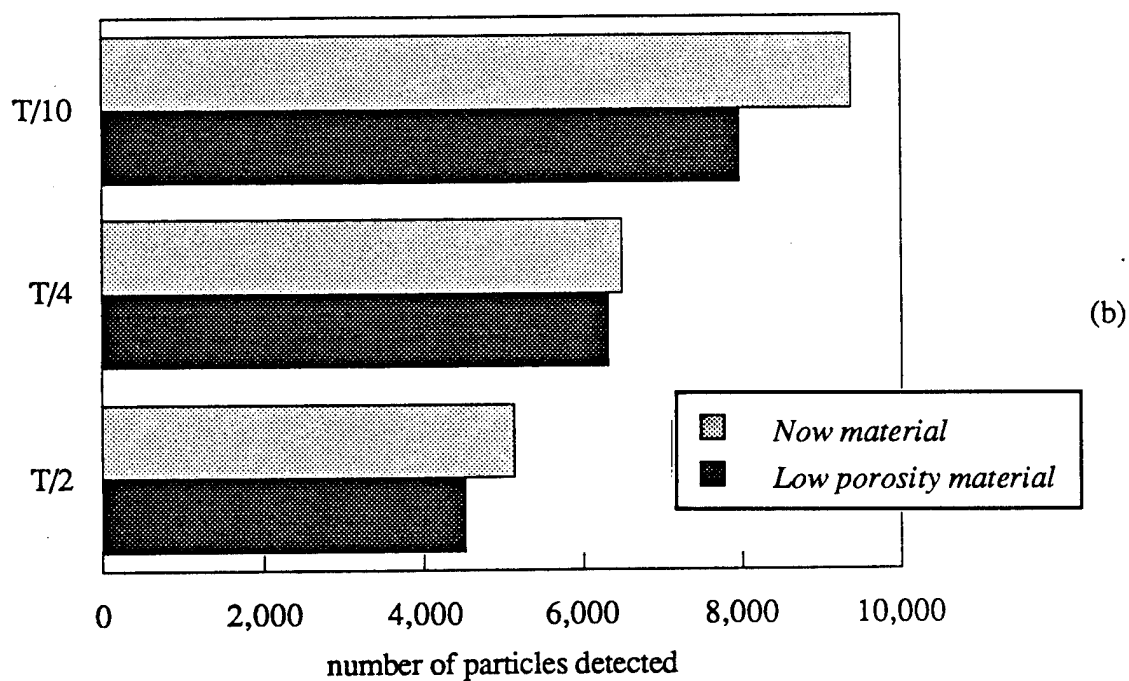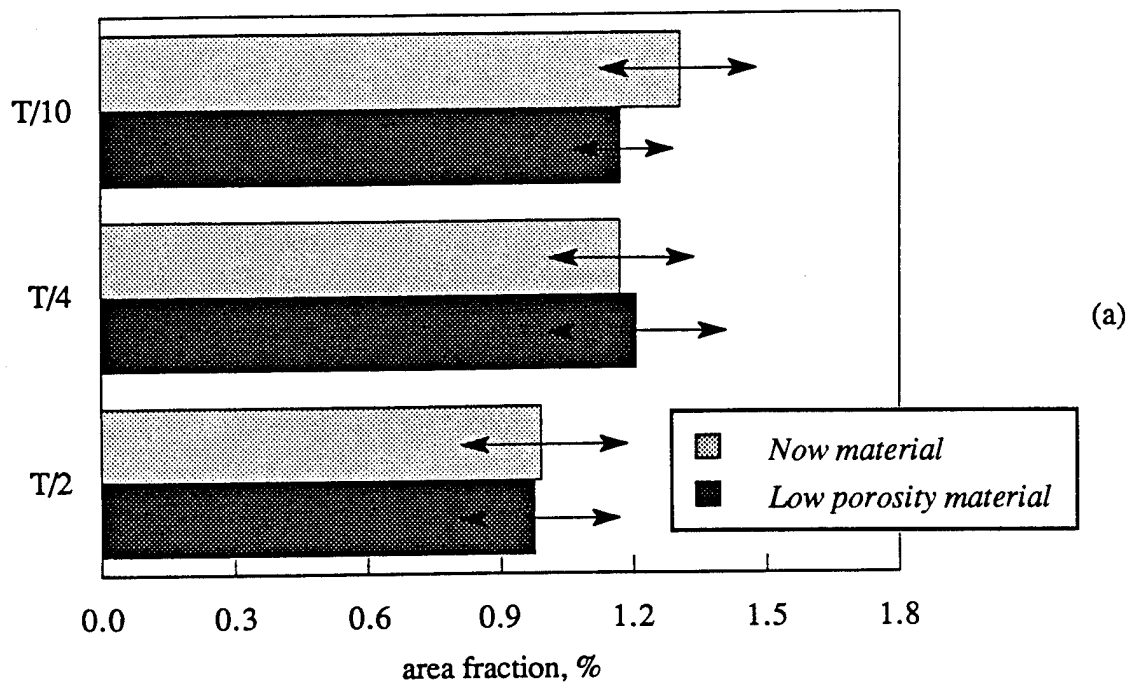
Figure 2.24. Quantitative metallographic results comparing *now* and *low porosity materials* at different plate locations. (a) Particle area fraction and (b) particle number density.
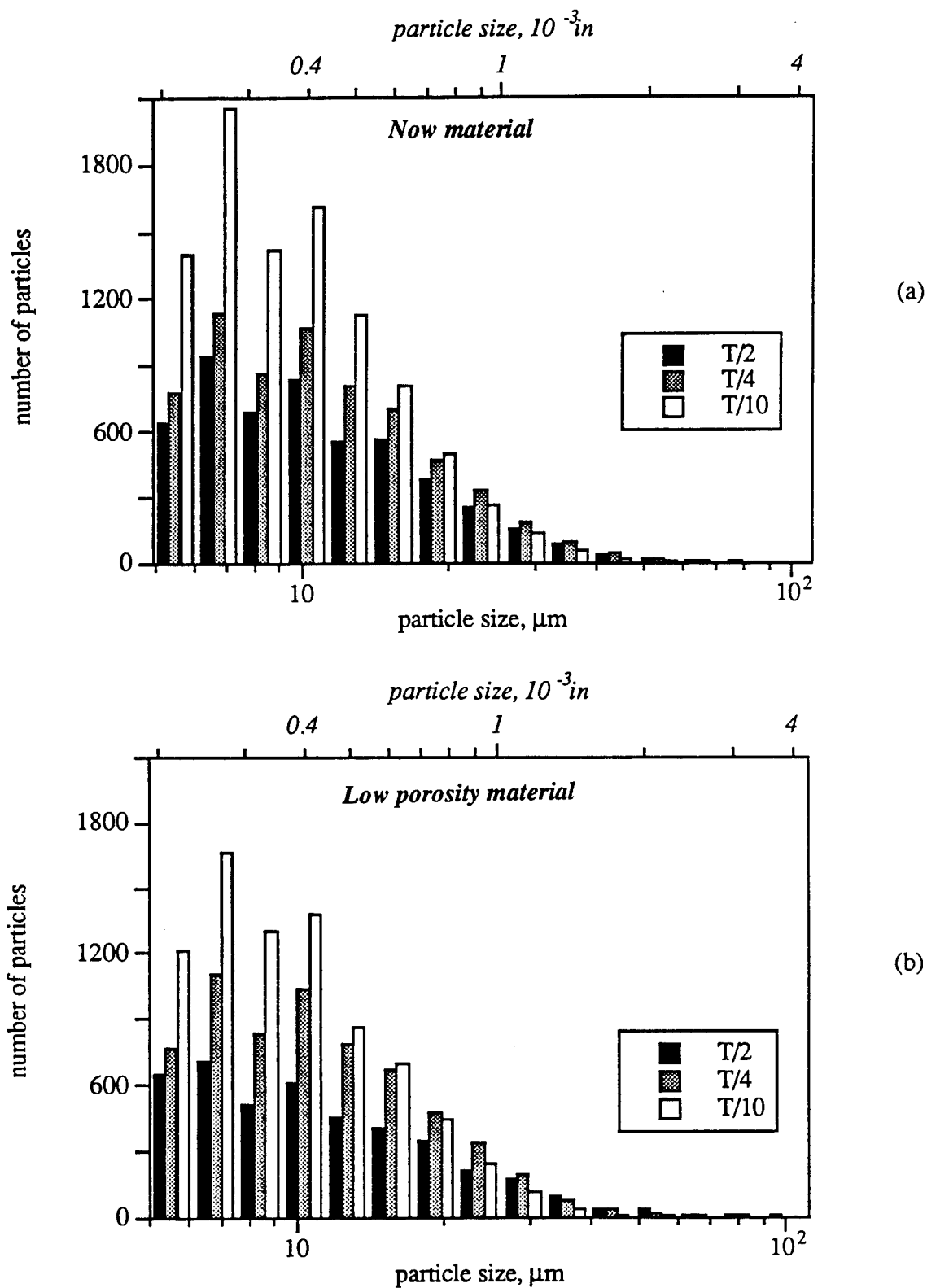
Figure 2.25. Particle size distribution histograms for (a) *now material* and (b) *low porosity material* at different plate locations.
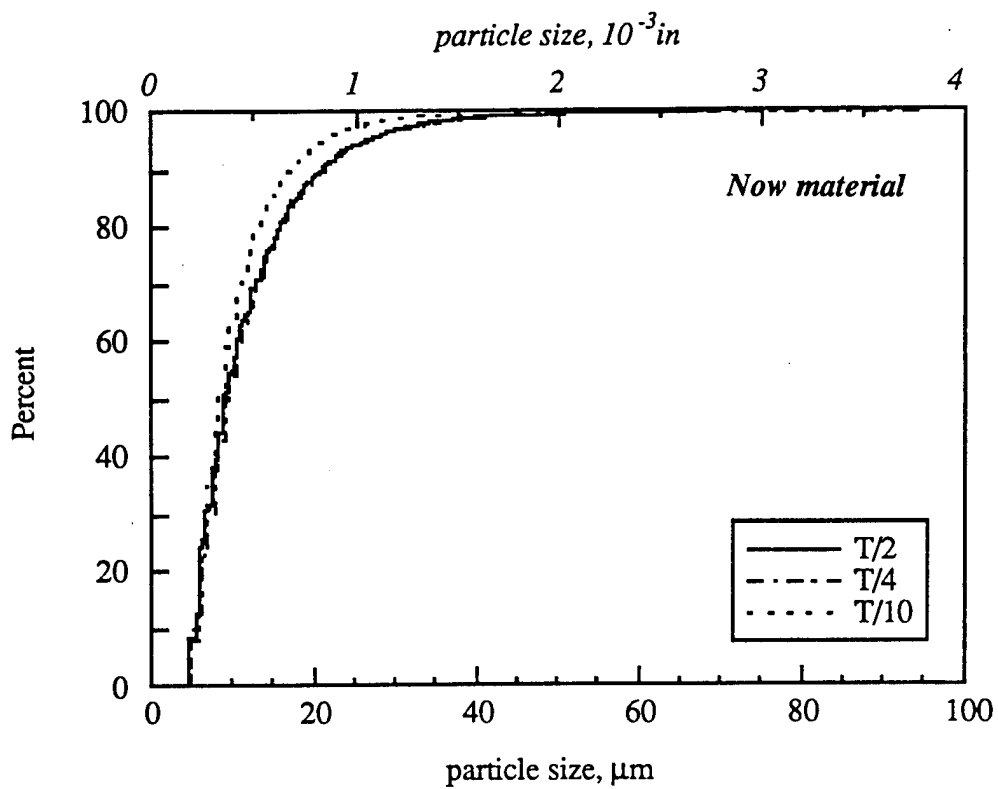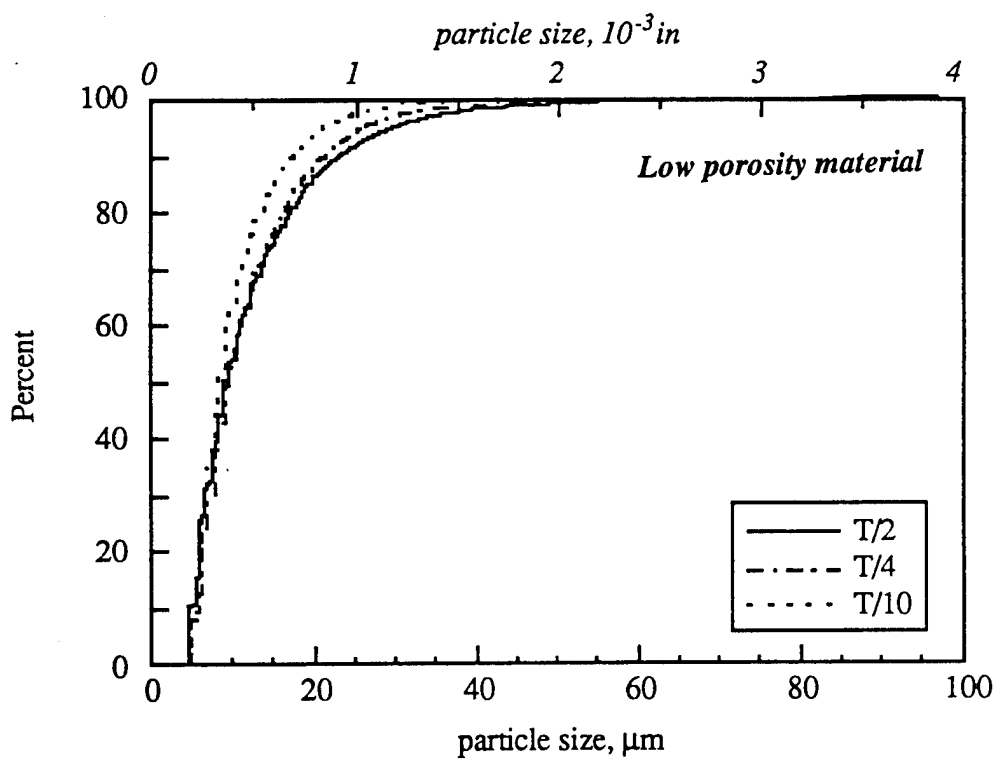
Figure 2.26. Cumulative probability plot of particle size distributions for (a) *now material* and (b) *low porosity material* at different plate locations.
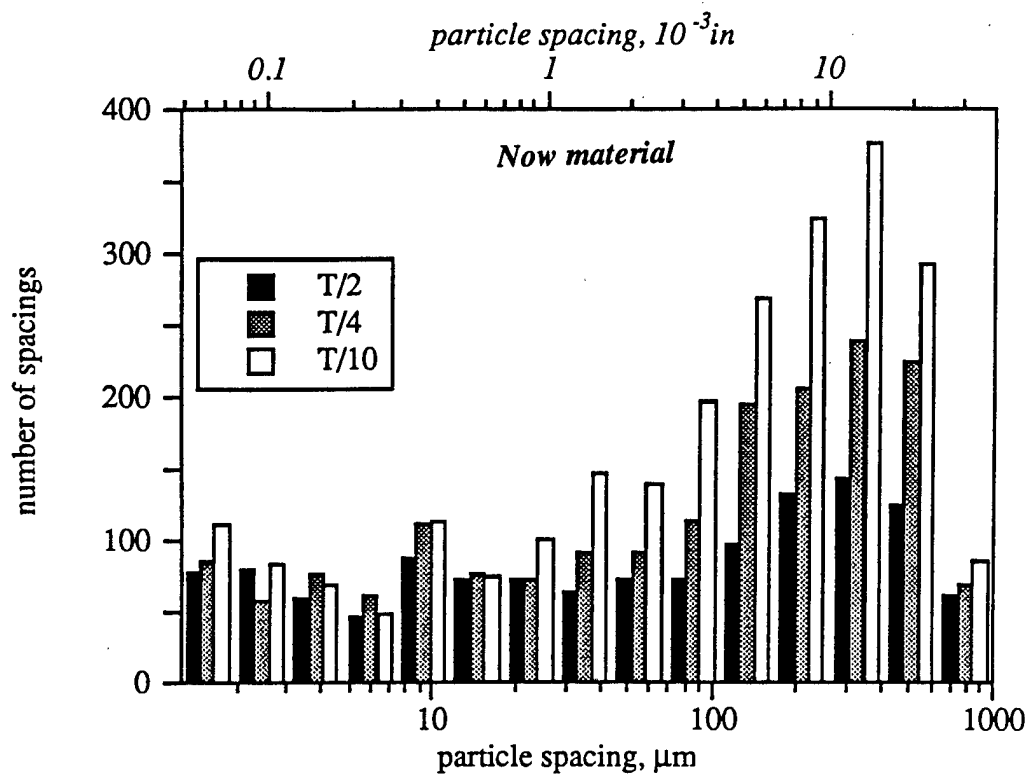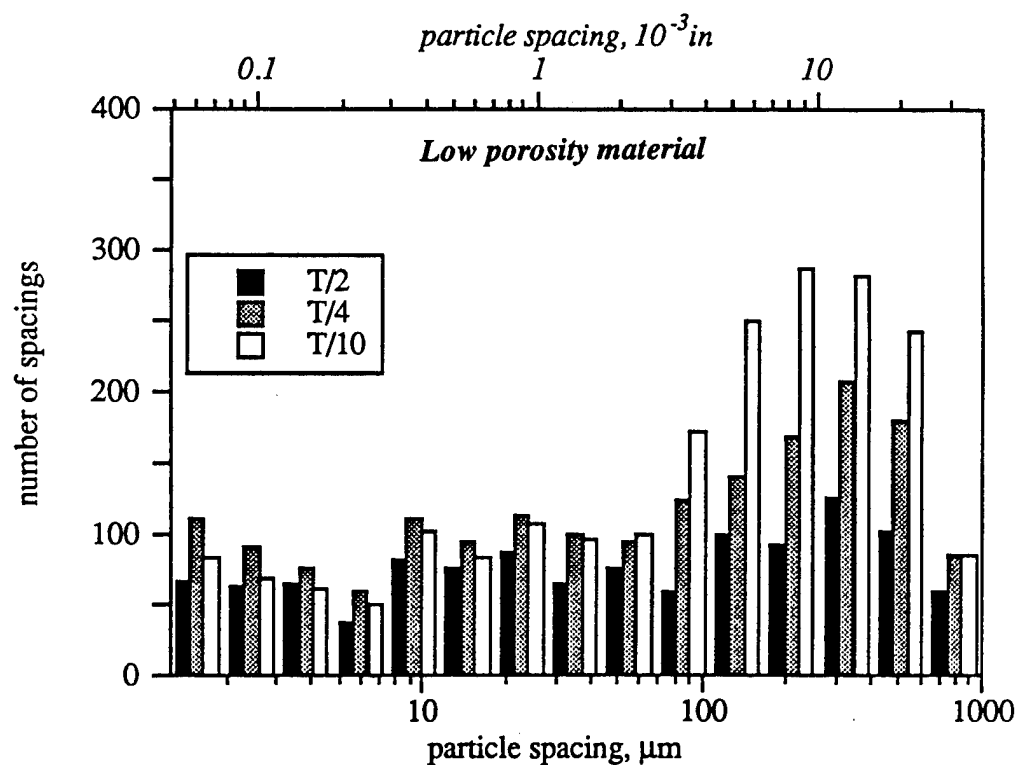
Figure 2.27. Histograms of the distribution of inter-particle specings for (a) *now material* and (b) *low porosity material* at different plate locations.
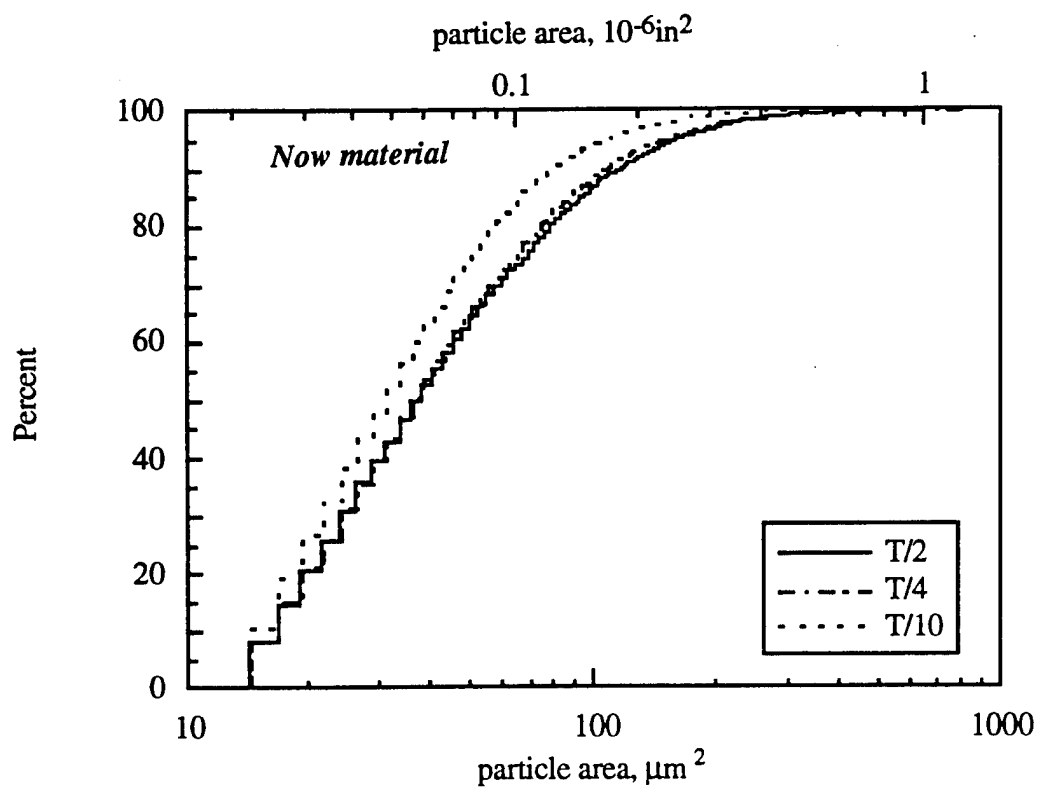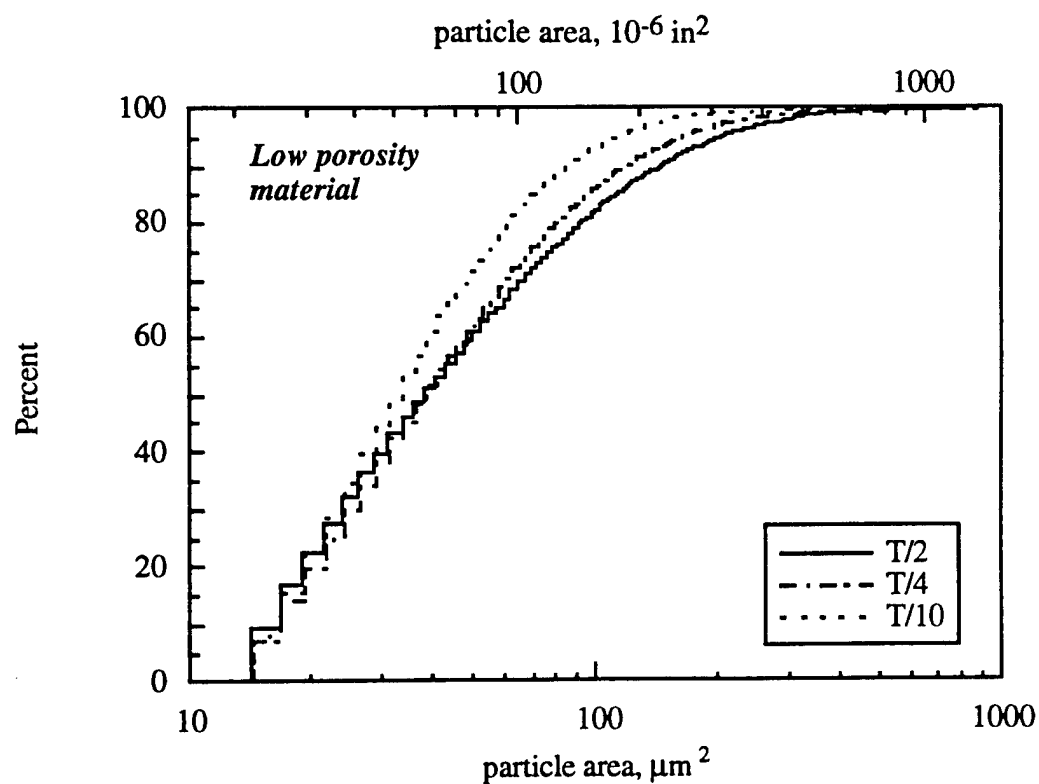
Figure 2.28. Cumulative probability plot of particle area distributions for (a) *now material* and (b) *low porosity material* at different plate locations.
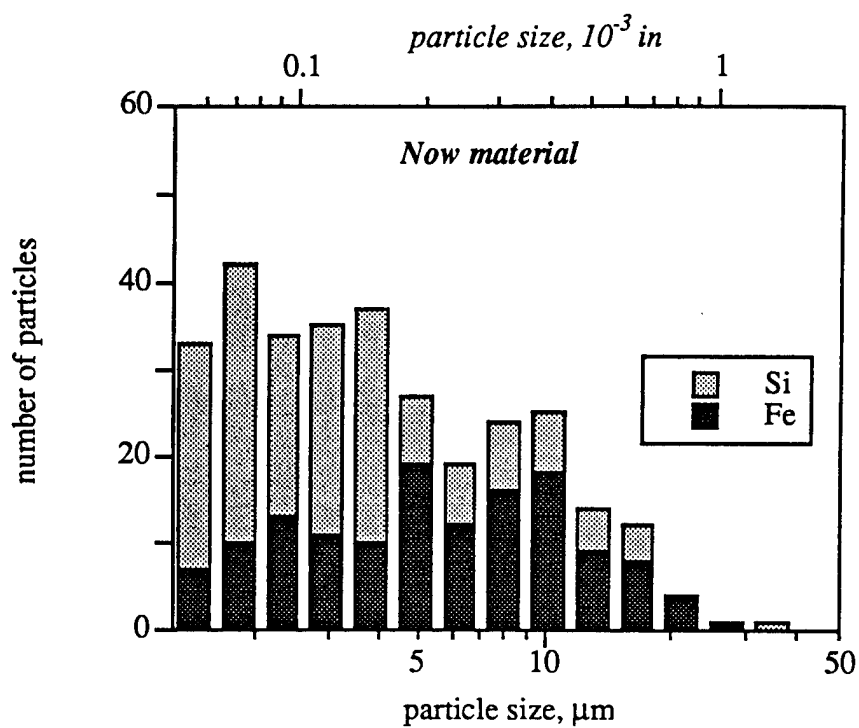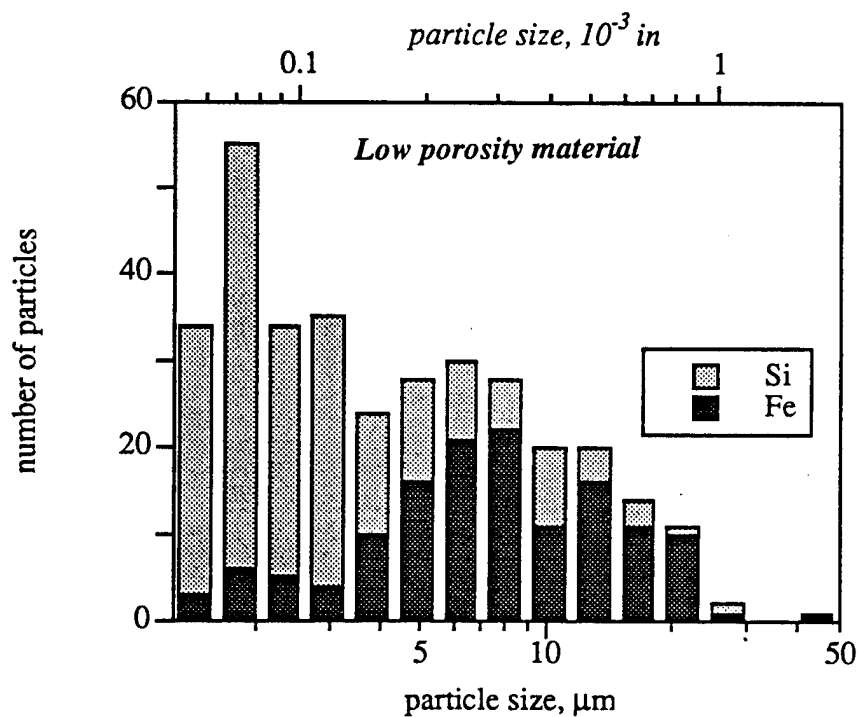
Figure 2.29. Particle size distribution histograms of Fe- and Si-containing particles for (a) *now material* and (b) *low porosity material*.
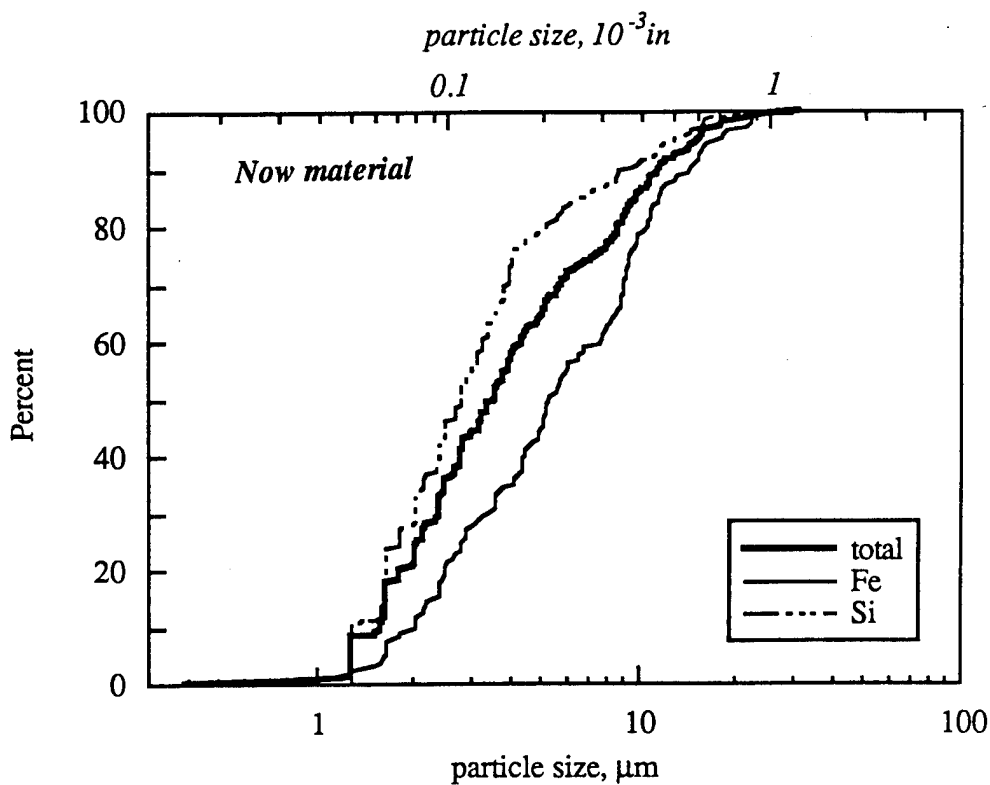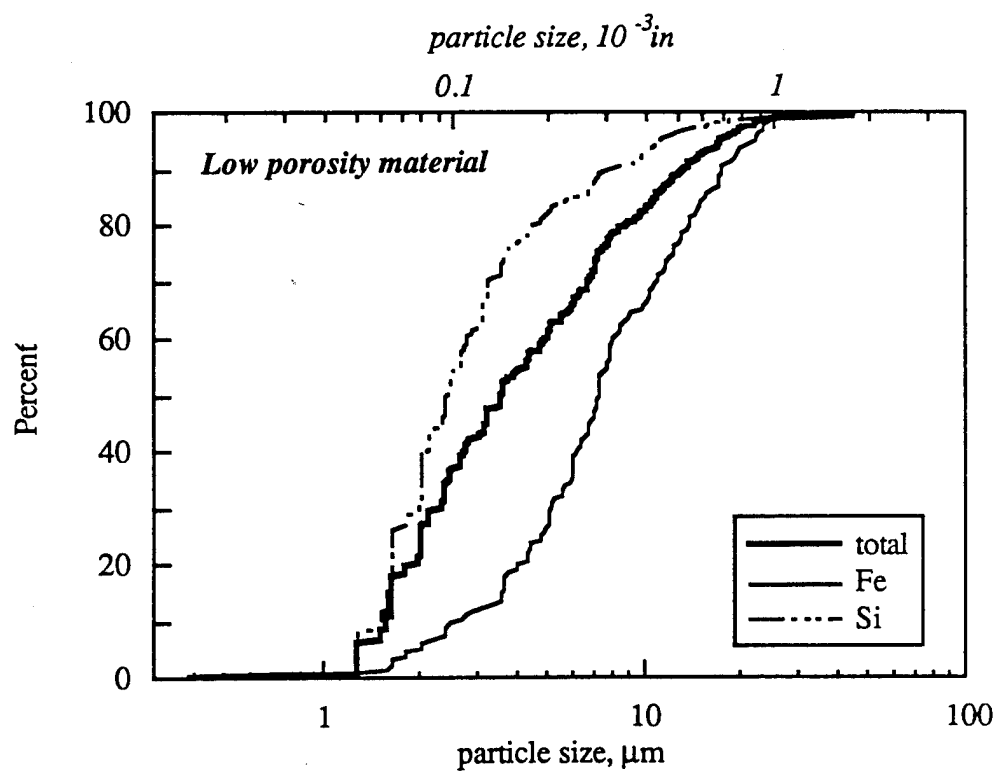
Figure 2.30. Cumulative probability plot of particle size distributions of total particles and Fe- and Si-containing particles for (a) *now material* and (b) *low porosity material*.
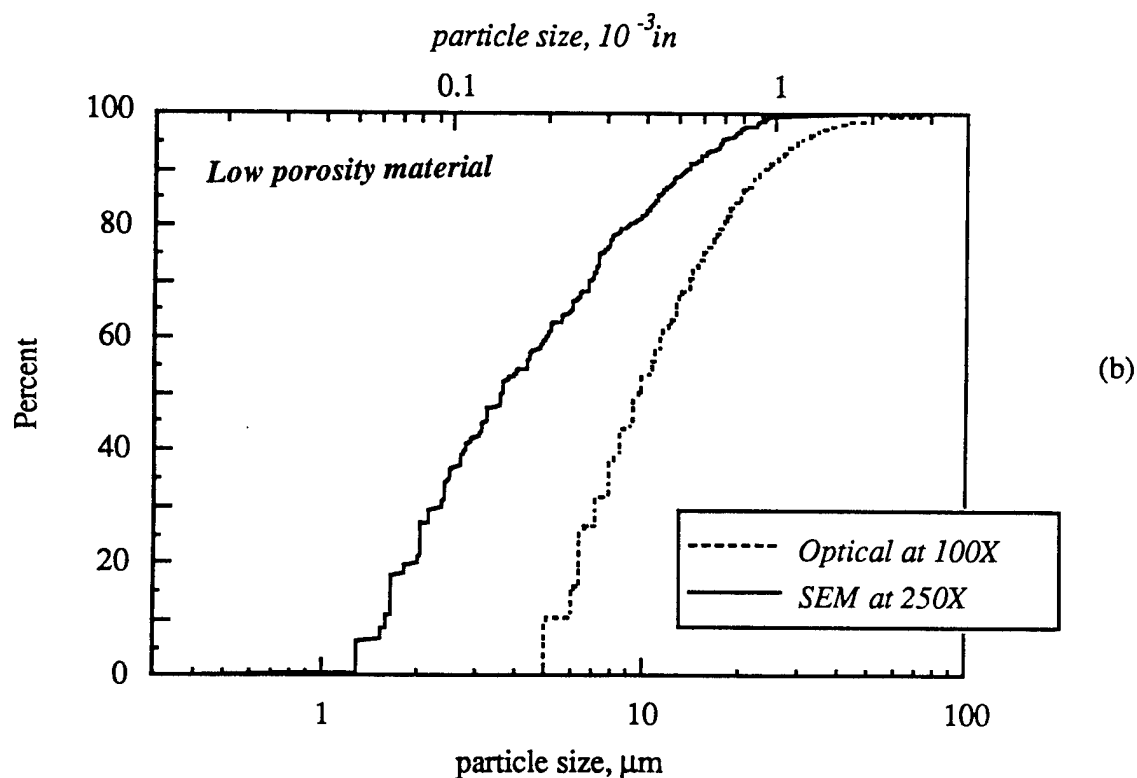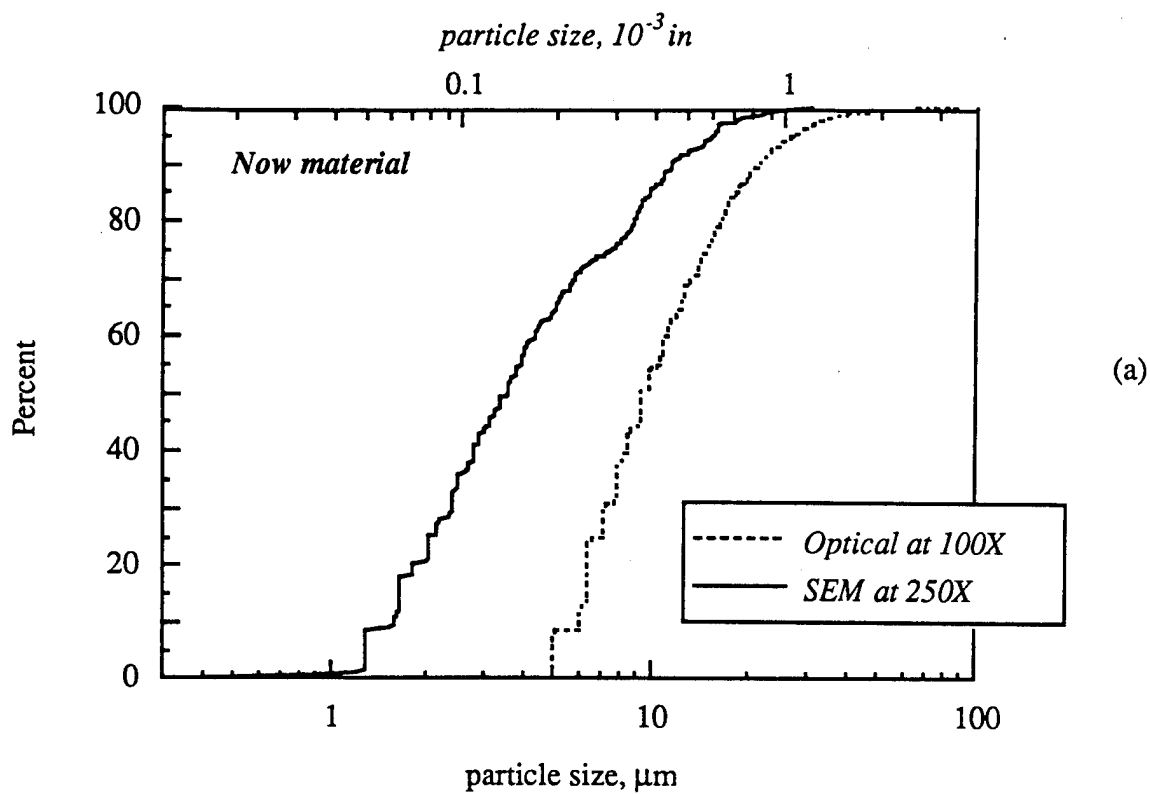
Figure 2.31. Comparison of the particle size distributions measured using optical metallography at 100X and using the SEM at 250X at the T/2 location for (a) *now material* and (b) *low porosity material*.
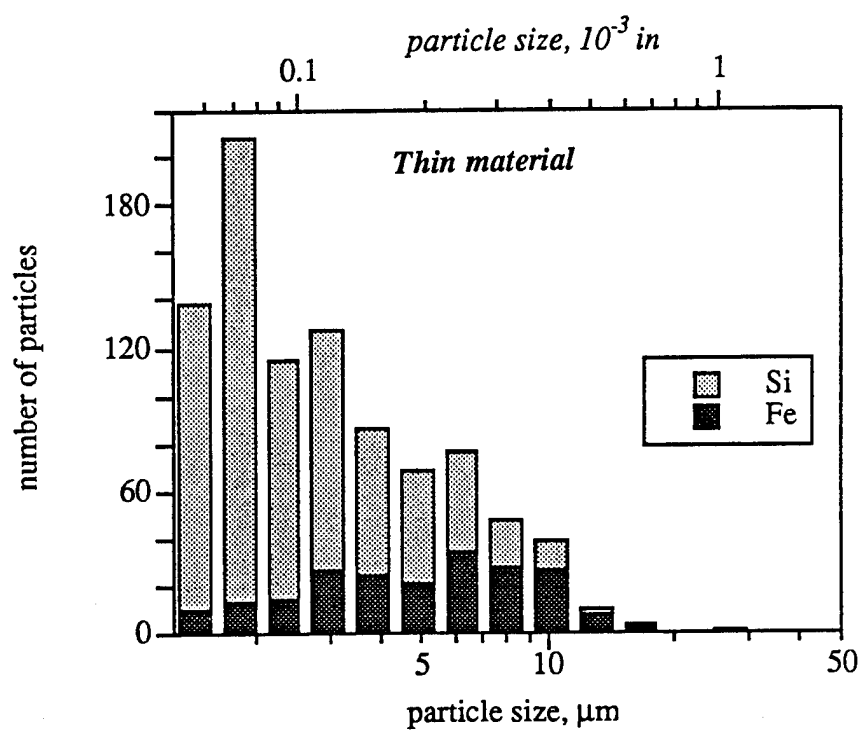
Figure 2.32. Particle size distribution histogram of Fe- and Si-containing particles for the *thin material*.
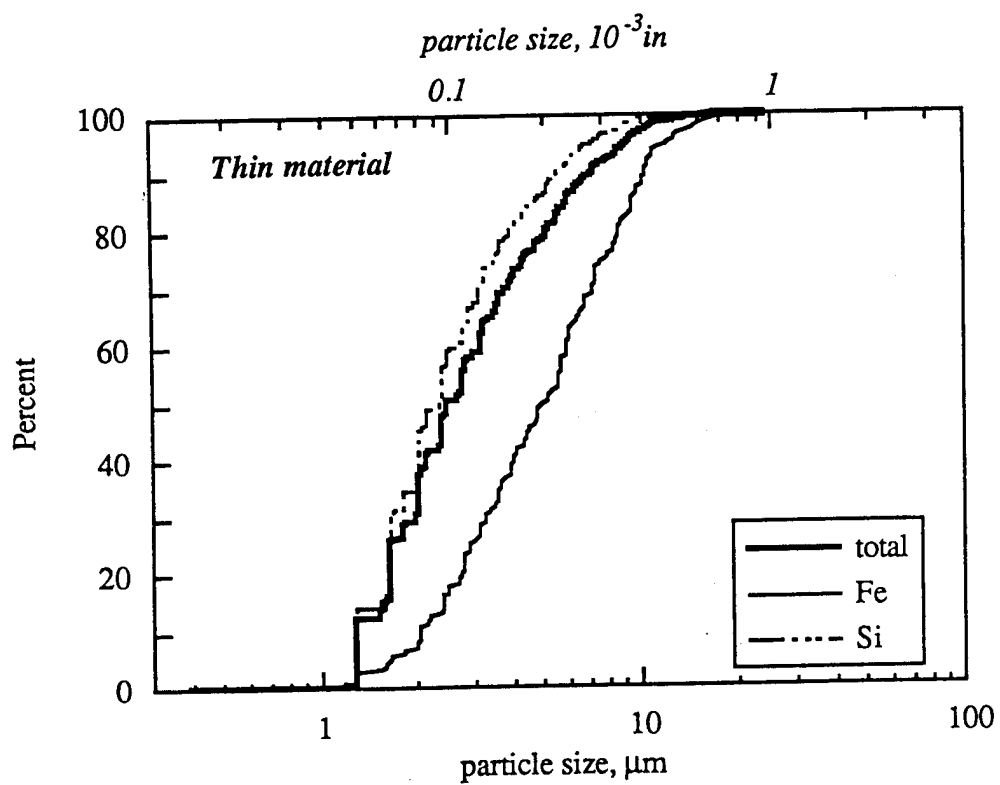
Figure 2.33. Cumulative probability plot of particle size distributions of total particles and Fe- and Si-containing particles for the *thin material*.

120
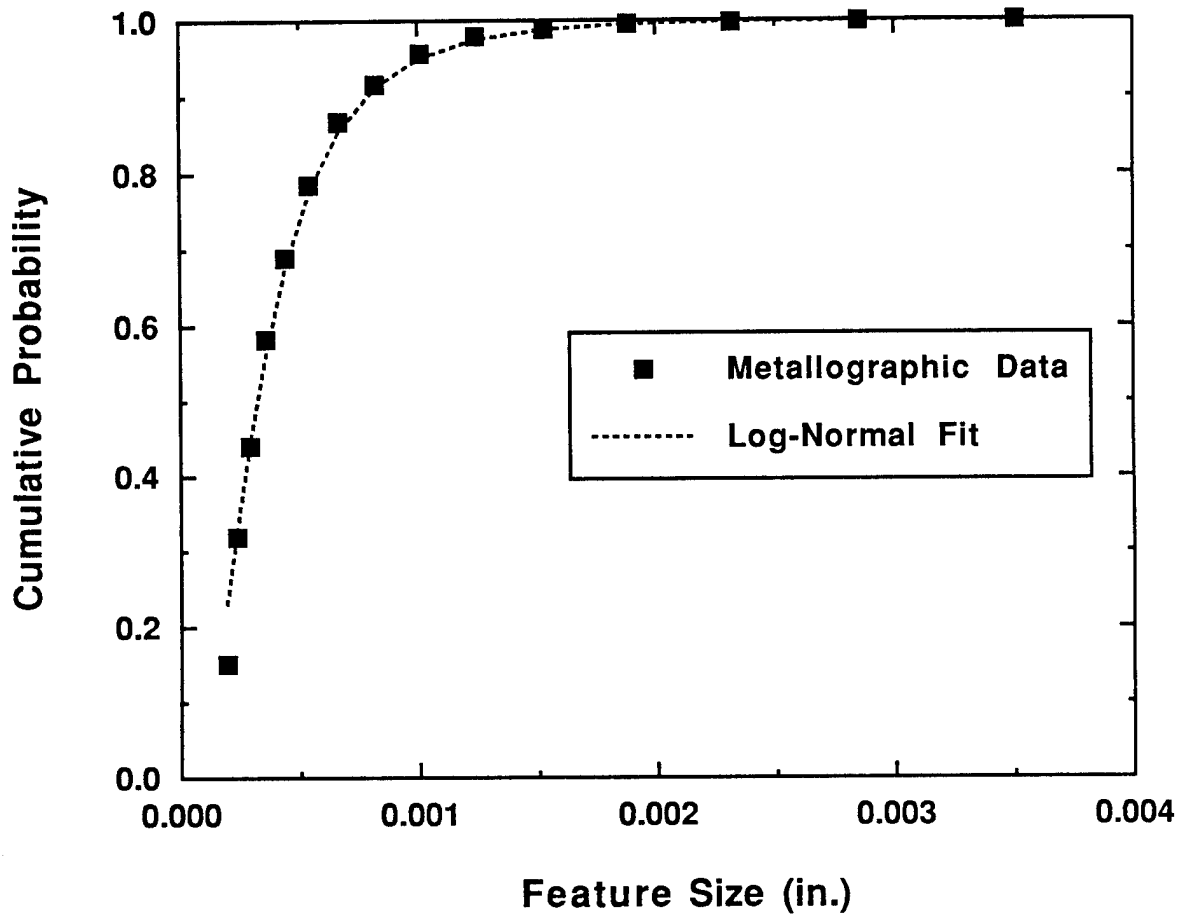
Figure 2.34. Comparison between the measured particle size distribution from quantitative optical metallography and the log-normal fit to the data for the *low porosity material*.
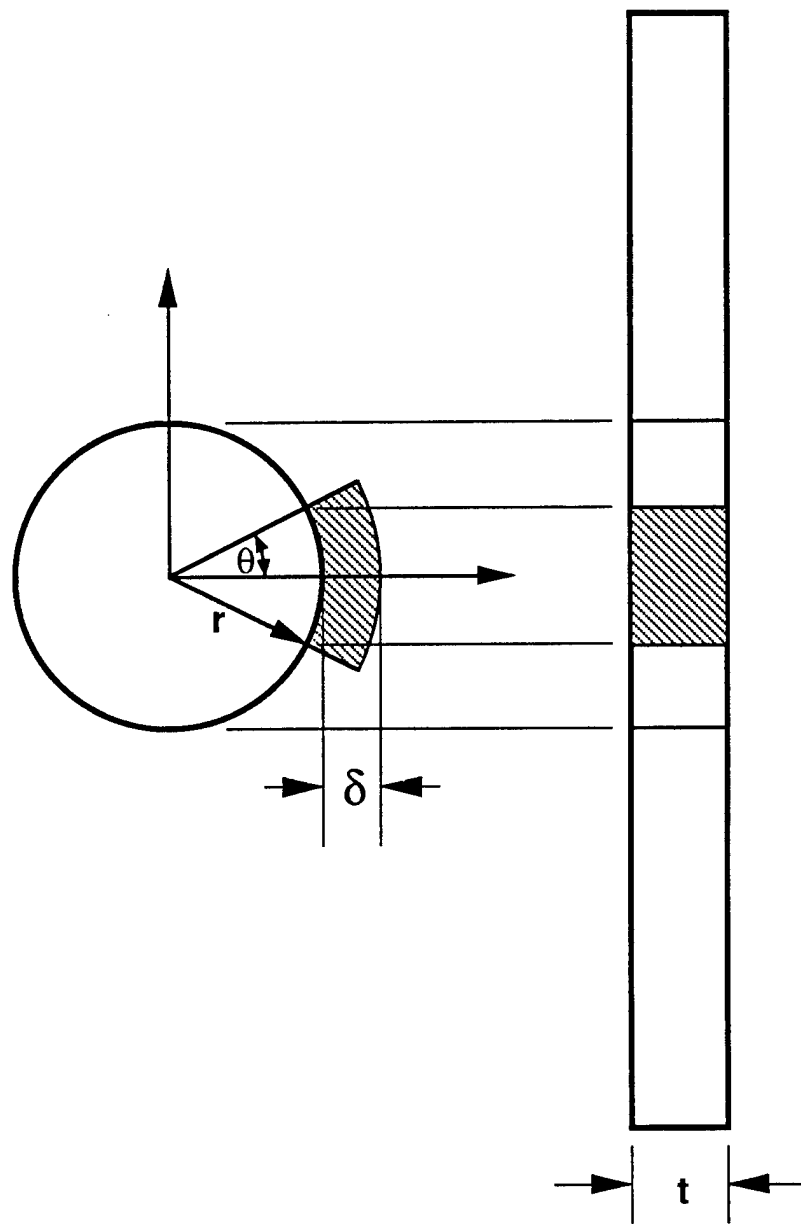
Figure 2.35. Definition of the high stress area due to the stress gradient on one side of a hole in an open hole fatigue specimen. The shaded region represents the high stress area.
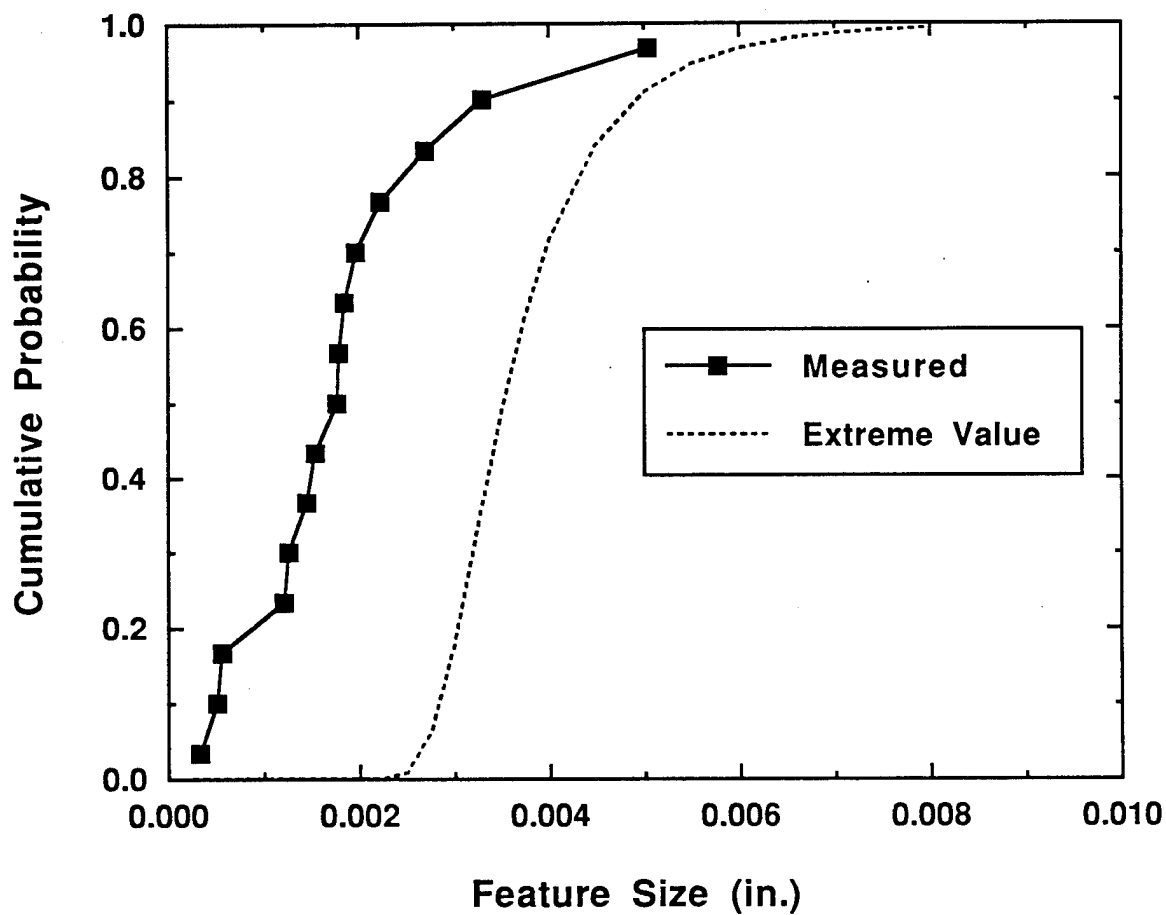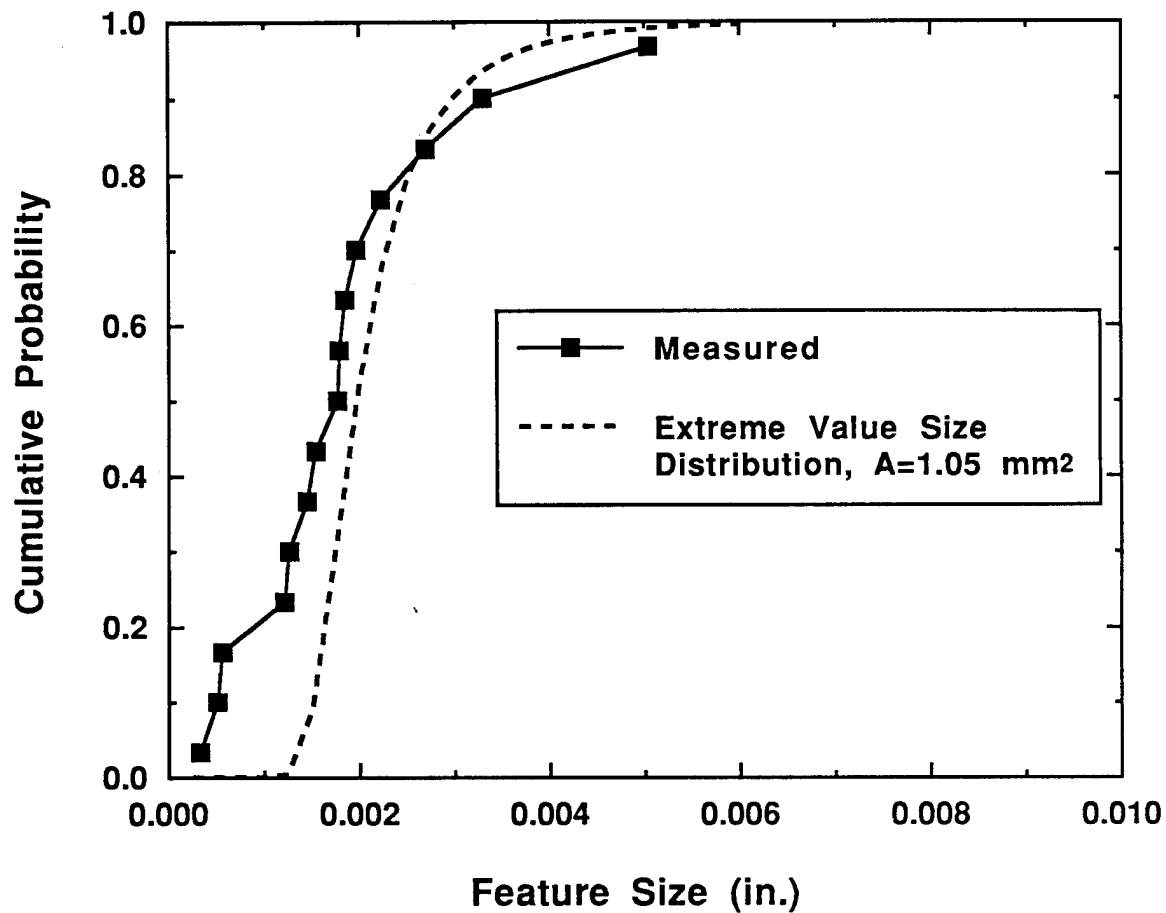
Figure 2.36. Comparison between the measured crack-initiating particle size distribution from fractography to the calculated extreme value distribution for the *low porosity material*.
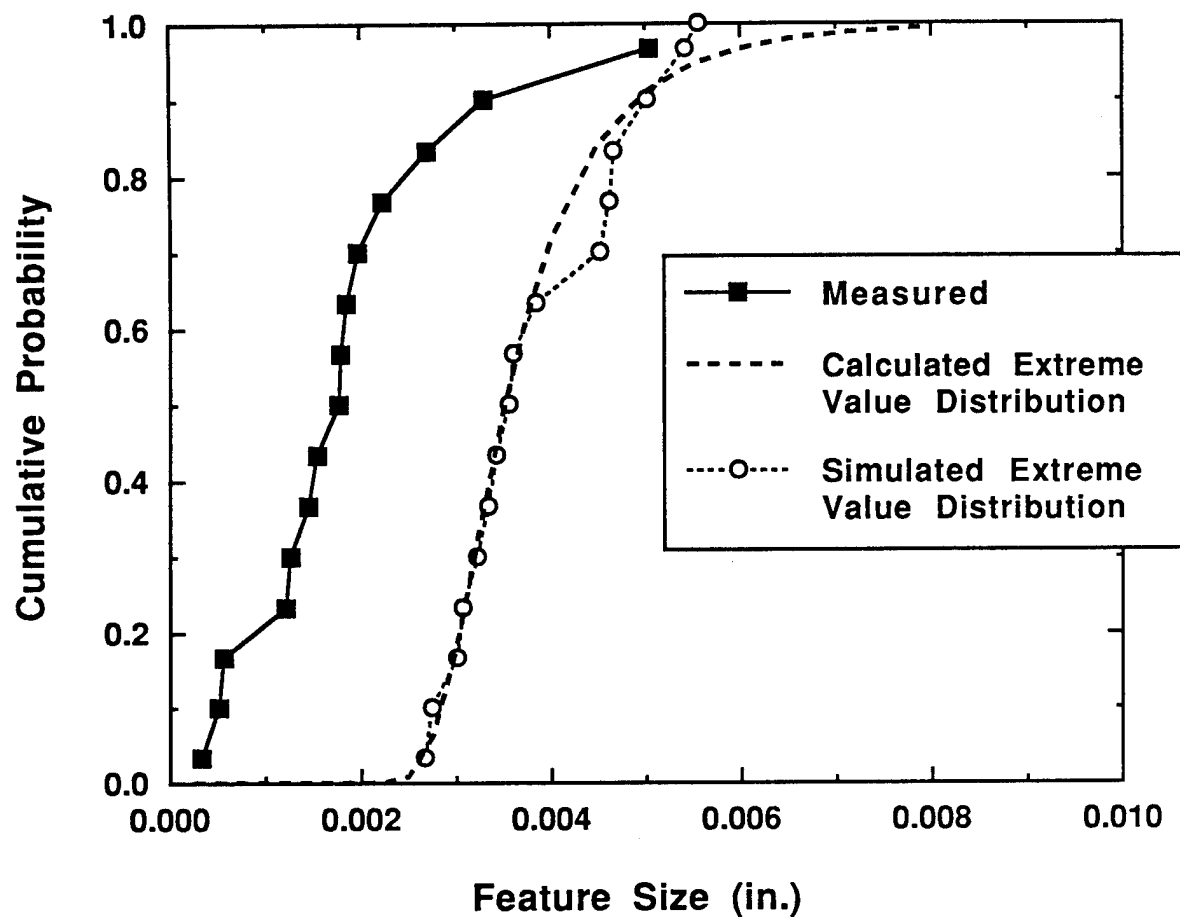
Figure 2.37. Comparison between the measured crack-initiating particle size distribution from fractography, the extreme value distribution from the simulation and the calculated extreme value distribution for the *low porosity material*.

Figure 2.38. Comparison between the measured crack-initiating particle size distribution from fractography and the calculated extreme value distribution based on a high stress area of 1.05 mm2 for the *low porosity material*.
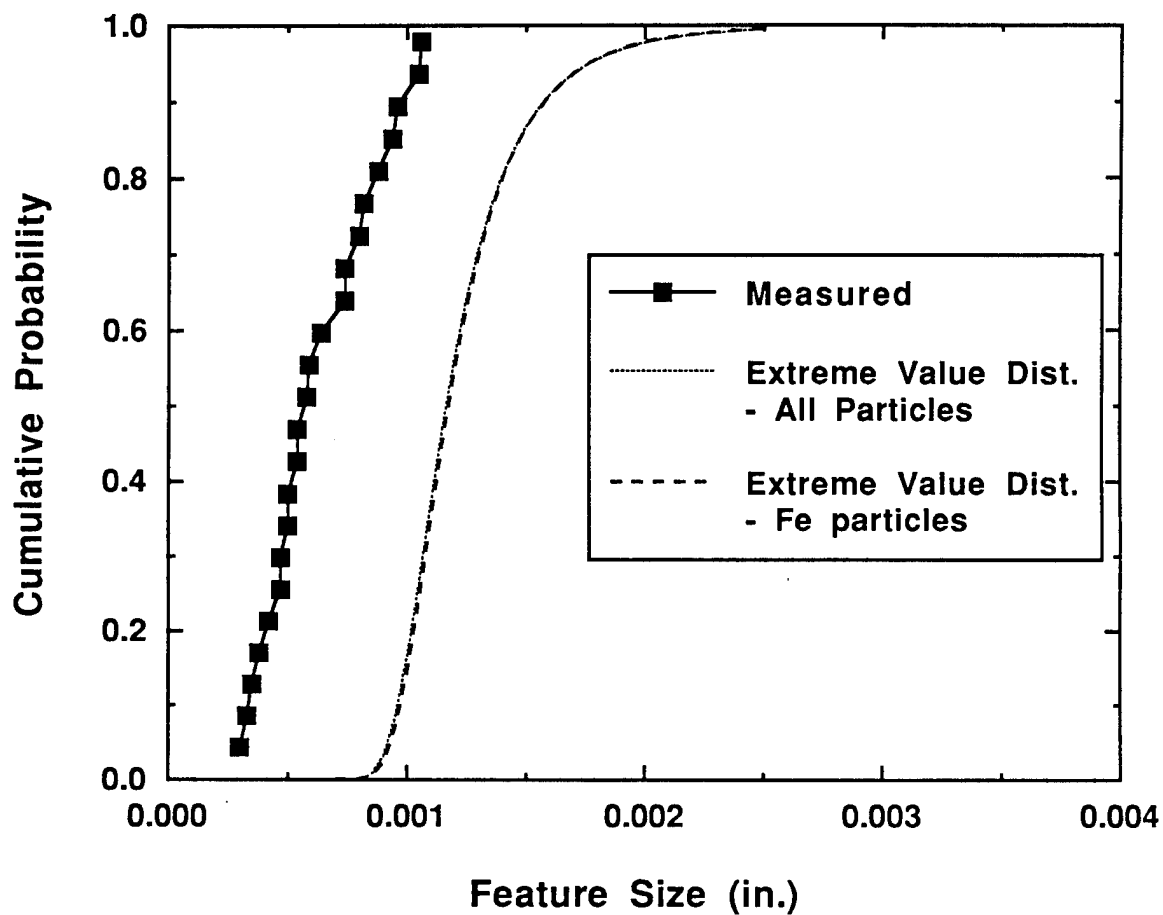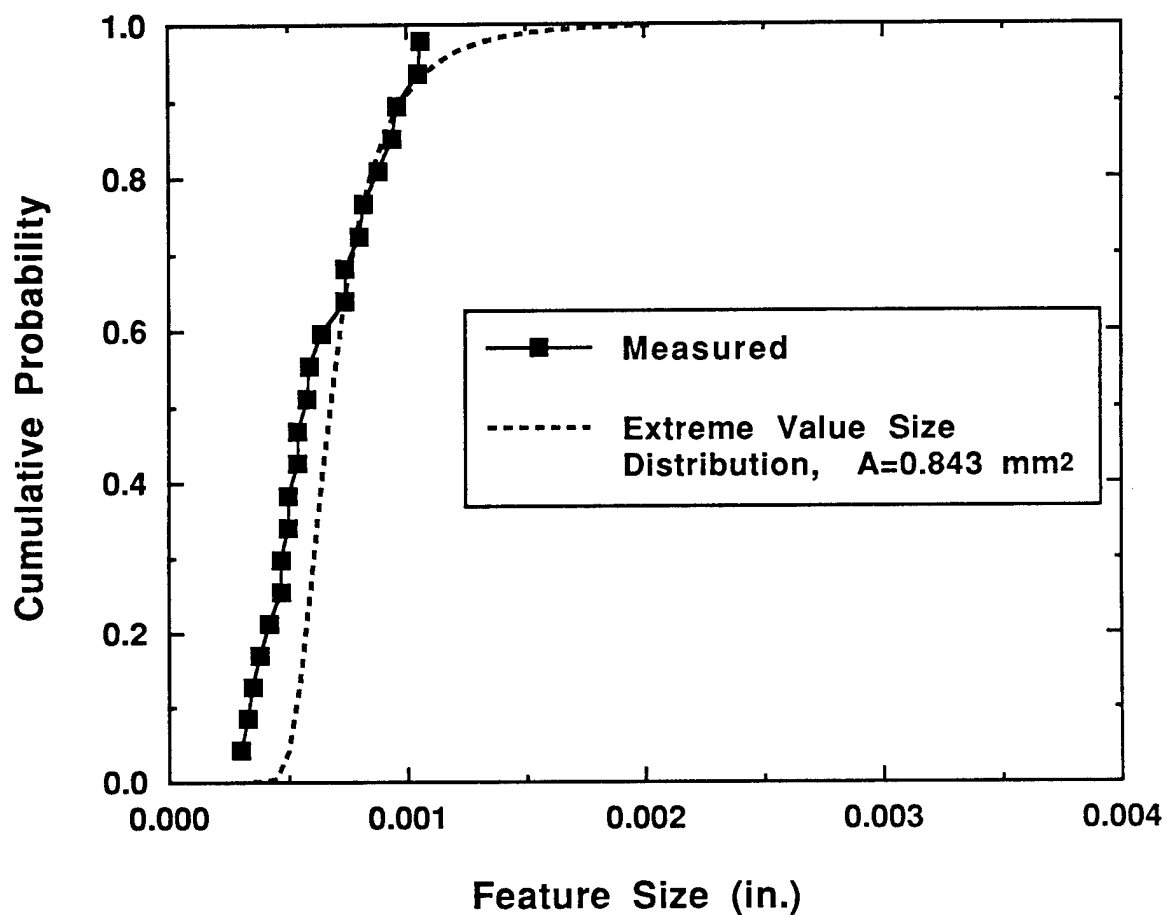
Figure 2.39. Comparison between the measured crack-initiating particle size distribution from fractography and the calculated extreme value distributions based on the total particle distribution aodnthe Fe-containing particle distribution of the *thin material*.

Figure 2.40. Comparison between the measured crack-initiating particle size distribution from fractography and the calculated extreme value distribution based on a high stress area of 0.843 mm2 for the *thin material*.
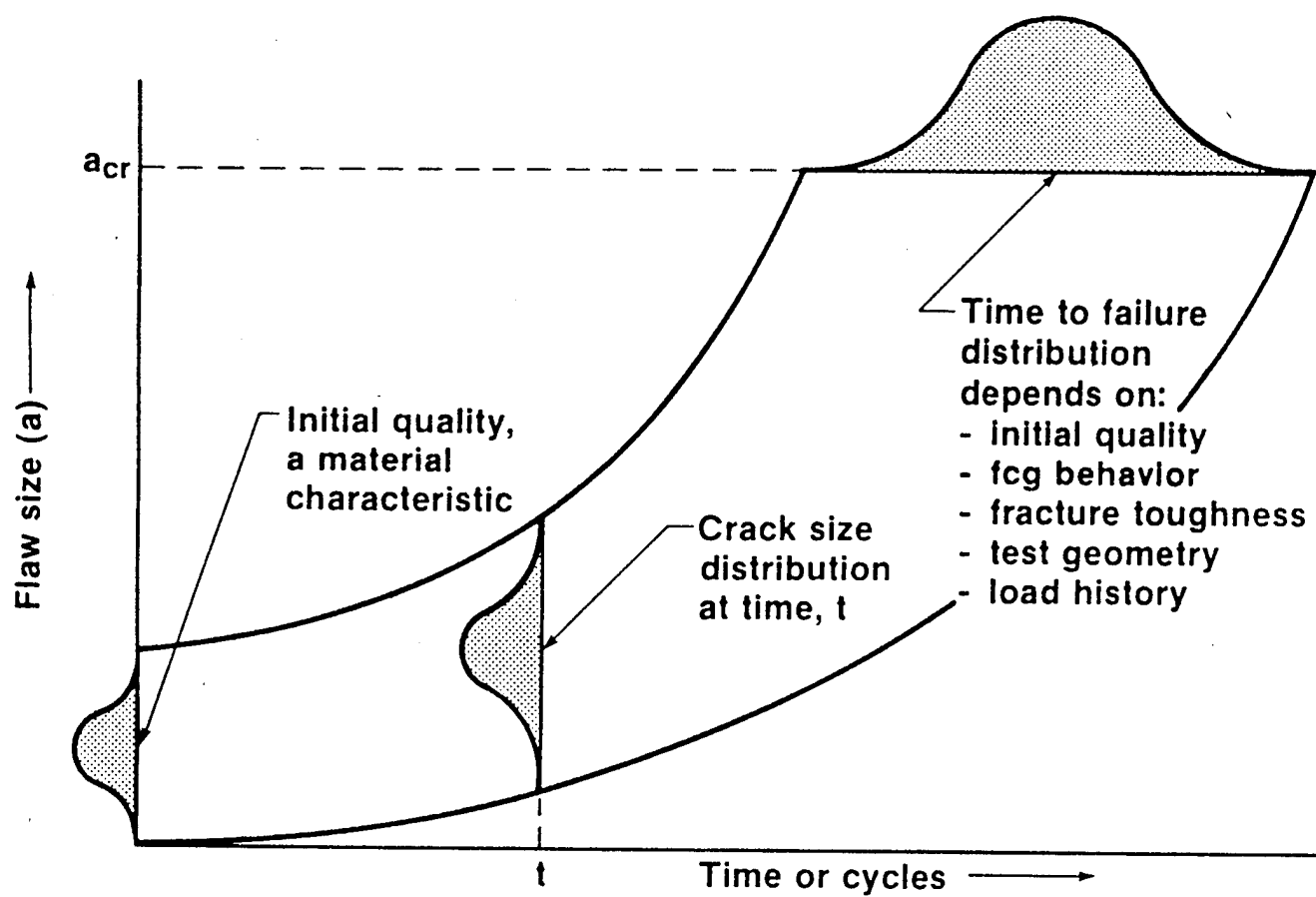
Figure 3.1. Schematic illustration showing the EIFS as an inherent material characteristic and the variation in the flaw size population with time.
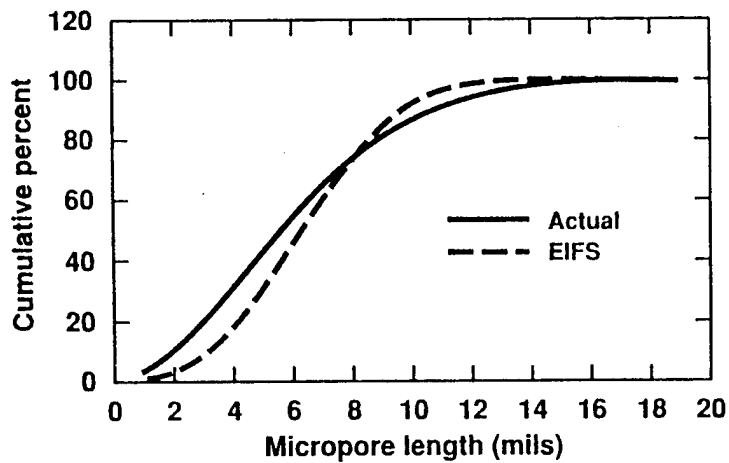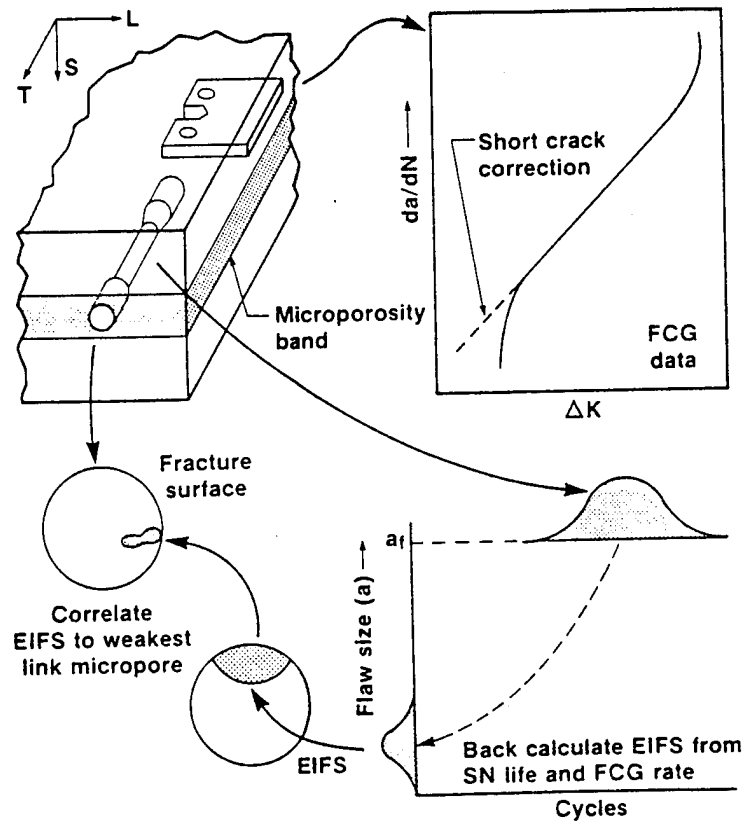
Figure 3.2. Analysis path employed to back-calculate the EIFS from material performance data and comparison of the back-calculated EIFS with the actual crack-initiating feature distribution.
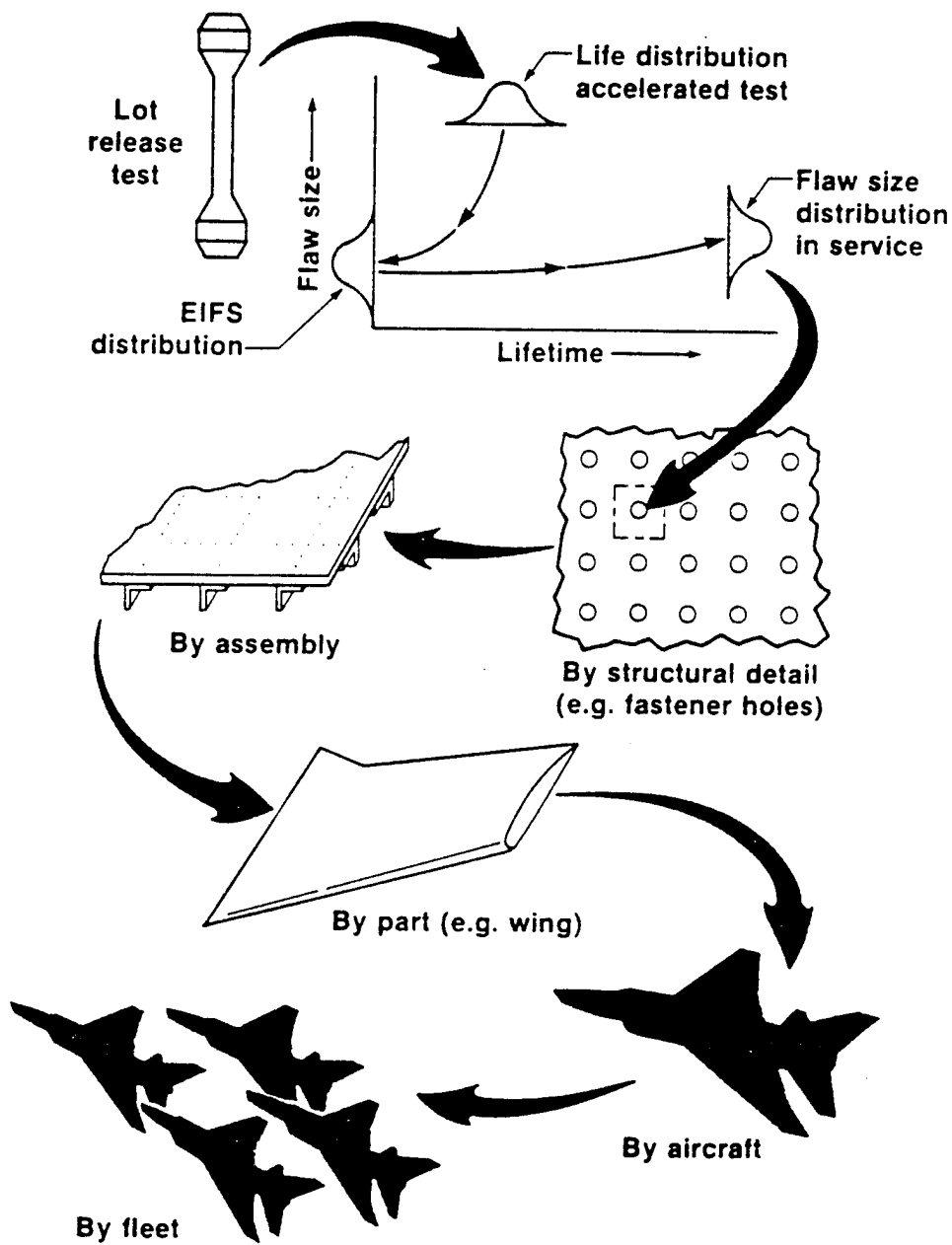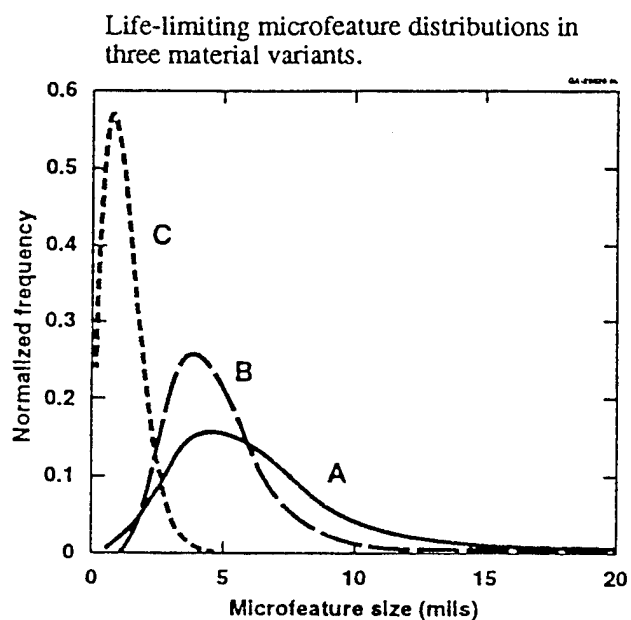
Figure 3.3. Conceptual model showing incorporation of initial material quality into life analysis from coupon to component, to aircraft, to entire fleet.

Life-limiting microfeature distributions in
three material variants.

Microfeature distribution can be related to
potential for multi-site damage.

| Flaw | Calculated no. flaw exceedances per 1000 fastener holes* | | | | | |
| size | one lifetime** | | | two lifetimes** | | |
(in.)	A	B	C	A	B	C
0.03	196	3	0	850	850	44
0.05	2	0	0	633	499	1
0.1	0	0	0	195	3	0
0.2	0	0	0	3	0	0

* Calculated after Manning and Yang
** Fighter lower wing spectrum

Figure 3.4. Hypothetical calculation showing the effect of three initial EIFS populations on the
potential for multi-site damage.

Fracture Surface   **Equivalent Flaw**

(a)

Crack-initiating
microstructural
feature

L_{max}

$c = L_{max}$

$2a$

$a/c = 0.8$

(b)

$2a$

c

Crack-initiating
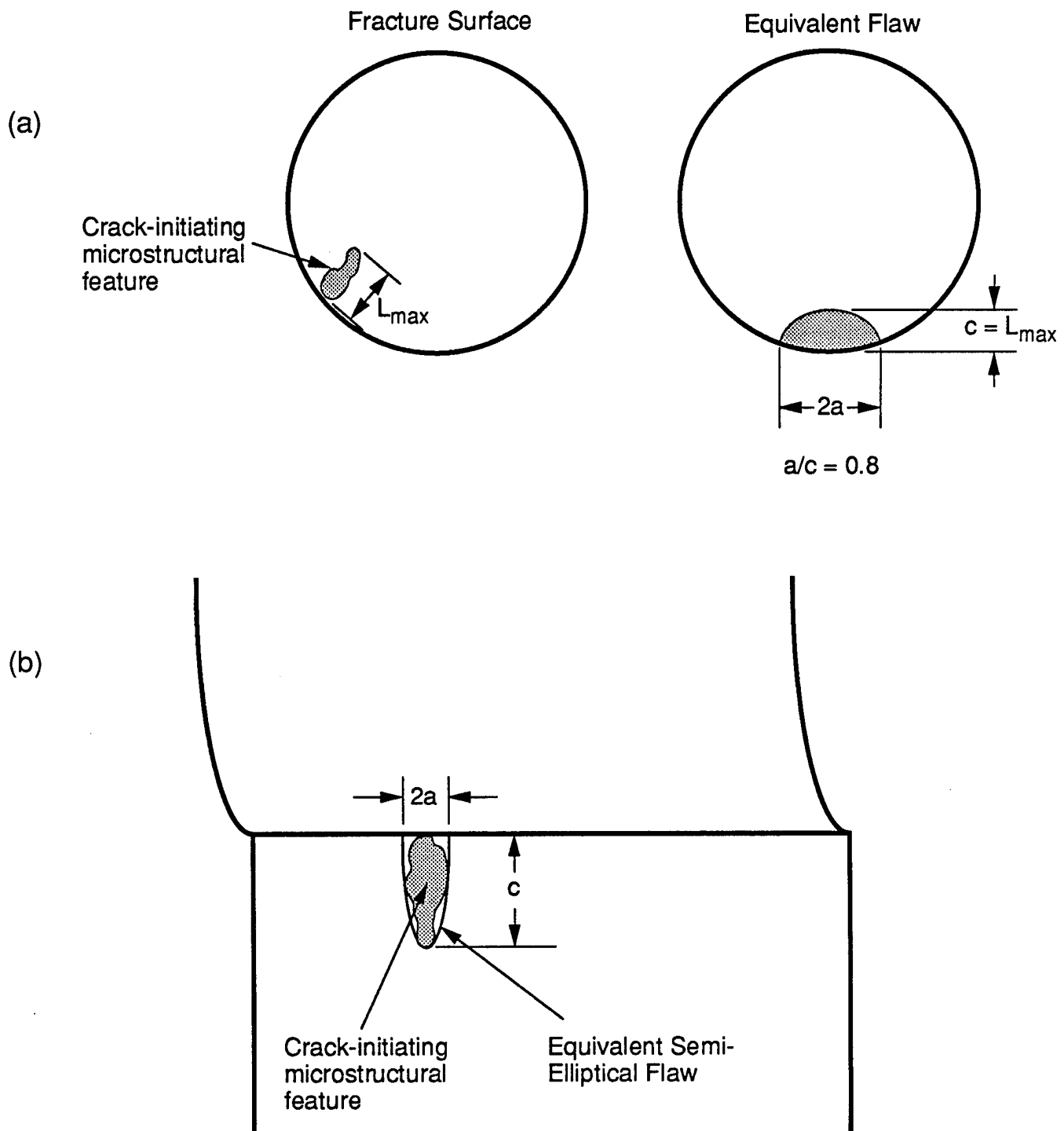microstructural
feature

Equivalent Semi-
Elliptical Flaw

Figure 3.5. Representation of a crack-initiating microstructural feature as an equivalent semi-elliptical flaw in a) a smooth fatigue specimen and b) an open hole fatigue specimen.
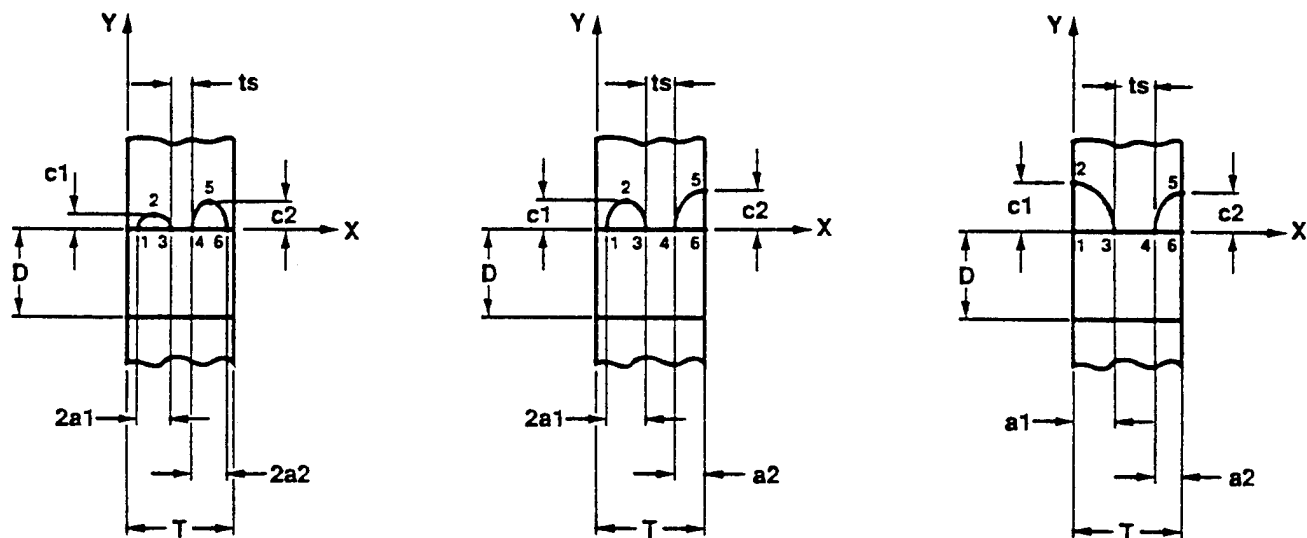
132

Figure 3.6. Schematic representation of cracks located along bore of a hole, a) two surface cracks, b) surface and corner crack, and c) two corner cracks.
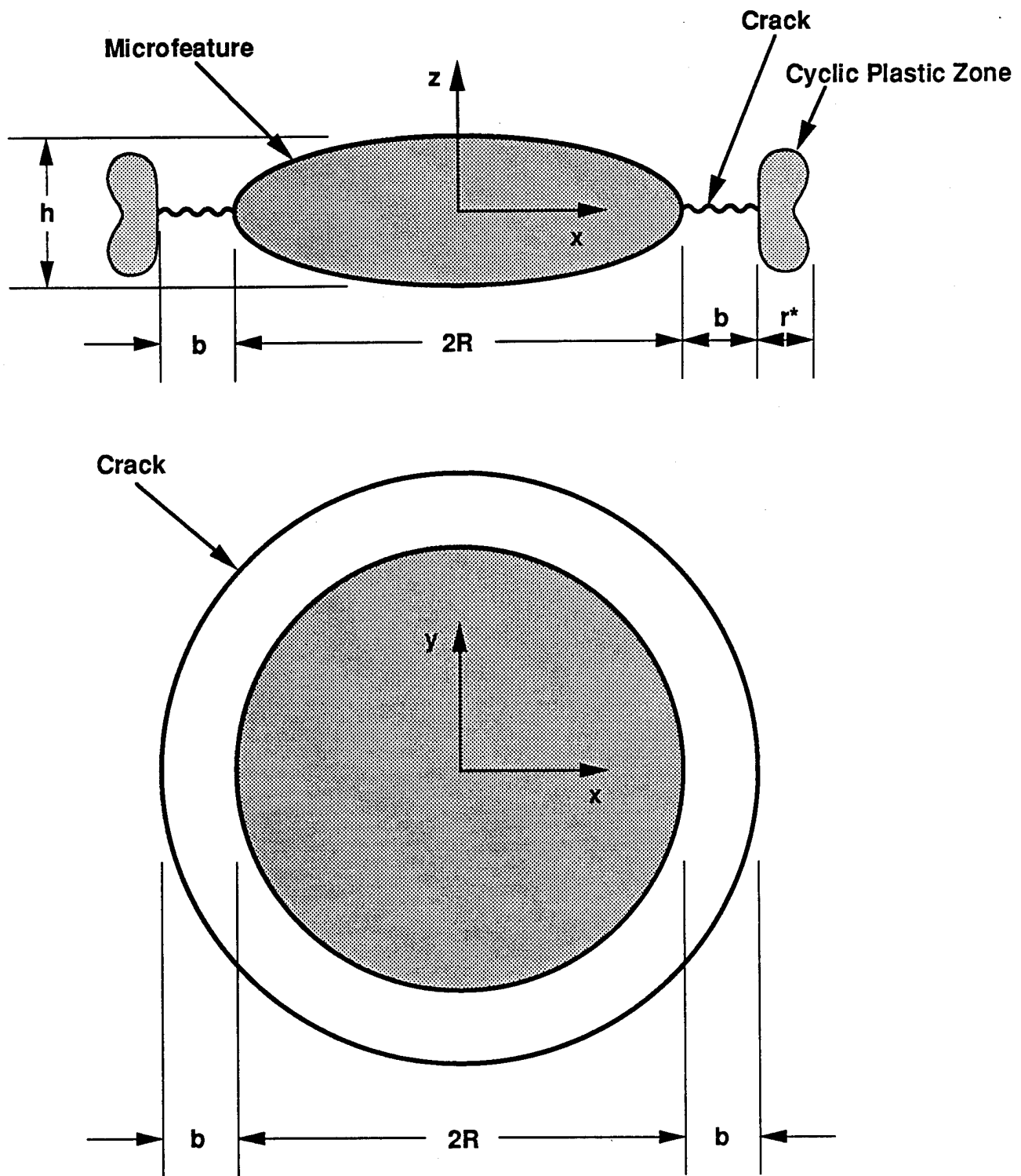
133

Figure 3.7. Model for an ellipsoidal microfeature which contains an equatorial crack .

GA-22677.1

ΔK (MPa $\sqrt{m}$)

Product thickness		Number
(in.)	(mm)	of tests
◯ 2.250	57.15	1
☐ 3.750	95.25	1
△ 4.625	117.48	2
◇ 5.670	144.02	1
▽ 5.900	149.86	1

$$\frac{da}{dN} = 3.9 \times 10^{-10} \Delta K^{4.175}$$

$\Delta a / \Delta N$ (in./cycle)

$\Delta a / \Delta N$ (m/cycle)
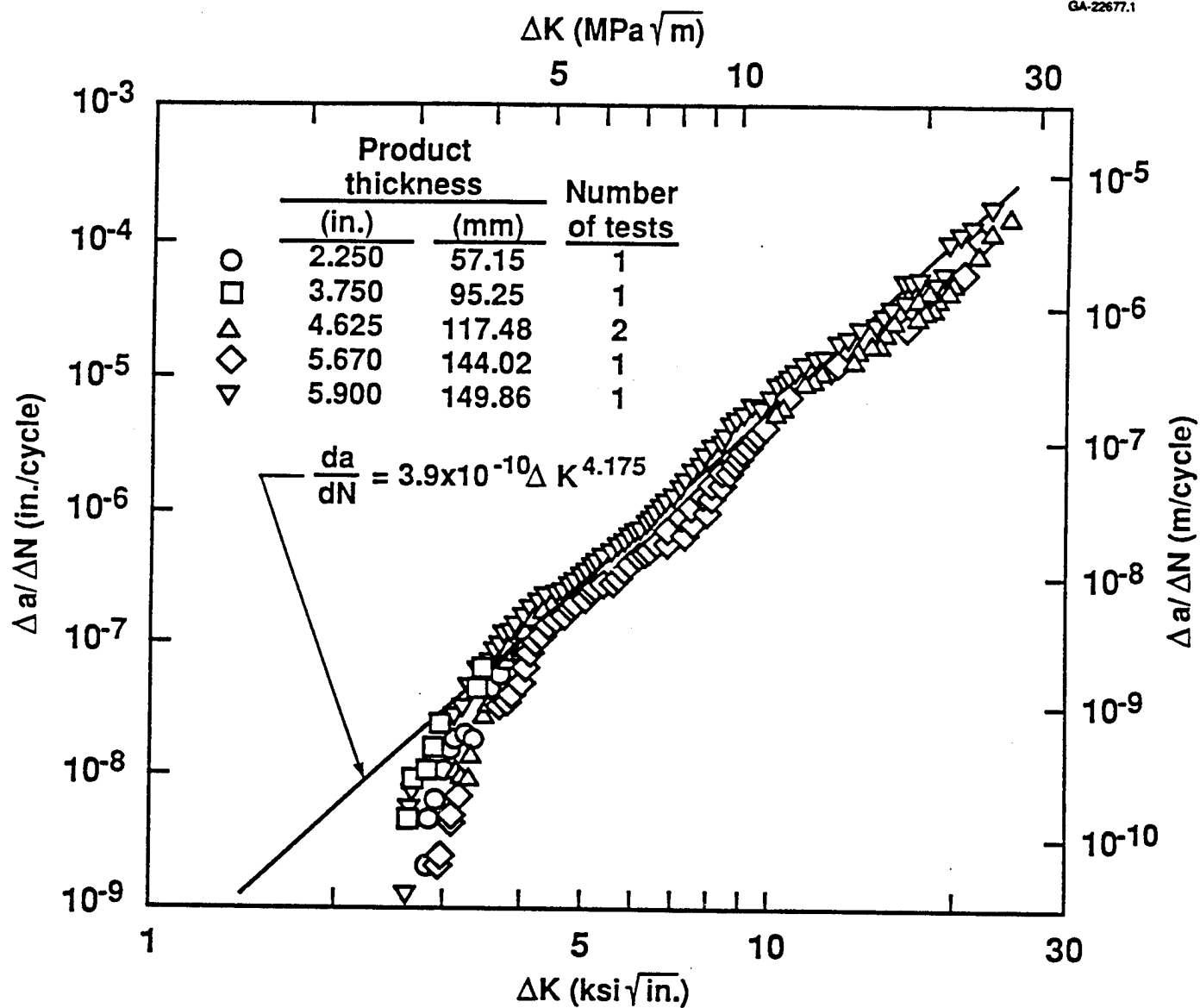
ΔK (ksi $\sqrt{in.}$)

Figure 3.8. Fatigue crack growth rate data for 7050-T7451 plate of various thicknesses. Tests conducted at R=0.1, T-L orientation, T/4 location, high humidity air.
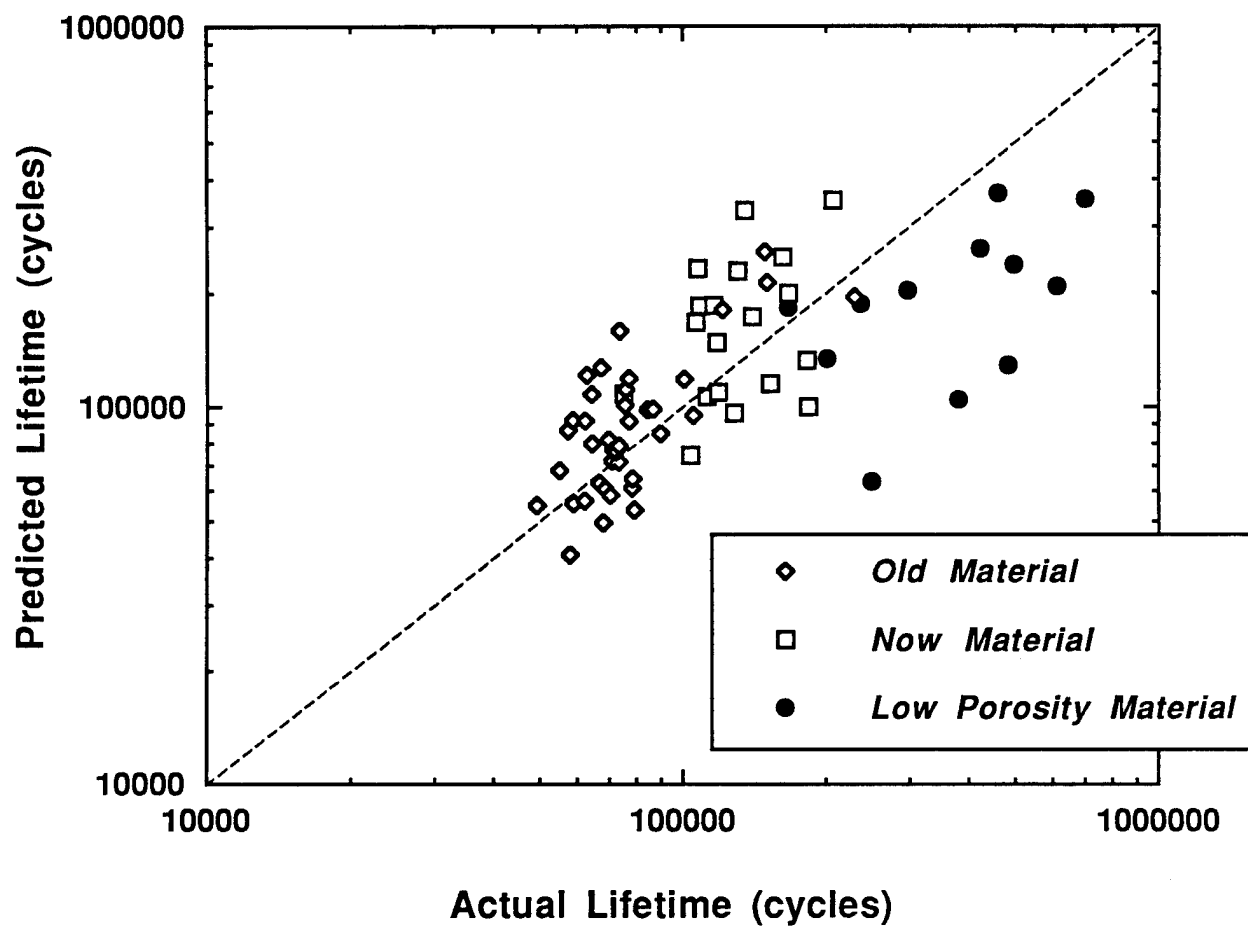
135

Figure 3.9. Plot of the predicted smooth specimen fatigue lifetime versus the actual life for the *old*, *now*, and *low porosity materials* without incorporating the Trantina-Barishpolsky analysis.
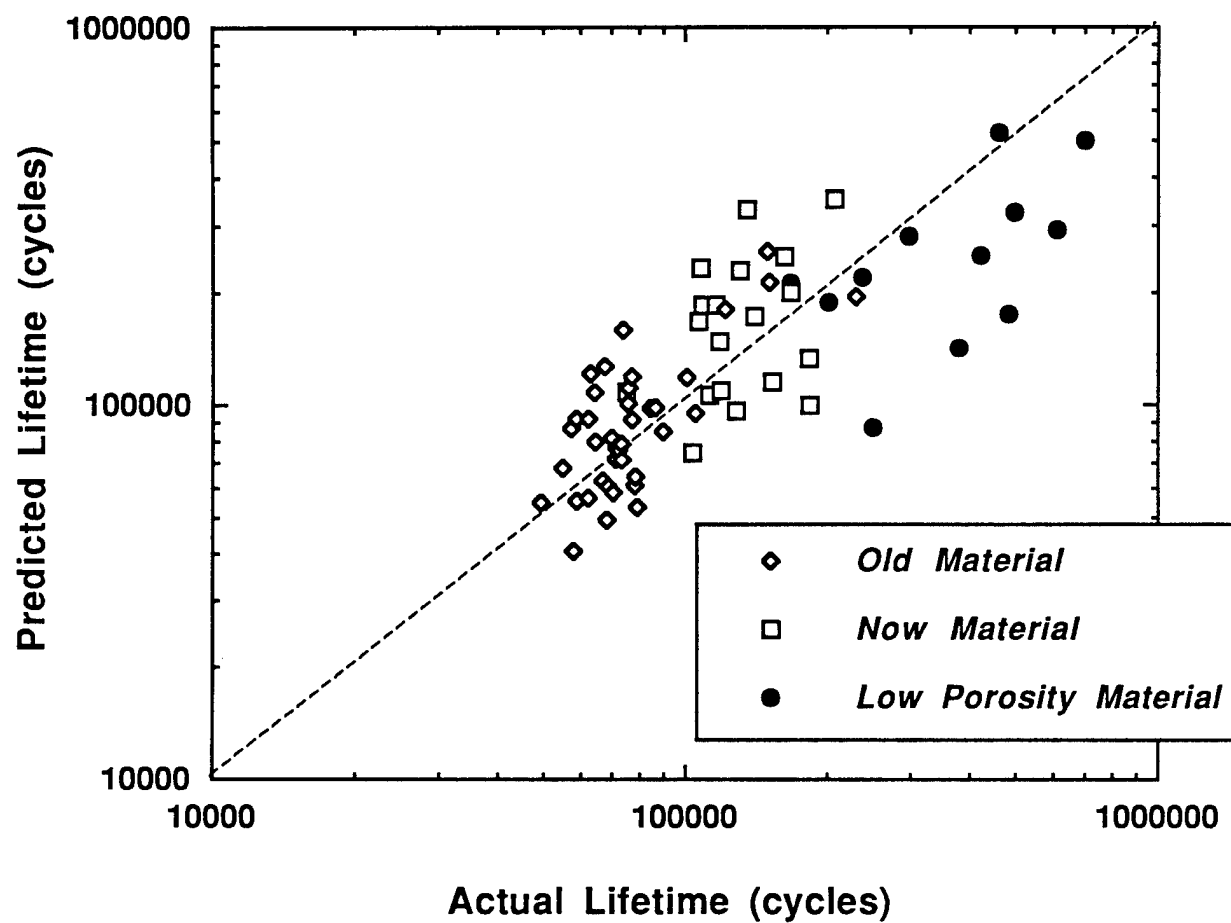
Figure 3.10. Plot of the predicted smooth specimen fatigue lifetime versus the actual life for the *old*, and *now* variants without incorporating the Trantina-Barishpolsky analysis and the *low porosity* variant using the Trantina-Barishpolsky analysis.

Figure 3.11. Comparison between the actual smooth fatigue lifetime distribution and the predicted lifetime distribution based on the input extreme value distribution parameters for the *old material*. Tests conducted at 35 ksi max. stress, R=0.1, LT orientation, T/2 location, 30 Hz. in lab air.
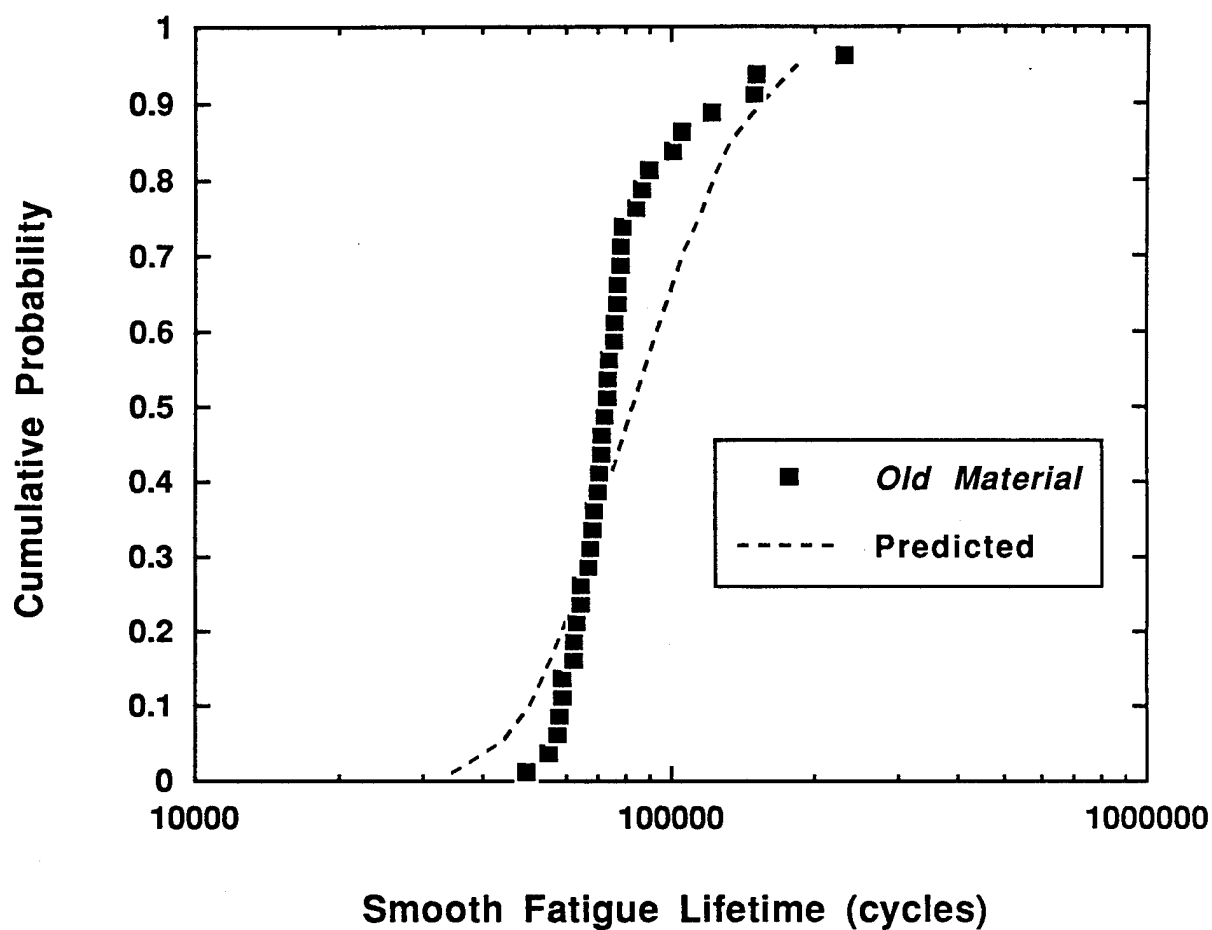
138

Figure 3.12. Comparison between the actual smooth fatigue lifetime distribution and the predicted lifetime distribution based on the input extreme value distribution parameters for the *now material*. Tests conducted at 35 ksi max. stress, R=0.1, LT orientation, T/2 location, 30 Hz. in lab air.
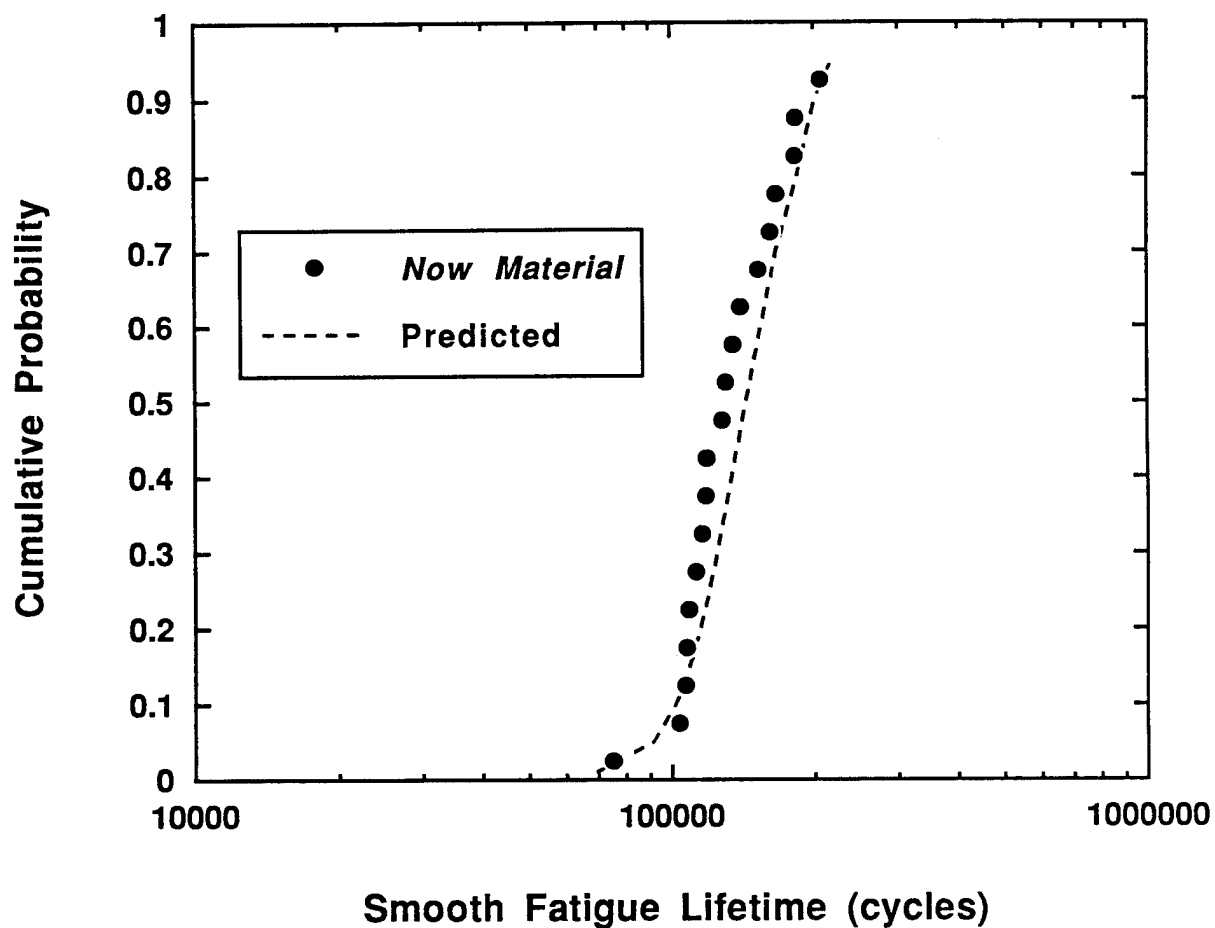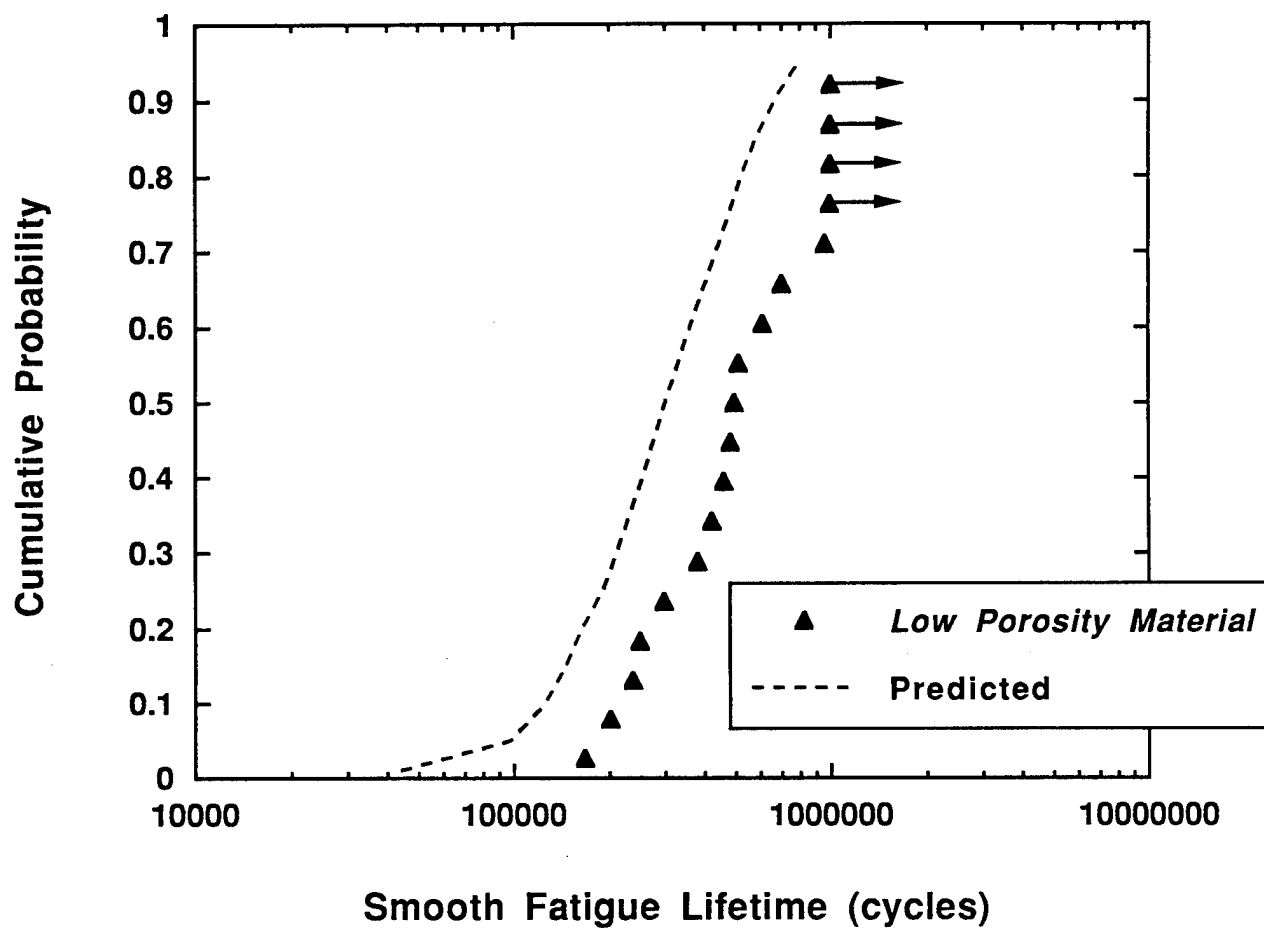
Figure 3.13. Comparison between the actual smooth fatigue lifetime distribution and the predicted lifetime distribution based on the input extreme value distribution parameters for the *low porosity material*. Tests conducted at 40 ksi max. stress, R=0.1, LT orientation, T/2 location, 30 Hz. in lab air.

Micropore

a) Interior porosity of 710 µm².
   Actual life: 80,700 cycles,
   Predicted life: 80,000 cycles.

Constituent
Particle
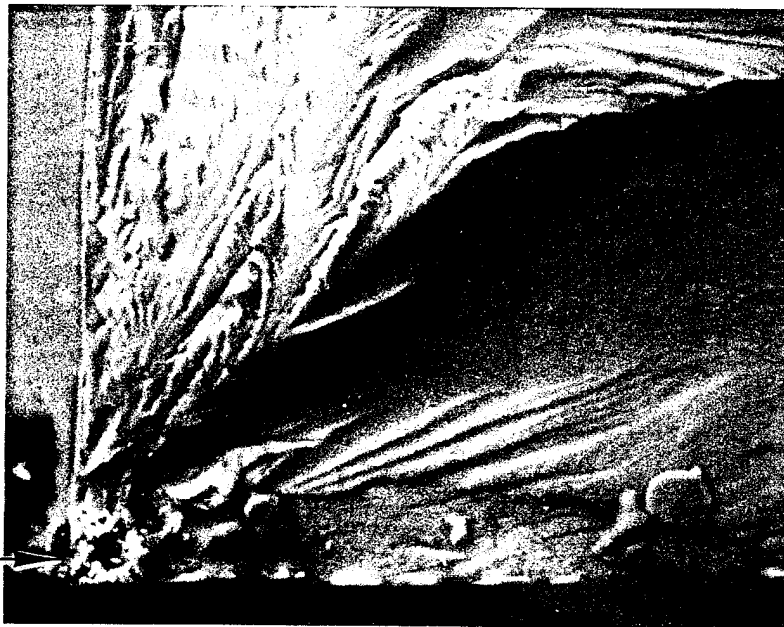
b) Corner particle of 324 µm².
   Actual life: 79,500 cycles.
   Predicted life: 74,500 cycles.

Figure 3.14. Verification of the model for predicting open hole specimen fatigue life for a) fatigue crack initiation at a pore at the center of the hole bore and b) initiation at a particle at the corner of the hole bore and specimen surface.

Figure 3.15. Comparison between the open hole fatigue life test data and the calculated S/N curve for the *old material*. The testing was done at R=0.1, LT orientation, T/2 location, 30 Hz in lab air.

142
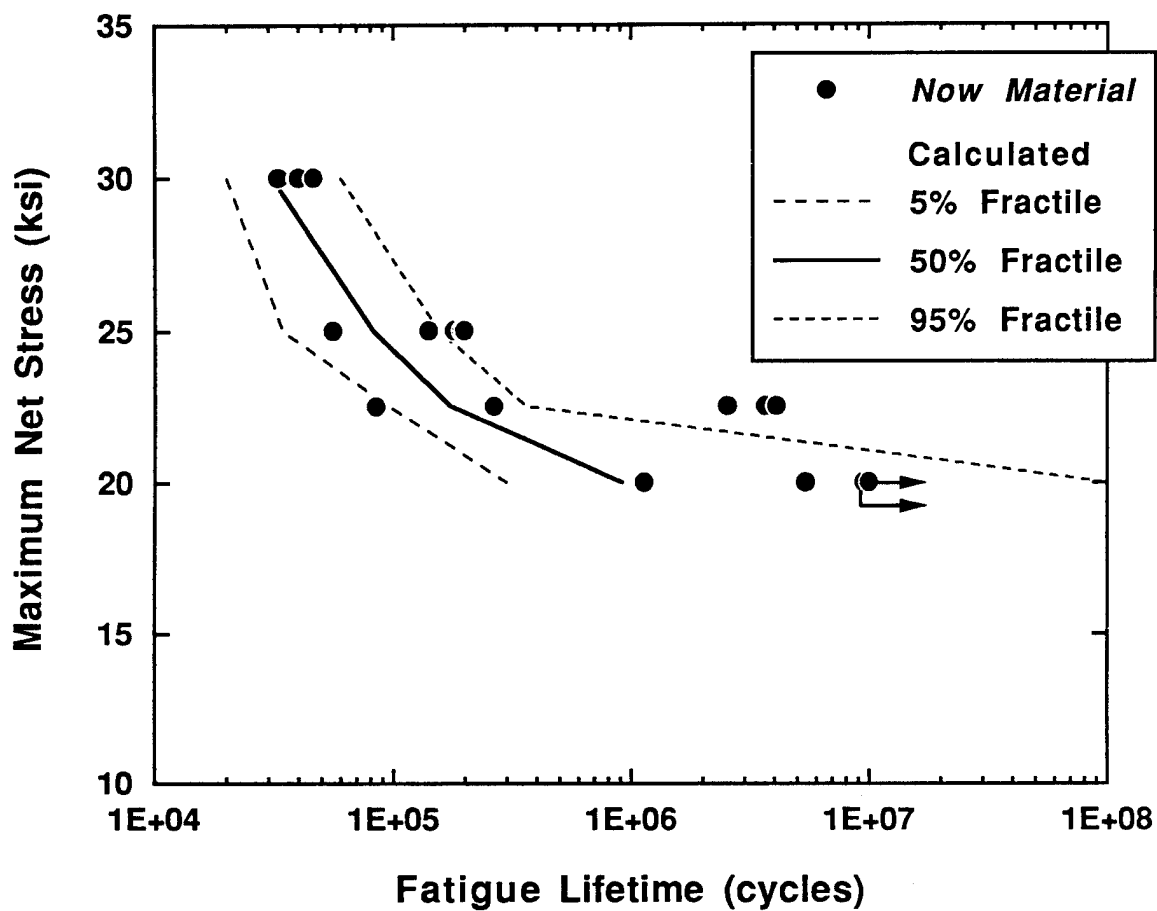
Figure 3.16. Comparison between the open hole fatigue life test data and the calculated S/N curve for the *now material*. The testing was done at R=0.1, LT orientation, T/2 location, 30 Hz in lab air.

143
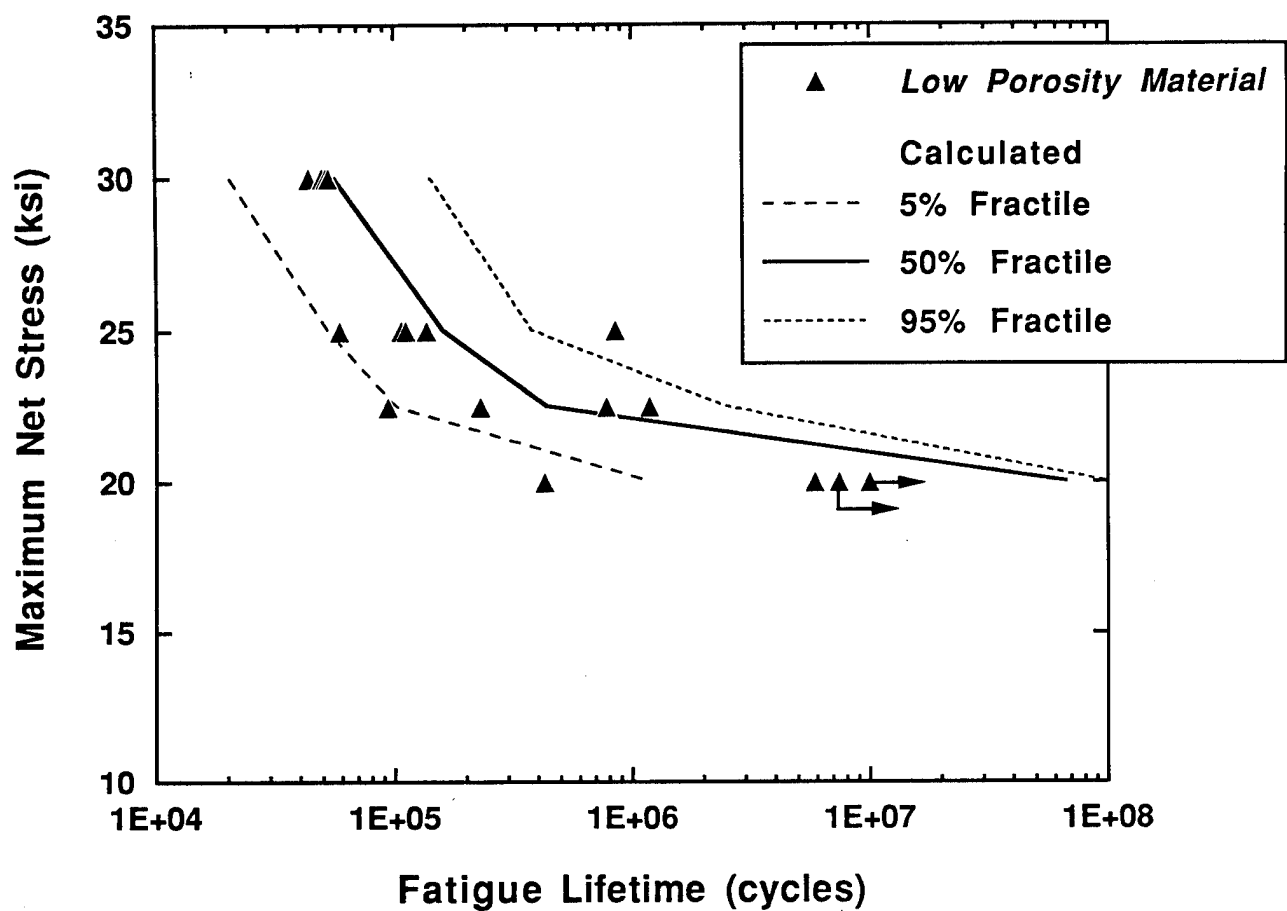
Figure 3.17. Comparison between the open hole fatigue life test data and the calculated S/N curve for the *low porosity material*. The testing was done at R=0.1, LT orientation, T/2 location, 30 Hz in lab air.
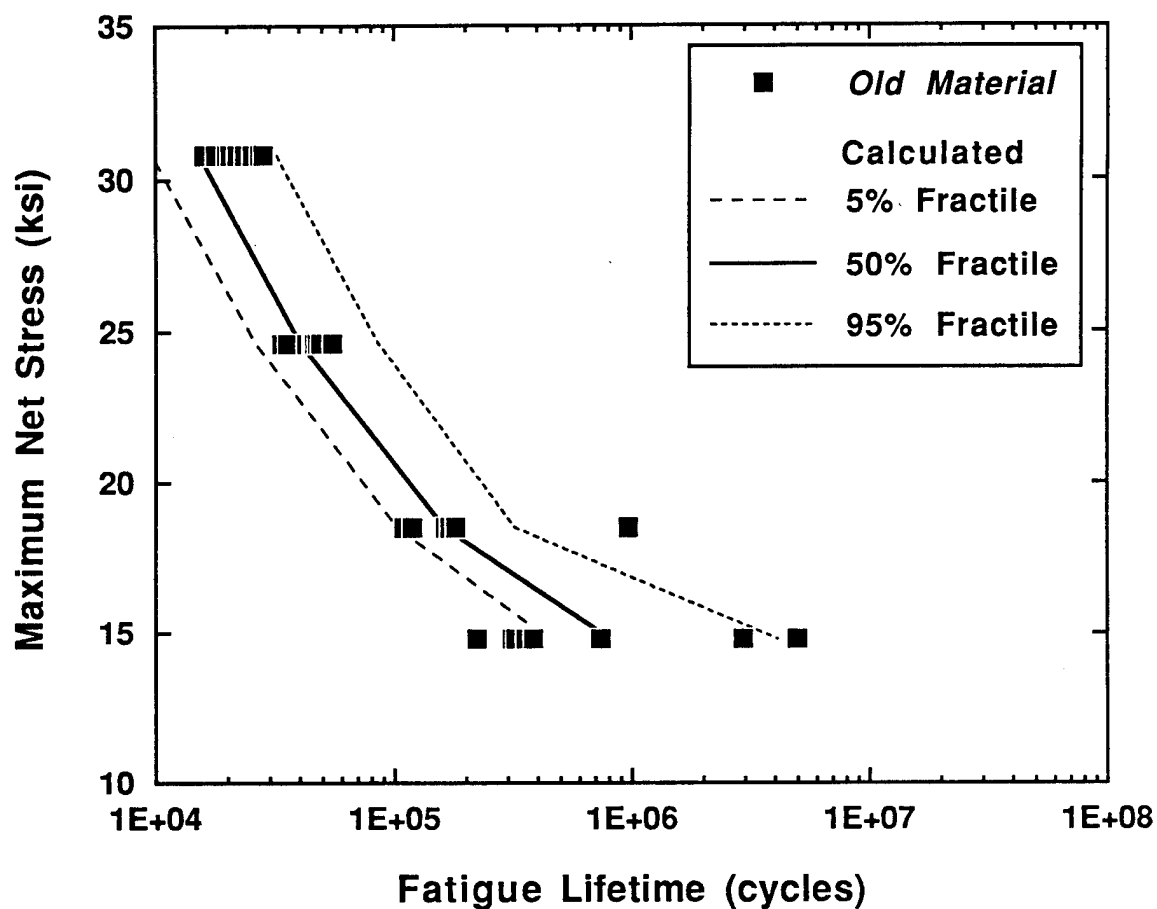
144
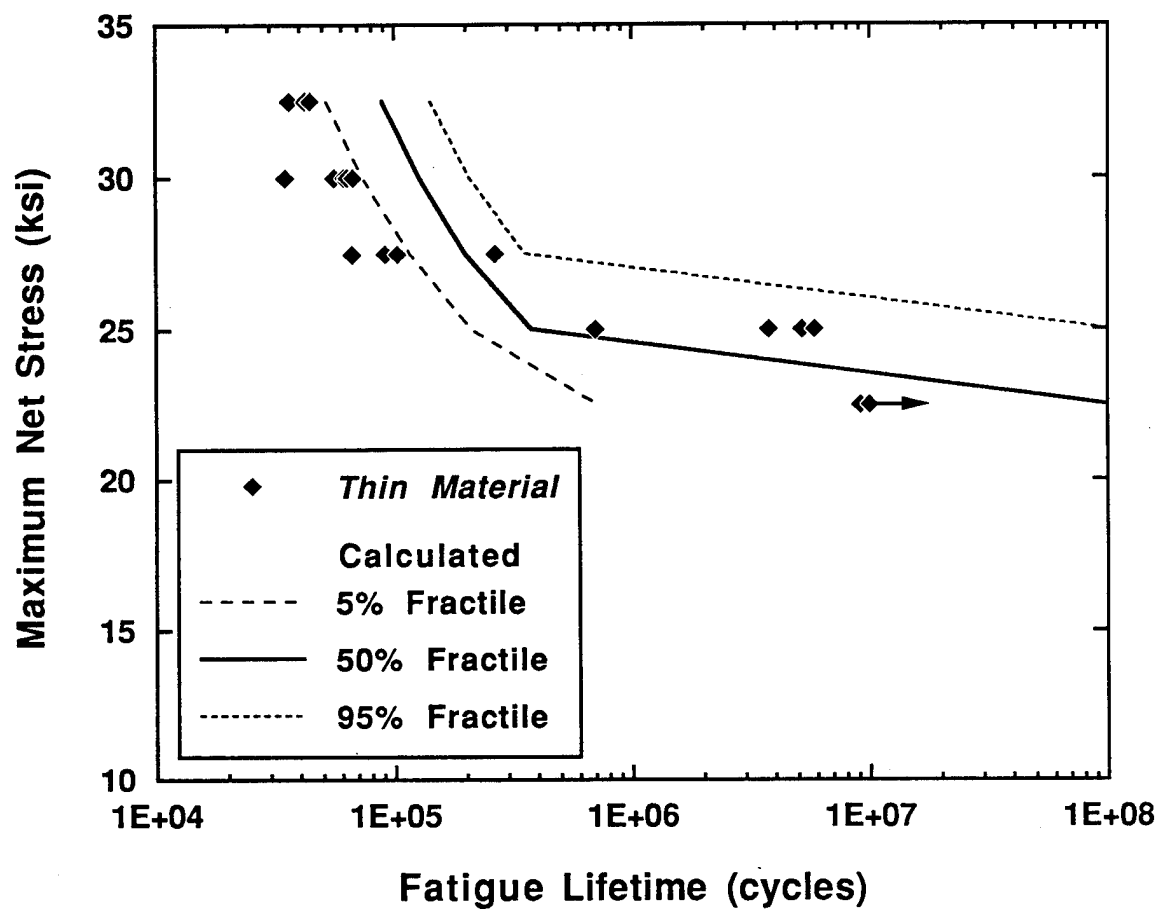
Figure 3.18. Comparison between the open hole fatigue life test data and the calculated S/N curve for the *thin material*. The testing was done at R=0.1, LT orientation, T/2 location, 30 Hz in lab air.
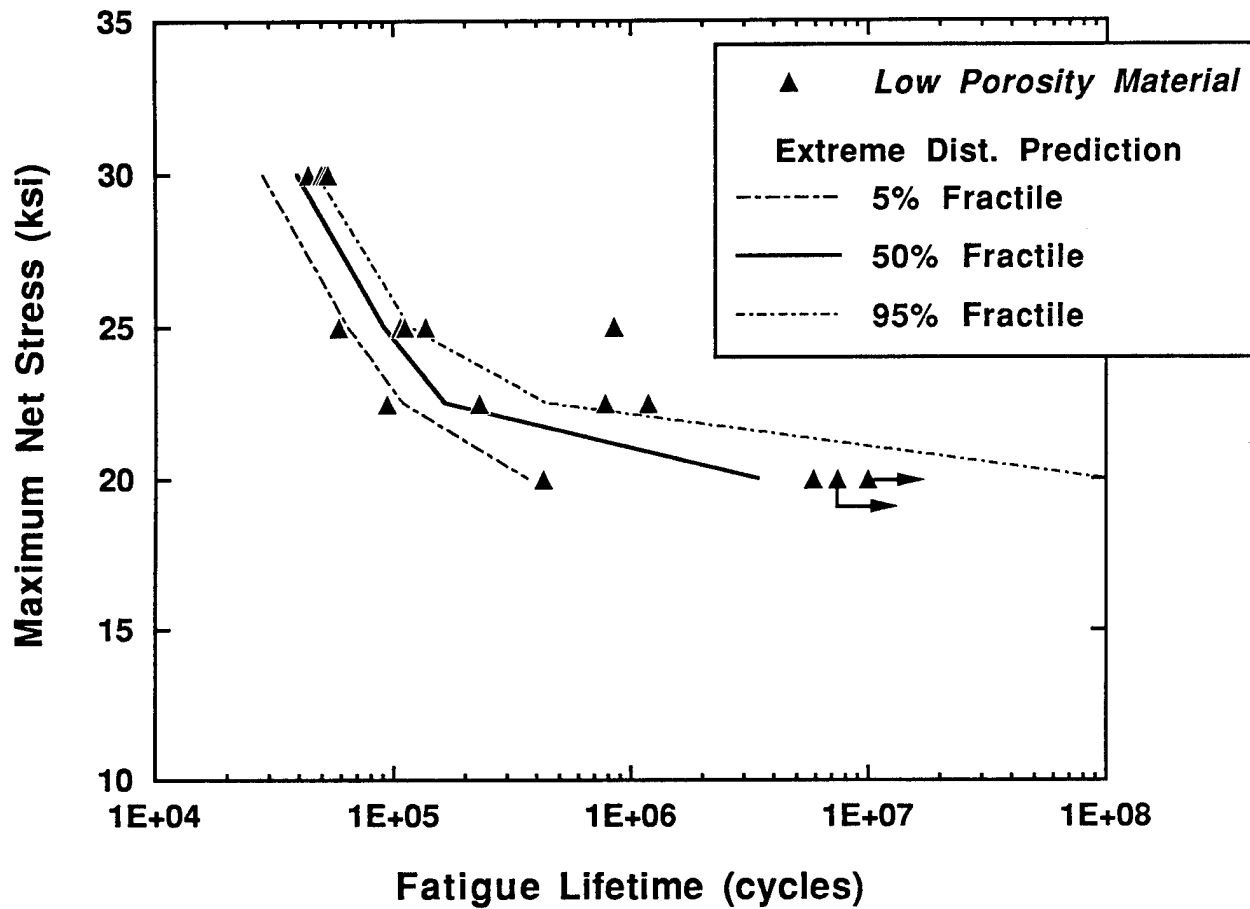
Figure 3.19. Comparison between the open hole fatigue life test data and model predictions made using scaled microfeature distributions from random plane metallography for the *low porosity material*. The testing was done at R=0.1, LT orientation, T/2 location, 30 Hz in lab air.

146
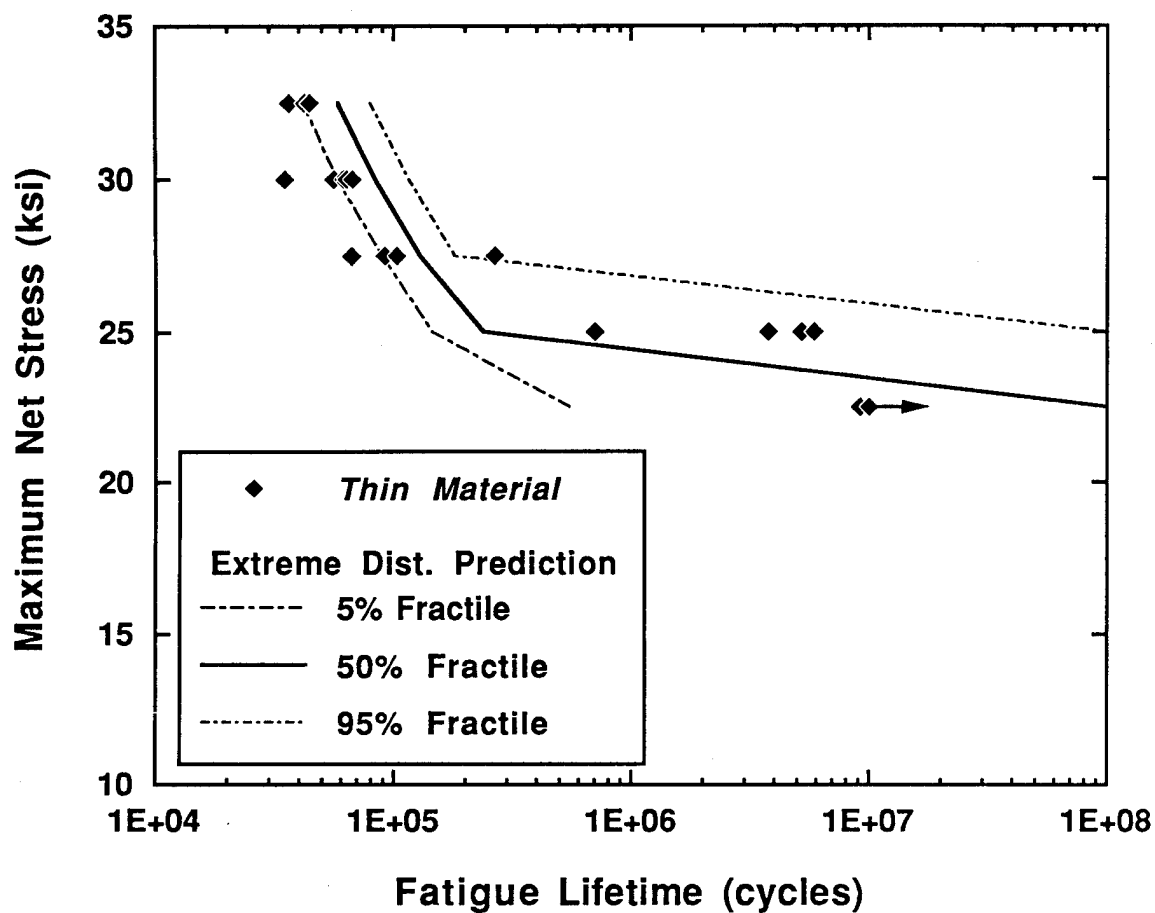
Figure 3.20. Comparison between the open hole fatigue life test data and model predictions made using scaled microfeature distributions from random plane metallography for the *thin material*. The testing was done at R=0.1, LT orientation, T/2 location, 30 Hz in lab air.
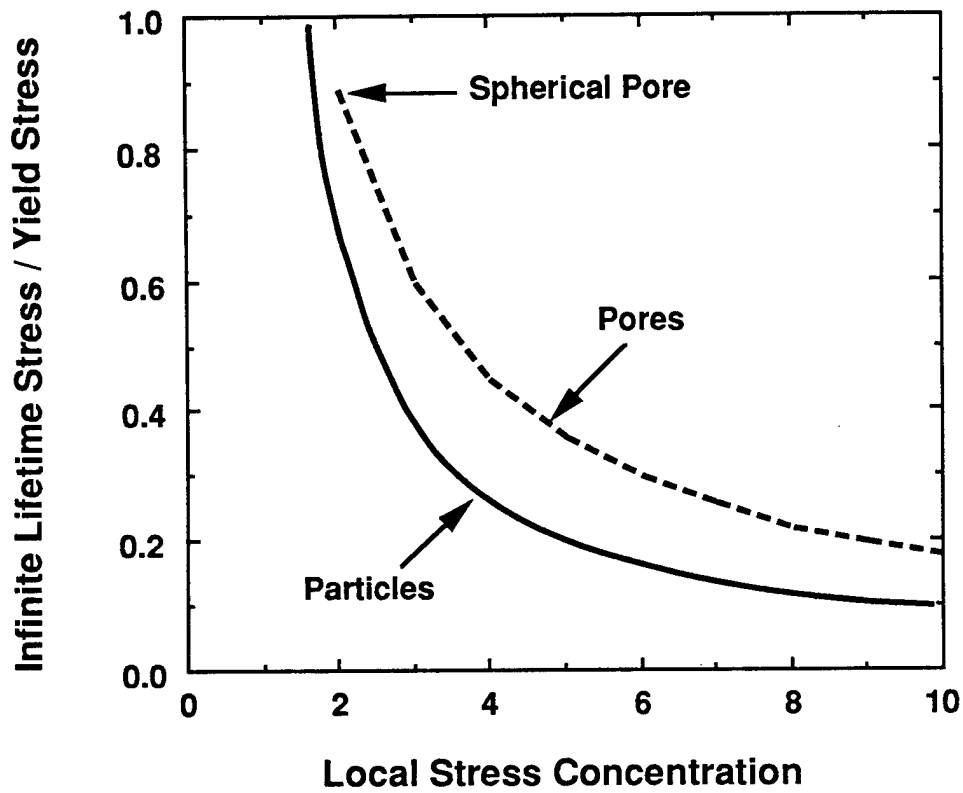
Figure 3.21. Plot of the sensitivity of the infinite life stress to the local stress concentration factor for both pores and cracked particles.

148
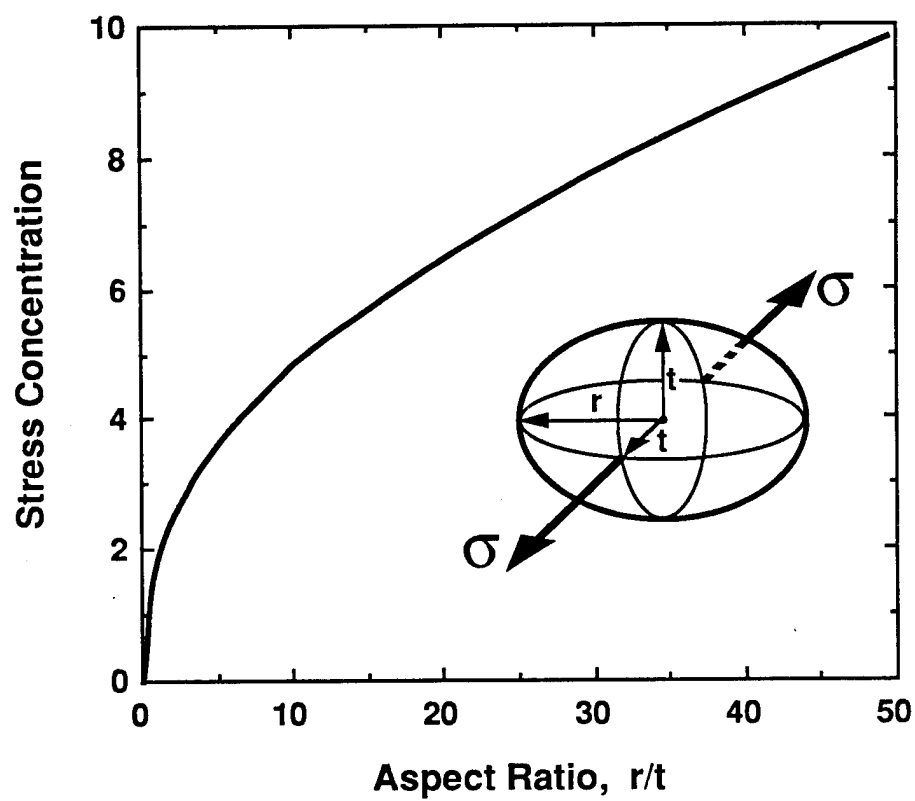
Figure 3.22. Stress concentration for a circular cavity of elliptical cross-section as a function of the aspect ratio.

149
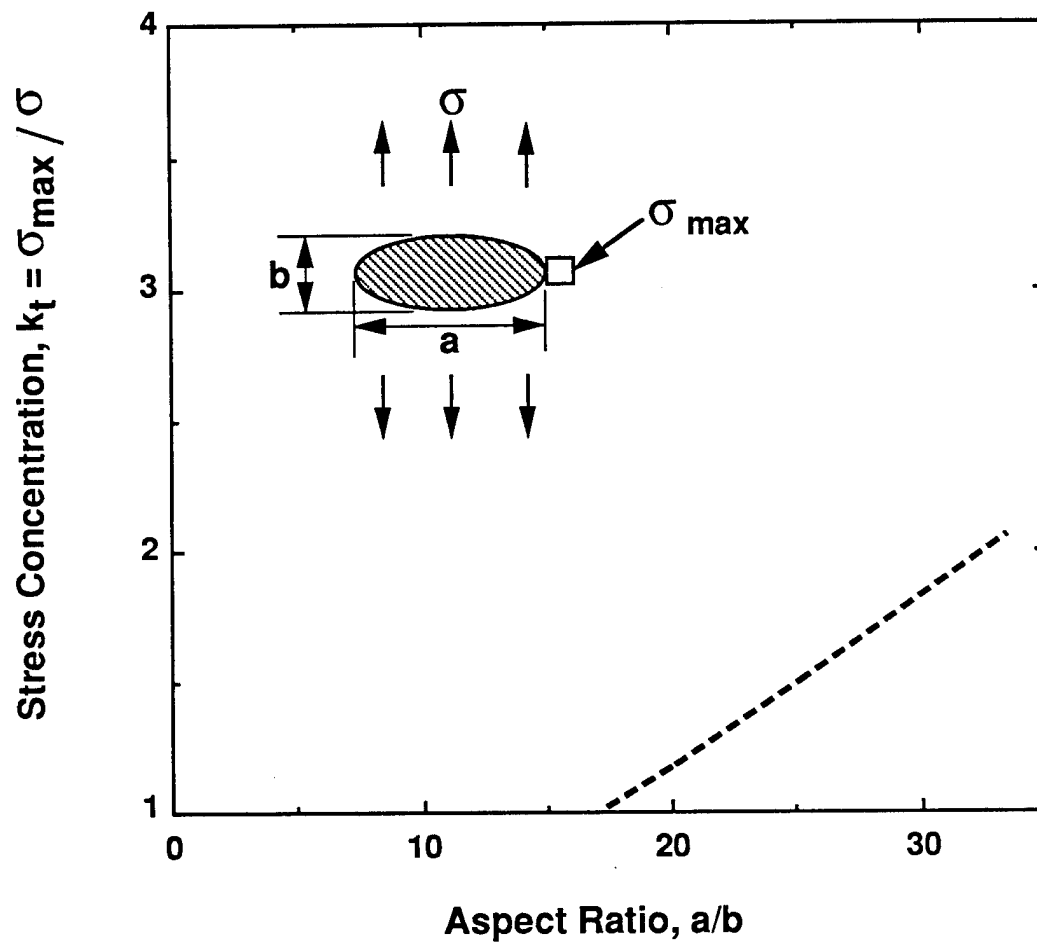
Figure 3.23. Stress concentration factor for an uncracked isolated rigid, elliptical, cylindrical particle.
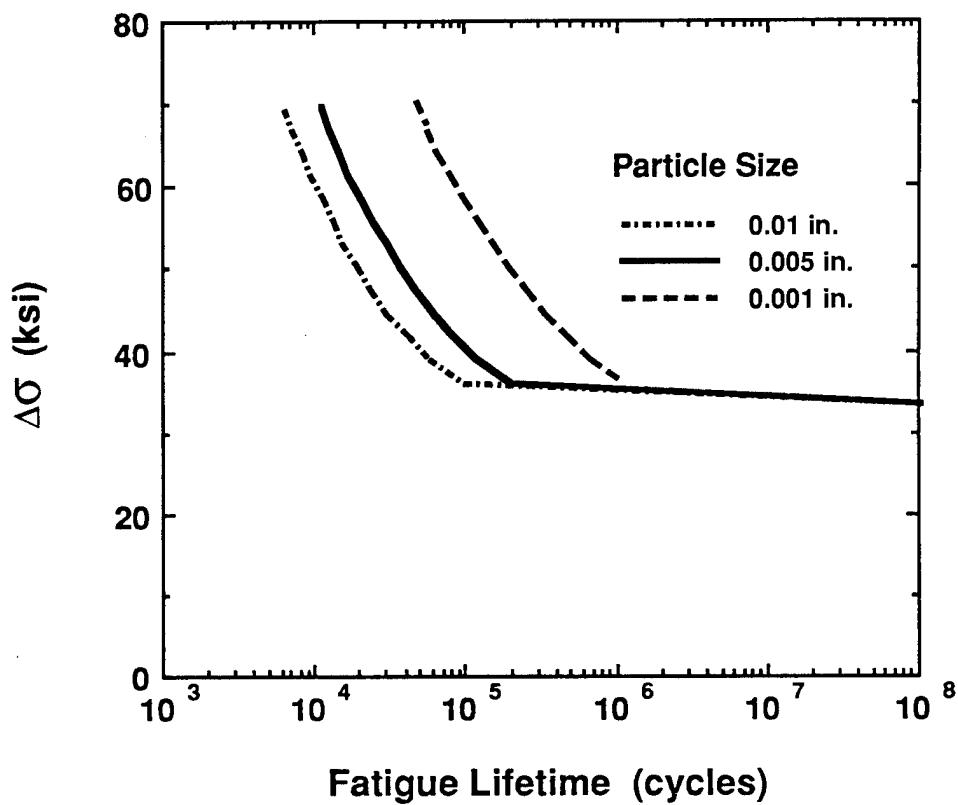
Figure 3.24. Sensitivity of fatigue stress versus lifetime (S/N) curve to particle size for yield a strength of 70 ksi.

151
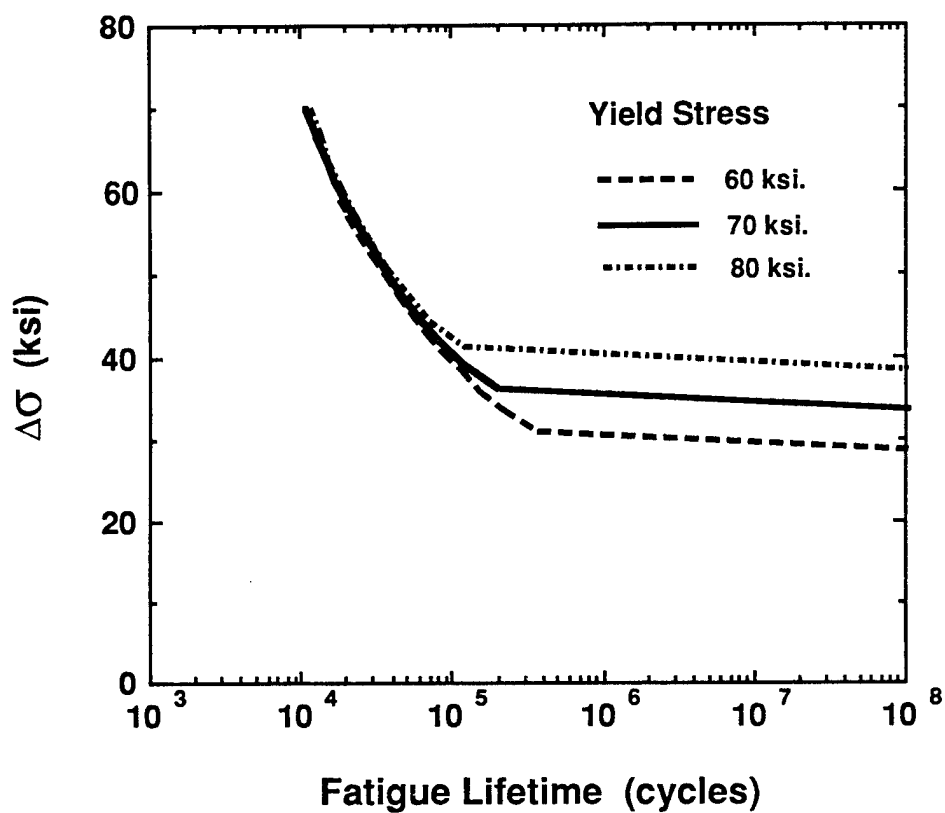
Figure 3.25. Sensitivity of fatigue stress versus lifetime (S/N) curve to yield stress for a particle size of 0.005 in. and local stress concentration $k_t = 2.0$.

152
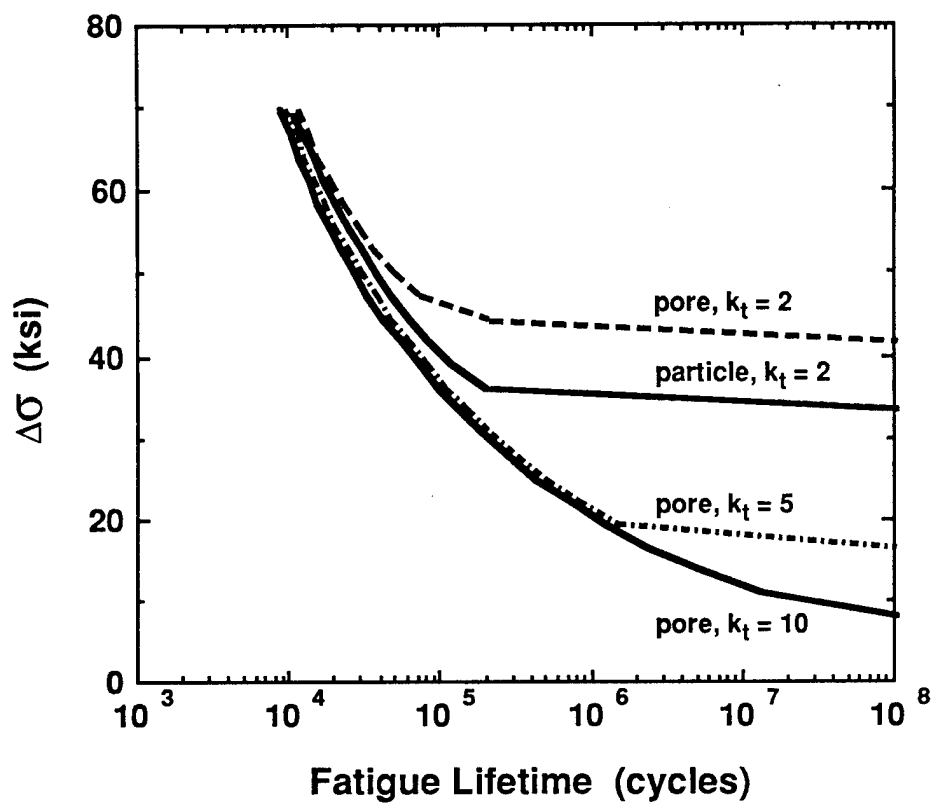
Figure 3.26. Comparison of fatigue stress versus lifetime (S/N) curves for particles and pores at different shapes which result in different k_t factors for yield strength 70 ksi., particle size = 0.005 in.
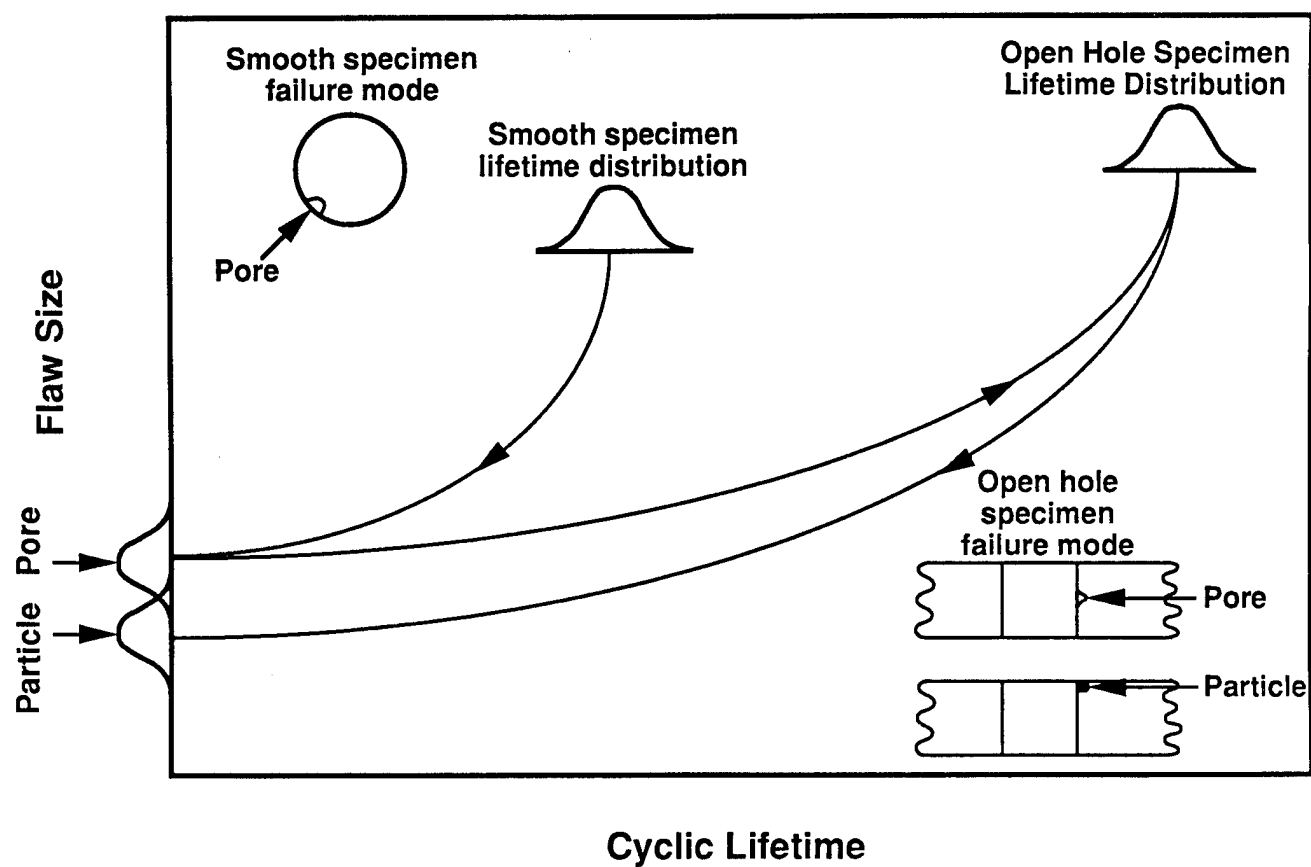
Figure 3.27. Schematic illustration of the procedure used to calculate equivalent lifetime micro-feature distributions for open hole specimen failures initiated at pores in the hole bore or at particles at the hole corner.

154
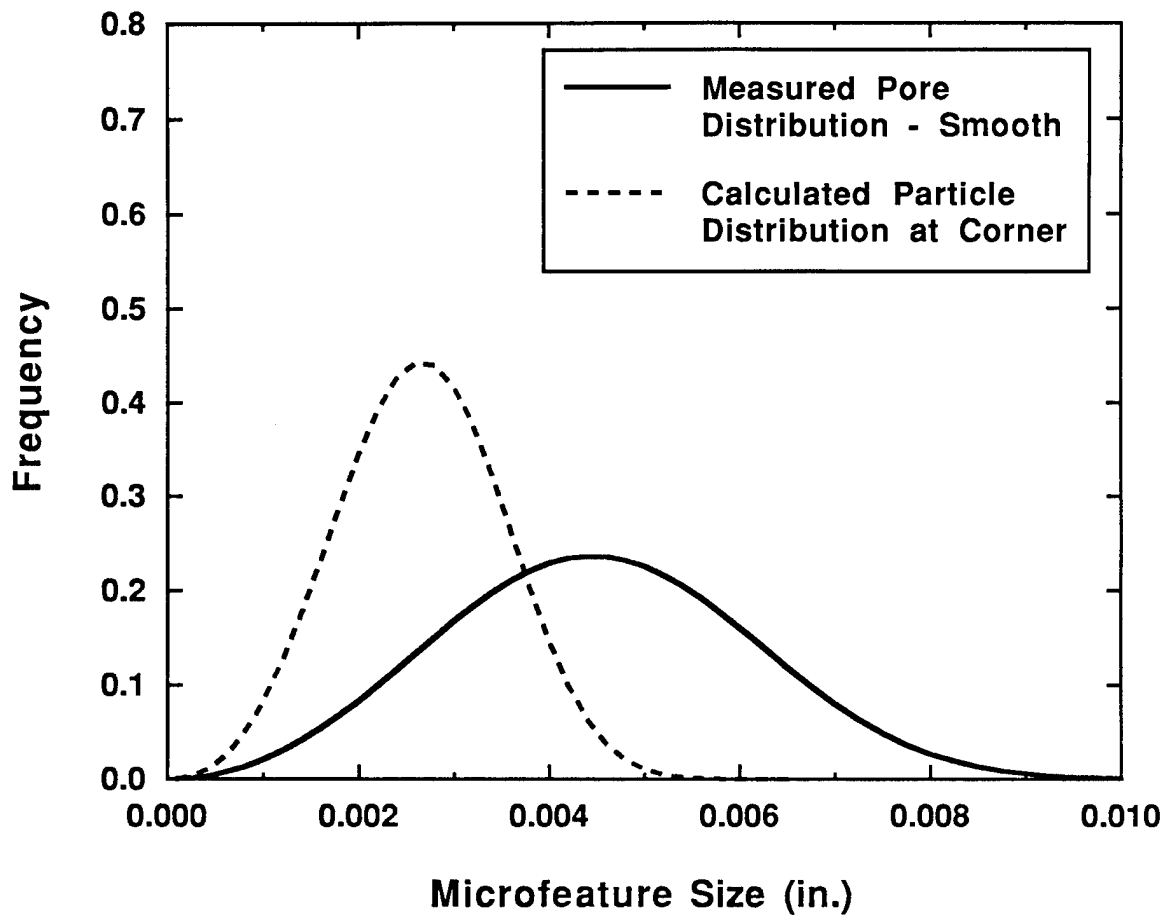
Figure 3.28. Measured extreme value pore distribution from smooth specimen tests of the *now material* and the calculated particle distribution for corner initiation sites in open hole specimen tests which results in equivalent lifetimes as pore initiated failures in the *now material*.

155
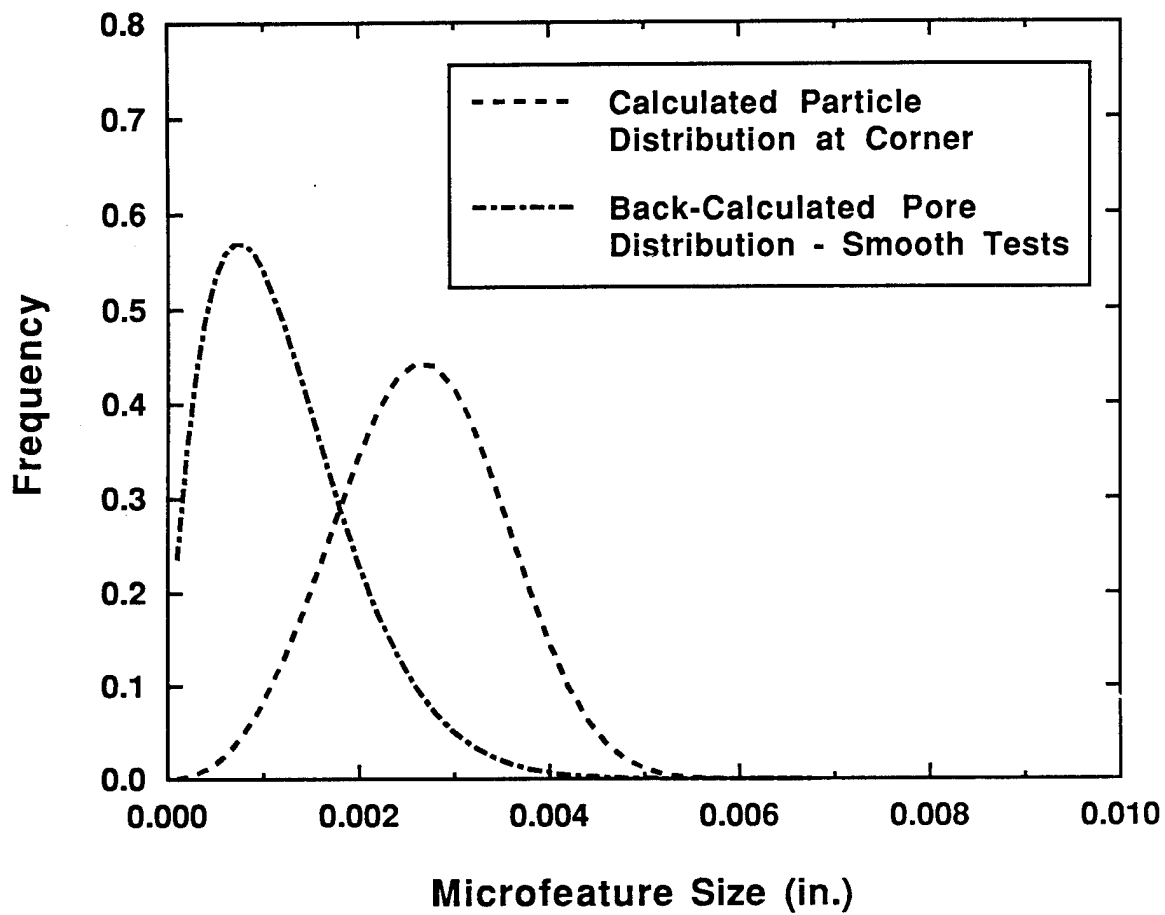
Figure 3.29. Calculated "equivalent life" particle distribution for corner initiation sites in open hole specimen tests and the pore distribution back-calculated from smooth specimen data for the *low porosity material*.

156
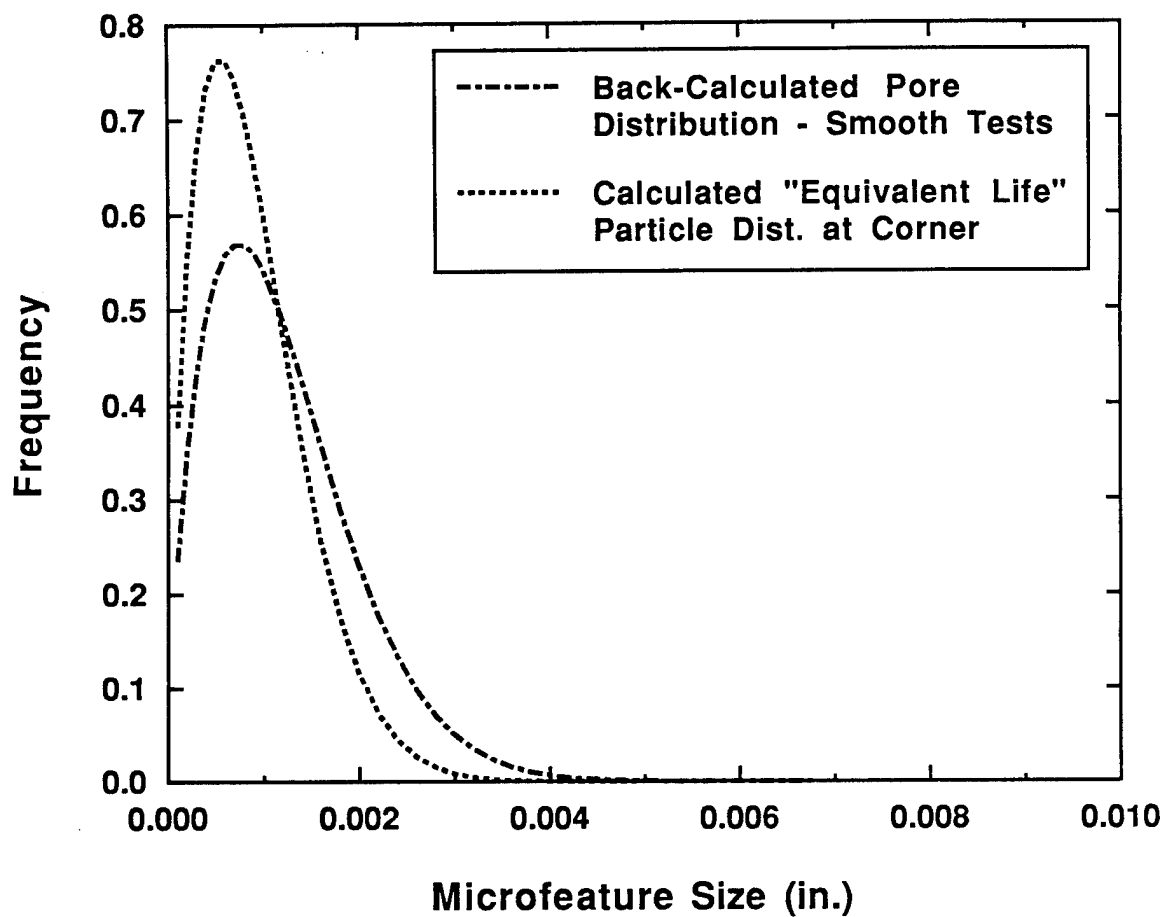
Figure 3.30. Back-calculated pore distribution from smooth specimen data for *low porosity material* and "equivalent life" particle distribution for corner initiation sites in open hole specimen tests.

157

Distribution

	No. of Copies
Office of Naval Research	
Attn: Scientific Officer, N00014	1
Administering Contracting Officer	1
Dr. L. E. Sloter, Code - 4421	1
Dr. A. K. Vasudevan, Code - 332	1
Y. Rajapakse, Code - 1132SM	1
800 N. Quincy Street	
Arlington, VA 22217-5660	
Director	1
Naval Research Laboratory	
Attn: L. Gause	
4555 Overlook Avenue S.W.	
Washington, DC 20375-5000	
Defense Technical Information Center	2
Attn: DTIC-FDAB	
Building 5, Cameron Station	
Alexandria, VA 22304-6145	
Naval Air Warfare Center	
Aircraft Division Warminster	
Attn: Code 4.3.3.1.R	5
Code 7.2.5.5	2
Dr. Margery E. Hoffman, Code 4333	1
P.O. Box 5152	
Warminster, PA 18974-0591	
Naval Air Warfare Center Aircraft Division	
Aerospace Materials Division	
Attn: Commander Code 4.3.4, Bldg 2188, MS-3	1
W. E. Frazier, Code 4.3.4.2	1
22541 Millstone Road	
Patuxent River, MD 20670-5304	
Naval Air Systems Command	
Attn: Subra S. Bettadapur, AIR - 4.3.4. 55B	1
Dave Cadman, AIR - 4.3.3.1	1
Wayne Koegel, AIR - 4.3.4 WK	1
Kal Leikach, AIR - 4.3.3.1	1
Mike McMahon, AIR - 4.3.3	1
Don Polakovics, AIR - 4.3.3.1	1
1421 Jefferson Davis Highway	
Arlington, VA 22243	
Naval Aviation Depot	1
Attn: J. T. Cammett, Code 4.3.4.1	
P.S.C Box 8021	
Cherry Point, NC 28533-0021	

	No. of Copies
Center for Naval Analysis 4401 Fort Avenue P.O. Box 16268 Alexandria, VA 22302-0268	1
Commander United States Naval Academy Attn: Mechanical Engineering Dept. Annapolis, MD 21402	1
Commander U.S. Naval Postgraduate School Attn: Technical Library Monterey, CA 93943	1

Commanding Officer
Wright Laboratory
Attn:　　Dr. Kumar V. Jata, WL/MLSA 1
   Verner J. Johnson, WL/FIB AA 1
   Dr. John W. Lincoln, ASC/ENFS, Bldg. 125 1
   Dr. Ted Nicholas, WL/MLL 1
   Neal Ontko, WL/MLSE, Bldg. 652 1
   Jerry Petrak, WL/MLLM 1
   James L. Rudd, WL/CCI, Bldg. 45 1
   Dr. G. Sendeckyj, WL/FIBEC 1
Wright Patterson AFB, OH 45433

Administrator
National Aeronautics and Space Administration
 Langley Research Center
Attn: Technical Library 1
   Tom Bales, MS 188A 1
   Dr. Charles E. Harris, MS - 188E 1
   W. Barry Lisagor, MS 188A 1
   Dr. James C. Newman, MS-188-E 1
   Dr. Robert S. Piascik, MS-188-E 1
Hampton, VA 23665

Administrator
National Aeronautics and Space Administration
 Lewis Research Center
Attn: Technical Library 1
   Dr. Hugh R. Gray, MS 49-1 1
21000 Brookpark Road
Cleveland, OH 44135

Administrator 1
National Aeronautics and Space Administration
 George C. Marshall Space Flight Center
Attn: Technical Library
Huntsville, AL 35812

Administrator
National Aeronautics and Space Administration   1
  Headquarters
Attn: Tom Crooker, Code RNH
600 Independence Ave S.W.
Washington, DC 20546

Administrator
National Aeronautics and Space Administration
  Lyndon B. Johnson Space Center
Attn: Technical Library   1
        Royce G. Forman, Materials Branch (EM2)   1
Houston, TX 77058-0001

Commanding Officer   1
Advanced Systems Research and Analysis Office ASRAO
Attn: Library M/S 219-3
Ames Research Center
Moffett Field, CA 94035-1000

Commanding Officer   1
Picatinny Arsenal
PLASTEC
Attn: Librarian, Code DRDAR-SCM-0, Bldg. 351N
Dover, NJ 07801

U.S. Department of Transportation
  FAA Technical Center
Attn: Technical Library   1
        Dr. Catherine A. Bigelow, AAR-430, Bldg 210   1
        Dr. Paul Tan, AAR-433, Bldg. 210   1
Atlantic City International Airport, NJ 08405

Center for Information and Numerical Data   1
  Analysis and Synthesis (CINDAS)
Attn: Harold Mindlin
Purdue University
1293 Potter Engineering Center
West Lafayette, IN 47907-1293

Boeing Co. Wichita Division   1
Attn: Technical Library, K78-38
P.O. Box 7730
Wichita, KS 67277-7730

Boeing Vertol Company   1
Attn: Technical Library
P.O. Box 16858
Philadelphia, PA 19142

General Electric Company
Attn: Technical Library   1
One Neuman Way
Cincinnati, OH 45215

General Electric Company   1
Attn: Technical Library
P.O. Box 8555
Philadelphia, PA 19101

Lockheed Martin Aeronautical Systems Company
Attn: Technical Information, Dept 72-34, Zone 26   1
        Dr. Thomas Brussat, Dept. 73-E, Zone 0987   1
        Dr. David J. Chellman, Dept. 7J/C1, Zone 0150   1
        D. G. Richardson, Dept. 73-C2, Zone 0150   1
        Wes W. Sullins, Dept. 73-B4, Zone 0160   1
86 South Cobb Drive
Marietta, GA 30063

Lockheed Martin/Missles and Space Company   1
Attn: Technical Library
1111 Lockheed Way Sunnyvale, CA 94088

Lockheed Martin Tactical Aircraft Systems
Attn: Administrator, Technical Library   1
        Dr. G. W. Henderson, MZ 2853   1
        Dr. Sherrell D. Manning, MZ 4267, Bldg. 500   1
P.O. Box 748
Ft. Worth, TX 76101

McDonnell-Douglas Aerospace East
Attn: Technical Library   1
        Craig Brooks, M/C 0012741   1
        Dianne Chong, M/C 1066089   1
        Charlie Saff, M/C 1022147   1
        Dr. K. K. Sankaran, M/C 1111041   1
P.O. Box 516
St. Louis, MO 63166

McDonnell-Douglas Aerospace West
Attn: Technical Library, M/C 212-10   1
        Ravijit Kahandal, M/C 35-80   1
        Michael Tarkanian, M/C 801-38   1
3855 Lakewood Blvd.
Long Beach, CA 90846

McDonnell Douglas Aircraft Company
Attn: Amar S. Amin, M/C TA-EE3 (54-03)   1
        Robert. G. Eastin, M/C TA-EEO 159-59   1
1510 Hughes Way
Long Beach, CA 90810-1864

McDonnell Douglas Aerospace MDA
Attn: Jin C. Yu   1
2401 East Wardlow Road
Long Beach, CA 90807-4418

Northrop Grumman Corporation   1
Attn: Technical Library
South Oyster Bay Road
Bethpage, Long Island, NY 11714

Northrop Grumman Corporation
Attn: Technical Library   1
        Dr. Suphal P. Agrawal   1
        Dr. Govind R. Chanani   1
One Northrop Avenue
Hawthorne, CA 90250

Pratt & Whitney
Attn: Technical Library   1
P. O. Box 109600
W. Palm Beach, FL 33410

Rockwell International / North American Aircraft Division   1
Attn: Technical Library
P.O. Box 92098
Los Angeles, CA 90009

Rockwell International Science Center
Attn: Technical Library   1
Thousand Oaks, CA 91360

Sikorsky Aircraft   1
Attn: Technical Library
North Main Street
Stratford, CT 06601-1381

A. Conli   1
Ford SRL Lab
Mail Drop 3182
P.O. Box 2053
Dearborn, MI 48121

Dr. Joseph P. Gallagher   1
University of Dayton Research Institute
Structural Integrity Division
300 College Park
Dayton, OH 45469-0120

Prof. A. F. Grandt   1
School of Aeronautics and Astronautics
Grissom Hall
Purdue University
W. Lafayette, IN 47907

Prof. Ben M. Hillberry   1
Purdue University
School of Mechanical Engineering
W. Lafayette, IN 47907-1288

Prof. David Hoeppner   1
University of Utah
Dept. of Mechanical Engineering
3209 Merrill Engineering Building
Salt Lake City, UT 84112-0001

Stephan J. Hudak, Jr.   1
Southwest Research Institute
6220 Culebra Road
P.O. Drawer 28510
San Antonio, TX 78284

Dr. M. A. Przystupa   1
University of California, Los Angeles
Department of Materials Science and Engineering
School of Engineering and Applied Science
405 Hilgard Avenue
Los Angeles, CA 90024-1595

Richard Rice   1
Engineering Mechanics Department
Battelle
505 King Avenue
Columbus, OH 43201-2693

Prof. Ashok Saxena   1
Georgia Institute of Technology
School of Materials Science & Engineering
Atlanta. GA 30332-0245

Edgar A. Starke, Jr.   1
Engineering and Applied Sciences
University of Virginia
Dept. of Materials Science
Thornton Hall A125
Charlottesville, VA 22901

Prof. R. P. Wei   1
Dept. of Mechanical Engineering and Mechanics
Lehigh University
19 Memorial Drive West
Bethlehem, PA 18015

Dr. Jann Yang   1
Dept. of Civil Engineering
University of California at Irvine
Irvine, CA 92717